



**University of
Nottingham**

UK | CHINA | MALAYSIA

Advanced modular modulation, control and magnetic integration of MAB converters

Thesis submitted to the University of Nottingham for the degree of

Doctor of Philosophy, 2024

Yicong Cai

20382562

Supervised by

Chunyang Gu

Jing Li

He Zhang

Abstract

Multi-input multi-output (MIMO) DC-DC converters are widely used in the on-board propulsion or traction systems of transportation electrification applications for power density enhancement. Among these converter topologies, multiple active bridge (MAB) converters, which can be regarded as an extended MIMO version of Dual active bridge (DAB) converters, has been recently developed aiming to decrease the weight and/or volume consumption of active components and enhance the availability. However, the conventional control and modulation strategies like proportional-integral (PI) control with single phase shift (SPS) modulation are not suitable for its nonlinear voltage characteristics, facing the drawbacks of low power transfer quality and efficiency, slow dynamic responses and limited controllable power transfer capability. In addition, accompanied by the growth of the power density demanding, the tendency of power density improvement leads to the magnetic integration investigation of the isolated HF links, that is to integrate the series inductors and a high frequency transformer (HFT) into a single magnetic component by increasing the leakage inductance of the HFT.

Therefore, this thesis firstly proposes a series of advanced control methods combined with the modulation algorithms to improve the efficiency of power transfer, quality of power transfer, dynamic performance, control accuracy, and control flexibility for the MAB converter systems. In modulation part, non-ideal effects which are commonly ignored in conventional modulations are evaluated with their impacts aimed to promote the quality of power transfer. After evaluations, generalized phase shift (GPS) modulation was utilized in the decoupling algorithm to quantitatively characterize the relationship between the phase shift and the port average current, aiming at achieving the ‘modular’ switching of the fundamental modulations. Based on these modulations, a Newton-Iteration based decoupling algorithm combined with a current decoupling control algorithm is proposed. This control strategy composes of the DC reference current generators and the current to phase shifts decoupling algorithm, which divides the MAB converter with N ports, into $N - 1$ virtual DAB sub-branches. Besides the switching of modulations, the decoupling control strategies are also switchable. In this thesis, a power

decoupling based configurable control (PDC-MPC) strategy inspired by the model predictive control (MPC) was developed to improve the transition performance.

To achieve the magnetic integration while promising the accuracy of voltage control, the leakage inductance of the integrated transformer should be large and accurate enough. Hence, the first step is to estimate the leakage inductance accurately, and judge whether structural modification is required for the selected core at the transformer design stage to achieve the aimed leakage inductance. This thesis proposed a reluctance-based leakage inductance evaluation strategy for the accurate estimation with air-path leakage considered. As the common calculations of the winding-arrangement-dominated leakage inductance commonly ignores the air-path leakage fluxes. Based on the estimation of the threshold leakage inductance, an optimized magnetic integration procedure for planar transformer has been developed. Then, a novel radially symmetrical star-shape core (RSSC) high frequency multi-winding transformer (HFMT) with split windings for the generalized N-port MAB converters is proposed. The developed HFMT can adjust the leakage inductances within a wide range by the magnetic integration control parameters, which includes lengths of extension legs, side and central pillars, horizontal air gaps, turns of windings and winding distribution ratio. Port consistency is promised by the insertion of vertical flux barriers.

The feasibility and effectiveness of the proposed improved modulation, modular decoupling control strategies and controllable integrated HFMT have been validated by the simulations and experiment. Results of the validations shows good matches about the proposed issues.

Acknowledgements

First and foremost, I am extremely grateful to my supervisors, Dr. Chunyang Gu, and Prof. Jing Li, and Prof. He Zhang for their invaluable advice, continuous support, and patience during my Ph.D. study and research. This is the basis for my continued growth during my Ph.D. candidate stage. I would also like to sincerely thank Dr. Jiajun Yang, Prof. Giampaolo Buticchi and Dr. Sandro Guenter for their technical support, experience sharing and encouragement. I would like to thank all the members of the power electronics machine control (PEMC) research group, especially my fellow graduate students, for the interesting discussions and for all the fun we had together in the past four years. Additionally, I would like to thank Miss. Yingzhi Chen, for the perfect timing of her appearance not only helped me immerse myself in the research work during my candidate stage but also encouraged me to face the life after graduation bravely.

Last but not the least, I would like to thank my parents. Without their support, help and motivation, I would never have been able to pursue my dreams.

Ningbo, Sept 17, 2024

Yicong Cai

List of Publication

Journal papers

1. **Yicong Cai**; Jing Li; Chunyang Gu; Jiajun Yang; Sandro Guenter; Giampaolo Buticchi; and He Zhang, ‘A Modular Modulation Decoupling Algorithm for Multiple Active Bridge Based Multiport EV Charger’, in IEEE Journal of Emerging and Selected Topics in Power Electronics 2024 Vol. 12 Issue 4 Pages 3637-3649, DOI: 10.1109/JESTPE.2024.3393867
2. **Yicong Cai**; Chunyang Gu; Jing Li; Jiajun Yang; Sandro Guenter; Giampaolo Buticchi; and He Zhang, ‘Dynamic Performance Enhancement of a Triple Active Bridge With Power Decoupling-Based Configurable Model Predictive Control’, in IEEE Transactions on Transportation Electrification 2023 Vol. 9 Issue 2 Pages 3338-3349, DOI: 10.1109/TTE.2022.3226471
3. **Yicong Cai**; Chunyang Gu; Jing Li; Jiajun Yang; Sandro Guenter; Giampaolo Buticchi; and He Zhang, ‘Magnetic Integration for a Dual Active Bridge Converter Planar Transformer With Accurate Leakage Inductances Estimation’, in IEEE Access, vol. 12, pp. 112278-112289, 2024, doi: 10.1109/ACCESS.2024.3442288.
4. **Under major revision: Yicong Cai**; Chunyang Gu; Jing Li; Jiajun Yang; Sandro Guenter; Giampaolo Buticchi; and He Zhang, ‘A Radially Symmetrical Star-shape Core Multi-winding Transformer With Controllable Magnetic Integration for N-port MAB converters’, in IEEE Transactions on Power Electronics.

Conference papers

1. **Yicong Cai**; Chunyang Gu; Jing Li; Jiajun Yang; Giampaolo Buticchi; and He Zhang, ‘An Advanced Extended Phase Shift Modulation Strategy of Dual Active Bridge Converter Considering Magnetizing Inductance’, IECON 2021 – 47th Annual Conference of the IEEE Industrial Electronics Society 13-16 Oct. 2021, 2021, Pages: 1-6, DOI: 10.1109/IECON48115.2021.9589305
2. **Yicong Cai**; Giampaolo Buticchi; Chunyang Gu; Jing Li; Edivan Laercio Carvalho; and He Zhang, ‘Comparison of Decoupling Control Strategies for Multiple Active Bridge DC-DC Converter’, 2023 IEEE 17th International Conference on Compatibility, Power Electronics and Power Engineering (CPE-POWERENG) 14-16 June 2023, 2023, Pages: 1-6, DOI: 10.1109/CPE-POWERENG58103.2023.10227395

Patent Application

1. **Yicong Cai**, Chunyang Gu, Jing Li, and He Zhang, Chinese invention patent application, Application No: 2202311703855.6 “A multiport transformer designed for the multiple active bridge converters used in more electric aircrafts”

Contents

Abstract	2
Acknowledgements	4
List of Publication	5
Contents	6
List of figures	9
List of tables	17
Abbreviations	20
List of symbols	23
1. Introduction	25
1.1 Isolated Bidirectional DC-DC Converter and isolated MIMO systems in electrified transportation applications	25
1.2 MIMO DC-DC converter topologies	32
1.2.1 Configurations using DAB converters	32
1.2.2 MAB converters and other MIMO converter configurations	33
1.3 Aims and objectives	36
1.4 Major research contributions	38
1.5 Thesis organization	39
2. Literature Review	42
2.1 Chapter overview	42
2.2 Modulation strategies of MAB converters and modulation optimization by considering non-ideal effects	43
2.2.1 Fundamental modulation strategies in DAB converter	43
2.2.2 GPS modulation developed from fundamental modulations	46
2.2.3 Non-ideal effect involved in the MAB power characteristics of modulation	47
2.3 Advanced nonlinear control strategies for dynamic and steady-state performance improvement of the MAB converters	49
2.3.1 Nonlinear control methods	49
2.3.2 Decoupling control for MAB converters	53

2.4 Research on design and implementation of HF transformer in MAB converters with accurate leakage inductance estimation.....	57
2.5 Summary of this chapter.....	62
3. Modulations strategies considering the non-ideal effects to improve MAB power transfer quality	65
3.1 Chapter overview	65
3.2 A modified EPS modulation for the DAB converters considering the transformer magnetizing inductance	65
3.2.1 Power characteristic and soft switching condition for magnetizing inductance involved SPS modulation.....	67
3.2.2 An advanced EPS modulation and its ZVS condition for DAB converter considering the magnetizing inductance.....	71
3.3 A modulation related parameter dependency evaluation based on the non-ideal effects involved in MAB power characteristics.....	75
3.3.1 Analysis of the dead-time effect.....	76
3.3.2 Saturation of the HF transformer.....	80
3.3.3 Dependency evaluation for the common parameters involved in modulation power characteristics.....	82
3.4 Simulation and experimental validation.....	84
3.5 Summary of this chapter.....	89
4. Modular modulation based decoupling control strategies and its dynamic performance optimization.....	91
4.1 Chapter overview	91
4.2 Generalized phase shift modulation based decoupling control with model predictive control strategy for dynamic performance enhancement.....	93
4.2.1 A general introduction of applying Newton iteration with MPC control in MAB converter	93
4.2.2 A novel MPC based power decoupling control strategy for TAB converter.....	95
4.3 A modular modulation algorithm based decoupling control of Multiple Active Bridge converter for power transfer efficiency and flexibility improvements	106
4.3.1 Multiple Active Bridge Based Multiport EV Charger	106
4.3.2 An online offline Newton decoupling (O ² ND) algorithm for current decoupling.....	107
4.3.3 Case study of the ‘Modular’ modulation with the O ² ND current decoupling algorithm.....	114
4.4 Simulation and experimental validation.....	115

4.4.1 Experimental validation for the PDC-MPC.....	115
4.4.2 Experimental validation for the O ² ND algorithm.....	125
4.5 Summary of this chapter.....	134
5. Design of multi-winding integrated HF transformers with accurate and controllable leakage inductances	136
5.1 Chapter overview	136
5.2 Magnetic Integration for a DAB Converter Planar Transformer with Accurate Leakage Inductances Estimation	137
5.2.1 Definition of the equivalent leakage, magnetizing inductance with an optimized magnetic integration procedures for two-port integrated planar transformers	138
5.2.2 Core and winding design of the integrated two-port planar transformer	141
5.2.3 Accurate estimation of the equivalent magnetizing and leakage inductance.....	143
5.3 A Radially symmetrical star-shape core multi-winding transformer with controllable magnetic integration for N-port MAB converters.....	153
5.3.1 Integration theory for the N-port RSSC HFMT	154
5.3.2 A four-port case study of the proposed HFMT scenario applied in a QAB converter	160
5.3.3 Impact of the magnetic integration control parameters and generalized design procedures for the proposed RSSC HFMT.....	164
5.4 Saturation evaluation for the practical multiport HF transformers.....	171
5.5 Simulation and experimental validation.....	175
5.5.1 Simulation and experimental validation for the two-port integrated planar transformer designed by the reluctance-based strategy	175
5.5.2 Simulation and experimental validation for the four-port case study of the proposed RSSC HFMT.....	182
5.6 Summary of this chapter.....	191
6. CONCLUSIONS AND FUTURE WORK.....	193
6.1 Conclusions	193
6.2 Future work	195
REFERENCES	196

List of figures

Fig. 1.1.1 A typical MEE system in MEA applications	27
Fig. 1.1.2 MEA distribution structure with LVDC and HVDC network	27
Fig. 1.1.3 Power systems have the same function with MIMO converters but organized by multiple SISO converters	29
Fig. 1.1.4 An example of a DC-based EPDS with MIMO converters involved in its topology.....	30
Fig. 1.1.5 EV power systems with multiple input sources, a) conventional topology with multiple SISO converters. b) MIMO topology	31
Fig. 1.2.1 Topology of a conventional DAB converter in a common DC-link MIMO system	32
Fig. 1.2.2 Multiport power conversion configurations, (a). Traditional topology with an array of DABs linked to a common DC bus. (b). MMAB configuration with secondary sides of two-port transformers directly linked to a common AC bus. (c). MAB topology with a MT linked to voltage-level varied loads.....	35
Fig. 1.2.3 MAB configured electric traction system [87]	36
Fig. 1.5.1 Story line of the thesis	41
Fig. 2.3.1 Block diagram of OA based decoupling control.....	53
Fig. 2.3.2 Block diagram of SMC based decoupling control.....	55
Fig. 2.3.3 Block diagram of state-space linearize decoupling control.....	56
Fig. 3.2.1 Equivalent circuit of a practical transformer in the DAB converter.....	66
Fig. 3.2.2 (a) T-shaped transformer equivalent circuit (b) π -shaped equivalent circuit...	67
Fig. 3.2.3 Comparison of average power transfer calculated by the power characteristic with the ideal SPS and SPS considering existence of L_m when $a = 5$	68

Fig. 3.2.4 Waveforms of the non-ideal SPS modulated DAB converter.....	69
Fig. 3.2.5 (a) Waveforms of EPS modulated DAB when $0 < D_o \leq \frac{D_{IN,1}}{2}$ considering L_m	
(b) Waveforms of EPS modulated DAB when $\frac{D_{IN,1}}{2} < D_o \leq 1$ considering L_m ...	72
Fig. 3.2.6 (a) ZVS area of EPS modulation with L_m neglected (b) ZVS area considering	
L_m	73
Fig. 3.2.7 (a) MEPS modulation (b) AEPS modulation.....	74
Fig. 3.2.8 Power characteristics of AEPS and MEPS modulation strategy	75
Fig. 3.3.1 Generic voltage waveforms of the SPS modulated DAB converter and its	
switchers.....	77
Fig. 3.3.2 Voltage polarity reversal phenomenon during the dead-time	78
Fig. 3.3.3 Ideal (black) and non-ideal (blue) dead-time considered curve of the transferred	
power with D_o	78
Fig. 3.3.4 Voltage and current waveforms at the transformer node of a DAB converter, (a)	
when transformer is saturated. (b) when transformer is operating normally.....	81
Fig. 3.4.1 Power transferred under SPS modulation with $M = 5, 20$ and 100	84
Fig. 3.4.2 Voltage and current of primary and secondary bridge for SPS modulation with	
L_m considered ($D_o = 0.1$).....	85
Fig. 3.4.3 Power of two advanced EPS modulation methods with $M=5$	85
Fig. 3.4.4 Voltage and current of primary and secondary bridge ($D_o = 0.1$)	86
Fig. 3.4.5 (a) Voltage and Current waveform (1000W) (b) Voltage and Current waveform	
(3200W)	86
Fig. 3.4.6 (a) Current waveforms of MEPS (3200W) (b) Current waveforms of AEPS	
(3200W)	87
Fig. 3.4.7 Practical DAB plant with HF (50kHz) transformer.....	88

Fig. 4.2.1 A general topology of TAB converter with one input port and two output ports with pure resistive loads	96
Fig. 4.2.2 Generic voltage waveforms of the SPS modulated TAB converter.....	97
Fig. 4.2.3 Flowchart of the initialed reference current search of MPC.....	98
Fig. 4.2.4 Relationship of current decoupling when $A = B = C = 12D$	102
Fig. 4.2.5 Control diagram of proposed MPC	102
Fig. 4.2.6 Flow chart of the enhanced binary search for current prediction	105
Fig. 4.3.1 The definition of the ‘modular’ in the proposed decoupling control strategy.	106
Fig. 4.3.2 Block diagram of the proposed current decoupling control.	107
Fig. 4.3.3 Operation logic of three iterative current decoupling algorithms: ND (left), SND (middle), O ² ND (right).....	111
Fig. 4.3.4 Outer phase shift ratios after each iteration of three iterative current decoupling algorithms, where $D1 = 0$, $D2$, $D3$, and $D4$ are outer phase shifts: $D2,1$, $D3,1$, and $D4,1$. (a) Under the initial reference voltage. (b) Under $V4_{ref} = 2$ pu condition.	112
Fig. 4.3.5 Control complexity (measured by multiplications) with the increase of number of ports N for three current decoupling algorithms.	113
Fig. 4.3.6 The load side equivalent circuit of the MAB converter.....	115
Fig. 4.3.7 Control diagram of the proposed modular decoupling control with PI controller used as the current reference generator.....	115
Fig. 4.4.1 Simulation waveform: Step change of referenced voltage from 45V to 50V at port 3 with PI controller and PI with power decoupling.....	118
Fig. 4.4.2 Simulation waveform: Output voltage of port 2 and port 3 at initiating stage under PI with decoupling and preliminary MPC	118

Fig. 4.4.3 Simulation waveform: Voltage waveform of port 2 and port 3 with finalized PDC-MPC.....	118
Fig. 4.4.4 Simulation waveform: Step change of load (50% to 25% at port 3) for PI controller and PDM-MPC.....	119
Fig. 4.4.5 Simulation waveform: Step change of referenced voltage at port 3 for PI controller and PDM-MPC.....	119
Fig. 4.4.6 TAB converter plant used in the experimental verification.....	121
Fig. 4.4.7 Execution time of three control methodologies.....	122
Fig. 4.4.8 Evaluation of deviation coefficient β and steady state voltage ripple	122
Fig. 4.4.9 Open-loop examination with average port DC reference current variation...	123
Fig. 4.4.10 Waveforms of AC voltage and AC current at each port (a) Port 1, (b) Port 2, (c) Port 3.....	124
Fig. 4.4.11 Transition waveform comparison between PI + Decoupling and proposed MPC (a) Initiating stage, (b) Step change of loads, (c) step change of V_{ref}	124
Fig. 4.4.12 Port voltage waveforms of the QAB converter with two control method under different step changes. (a) Step change of V_{ref2} from 54 V to 58 V with the loads condition 1. (b) Step change of R_{L4} from 250 Ω to 100 Ω with the loads Condition 2.	127
Fig. 4.4.13 Waveforms of AC voltage and AC current in each port with different modulation strategies under loads condition 1. (a) SPS modulation. (b) SSPS modulation.	128
Fig. 4.4.14 Execution time of three decoupling algorithms.....	129
Fig. 4.4.15 The open loop validation of the O ² ND current decoupling algorithm.....	129
Fig. 4.4.16 Open-loop test with step change in reference DC current.	130

Fig. 4.4.17 Experimental results of the output port voltages in the QAB converter with SSPS modulation under loads condition 1. (a) O ² ND decoupling control. (b) PI control.....	131
Fig. 4.4.18 Experimental results of the output voltages in the QAB converter with SSPS modulation under two control strategies. (a) PI control with step change in V_{ref2} under loads condition 1. (b) O ² ND current decoupling control with step change in V_{ref2} under loads condition 1. (c) PI control with load step in $RL2$ under loads condition 2. (d) O ² ND current decoupling control with load step in $RL2$ under loads condition 2.	132
Fig. 4.4.19 The waveforms of resultant AC current and voltage of two upper switches in Port 2.....	133
Fig. 4.4.20 Waveforms of the AC voltage and AC current in each port under SSPS modulation to achieve the soft switching.....	134
Fig. 5.2.1 The leakage inductance distribution map of controllable magnetic integration with their realization scenarios and adjusting parameters.....	139
Fig. 5.2.2 The transformer magnetic integration procedures with the proposed reluctance-based evaluation strategy providing the threshold leakage inductance.....	141
Fig. 5.2.3 The geometry of the ER51/38.1/25-JNP96 core.....	142
Fig. 5.2.4 Mean magnetic path in the magnetic core.	144
Fig. 5.2.5 The equivalent magnetic circuit of the core.	144
Fig. 5.2.6 The vertical MMF distribution for a planar transformer.....	145
Fig. 5.2.7 The shortest and the longest (enclose the entire coil) magnetic path of the self-leakage flux.	147
Fig. 5.2.8 The equivalent cross-sectional area. (a) The vertical air-path self-leakage reluctance, (b) The horizontal air-path self-leakage reluctance.	148
Fig. 5.2.9 The shortest and the longest magnetic path of the mutual-leakage flux.....	149

Fig. 5.2.10 Equivalent magnetic circuit of the transformer.	150
Fig.5.2.11 Two winding arrangements for the validation of the proposed, (a) Insulation thickness $h_i = 0.05$ mm, thickness of the gap between two coils is $h_g = 3.9$ mm. (b) Insulation thickness $h_i = 0.2$ mm, thickness of the gap between two coils is $h_g = 0.4$ mm.....	152
Fig.5.3.1 3D overall and port winding configuration of a four-port example from the proposed RSSC HFMT	155
Fig.5.3.2 Equivalent magnetic circuit of the proposed RSSC HFMT	156
Fig.5.3.3 3D and 2D view of the four-port cross-shape core. (a). 3D configuration of the core. (b). 2D front, side views, and top view of the core.	160
Fig.5.3.4 Mean flux paths, (a). without flux barriers between two adjacent pillars (black) and opposite pillars (red). (b) with flux barriers between two adjacent pillars (orange).	162
Fig. 5.3.5 3D core configuration of the EE separate scenario	166
Fig.5.3.6 Relationship between extension leg length l_e and self, magnetizing(mutual), leakage inductances.....	167
Fig.5.3.7 Distribution ratio verses self inductance, mutual inductance, and. leakage inductance	168
Fig.5.3.8 Thickness of central horizontal air gap verses self inductance, mutual inductance, and leakage inductance.....	169
Fig.5.3.9 Thickness of side horizontal air gap verses, a). Self inductance, b). mutual inductance, c). Leakage inductance.....	170
Fig.5.3.10 The generalized design procedure of applying the proposed integrated HFMT in a N -port MAB converter.	171
Fig. 5.3.11 Efficiency test with voltage and current waveform, (a) 50V input voltage boost mode, (b) 100V input buck mode.....	190

Fig. 5.3.12 Voltage regulation test at 50V input, (a) Port 2, Port 3, and Port 4 are open circuits, (b) Port 2, Port 3, and Port 4 are connected to 10Ω symmetrical loads .	191
Fig.5.4.1 ER-shaped core structure.....	172
Fig.5.5.1 Two practical winding arrangements. (a). The traditional parallel spiraling winding structure. (b). The proposed middle connected parallel winding structure.	176
Fig.5.5.2 Flux lines plot with rated operating current direction.	177
Fig.5.5.3 Flux lines plot with current excitation direction in the secondary coil reversed.	177
Fig.5.5.4 Flux lines plot the current excitation direction in half of the primary and secondary coils reversed (use the reversion to neutralize the main flux generated by primary winding and secondary windings).	178
Fig. 5.5.5 Models of two winding arrangements in FEA simulation (a) Insulation thickness $h_i = 0.2$ mm, thickness of the gap between two coils is $h_g = 0.4$ mm, (b) The proposed arrangement with $h_i = 0.05$ mm, $h_g = 6.95$ mm.....	179
Fig.5.5.6 The transformer prototype and DAB converter.	180
Fig.5.5.7 Voltage and current waveform of the open-circuit test. (a) half rated voltage: $V_{dc} = 24$ V, (b) rated voltage: $V_{dc} = 48$ V.....	181
Fig.5.5.8 Voltage and current waveform of the transformer prototype operated in a DAB converter as an integrated HFT.	182
Fig.5.5.9 Flux line distribution in overlooking plane, a). Without flux barriers. (b) With flux barriers.	183
Fig.5.5.10 Configuration of the HFMT, (a) Bottom-half core before assembled. (b) The assembled HFMT	187
Fig.5.5.11 The proposed four-port HFMT operating in a QAB converter plant with one input port and three output ports connected to pure resistive loads	188

Fig.5.5.12 The port waveforms of the QAB converter, (a) Voltage waveforms, (b) Current waveforms..... 189

List of tables

TABLE 1.1 Classification of IBDC Topologies and Their Typical Models	25
TABLE 2.1 Average Transferred Power of the Decoupled DAB Branch in An Mab Converter with GPS Modulation.....	47
TABLE 2.2 Nonideal Effects of The Power Characteristics and Impact on Certain Element	49
TABLE 2.3 Comparison of Control Strategies for Constant Voltage Control In MAB Converter.....	51
TABLE 2.4 Comparison of Decoupling Control Strategies for Constant Voltage Control In MAB Converter	57
TABLE 2.5 Investigations and Innovations of the Integrated Planar Transformer.....	59
TABLE 3.1 Power Characteristic of DAB Converter with Dead-time Considered.....	80
TABLE 3.2 Specifications of the DAB converter.....	84
TABLE 3.3 Inner and Outer Phase Shift of Two Modulations	87
TABLE 3.4 Current Response of 3200W Average Power	88
TABLE 3.5 Measured Inductances in DAB Plant	89
TABLE 4.1 Generalized Partial Derivates of Average Current in DAB Branch with GPS Modulation	108
TABLE 4.2 Computational Burden of Three Decoupling Algorithms For N Ports MAB Converter With A -times Iterations	113
TABLE 4.3 Circuit Parameters and Specifications of TAB Converter in PLECS Simulation	116
TABLE 4.4 Comparison Between Three Control Strategies	120

TABLE 4.5 Circuit Parameters and Specifications of the TAB Converter in Experiment	121
TABLE 4.6 Comparison Between Two Control Strategies.....	124
TABLE 4.7 Parameters of the QAB Converter in Simulation and Experiment.....	125
TABLE 4.8 Steady State Voltage Ripple of Three Iterative Algorithm Applied Control Strategies and Pure PI Control	126
TABLE 5.1 Geometry Parameters of The Core	142
TABLE 5.2 Theoretical Results For Two Structures With Different Strategies	152
TABLE 5.3 Geometry Parameters and Specifications of the Cross-shape Core	160
TABLE 5.4 Electrical Specifications of the Four-port cross-shape HFMT	164
TABLE 5.5 Initial Geometry Parameters of The Core	165
TABLE 5.6 Core Geometry Parameters of The Separate EE Core.....	166
TABLE 5.7 Comparison between Separate HFMT and Integrated HFMT Scenario	175
TABLE 5.8 3D FEA Simulation Results For Two Winding Arrangements.....	179
TABLE 5.9 Open and Short Circuit LCR Measurement Results.....	182
TABLE 5.10 Simulation and Calculation Comparison For Length of Extension Leg l_e with $n_c = 3$ and $n_s = 1$	185
TABLE 5.11 Simulation and Calculation Comparison For Central Air Gap H_{ag} with $n_c = 3$ and $n_s = 1$	185
TABLE 5.12 Simulation and Calculation Comparison For Side Air Gap $H_{ag,s}$ with $n_c = 3$ and $n_s = 1$	186
TABLE 5.13 Simulation and Calculation Comparison For Winding Parameters With Initial Core Structural Parameters	186

TABLE 5.14 LCR Meter Experimental Results of The HFMT Prototype with Variable
Air Gaps 187

Abbreviations

AEPS	Advanced extended phase shift
CB	Current-based
CHB	Cascaded H-bridge
CHBR	Cascaded H-bridge rectifier
DAB	Dual active bridge
DPS	Dual phase shift
EB	Energy-based
EMB	Electro-mechanical batteries
EMB	Electro-mechanical batteries
EMI	Electro-magnetic interference
EPS	Extended phase shift
EPU	Electrical power unit
EPU	Electrical power unit
ESS	Energy storage systems
EV	Electric vehicle
FADEC	Full authority digital electronic controller
FCs	Fuel cells
FEA	Finite element analysis
GaN	Gallium-nitride
GPS	Generalized phase shift
HF	High frequency
HFMT	High frequency multi-winding transformer
HFT	High frequency converter
HFT	High-frequency transformer
HV	High-voltage
HVDC	High-voltage direct current
IBDC	Isolated bidirectional DC–DC converter
IGBT	Insulated gate bipolar transistors

IM	Induction machine
IPOP	Input-parallel-output-parallel
ISOP	Input-series-output-parallel
IUDC	Isolated unidirectional dc–DC converter
LCL	Inductor–capacitor–inductor
LF	Low frequency
LLC	Inductance-inductance-capacitance
LV	Low-voltage
LVDC	Low-voltage direct current
MAB	Multiple active bridge
MCU	Microcontroller unit
MEA	More electric aircraft
MEE	More electric engine
MEPS	Modified extended phase shift
MFT	Medium-frequency transformer
MIMO	Multi-input multi-output
MISO	Multiple-input single-output
MMAB	Modular multiple active bridge
MOSFETs	Metal-oxide semiconductor field effect transistor
MPC	Model predictive control
MT	Multi-winding transformer
MV	Medium-voltage
ND	Newton decoupling
O²ND	Online offline Newton decoupling
OA	Optimization algorithm
PCS	Power conversion system
PDC-MPC	Power decoupling based configurable control
PET	Power electronic transformer
PI	Proportional-integral
PM	Permanent magnet

PSD	Positive semi-definite
PWM	Pulse width modulation
QAB	Quadruple active bridge
RSSC	Radially symmetrical star-shape core
SC	Supercapacitor
SiC	Silicon carbide
SIMO	Single-input multiple-output
SISO	Single-input single-output
SMC	Sliding mode control
SND	Simplified Newton decoupling
SPS	Single phase shift
SSPS	Soft-switching phase shift
SST	Solid-state transformer
TAB	Triple active bridge
TPS	Triple phase shift
ZVS	Zero-voltage switching

List of symbols

\mathcal{R}_c	Core reluctance
$\mathcal{R}_{p\text{-eq}}$	Primary self reluctance of a two-port transformer
$\mathcal{R}_{s\text{-eq}}$	Secondary self reluctance of a two-port transformer
μ_0	Permeability of the air
μ_r	Relative permeability
ϕ_c	Core (magnetizing) flux
ϕ_s	Leakage flux
η	Efficiency
ρ	Resistivity
A_e	Cross-sectional area
A_p	Area product
A_w	Window area
B	Flux density
C_j	DC-link capacitance of port j
$D_{IN,i}$	Inner phase shift of port i in DAB or MAB converter
D_o	Outer phase shift in the DAB converter
$D_{i,j}$	Outer phase shift between port i and port j
f_c	Control frequency
f_s	Switching frequency
h	Height
i	Current
J	Current density
K_f	Waveform coefficient
K_u	Window filling factor
l	Length
L_m	Magnetizing inductance
L_{sn}	Equivalent inductance of port n
$L_{i,j}$	Resultant equivalent leakage inductance between port i and port j

M	Ratio between magnetizing inductance and primary side leakage inductance in DAB converter
MMF	Magnetic Motive Force
N	Number of ports of the MAB converter
n	Turn ratio of transformer in DAB converter
n_c	Number of turns for the central winding in RSSC HFMT
n_s	Number of turns for the side winding in RSSC HFMT
N_p	Number of turns for primary side winding in two-port transformer
N_s	Number of turns for secondary side winding in two-port transformer
P_n	Average injected/output power of port n
Q_n	Switches on the secondary side of DAB converter
$R_{D_{on}}$	Diode-on resistance
$R_{mos,on}$	MOSFET-on resistance
R_j	Load resistance of port j
S_n	Switches on the primary side of DAB converter
T_d	Dead time
$t_{initial}$	Initial settling time
T_{rise}	Temperature rise
T_s	Time of switching
Vol	Volume
V_{dip}	Dip voltage during dynamic
$V_{in,n}$	Input voltage of the port n
$V_{out,n}$	Output voltage of the port n
V_{p-p}	Peak to peak ripple voltage
W	Width

1. Introduction

1.1 Isolated Bidirectional DC-DC Converter and isolated MIMO systems in electrified transportation applications

With the trend of replacing low frequency (LF) transformers by the high-frequency (HF) transformers in the isolated DC-DC power converters, this ‘next-generation power conversion systems’ have been developed rapidly and applied in distributed generation and energy storage systems [1-3]. Under high frequency operation, especially for the power systems in electrified transportation applications, demand of power systems are not only limited in galvanic isolation and power density promotion, but also the bidirectional power transfer capability [4-6]. These isolated bidirectional DC–DC converter (IBDCs) topologies are initially evolved from some well-known traditional isolated unidirectional DC–DC converter (IUDC) topologies, flyback IUDC to dual-flyback IBDC, half-bridge IUDC to dual-half-bridge IBDC , etc. Besides the IBDCs composed of IUDCs with the same type, the IUDCs with different types also can compose IBDCs, to achieve a wide output voltage range and a bidirectional power flow. Based on the number of switches, TABLE 1.1 presents a classification of IBDC topology. The simplest IBDC topology is the double switch structure, such as: dual-flyback and Zeta-Sepic IBDC [7-9]. The typical model of triple switch topology is forward-flyback IBDC [10]. Quadruple switch topologies mainly contain dual push-pull IBDC, push-pull-forward IBDC, push pull-flyback, and dual-half- bridge IBDC [11-15]. The typical model of quintuple switch topology is full-bridge-forward IBDC [16]. The typical model of sextuple switch topology is half-full-bridge IBDC [17]. Octuple switch topology is mainly DAB IBDC.

TABLE 1.1
CLASSIFICATION OF IBDC TOPOLOGIES AND THEIR TYPICAL MODELS

Number of switches					
Double switch	Triple switch	Quadruple switch	Quintuple switch	Sextuple switch	Octuple switch
Dual flyback	Forward flyback	Dual half bridge	Full bridge forward	Half-full bridge	Dual active bridge

Under normal conditions, transferred power of isolated bidirectional DC–DC converters is proportional to the number of switches when the rated voltage and current of the power switches in the converter topologies are the same [18]. With eight switches, DAB converter is one of the biggest power-transfer-capacity IBDC topology. From the filter aspect, the output pulsation frequency for the forward-topology converter is the same as its switching frequency but for the push–pull, half and full-bridge-topology converters this frequency is twice of the switching frequency, providing smaller filter to themselves when the same output voltages are required. Besides these benefits, the DAB also has the advantages of ease of realizing ZVS, bidirectional power transfer, its modular and symmetric structure makes its practical manufacturing costs also kept at a relatively low level, etc. For these reasons, DAB converters have been widely used in on-board propulsion or power distributions such as electric vehicles (EVs) and more electric aircrafts (MEAs), serving as the key circuit of their power conversion systems in recent years[19] [20].

A. More electric aircrafts

Similarly to other commercial transportation industry, the civilian aircraft industry is facing challenges to emissions and fuel consumption reduction. Replacing mechanical and pneumatic systems with electrical systems is becoming a new trend in commercial aviation area, thus transitioning toward the MEA [21]. Once electrified, these AC and DC power systems, such as electric electro hydrostatic actuator, winding-deicing system, flight control electronics, and cabin pressurization system, requires power converters to coexist and work together [22]. This new type of aircraft has several obvious advantages, it not only greatly reduces the pollution to the atmosphere, but also can achieve higher reliability.

Combined with the usage of electric actuators, the embedded generation system has developed to a more electric engine (MEE) system, resulting in a lighter, more efficient, better performing, more reliable and less costly engine that can be more easily integrated into MEA systems [23].

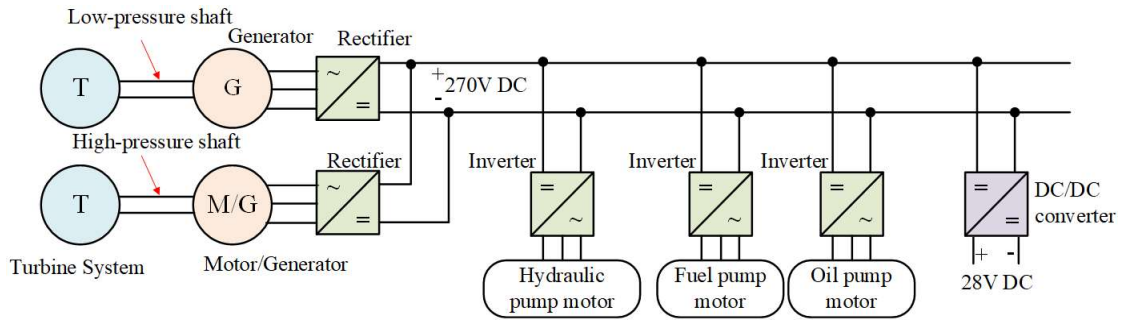


Fig. 1.1.1 An example of MEE system in MEA applications

Fig. 1.1.1 shows a distribution of MEE architecture example, the motors driving the pumps can be both permanent magnet (PM) motors or induction machines (IMs) controlled by the pulse width modulation (PWM) inverters [24], while the 28 VDC required for the full authority digital electronic controller (FADEC) and other flight controls are derived by DC/DC converters operating under 270 V DC supply [25]. This 270 VDC can be obtained by the aircraft rectifier or a battery pack.

To solve the similar issues found in the ground-based microgrids due to the electrical system complexity, other structural scenarios for future MEA microgrids have been proposed as well [26, 27]. A popular trend of the investigation is increasing the voltage level in these AC and DC grids [28, 29]. A grid structure that consists of a low-voltage direct current (LVDC) network and high-voltage direct current (HVDC) network is shown in Fig. 1.1.2.

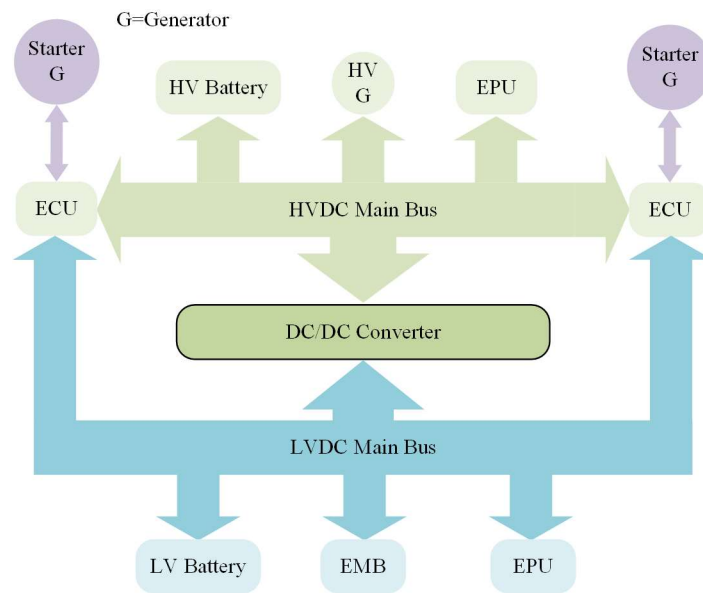


Fig. 1.1.2 MEA distribution structure with LVDC and HVDC network

The LVDC main bus is connected to the energy storage elements, such as low-voltage (LV) emergency batteries. These elements are connected together and controlled by the electrical power unit (EPU) to supply avionics circuitry [30]. Whereas the HVDC main bus is connected to the high-voltage (HV) generators to provide the required voltage and power for the HV batteries and other MEA equipment, these elements are controlled by the HV EPUs as well [31-35]. Starter generator systems is designed to provide the required power to start the engines of the aircraft when on the ground and additional power during the flight [36]. Although power electronics and electric machines are well mature technologies, further work is still needed for MEA applications in areas including: high temperature operating reliability, large temperature variations and high thermal cycle capability, areas, passive components reduction in topology, power density and fault-tolerant enhancement [37].

B. Electric vehicles

Since EVs performing as distributed energy sources to stabilize utility grids are taking up a bigger penetration in the market [38]. Realizing bidirectional power conversion is becoming a new hot spot in the research of EV charging systems [39]. With the merits of galvanic isolation, high efficiency and power density, flexible buck/boost capability and good controllability, DAB converters are also widely investigated and applied in EV fast charging applications [5, 6, 40, 41].

For both MEA and EV power conversions, multiple sources and components are connected to a common HV or LV DC buses through independent IBDCs, forming a series of single-input single-output (SISO) branch-system. These independent converters are used to manage different input or output sources and regulate output power of different loads. To optimize the efficiency and improve the power density of a multi-source multi-load structure, the multi-input multi-output (MIMO) converter has been proposed as an alternative. Functionally, MIMO converters is similar to a system synthesized by connecting several SISO converters to a common DC bus as shown in Fig. 1.1.3.

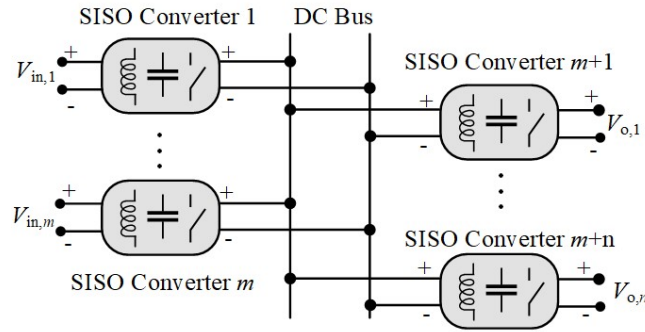


Fig. 1.1.3 Power systems have the same function with MIMO converters but organized by multiple SISO converters

Compared with the conventional power system architecture with independent SISO IBDC converters, MIMO DC–DC converters have the advantages of reduced component count, higher power density, and fewer power conversion stages [42]. In addition, range of control limitation, control accuracy, components cost, and other drawbacks associated with multi-SISO systems further degrade their popularity and drives the direction of their evolution to the MIMO converter systems. Single-stage multiport converters can be categorized into multiple-input single-output (MISO), single-input multiple-output (SIMO), and MIMO topologies. In early stage, input of MISO converters were constructed by connecting multiple voltage sources [43]. This configuration brings a severe drawback, if one voltage source is diminished, the output voltage will be unreliable. To prevent multiple sources from being shorted together, an active switch must be connected in series with each input source, which brings additional components burden to the system.

SIMO converters can be classified into isolated and non-isolated configurations [44]. The isolated SIMO topologies have only one output voltage regulated, all the other ports rely on the turn ratios adjustment of a transformer with multiple secondary windings. Therefore, independent output voltage regulation is not achieved [45]. Whereas the non-isolated SIMO can not satisfy the required safety demand since output ports have to share the same ground [46, 47]. Hence, SIMO topologies are not popular in electrified transportation applications.

MIMO converters can not only combine the advantages of both MISO and SIMO, but also reduce the cost and improve the efficiency of the system. The clean energy based power conversion systems employing MIMO converters has been escalated by combining diverse

sources, such as photovoltaic panels, wind turbines, fuel cells (FCs), and batteries [48-50]. Comparing to the conventional single-source power conversion and supply systems, this multi-source system has higher flexibility, longer service life, and improved effectiveness. Therefore, the integrated power supply system is promising in many situations, such as energy harvesting of wireless sensor networks, electric vehicle applications, electric traction system and future residential power supply systems [51-53].

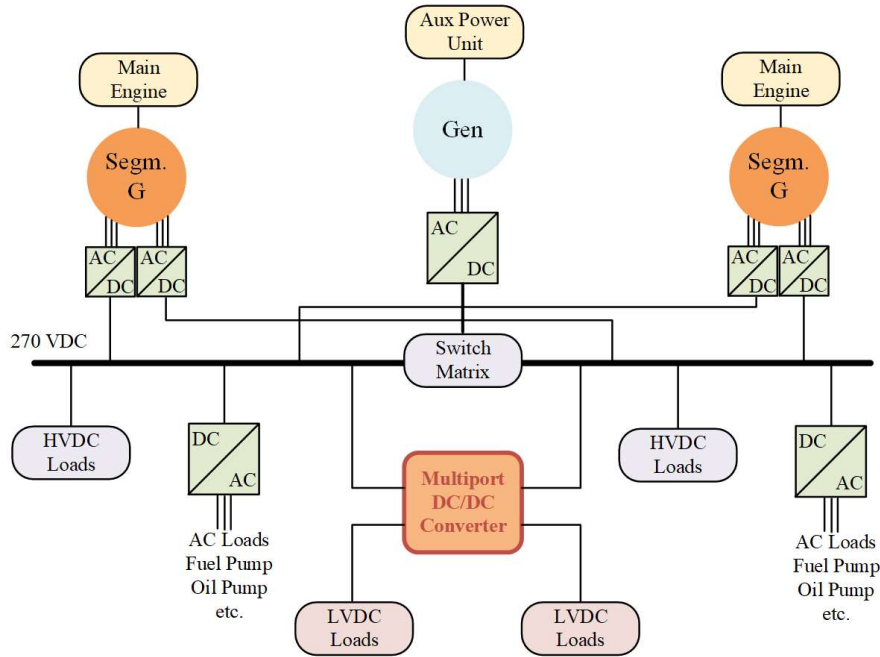


Fig. 1.1.4 An example of a DC-based EPDS with MIMO converters involved in its topology

Applying MIMO converters can simplify structure between 270 VDC bus and LVDC loads, the Fig. 1.1.4 shows an example of a EPDS with multiport power converters topology, in which the MIMO converters are highlighted in red. Compared to the topology in Fig. 1.1.2, multiple separate SISO converter branches are replaced by the MIMO converter, segmented starter/generators with segmented inverter configurations are placed instead of traditional generators with inverters.

In hybrid EVs' power systems with varied port voltage levels, fuel cell (FC) is used with energy storage systems (ESSs) such as batteries or supercapacitor (SC) [54]. Association of FC and ESSs can provide a significant reduction of the hydrogen consumption for the FC [55-58]. Since FC, ESSs and SC commonly have different voltage levels, IBDC converters are required for each input sources to provide the specific voltage levels of various loads and control power

flow between them. However, using SISO IBDCs for each input sources may lead to the increase of price, mass, and losses. Consequently, in these power systems, MIMO dc–dc converters have been used.

The conventional power systems on EV with multiple SISO converters for each port is shown in Fig. 1.1.5 (a), which faces the problems of large in volume, expensive in cost and high level of complexity in control.

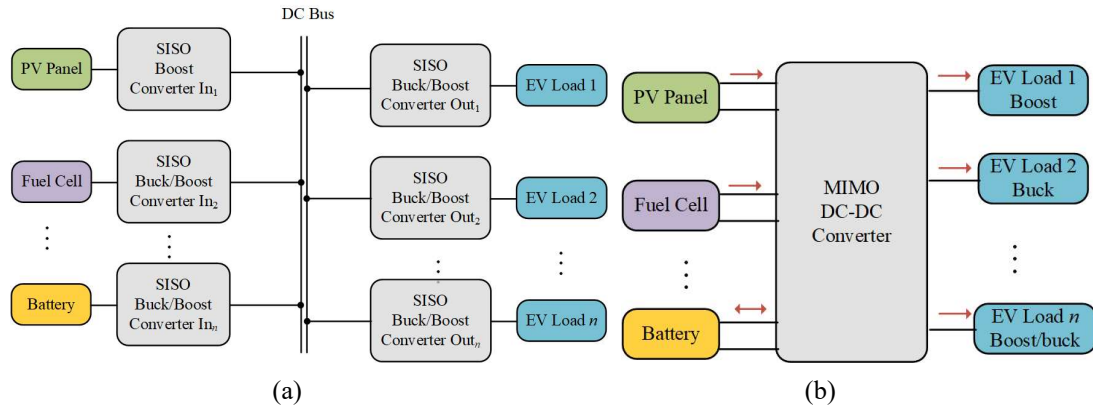


Fig. 1.1.5 EV power systems with multiple input sources, a) conventional topology with multiple SISO converters. b) MIMO topology

Applying MIMO converters in this configuration as shown in Fig. 1.1.5 (b) can reduced the above-mentioned drawbacks effectively [59]. Multiple input terminals for hybridization of an EV can improve the reliability of operation [60-62]. Whereas the various output terminals of the converter can perform both boost and buck functionality simultaneously. If IBDC MIMO converters are implemented, this power system can not only supply power to EV loads, but also performing as distributed energy sources to stabilize utility grids are taking up a bigger penetration in the market [38]. Similar replacement also happened in the charging applications of EVs. To improve the charging efficiency and flexibility, multiport EV chargers with improved topologies were proposed by researchers. For example, in [63] the authors investigated a ring-connected DAB topology for EV fast-charging stations. In reference [64], the authors proposed a cascaded H-bridge (CHB) power electronic transformer (PET) structure to achieve multiport ultrafast charging. Different from these topologies, the multiple active bridge (MAB) topology charger can realize the interconnection of multiple EVs under different charging voltage specifications to achieve simultaneously fast charging/discharging with the high degree of freedom in charging port control [65].

Although with many merits, MIMO converters have not received as much attention as MISO or SIMO converters, and several issues for typical MIMO converter topologies still remained to be investigated.

1.2 MIMO DC-DC converter topologies

1.2.1 Configurations using DAB converters

As the origin of many MIMO converter topologies, DAB converter was first proposed in the early 1990s [66-68]. However, because of the performance limitations of power devices, the power losses of DABs were significant, and the efficiency was unacceptable during that period. In recent years, the advances in new power devices including the development of silicon carbide (SiC) and gallium-nitride (GaN) based power devices, and magnetic materials, especially the iron-based nanocrystalline soft magnetic have made DAB converters feasible for eliminating bulky and heavy transformers from power conversion systems (PCSs) [69]. Thus, DAB-IBDC has regained the attention of numerous researchers.

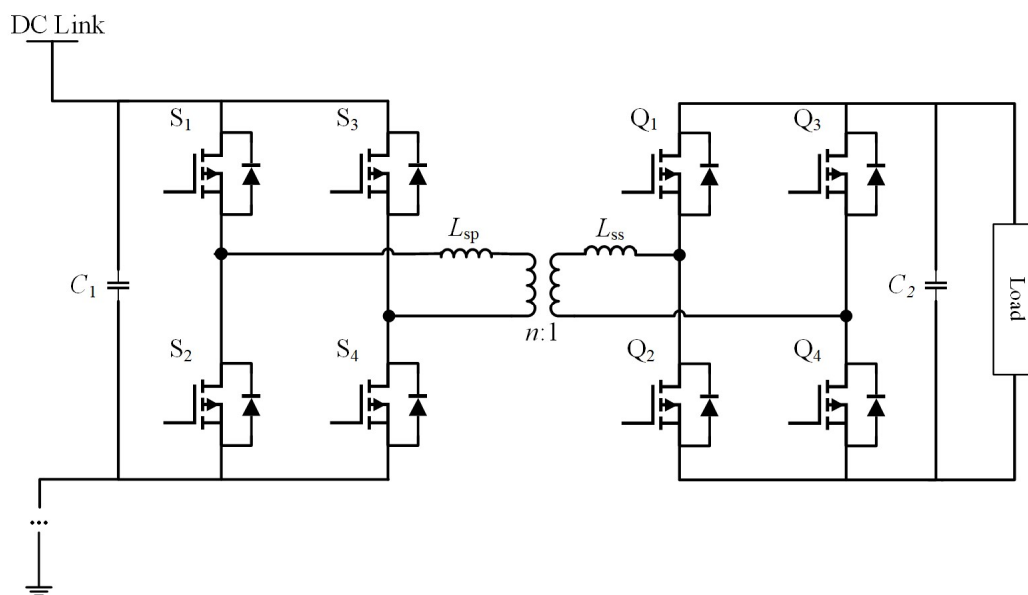


Fig. 1.2.1 Topology of a conventional DAB converter in a common DC-link MIMO system

The topology of a conventional DAB converter is shown in Fig. 1.2.1. DAB converter is a popular isolated DC-DC converter topology composed of two H-bridges with one at input side and another at output side and a HF PET [67, 70-72]. The first H-bridge provides square wave AC voltage with an adjustable duty ratio to the primary winding of the HF transformer. Each

H-bridge consists of four switches S_1 , S_2 , S_3 and S_4 , these switches could be insulated gate bipolar transistors (IGBTs) or metal-oxide semiconductor field effect transistor (MOSFETs) for high power applications [73, 74]. Secondary side H-bridge, also assembled by four switches connected to the secondary side winding of the transformer, Q_1 , Q_2 , Q_3 and Q_4 . The operation is bidirectional, that is, each H-bridge can be considered as primary or secondary depending on the direction of power flow. For each half-bridge, the upper switch is always operating complementary to the lower switch. On, off-delay time are inserted between each pair of upper and lower switches to prevent the short circuit of the half-bridge, this delay is named as the dead-time. Each H-bridge provides a resultant voltage waveform, where the inner and outer phase shifts modify the proportion of the rising edge, and the phase difference between two waveforms, respectively. Typical traditional DAB configuration also applies two series inductors to store the transferred power temporarily at the primary and secondary node of the transformer. H-bridge provides square wave voltage with an adjustable duty ratio to the windings of the HF transformer.

Current research topics of the DAB converter mainly focuses on four aspects of subjects [75]: basic power characterization and modulation, control strategies, soft switching, and hardware design and optimization.

1.2.2 MAB converters and other MIMO converter configurations

There are three important requirements for the converters used in transportation systems, high efficiency, high power density and high-level insulation. High efficiency means less power loss, which requires smaller cooling equipment and reducing the weight. High power density could reduce the volume of the converter system thus decrease the fuel and battery consumption. As power transferred in the transportation system is usually kilowatt-level, high-level insulation promises the safety of the converter system in case of faults during the operation [76]. As mentioned before, traditional transportation electrical systems topology is an array of DAB converters linked to a common DC bus as shown in Fig. 1.2.2(a), whereas red arrow indicates the direction of the power flow. A DAB includes a medium-frequency or high-frequency transformer (MFT/HFT) to realize voltage matching and electrical isolation [70, 72, 77, 78].

Power could be transferred bidirectionally by means of phase shifts [67]. However, this configuration has relatively low power density as transferring power between N ports require $2N$ H-bridge converter branches, and the same number of two-port transformers.

To improve the power density, modular multiple active bridge (MMAB) converters and MAB converters have been developed in recent years. Comparing to the multiple DAB configuration, MMAB shares a common AC bus as shown in Fig. 1.2.2(b), which reduces the number of components significantly [79-82]. Each basic DC ports in this topology consist of a DC capacitor, a H-bridge circuit and a HF transformer.

According to [81], if regard DC sides as input sides and AC sides as output sides, main types of combinations of power submodules in one port can be classified into two types: 1) submodules are input-series-output-parallel (ISOP) to meet higher DC voltage ratings, and 2) submodules are input-parallel-output-parallel (IPOP) to achieve higher current ratings. Only the submodules in the same port have to be the same type, while in different ports they can be diverse. Similarly, power semiconductors of submodules in the same port follow the same switching orders. Research [7] shows that submodules in one port can always be simplified as one single submodule with equivalent parameters regardless of their combination. Therefore, MMAB converters can be regarded as an equivalent converter with only one submodule in each port.

MMAB is firstly proposed in [83]. As a modular design of DAB, MMAB also has advantages of great power density and galvanic isolation. Besides, MMAB is scalable and can achieve wide-range power and voltage ratings with combinations of modular H-bridges [82].

However, involvement of multiple ports inevitably adds to the control difficulty and ZVS realization of MMAB converters since power flows are strongly coupled among ports. If MMAB converter is operating under hard switching mode, sever power losses and electromagnetic interference (EMI) from semiconductors would significantly reduce the efficiency and reliability of system. Hence, MMAB converters usually have higher requirements in modulation, the traditional single phase shift (SPS) is not suitable for its application [82]. As for generalized MMAB topology converter, a comprehensive analysis for operation region in various operating conditions is necessary.

Despite the improvement of system power density, number of transformers maintain the same comparing to the DAB array topology. Therefore, MAB converter is considered as a better solution for volume-limited applications, since MMAB topology has the same high-level of control difficulty and ZVS realization as the MAB topology, but MAB can use multiport transformer to replace the AC link to improve the system power density.

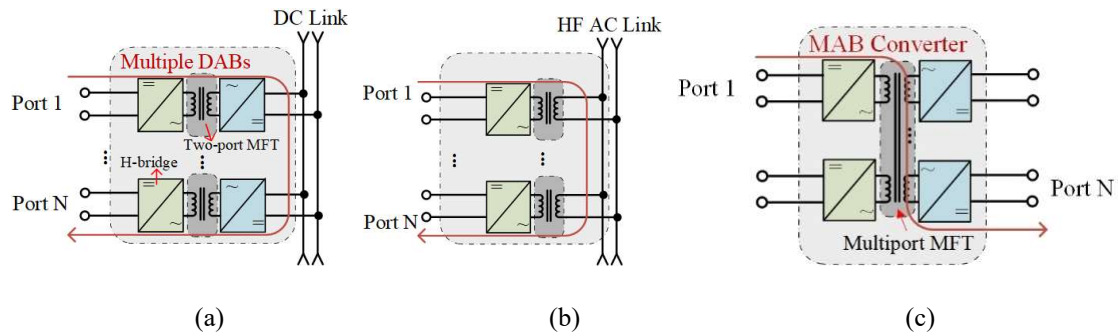


Fig. 1.2.2 Multiport power conversion configurations, (a). Traditional topology with an array of DABs linked to a common DC bus. (b). MMAB configuration with secondary sides of two-port transformers directly linked to a common AC bus. (c). MAB topology with a MT linked to voltage-level varied loads.

MAB converters, which can be regarded as an extension of the DAB converters integrating multiple two-port transformers into a multi-winding transformer (MT), as shown in Fig. 1.2.2(c). Consequently, employing the MAB instead the DAB in MEA and EV systems can reduce the total number of HFT, LV cells, auxiliary components as well as their power supply, resulting in lower cost [84].

The generic topology of the MAB converter has N ports, these ports can be switched to input or output according to the requirements. It can be interfaced with buses and a variety of loads to achieve simultaneous power flow between any two ports, this characteristic makes the MAB highly flexible. If varied voltage rating is required during the operation, N H-bridges can be linked through a HF MT with unified turn ratios to promise the initial port consistency, where adjustment of the voltage level is achieved by the control theory. Otherwise, turn ratio can be designed based on the voltage rating between ports. When decoupling control is applied to the MAB converter, two arbitrary ports in the MAB converter can be regarded as a virtual DAB subbranch linked by a single-phase PET, whose primary and secondary side equivalent leakage inductances equal to the port series inductances.

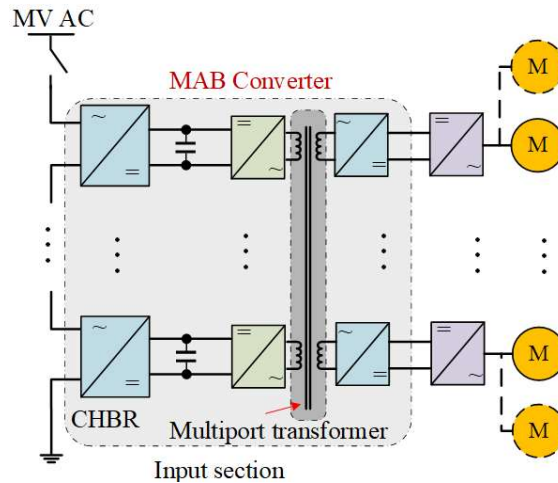


Fig. 1.2.3 MAB configured electric traction system [85]

Fig. 1.2.3 shows an example of MAB topology proposed for electric traction applications [85]. The main idea of this topology is to convert single-phase medium-voltage (MV) line frequency AC voltage into several MF voltages. In this scenario, multiport PET can be divided into three parts. The first part is a cascaded H-bridge rectifier (CHBR) linked to the grid sides; several DAB circuits are connected between to provide the isolation. The cell number of CHBR is determined by the AC grid voltage level and the rated voltage of power electronics devices. The second part is the MAB isolation units, which contains a group of MF inverters, rectifiers, and a MT whose secondary windings are determined by the demand of loads. The third part is the load and load converters. The load-side converters can be of different types, such as two-level inverters for motor drive, inverters for the multiphase motor, and cascaded inverter for higher voltage motors.

This attractive converter topology can be further enhanced to improve the power density by applying magnetic integrated MT, which employing transformer leakage inductances as the main energy transfer elements. Investigation of this integrated MT is of vital importance. To achieve the flexible operation of the MAB under nonlinear power characteristic, realizing ZVS for example, advanced modulation and control strategies need to be developed.

1.3 Aims and objectives

The study of this PhD aims to develop a generalized modulation strategy and a decoupling based modular control scheme of the integrated MAB converter to promote its power density while realizing flexible and accurate control with good dynamic performance. The design of such modular control system will allow MAB switching between fundamental modulations to achieve highest power transfer efficiency. In addition, control strategy in this proposed method is also modular if any other constraints are required. Whereas development of the integrated high frequency multi-winding transformer (HFMT) greatly enhanced the power density of the system, leakage inductance can be adjusted according to its parameters while port consistency is maintained.

The aim of this research can be achieved through the following objectives:

- a) Modify and develop modulations to improve power transfer efficiency, accuracy and steady state performances: Modulations is the framework for MAB converter to realize the high-efficient power transfer, quality of the power transfer. Non-ideal effects involved in the power characteristics of the modulation may bring errors to the control. Meanwhile, involving too many modifications for these effects in the modulation leads to unaffordable computational burden for the control systems. Thus, a trade-off investigation is necessary to balance the complexity of modulation and power transfer quality and efficiency.
- b) Developing a flexible control system with accurate dynamic responses while promising ZVS: Characteristic of MAB is different from DAB converter, traditional PI faces the drawback of slow dynamic performance and limited controllable range of power transfer. Advanced nonlinear control strategies are required for MAB to realize good dynamic and steady-state performance. In addition, these control methods should have high level of flexibility to suit asymmetric voltage ratings in output ports and achieve constraints like ZVS switching.
- c) Propose and design an integrated MT with accurate leakage estimation and controllable inductances: Integrated MT required large-enough leakage inductances to replace the traditional series inductors. Error between practical leakage inductance of the designed transformer and aiming values are required to be as small as possible since they are directly

involved in the power transfer characteristics. Moreover, leakage inductance of the integrated MT should be able to adjust individually.

- d) Validation of the proposed scenarios: All the above listed investigation and achieved analytical design results should be verified through simulations and experiments.

1.4 Major research contributions

The main goal of this research is to realize the flexible control with modular modulation promising the power transfer efficiency, quality, dynamic and steady-state performance of the MAB converter with integrated MT. With the accordance, the main contributions of this thesis compared to the existing literature can be divided into control and modulation part, and hardware MT design part.

The contributions for modulations include:

- a) Proposed a modified extended phase shift (EPS) modulation for the DAB converter considering the transformer magnetizing inductance to improve the power transfer performances.
- b) Modified power transfer characteristics by evaluating and involving other non-ideal effects that can have impact on the power transfer steady state performance and control accuracy.
- c) Applying the generalized phase shift (GPS) modulation with decoupling control for MAB converter to improve the efficiency of power transfer.

The contributions for control include:

- a) Proposed a power decoupling based configurable control (PDC-MPC) control using model predictive control (MPC) to enhance the dynamic performance of the MAB converter.
- b) Proposed a modular decoupling algorithm for decoupling control of MAB converter to optimize the flexibility of the control while maintaining their advantages and restrict the computational burden by combing the above modulation and control contributions.

The contributions for integrated MT design are:

- a) Proposed a reluctance-based leakage inductance estimation and core design process to estimate the leakage inductance and following decide whether core modification is required to achieve the aimed leakage inductance values.
- b) Proposed a radially symmetrical star-shape core (RSSC) core structure and split winding configuration for the integrated HFMT to design an integrated MT with controllable leakage inductance.

1.5 Thesis organization

The rest of the thesis chapters is organized as follows:

Chapter 2 presents the literature review of the fundamental modulations and GPS modulation strategies for the DAB and MAB converter, non-ideal effects involved in power characteristics have been involved in this part of review as well. Following that, advanced nonlinear controls including decoupling control and other control methods investigated by other researchers to promote the dynamic performances for MAB converter have been reviewed. Finally, magnetic integrated HF transformer with estimation strategies for its leakage inductances realized by other work have been reviewed.

Chapter 3 describes the modulation strategies considering the non-ideal effects to improve the power transfer quality. A modified EPS modulation considering magnetizing inductances has been proposed for DAB converters with its effectiveness validated by the simulation and experimental results. Other typical non-ideal effects including the dead-time effect and saturation of transformer have been investigated, with some of power characteristics provided.

Chapter 4 proposed a modular modulation based nonlinear decoupling control strategies and enhanced its dynamic performance by applying MPC in voltage control. This modular decoupling control equipped with high level of flexibility, its modulation can be switched between fundamental modulations to promise the efficiency of power transfer whereas its control method is switchable as well to satisfy the constraints. Simulation and experimental

validation on a triple active bridge (TAB) and quadruple active bridge (QAB) converter have validated their effectiveness and improvement in dynamic and steady-state performance under asymmetrical output voltage rating conditions.

Chapter 5 firstly presents an accurate estimation strategy of the equivalent magnetizing and leakage inductance. Based on this strategy, a design process for magnetic integrated transformer judging whether core modifications are necessary is proposed. Then, a radially symmetrical star-shape core MT with split winding configuration for N-port MAB converters is proposed. This RSSC scenario has higher power density comparing to the separate MT and series inductors scenario, its leakage inductance can be adjusted by modifying the core and winding parameters to achieve the controllable magnetic integration. A four-port case study is simulated, and a prototype of this case study is manufactured in experimental validations.

Chapter 6 summaries the key conclusion of this thesis and the recommendations for some potential research work that can be addressed in the future. The story line of this thesis can be illustrated by Fig. 1.5.1.

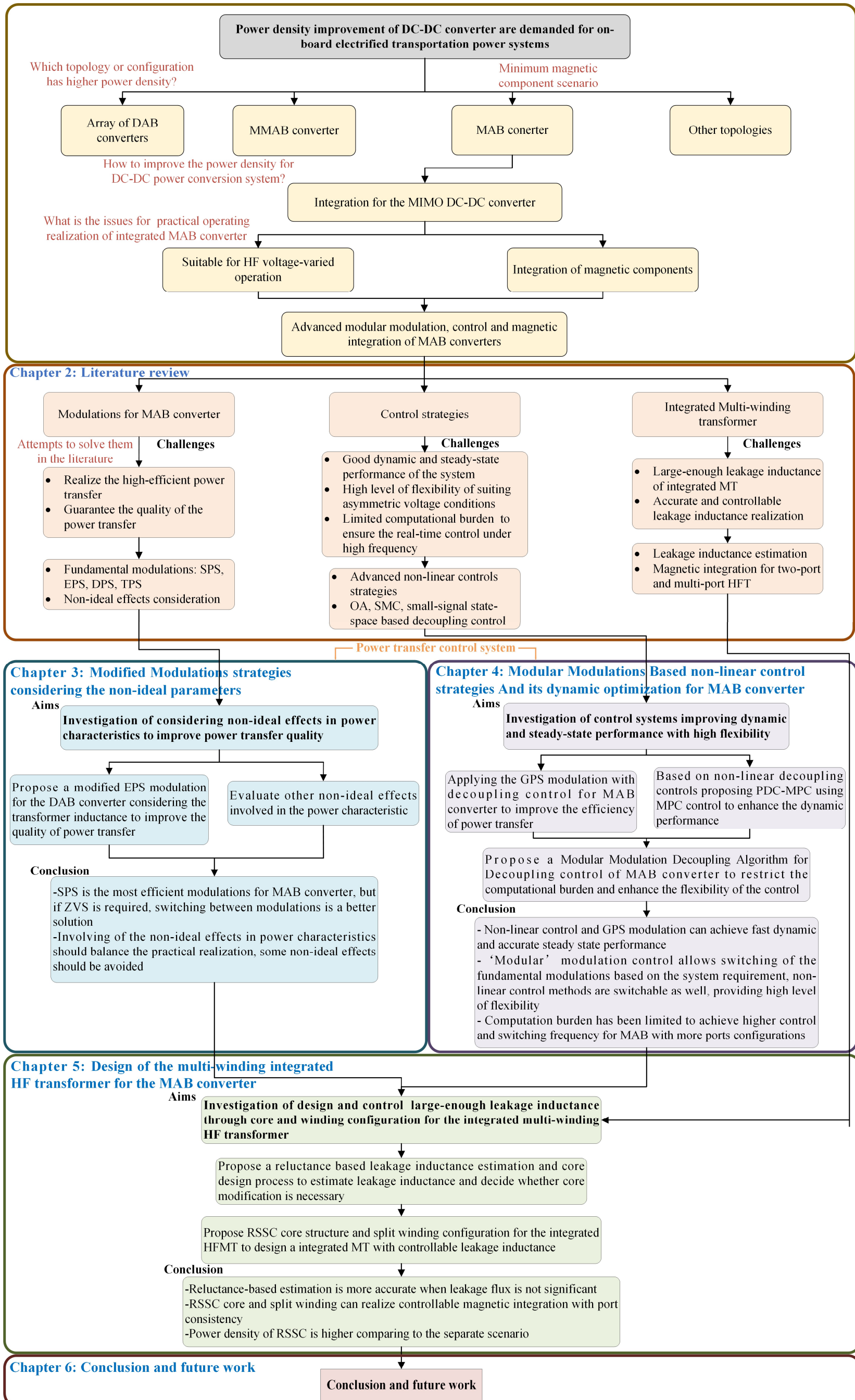


Fig. 1.5.1 Story line of the thesis

2. Literature Review

2.1 Chapter overview

Isolated DC-DC power converters with high power density have contributed to their widespread use in electrified transportation applications, such as MEAs [4], railway and EVs [86, 87]. To cooperate with the different operation requirements while realizing power transfer with high efficiency and quality, such as soft switching, constant power output, etc., modulation strategies have been developed. In recent years, for the consideration of the power density enhancement, multi-port DC-DC configurations have been proposed to replace the array of DABs and other SISO converters configuration in large power transfer, distribution and propulsion systems. Among them, MAB converter is one of the most popular topologies. To figure out multiple ports with asymmetrical voltage requirements and nonlinear power transfer characteristics, advanced modulation and nonlinear control strategies have been proposed to realize the independent port-voltage control.

In this Chapter, review of the fundamental modulation strategies for DAB converters including SPS, EPS, DPS and TPS are firstly introduced. Power transfer characteristic of the modulation is the framework of the real-time control system, generation of the control variables always rely on the indication of the selected modulation. This research proposed an idea of designing an integrated control system which included several modulations strategies and allowing switch of fundamental modulations to meet different operating requirement. GPS modulation which can provide fundamental modulations switching to achieve more system flexibility for the MAB converter is hence reviewed and modified in the later chapters.

The second part of the review relates to the control strategies of the MAB converter. Control of MAB converter should realize good dynamic and steady-state performance of the system. Traditional PI is not suitable for the MIMO system due to its low dynamic and narrow controllable range. In addition, high level of control flexibility is a significant issue since port voltage can be varied during operation. Finally, computational burden of the control system

should be limited to ensure the real-time control. To meet these needs, researchers have investigated decoupling control which decouples the MAB into several sub-branches. Among them, optimization algorithms based decoupling control, steady state based decoupling control, and sliding mode decoupling control are some of the most popular ones, which are reviewed and compared.

The final part of the review aimed to explore the power density improvement in the hardware aspect, that is applying magnetic integrated HF MT in the MAB topology. With series inductors integrated on the transformer by increasing leakage inductances, power density of the practical system can be promoted significantly. Two port and multi-winding transformer scenarios are review with accurate leakage inductance estimation strategies to help develop the controllable magnetic integration transformer design for the MAB converter.

2.2 Modulation strategies of MAB converters and modulation optimization by considering non-ideal effects

2.2.1 Fundamental modulation strategies in DAB converter

Control of the average transferred power is realized by means of phase shift modulation and control techniques [18, 88]. Responsibility of the modulations is realizing the power transfer with high quality and efficiency. Hence, power transfer characteristics in modulation is of vital importance, as this characteristic is the framework indicating the relationship between control variables and controlled object, that is the transferred power. Since topology of the MAB converter can be regarded as an extension version of the DAB converter, its modulation strategies can be inherited from fundamental modulations of DAB converter, which includes: SPS, EPS [89, 90], dual phase shift (DPS) and triple phase shift (TPS) modulations [27, 28]. Based on these strategies, a GPS modulation is developed which is capable to switch between these fundamental modulations to provide power transfer with high quality while meeting constraints.

A. SPS modulation

SPS modulation is the most basic and most widely used modulation strategy for DAB converter [66, 67, 91]. In SPS modulation, the cross-connected switch pairs in both H-bridges are switched in turn to generate phase-shifted square waves with 50% duty ratio to the primary and secondary sides of the transformer. The outer phase shift between these two voltage square waves is the only degree of freedom, both magnitude and direction of the power transfer depends on this variable [92, 93].

Besides the advantages of easy implementation, SPS modulation also draws attention by its high dynamic, and ease of realizing zero-voltage switching (ZVS) control, etc. However, in this method, the control of the power flow depends on series inductors that might result in great circulating power when the outer phase shift is significant, then both the RMS and peak current increase. Low voltage regulation and high RMS current could lead to the undesired copper losses. Moreover, the converter might not be able to achieve ZVS under large phase shifts as well. Thus, leading to high power loss and great reduction of efficiency.

B. EPS and DPS modulation

SPS modulation can satisfy the majority of DAB applications owing to its simplicity. However, when DC voltage ratio deviates from unity, the SPS-modulated DAB may have a high circulating current or power flow back, and losing ZVS operation [94]. Considering the different applications and voltage ranges with multiple output ports, the voltage gain between two arbitrary ports may diverge from unity further. For these scenarios, advanced modulation strategies such as EPS or TPS modulation, have been introduced to achieve zero-voltage switching while reducing the RMS and peak currents of leakage inductors [18, 89, 95].

To reduce the backflow power of the DAB converter, decrease the current stress, promote system efficiency and extend ZVS operating range[96-98]. EPS modulation has been proposed as an improved method of SPS modulation [92, 99]. Duty ratio of the primary H-bridge voltage waveform in the EPS modulation is not confined to 50%. EPS modulations fix the inner phase shift of secondary bridge as 0. While outer phase shift and primary inner phase shift are two

controlled variables. EPS modulation can have two possible waveforms distinguished with the value of primary inner and outer phase shift [99, 100].

Double Phase Shift modulation was proposed in [101]. Unlike EPS modulation, DPS modulation, inner phase shift is not zero for both primary and secondary H-bridges. However, the cross-connected switch pairs in both perform the switching based on the same inner phase shift, which is $D_{IN,1} = D_{IN,2}$. Hence, DPS modulation has the same degree of freedoms of EPS.

Comparing to the SPS modulation, DPS reduces the current stress and steady-state current [102]. Researchers have discussed its control, power loss and soft switching with other optimization strategies in [93, 102, 103]. Its benefit includes, improved the system efficiency, expanded the range of soft switching while minimized output capacitance [104]. And compared with EPS modulation, operating states of the two bridges will be the same when voltage or power flow direction is reversed. Similar to EPS modulation, there are two possible conditions for the waveforms of DPS modulated DAB converter. A drawback of the DPS modulation is the inrush current at the capacitor charging stage. A start-up circuit to suppress the inrush current with a set of auxiliary circuits is proposed in [105].

C. *TPS modulation*

TPS modulation was proposed in [106]. The cross-connected switch pairs in both H-bridges of the TPS modulated DAB switched with inner phase shifts, and their values could be unequal. Consequently, TPS modulation is a unified form of phase shift modulation, SPS, EPS, and DPS can also be regarded as special cases of TPS modulations. TPS was developed to extend the range of ZVS down to no-load condition, reduce both the RMS and peak current and could provide significant reduction in volume for the transformer as the temporary energy storage inductor in transformer is decreased in value.

Comparing to SPS, EPS, and DPS modulations, TPS modulation has the highest difficulty to be implemented in the DAB system since three degree of freedoms demands high computational burden during the real-time control. Investigations on TPS modulation and TPS modulated control system mainly focuses on the optimization of operation in performance, and

reduction of real-time calculation. In [107] An optimal modulation enables minimum conduction and copper losses was presented with TPS control. In [75], an optimized TPS modulation scheme is proposed with an inductor–capacitor–inductor (LCL) resonant tank to reduce the conduction loss and improve ZVS performance. There also exists works that introduced a look-up table to store the optimized modulation parameters and arrange the hierarchies of three phase shifts during the control operation [108]. A fully normalized algorithm which evaluates three simple expressions that fit the optimal solutions is proposed to implement the optimal TPS modulation strategy in DAB converter [109], implement of the algorithm allows the control system operates with reduce computational in real-time and valid for the whole operating range. Besides applying nonlinear algorithms, in [110], researchers also explores the possibility of introducing an AI-based TPS modulation to achieve the minimized current stress and improve control accuracy. Stability analysis method has also been developed to determine the stability and promote the precision in the determination [111]. With three degrees of freedoms, waveforms of TPS modulated DAB converter can have multiple possibilities.

2.2.2 GPS modulation developed from fundamental modulations

GPS modulation is an integrated modulation strategy aiming to sketch all the possible power transfer characteristics in a DAB converter. The average power flows between two arbitrary ports can have can have 14 possible wave situations if all the three degree of freedoms for one DAB are involved [85]. This modulation is especially suitable for decoupling controlled MAB converter since when power matrix is decoupled to the virtual DAB sub-branches, waveforms and phase shift can be variable, and a modulation that can involve all these conditions is indispensable.

Average transferred power of the GPS modulation under different achievable outer and inner phase shifts combinations could be represented in [85]. All the power characteristics of fundamental modulation including SPS, EPS, DPS and TPS can refer to this table once the MAB is decoupled into DAB branchers. And by locating the phase shift conditions of decoupled DAB branch to power characteristic, control can be applied. Thus, GPS modulation

provides quantified indications for the power transfer relationship and further supports the ‘modular’ modulation decoupling control.

TABLE 2.1

AVERAGE TRANSFERRED POWER OF THE DECOUPLED DAB BRANCH IN AN MAB CONVERTER WITH GPS MODULATION

Zone	Conditions of Phase shifting	Average Transferred Power
A	$D_{IN,i} > D_{IN,j}$ and $0 \leq D_{j,i} < D_{IN,i} - D_{IN,j}$	$\text{sgn}(D_{j,i}) \times \frac{V_j V_i}{2f_s L_{j,i}} (1 - 2D_{IN,i}) D_{j,i}$
B	$D_{IN,i} \leq D_{IN,j}$ and $0 \leq D_{j,i} < D_{IN,j} - D_{IN,i}$	$\text{sgn}(D_{j,i}) \times \frac{V_j V_i}{2f_s L_{j,i}} (1 - 2D_{IN,j}) D_{j,i}$
C	$ D_{IN,i} - D_{IN,j} \leq D_{j,i} < \min[(D_{IN,i} + D_{IN,j}), 1 - (D_{IN,i} + D_{IN,j})]$	$\text{sgn}(D_{j,i}) \times \frac{V_j V_i}{2f_s L_{j,i}} [2D_{j,i}(1 - 2D_{IN,i}) - (D_{j,i} - D_{IN,i} + D_{IN,j})]$
D	$D_{IN,j} + D_{IN,i} \leq \frac{1}{2}$ and $(D_{IN,j} + D_{IN,i}) \leq D_{j,i} \leq \frac{1}{2}$	$\text{sgn}(D_{j,i}) \times \frac{V_j V_i}{2f_s L_{j,i}} [2D_{j,i}(1 - D_{j,i}) - 2D_{IN,i}^2 - 2D_{IN,j}^2]$
E	$D_{IN,j} + D_{IN,i} > \frac{1}{2}$ and $1 - D_{IN,j} - D_{IN,i} \leq D_{j,i} \leq \frac{1}{2}$	$\text{sgn}(D_{j,i}) \times \frac{V_j V_i}{2f_s L_{j,i}} (1 - 2D_{IN,j})(1 - 2D_{IN,i})$

From the previous review of TPS modulation, it is obvious that GPS modulation also requires huge computational burden (hundreds of multiplications within one real-time control period) to achieve accurate real-time control. As this modulation is planned to apply in MAB converters, calculations of multiple GPS modulated virtual DAB branches will inevitably happen simultaneously. Traditional proportional-integral (PI) control will not be able to achieve good dynamic and steady state performances within one or several control periods since model of the plant is not involved in a PI controller. A proper solution is introducing the nonlinear control strategies to accelerate the calculation and enhance the control accuracy.

2.2.3 Non-ideal effect involved in the MAB power characteristics of modulation

In practical DC-DC conversion systems, modulations often been considered together with the control theories as an entire control system, where power characteristics in modulations are usually established under some ideal conditions. In a complex MIMO system, control is required to balance the control accuracy and practical real-time calculation. Complicated modulations considering non-ideal effects do provide more accurate control variables with

better steady state performances; however, hardwires may not be able to accomplish such huge number of calculations within one or several switching periods.

Nevertheless, under certain circumstances, some non-ideal effects can be involved to improve the control accuracy, and some of non-ideal effects once appeared, will severely disturb the normal operation of the system. Hence, these non-ideal effects should not be neglected. For example, to improve the control accuracy, magnetizing inductance can be included in the power characteristics. Magnetizing inductance of the HF transformer in the DAB converter is usually assumed to be much larger than its leakage inductance, thereby the magnetizing current can be negligible. [112-114] investigated its influence on power characteristics if magnetizing inductance are not neglected, results show that the magnetizing inductance impacts the soft-switching region, the power transfer capability, and the leakage inductor current. Besides modifying the modulation to provide more accurate control variables, considering magnetizing inductance can also optimize the system operation. Research [115] used the modified EPS modulation with magnetizing inductance considered to promote the ZVS performance. A SPS modulation considering the RMS currents of the converter that include the effects of magnetizing inductance is proposed, showing the relationship between magnetizing inductance and overall system performance, which indicates the power density improvement for the system [112].

Except the magnetizing inductance of the HF transformer, there are several other non-ideal effects that can have impact on the power characteristics of the modulation strategy which are commonly ignored. With the development of SiC and GaN switching devices, operation frequency of the DAB or MAB application becoming higher and higher [116]. Disregard of their dead-time might be reflected on the accuracy of the control under high switch frequencies, or even reducing the reliability of the converter systems. Research [117] provides a detailed evaluation of the phenomena that could appear when dead-time can not be neglected. Following this consideration, some researchers analyzed the EPS modulation with dead-time for DAB converters, in which work intervals of inductor current zero point is used to distinguish conditions of each sub mode [118]. Similarly, there also exists works analyzed the DPS and TPS

modulations with dead-time for DAB converters, respectively [119, 120]. The TPS work focuses on realizing ZVS operation, while the DPS one considered all kinds of voltage distortion phenomena might affect the transmission power and proposed a special operation mode defined as recessive-dead-time mode. Other nonideal effects that may affect the power characteristic and their impact to the element are shown in the TABLE 2.2.

TABLE 2.2

NONIDEAL EFFECTS OF THE POWER CHARACTERISTICS AND IMPACT ON CERTAIN ELEMENT

Nonideal effects	Description	Related element
Dead-time effect of the switches	Dead-time of the switch is close to the time of phase shift, causing error between ideal and practical phase shift	D
Saturation of transformer	Saturation of the core can lead the decrement of inductance, resulting large current and threatening the safety of the system	L and entire equation
Measurement of leakage inductance	Measurement error between leakage inductance value in power characteristic and practical value	L
Oscillate of frequency	Unstable or noise-mixed digital signals may lead to the ripple of switching frequency, changing the relative permeability of the core	f and L

2.3 Advanced nonlinear control strategies for dynamic and steady-state performance improvement of the MAB converters

2.3.1 Nonlinear control methods

However, complicated electromagnetic paths of the multi-winding transformers in a MAB bring nonlinear power transfer behavior, requiring intensified modeling and control scenarios. These nonlinear control scenarios can be modified from some nonlinear control strategies that has been proposed to improve the dynamic performance or achieving particular control objectives for MAB converters. MPC is a good solution that has been investigated and implemented by many researchers.

A. MPC control

MPC is a nonlinear control method that has been recently implemented in power systems and power electronic converter controls [121-123]. This method has the benefits of fast

dynamics, easy inclusion of nonlinearities, simple digital implementation, and can satisfy a set of constraints simultaneously. The control actions of MPC are obtained through online processing of an optimization problem with a predesigned cost function over a finite prediction horizon within each time step. Multistep prediction horizons are commonly implemented in converters with simple topologies operated at low switching frequencies, whereas single-step horizon allows more flexibility [124, 125].

There are a few publications focusing on controlling DAB converters using MPC [94], some of which have focused on combining MPC with advanced modulation strategies [126, 127], whereas others have focused on practical implementations in DC microgrid [128-130]. Quantified modeling and control methodologies of specific MIMO converters have also been investigated, such as TAB and QAB converters. Ref [131] proposed a modeling technique utilizing decoupling matrix-based PI for TAB converter to improve the dynamics. Ref [132] realized the TAB voltage balancing with reduced control variables through hardware modification, a generalized input impedance model of MAB converter investigated with the validation of TAB and QAB converters [133].

MPC strategies used in the voltage control of DAB reported above can be classified into three variable prediction modes:

- a. Directly predict the phase shift with a fixed step size change through the cost function. This mode compares the difference between the predicted phase shift and the reference phase shift in cost function. Based on the result of cost function, system increases or decreases the phase shift of next control loop with a fixed step size to process the control.
- b. Predict the DC current with a fixed step size through the cost function. This mode compares the predicted DC current and the reference one in cost function. Based on the result of cost function, system increases or decreases the DC current of next control loop with a fixed step size to process the control.
- c. Predict the DC current with the adaptive step and compensate the prediction error. This mode compares the predicted DC current and the reference one in cost function. Based on the result of cost function, system increases or decreases the DC current of next control loop with

a variable step size to process the control and reach steady state as fast as possible. Linearized fixed-step prediction methodologies of a and b have been validated to be effective in DAB applications through many researchers. However, for MIMO system under high switching frequency, linearized searching mode is not efficient enough and faces the danger of overrun.

B. Nonlinear controls for MAB converter

The decoupling of the desired power of each port analyses MIMO systems as multiple isolated virtual DAB branches, which reduces the burden of replacing modulation methods. whereas MPC provides good dynamic performance in searching of the desired power. The MAB converter voltage control strategies proposed by researchers can be classified into three main categories, whose features have been listed in TABLE 2.4

TABLE 2.3

COMPARISON OF CONTROL STRATEGIES FOR CONSTANT VOLTAGE CONTROL IN MAB CONVERTER

	Linear/Nonlinear	System modeling	Dynamic performance	Control Complexity	Characteristics
PI	Linear	Not necessary	Poor	Low	Easy to realize. Suitable for systems which only requires good steady state performance.
Small signal state-space	Linearized by averaging	Small-signal based state-space model with switching events included	Good	High	Accurate system modelling [134]. Suitable for MAB converter with limited ports.
Decoupling based control	Solved by nonlinear optimization algorithms	Large-signal inductance matrix-based system model	Good	Depending on decoupling algorithms	Flexible in modulation strategy selection. Control accuracy depends on the measurement accuracy of the components. Reduced complexity, suitable for generic MAB converter with control constraints [131].

Utilizing $N - 1$ PI voltage controllers to generate outer phase shifts through SPS modulated power characteristics is the simplest and the most used DC voltage control method for an n -

port MAB converter. However, this strategy has relatively poor dynamic performance and control flexibility, as the closed-loop transfer function is constructed based on the simplified power characteristics, and the controllable range is limited by the linearized intervals. The lack of numerical system modeling makes PI controlled MAB converter hard to meet the constraints.

The state-space small signal modeling could provide enhanced dynamic performance. Applicability of this methodology has been validated in some of the multiport converter topologies with limited number of ports: e.g. TAB converters [134-136] and three-port inductance-inductance-capacitance (LLC) converters [137]. However, complexity of designing the controller might be increased significantly since the switching events are contained in the model of power transfer, especially when there are numerous ports involved in the converter topology. Moreover, the range of operation frequency must be restricted to ensure the accuracy of small-signal modeling.

Decoupling based control methods analyze the MAB converter as a coupling of multiple isolated DAB sub-branches. Optimization algorithms were introduced to perform the decoupling and generate control commands. For example, [63] uses the Bisection iterative method to solve the nonlinear equation and find the optimum operating points. Ref. [138] uses machine-learning techniques, which is more accurate, but requires huge amount of data preparation and associated training.

The traditional PI strategies control the n ports MAB with $n - 1$ individual PI controllers to generate the control variables based on the linearized simplified power characteristics. This method is faced with the drawback of poor dynamic performances and its maximum power transfer capability is restricted by the linearization modeling. To address this issue the decoupling control strategies were proposed which decouples the n ports multi-input multi-output (MIMO) systems into $N - 1$ SISO sub-systems to generate the n dimensional control variables. Moreover, GPS modulation also requires a nonlinear control system to improve the dynamic performance and help it achieve the switching between fundamental modulations. These decoupling strategies proposed by the researchers can be classified into two main categories:

1. Utilize the optimization algorithm (OA) or other nonlinear methods to decouple the MIMO system and find the optimum operating directly from the power characteristic.
2. Establish a small signal state-space linearization model around a constant operating point to decouple the power characteristics and design the controller based on the linearized model.

2.3.2 Decoupling control for MAB converters

A. The OA based decoupling control

The OA based decoupling control, whose process is sketched in the block diagram of Fig. 2.3.1, engages numerical analysis, to calculate the accurate results through iterative root-find algorithms. The optimum operating searching for a set of voltage specifications can be realized by a two-stage control. In the first stage the voltage controller generates the referenced DC current by analysing the error between the referenced output voltage and the measured ones. After that, the decoupling calculator supported by the OA takes charge of the outer phase shifts generation. This methodology has high control flexibility, both voltage controller and decoupling algorithms are replaceable. In [139], for example, the MPC is utilized to identify the reference current from the voltage, whereas Newton method is used for the root-find. Inner phase shift can be imported to before the second stage to satisfy the constraints. MPC based control approach employing a prediction model based on TPS modulation is developed to improve the dynamic performance and maintain a desired output voltage level without violating a minimum current stress constraint [140].

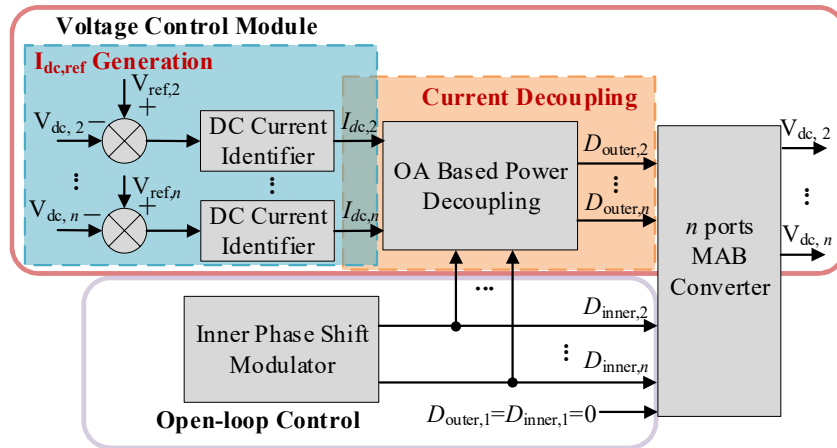


Fig. 2.3.1 Block diagram of OA based decoupling control

The iterative function requires the inversion calculation of a n -dimensional matrix repetitively in each control period. These calculation promises the accuracy of the control variable generation. However, with the increasement of the ports number, the dimension of the partial derivative matrix expands. If large number of ports are involved in the system, significant overhead of the real-time computation pressure will be exerted to the control microcontroller unit (MCU) and other hardware functional resources.

B. The SMC based decoupling control

The iterative algorithm can be replaced by the sliding mode control (SMC) to reduce the control complexity. SMC is a control strategy of variable structure control systems. The most significant property of this technique is the discontinuity of control, its switching characteristic guides the “structure” of the system keeps changing with time. This property forces the system to slide between a specified state trajectory representing the stabilized condition, named as the ‘sliding mode surface’ [141].

SMC control can be divided into two stages: the arrival stage and the sliding stage. In the arrival stage, the state is driven to a stable surface by an appropriate equivalent reaching law. In the sliding stage, the state slides toward the stable equilibrium point [142]. Different from unity feedback in the iterative algorithm decoupling, SMC uses an observer to generate error feedback and estimate of the internal state of a given system. Effectiveness of implementing SMC in DAB converters have been validated by many works. For example, a novel nonlinear SMC based control method for the input-parallel output-series modular DAB converter which regulates the DC-bus voltage and individual module voltages together is proposed in [143]. In [144], an adaptive SMC is proposed to control a DAB converter with an EPS modulation. The steady state operating theory of SMC lead to its inevitable chattering and degradation appearance. Some researchers have investigated optimization approaches to reduce this chattering in DAB area. Ref [145] presents a super twisting SMC incorporating the advantages of normal SMC and subsequently eliminates the chattering for the DAB converter. In [146], a double-integral SMC is developed to provides not only the zero steady-state error without any

chattering but also the fast transient response for DAB converters. All these works validated the potential of applying decoupling based SMC in the MAB converter.

Control block diagram is generally similar to the OA shown in Fig. 2.3.2, state controller generates the intermediate variables based on the feedback from state observers and reaching laws calculation, these intermediate variables are then decoupled to phase shifts and input to the plant.

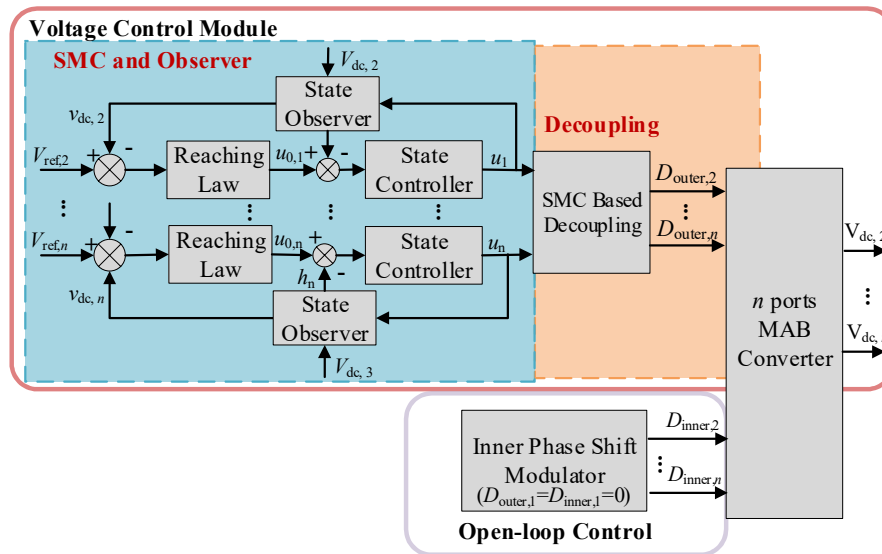


Fig. 2.3.2 Block diagram of SMC based decoupling control

Mathematically, convergence of the SMC updates the results through the reaching law calculation. Similar to the processes in the iterative decoupling, derivative calculating is also necessary. However, update through reaching law do not require a repeated high-dimensional matrix inversion. Which means from the system level, SMC based decoupling control has lower control complexity.

For both OA and SMC based decoupling control, system has high tolerance to the switching of modulation strategies. If use the GPS modulation as the indication of the power differential, the entire controllable range of outer phase shift is the same as the achievable range of the system [85]. Theoretically, the difference between OA and SMC decoupling is, SMC has lower real-time computation, it provides system better robustness to interference and improved dynamic performance whereas OA has better steady-state performance.

C. Small signal modelling based decoupling control

Unlike the previously introduced strategies that directly implements the nonlinear control methods, logic of the small signal modelling is to establish a linearized model and implement the linear control methods.

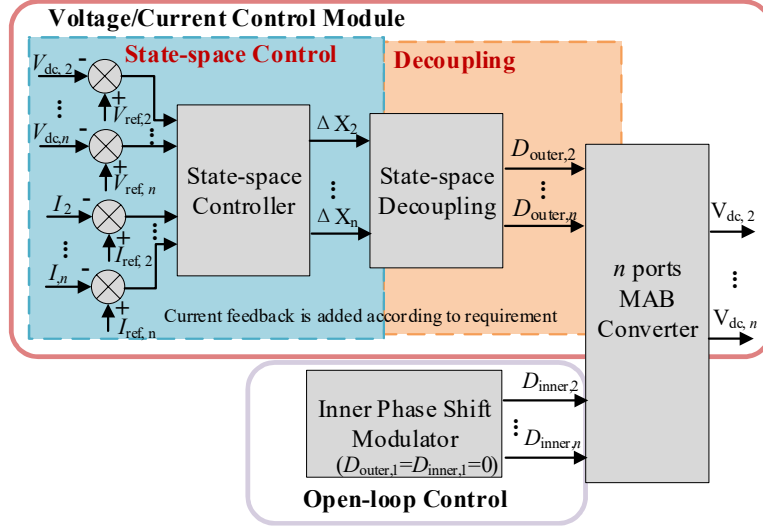


Fig. 2.3.3 Block diagram of state-space linearize decoupling control

The block diagram containing the entire control processes of has been shown in the Fig. 2.3.3. In this technique, linearization of the power characteristics is achieved by taking the Taylor series expansions around a constant operating point. Linearization provided the simplification of the real-time calculation. During the expansion, only lower order harmonics are considered due to the control complexity. The loss of information may cause the error involved with the higher order harmonics. Furthermore, small signal modelling restricts the controllable range, as the linearization implemented is only a local part of the entire system response.

D. Comparison of the Decoupling Control Strategies

To conclude, the OA and SMC based decoupling, has higher flexibility in controllable range, switching of operating frequencies, and the selection of the modulations. Among them, OA has better steady-state performance and higher control complexity. As the real-time calculation of the OA control involves the continuous inversion of n -dimensional matrix, increasement of ports can lead to severe overhead of computation. These two strategies are more suitable for

the MAB applications requiring accurate steady-state rating-varied voltage control with relatively low port numbers. The quadruple fast EV charger for example.

The small signal state-space modelling has a relatively low level of control flexibility and larger steady-state ripple. However, this method demands less online computation. As the inversion of the matrix is only performed once in each control period. Moreover, the switching of the control purpose can be easily realized. Constant current and constant voltage control can be switched or realized simultaneously according to the operation requirements. This method is suitable for the MAB applications requires a switching between current and voltage.

TABLE 2.4
COMPARISON OF DECOUPLING CONTROL STRATEGIES FOR CONSTANT VOLTAGE CONTROL IN MAB
CONVERTER

	System Modeling	Steady State Performance	Flexibility	Control Complexity	Application Scenarios
OA based	Large-signal inductance matrix-based system model.	Good	High	High	MAB converters requiring accurate steady-state rating-varied voltage control with relatively low port numbers.
SMC	Depends on the system requirement.	Ripple due to its operation theory.	High	Low, but needs observer	
Small signal state-space	Small-signal based state-space model with switching events included	Depends on the operating condition. Generally worse than the other two.	Low	Low	MAB converters whose control aim is more than the voltage controls involving large number of ports.

The distribution network of the onboard propulsion system in MEA for example. The comparison information has been listed in the TABLE 2.4.

2.4 Research on design and implementation of HF transformer in MAB converters with accurate leakage inductance estimation

A DAB includes a MFT or HFT to realize voltage matching and electrical isolation [70, 72, 77, 78]. For many DAB converters implemented in the transportation propulsion systems performing as the DC bus tie converter, promotion of power density and hardware volume reduction are two prior practical design objectives due to limited cabin space [147]. In recent years, power density has been regarded as one of the most important design targets for the DAB and its extension-topology converter systems, MAB converter as well. Many innovative transformer scenarios have been proposed with the power density improvement consideration since it is the largest component in the entire system. Under these trends, integrated gate-drive components [148, 149] and integrated transformers have been proposed [150, 151]. Since a high frequency transformer is usually the largest component by volume in the system, applying a planar transformer to replace the traditional ones has been considered as a first-step solution with effectiveness for miniaturization and weight-reduction of components.

Comparing to traditional wounded transformer, a planar transformer benefits from decreased size, and improved efficiency. In addition, gap between each turn of the winding in the wound-up transformer is not practically identical due to the manufacturing, leading to the inaccuracy in its parameter estimation. Whereas the planar windings in the planar transformer, once manufactured, all the parasitic parameters are relatively invariable fixed, which has better precision in inductance estimation [152]. This feature provides enhanced accuracy in the realization of these theoretical values [153].

Using the high-inductance series-connected inductors to store the energy temporarily is a conventional solution in DAB converters. With these inductors, interleave winding arrangement becomes the best solution for the transformer since it can cancel the magnetic field between windings. In recent years, effort of DAB integrations has been paid to integrating the series inductors and the high frequency transformer into a single magnetic component for power density optimization by increasing the leakage inductance of the integrated transformer. Effectiveness of this integration has been validated on specific DC-DC converter topologies, integrated LLC resonant converter, for example [154, 155]. Conventional interleaved winding is no longer suitable for integration as its leakage

inductance is neither large enough nor controllable [156]. To realize the magnetic integration, the integrated HFT should have large-enough and controllable leakage inductance, estimation of these inductances should be accurate, which requires leakage estimation strategies.

A. Estimation of leakage inductance transformer

Effort should be paid to realize the controllable magnetic integration requirements besides satisfying the fundamental electrical power specifications for DAB converters. A precise theoretical leakage inductance estimation strategy needs to be developed combined with instructions of magnetic integration help selecting the winding and the core setups that can realize the aimed values of the leakage inductance.

The investigations and innovations of the integrated planar transformer achieving accurate magnetic integration can be divided into two types: 1) core-structure, 2) winding arrangement, as listed in detail in TABLE 2.5.

TABLE 2.5
INVESTIGATIONS AND INNOVATIONS OF THE INTEGRATED PLANAR TRANSFORMER

	Core Structure		Winding Arrangement	
Magnetic Integration Scenario	Insert the air gap, controllable integration realized by adjusting the dimension of the gap [157].	Insert the magnetic shunt, controllable integration realized by adjusting shunt dimension and changing shunt materials [158-160].	Interleaved winding arrangement to achieve a small-value low controllability magnetic integration [161].	Sectional winding arrangement to achieve the maximum leakage inductance without core modification [153].
Leakage Inductance Evaluation	Energy in the winding and insulation layers is recognized as neglectable compared to the one in the airgap or shunt according to [159, 162]. Estimation of these leakage inductances only considers the leakage flux in the core, air gap and shunt.		Energy based evaluation based on the MMF distribution [163]. Air-path leakage flux is not included in the evaluation.	

Inserting the magnetic shunt or air gap can provide a higher leakage inductance. Ref. [158-160] investigated realizing the desired higher leakage inductance by inserting a magnetic shunt with low permeability. Ref. [157] proposed a novel asymmetrical winding arrangement

and a core structure with horizontal air gap to generate controllable leakage inductances. The leakage inductance of a three-phase integrated transformer was enlarged by adjusting both the transformer and the core structure in [164]. Accurate estimation for the leakage inductances in these core-structure-changed scenarios is accomplished by calculating the energy stored in the shunt or the air gap. According to [159, 162], energy in the winding and insulation layers is far lower than that stored in the airgap or shunt. The leakage inductances can then be controlled by regulating the permeability of the shunt or the length of the air gaps, respectively. The windings of the transformer can also be arranged or manipulated to achieve a controllable leakage inductance when core structure has not been modified. Ref. [165] used the split winding arrangement and air gap to achieve magnetic integration. Modified calculation models are proposed to estimate electromagnetism and thermal characteristics more precisely in [166]. In [167], a high-frequency lumped equivalent circuit model for DDR with frequency-dependent parameters to analysis the leakage flux. However, for many of these research works, the estimation of leakage inductances relays on empirical formulas. In addition, most reluctance or energy-based model in published literatures only calculates the leakage flux in the core or windings with the air-path leakage flux ignored, and none provided an accurate achievable range of the magnetic integration from minimum to maximum with its corresponding winding arrangement for core-structure-unchanged planar transformers.

Once magnetic integration is applied, accuracy of the leakage inductance estimation becomes extraordinarily important since leakage inductance the of the HFT substituted the series connected inductors in modulation and control systems. Error between theoretical value and practical value of leakage inductance can affect the accuracy of control, stability and port consistency of the system.

Ref [159] demonstrated an energy based leakage inductance estimation strategy, which has been widely used by many researchers to evaluate or design a transformer [168-170]. This strategy assumes the magnetic field outside the coil is short-circuited by the core, and the magnetic pressure drop in the core is zero. Represent the magnetic energy stored in the winding, leakage inductance can be deduced. This evaluation only considered the energy stored in the

windings. Since the air has the same permeability as the copper, part of the energy is stored in the air of the window. The air-path leakage flux caused by the imperfect magnetic linking between two coils has been ignored. Estimated leakage inductance from this strategy will therefore be smaller than the actual value. Besides the energy evaluation, the equivalent leakage inductance can be calculated from the reluctance-based evaluation [171].

B. Realization of magnetic integration for two-port transformer and multi-port HF transformer

Some research works have considered modifying the core or winding structure to further improve the power density and realize the accurate leakage estimation. These works mainly focused on the SISO DC-DC converters applications. Ref [172] achieved both accurate leakage estimation and magnetic integration by inserting a segmental shunt horizontally in the central of a ER core. Similar strategies have been utilized in [154, 160, 173], where low-permeability magnetic shunts were inserted in the central of the planar transformers to provide a high leakage inductance and accurate estimation. These strategies assume the energy stored in the windings and insulation layers is far lower than that stored in the magnetic shunt. In addition, the leakage and magnetizing inductances can be controlled for a limited range of leakage inductance and shunt relative permeability by regulating the permeability of the shunt and the length of the air gaps, respectively [174, 175]. Besides shunt insertion, researchers also used winding arrangement approaches to achieve the magnetic integration. The traditional of transformer with E-shaped core placed all the windings on the central pillar, for which interleaved winding arrangement can achieve large leakage inductance. For example, in [176], secondary windings of a ER shaped integrated planar transformer are separated to upper and lower sides. Some transformer core configuration uses the center pillar of an E-shaped core for the leakage flux path, and the primary and secondary windings are wound without interleaving around the two outer pillars to achieve large leakage inductance [177]. Ref [161] shows a modification of this approach, which uses interleaved windings with an asymmetric number of turns on the side pillars, and results in reduced AC resistances. There also exist research works combines all the core, shunt/air gap and winding approaches to achieve the magnetic integration; [157] utilizes

partially interleaved windings and realizes the leakage inductance through an asymmetrical horizontal air gap on one of the outer legs.

Magnetic integration in MAB converter refers to integrating multiple magnetic components: N series-connected inductors L_{series} and a MT into a single magnetic component by increasing the leakage inductance of the integrated MT. There are some papers projected on configuring high frequency multi-winding transformers (HFMT) for MAB converters. In [178], a four-port square-shape-core transformer with only one balanced flux path shared by all windings is proposed. Ref [179] utilizes a regular EE shaped core for a four-port solid-state transformer (SST) with all windings located on the central pillar. For the MT core scenarios that rely on sharing the same flux path by all the windings to maintain the port consistency, air gaps need to be inserted into the core structure, or magnetic shunts need to be inserted between the windings if large leakage inductances are required to achieve magnetic integration [157, 159, 172]. However, insertion of shunt and air gaps lead to the ports hard to maintain the consistency. And currently, no works have considered magnetic integrations on a HFMT in MAB converters.

2.5 Summary of this chapter

In this chapter, reviews of existing works from researchers trying to figure out the issues in modulation, control and magnetic integration are presented. In modulation part, fundamental modulation strategies including SPS, EPS, DPS, and TPS are reviewed with their optimized version, some of them are coupled with advanced control methods applied in DAB converters are introduced as well. Compared to the DAB converter, power characteristic in MAB has no one-to-one correspondence relationship and is difficult to linearize. Hence, researchers proposed decoupling control strategies that decouple MAB into several DAB sub-branches and analyze the power characteristic from part to whole. This control strategy is of vital importance for this research as all the MAB converter control scenarios proposed in this research are based on the decoupling control. Combined with optimized algorithms and modified modulations which will be introduced in Chapter 3 and Chapter 4, decoupling based control can achieve good dynamic and steady-state performances with limited computational burden.

Since a virtual DAB sub-branch in decoupling control is a link between two arbitrary ports from the MAB converter, one H-bridge can be both primary and secondary sides of several sub-branches. Hence, if the modulation of MAB requires involving of all the inner and outer phase shifts, it must have the ability to represent the power characteristic under all the possible inner and outer phase shifts combinations. According to these researches, GPS modulation which can handle all these phase shift conditions are reviewed, which are introduced in detail in Chapter 4. Based on the contribution of GPS modulation, this research developed a decoupling control strategy that allows the switching of the fundamental modulations to be developed for the MAB converter.

The second part reviewed research implementing the advanced decoupling control methods in the MAB converters. Utilizing $N - 1$ PI voltage controllers to generate outer phase shifts through SPS modulation is the most realizable DC voltage control method for a N -port MAB converter. However, this strategy has relatively poor dynamic performance and control flexibility, as the closed-loop transfer function is constructed based on the simplified power characteristics, and the controllable range is limited by the linearized intervals. The lack of numerical system modeling makes PI controlled MAB converter hard to meet the constraints. Researchers thus developed OA based, steady-state modeling, and SMC decoupling control to control the MAB converter. Through the comparison of these three typical control scenarios from this work, OA based control is further improved in this research. Nonlinear control methods like MPC are applied in the OA based strategy. These strategies and improvements are proposed and verified in Chapter 4.

Following the review of the power transfer control and modulations, the practical realization scenarios of the magnetic integration for the HF transformer to improve the system power density have been investigated, as power density is one of the most important indexes of the on-board power transfer, distribution and propulsion MAB converter system. Many designs scenarios of the multi-winding transformers with novel core, winding or air gap configurations have been evaluated. Integrated transformer requires large transformer leakage inductance to replace the series inductors. In addition, an accurate leakage inductance estimation strategy is

also required as the replacement makes the leakage inductance directly involved in the power transfer characteristic. From the reviewed energy based leakage estimation strategy, a reluctance based estimation strategy is proposed in this research. Furthermore, an integrated multi-winding transformer scenario is developed after referring to other integrated transformer scenarios.

3. Modulation strategies considering the non-ideal effects to improve MAB power transfer quality

3.1 Chapter overview

This chapter focuses on the steady state performances of power transfer and starts with the optimization of the existed modulation, which includes the improvement of the ZVS and the voltage regulation in DAB converter. The traditional SPS modulation is easy to be implemented in the N -port active bridge converter systems as it only contains $N - 1$ control variables. However, this modulation strategy faces several severe drawbacks. For the consideration of the soft switching enhancement, system efficiency promotion and voltage regulation improvement, EPS is widely used in the DAB and MAB converter system. Since the integrated DAB and MAB system uses the integrated transformers with large leakage inductances to replace the series inductors, the ratio between the equivalent leakage and magnetizing inductance is not neglectable. Ignoring the magnetizing inductances in the power characteristics of the modulation might reduce the quality of power transfer. Hence, modified modulation strategies based on the EPS in DAB converter considering the ratio between leakage and magnetizing inductance have been proposed to improve the ZVS performance for the DAB and MAB systems.

Then, some non-ideal effect that can be considered in the modulations to improve the power transfer quality and control precision, together with some non-ideal effect that must be avoided are listed. Similar to the magnetizing inductances of the transformer, these non-ideal parameters can affect the accuracy of the power characteristics when establishing the modulation directly or indirectly, dead-time for example. Different parameters have various levels of influence on the system modeling, hence power dependency for these possible parameters is evaluated with some reasonable solutions provided in response.

3.2 A modified EPS modulation for the DAB converters considering the transformer magnetizing inductance

For practical transformer in the DAB converter, the equivalent leakage inductance in primary and secondary windings could be denoted as L_{s1} and L_{s2} . Both primary and secondary winding processes inner resistance, denoted as R_1 and R_2 . Permeability of the core is not infinite, magnetizing inductance and resistance in the core could be represented as L_m and R_m . While $n:1$ is the turn ratio of the transformer.

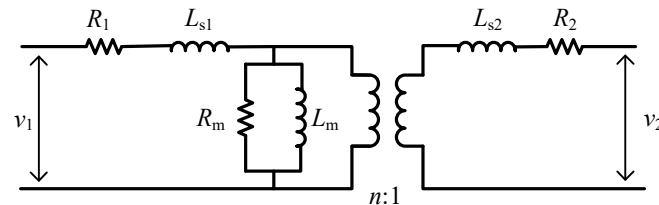


Fig. 3.2.1 Equivalent circuit of a practical transformer in the DAB converter

Generalized equivalent circuit of a two-port practical transformer is described as Fig. 3.2.1. For majority of modulation methods applied in LF operated DAB converters, SPS and EPS modulation for example, value of magnetizing inductance is assumed to be infinite in the equivalent circuit analysis [89, 180]. With this hypothesis, resultant reactance is dominated by the leakage inductances and the resistances in series connection, while magnetizing branch is neglected. As inductive reactance is proportional to the switching frequency, resistance will be less significant with the increase of frequency. For DAB converters operating at high switching frequencies, saturation of transformers could lead to the reduction of magnetizing inductance. This phenomenon would have an impact on power transfer and further affect the converter control and the ZVS conditions.

In Chapter 3.2, the T-shaped traditional transformer structure is replaced by the π -shaped equivalent circuit to investigate the impact of magnetizing inductance on soft switching conditions and power characteristic. First, average power transfer characteristic is redetermined for SPS modulation to verify the necessity of including magnetizing inductance in power calculation. Then, magnetizing inductance could extend the ZVS range is discussed, further with the enhancement in the soft switching provided by the reduction in magnetizing. Extend this analysis to EPS modulation. From the calculation of soft switching range, ZVS covered duty ratio maps are established. Based on the maps, an advanced EPS modulation method has

been proposed to improve the system voltage utilization and reduce the current stress. Finally, simulation and experimental validation are performed to investigate the performance of proposed modulation and validate the supposed analysis.

3.2.1 Power characteristic and soft switching condition for magnetizing inductance involved SPS modulation

Assume the switching frequency is beyond 20 kHz where reactance is dominated by the inductance and resistance could be neglected. Fig. 3.2.2(a) shows the T-shaped equivalent of a common two-port transformer applied in a DAB converter. This equivalent circuit could be transferred to π -shaped circuit shown in Fig. 3.2.2(b) to simplify the ZVS analysis.

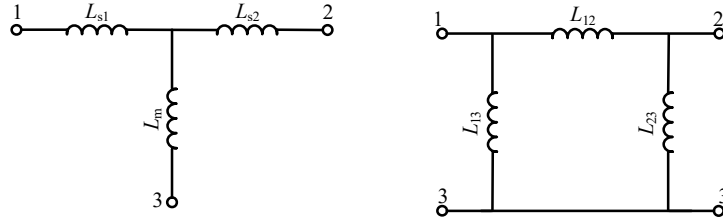


Fig. 3.2.2 (a) T-shaped two-port transformer equivalent circuit (b) π -shaped equivalent circuit

Define M as the ratio between magnetizing inductance and primary side leakage inductance, $L_m = ML_{s1}$. To simplify the calculation, define $L_{s1} = aL_{s2}$ with $a \in (0, \infty)$. Components in π -shaped equivalent circuit can be represented as (3.1) with M and a .

$$\begin{cases} L_{12} = \frac{L_{s1}L_{s2} + L_{s2}L_m + L_{s1}L_m}{L_m} = \frac{(aM + M + 1)}{aM} L_{s1} \\ L_{13} = \frac{L_{s1}L_{s2} + L_{s2}L_m + L_{s1}L_m}{L_{s2}} = (aM + M + 1)L_{s1} \\ L_{23} = \frac{L_{s1}L_{s2} + L_{s2}L_m + L_{s1}L_m}{L_{s1}} = \frac{(aM + M + 1)}{a} L_{s1} \end{cases} \quad (3.1)$$

Power transfer between two nodes solely related to the L_{12} branch. L_{13} and L_{23} affect the voltage and current of primary and secondary H-bridge individually. They inject inductive current to modify the resultant current at switching instants to provide extension in ZVS range. A similar strategy of reducing magnetizing inductance in HF transformers have been proved as

an effective hardware design solution to improve the system efficiency of LLC converter [181, 182]. An ideal SPS modulated DAB converter, average power transfer characteristic is:

$$P = \frac{nV_1V_2D_{2,1}(1 - D_{2,1})}{2f_sL_s} \quad (3.2)$$

where $D_{2,1}$ is the outer phase shift between primary and secondary bridge. For DAB converter, it does not have decoupled sub-branch, use D_o to replace $D_{2,1}$ in the following equations.

Assume the resultant series inductance $L_s = \left(1 + \frac{1}{a}\right)L_{s1}$. Substitute leakage inductance by L_{12} gives the power characteristic (3.3) for π -shaped DAB converter model.

$$P = \frac{nV_1V_2D_o(1 - D_o)}{2f_s \frac{(aM + M + 1)}{aM} L_{s1}} \quad (3.3)$$

Plot the calculated power with ideal SPS modulation in Fig. 3.2.3, where $a = 5$. The trend shows that the decrement of M could lead to error in power calculation, which means ideal SPS modulation with M considered as infinite is not accurate. For example, if value of M equals to 5, power transfer in practical is 96% of the calculation result from ideal SPS modulation.

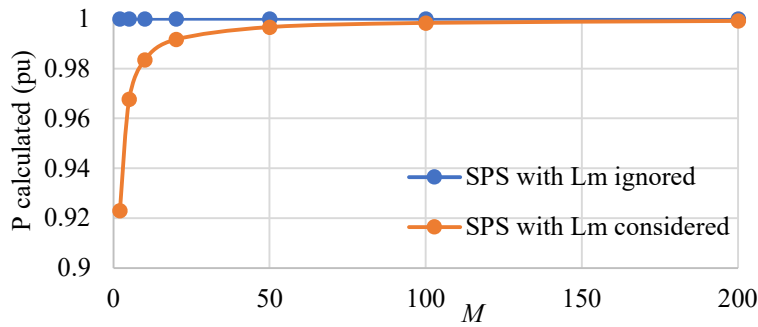


Fig. 3.2.3 Comparison of average power transfer calculated by the power characteristic with the ideal SPS and SPS considering existence of L_m when $a = 5$

Hence, it is necessary to include magnetizing inductance in the power characteristic of the modulation strategy. Involving the L_m also loosen the restriction of realizing the soft switching for the system. Soft switching in the active bridge can be classified into two groups according to their ZVS considerations [117] [183]:

1. Current-based (CB) ZVS: The largest group of publications does not consider the (parasitic) switch capacitances and assumes that ZVS of a bridge leg is achieved when the drain-to-source current of the switch which initiates the commutation (turn-off) is positive at the switching instant.
2. Energy-based (EB) ZVS: When considering CB ZVS, substantial parts of the ZVS regions involve incomplete bridge commutations due to the presence of (parasitic) switch capacitances.

In this research, all the ZVS refers to the ZVS-on of the CB ZVS with the consideration of the dead time effect. This constraint can be satisfied by some soft switching based modulations, soft-switching phase shift (SSPS) used in the Chapter 4 modified from the EPS modulation in the DAB topology for example [85]. Assuming ideal power devices and transformers without considering the device parasitic capacitance. Waveforms of SPS modulated DAB system considering the existence of the L_m is sketched in the Fig. 3.2.4.

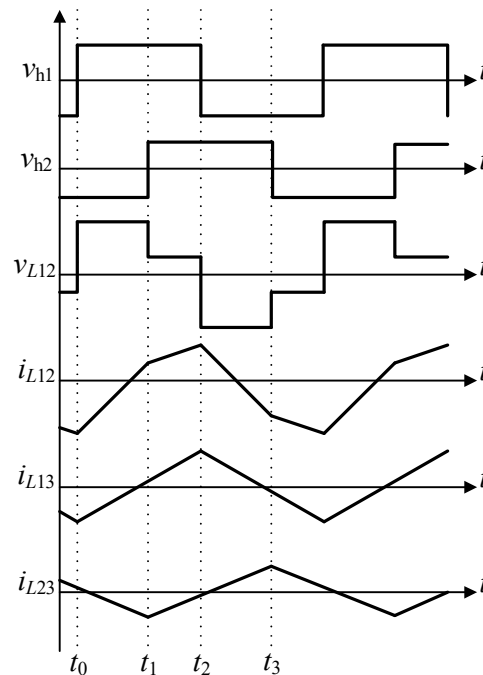


Fig. 3.2.4 Waveforms of the non-ideal SPS modulated DAB converter, where t_0 and t_2 are the rising and falling edges of primary H-bridge, t_1 and t_3 are the rising and falling edges of secondary H-bridge.

Soft switching in DAB system refers to the ZVS-ON, whose condition can be defined by the current flow upon the switching transistor is negative at the device turned ON instant [94, 184, 185]. For DAB converter, soft-switching conditions is ((3.4).

$$\begin{cases} i_L(t_0) < 0 \\ i_L(t_1) > 0 \end{cases} \quad (3.4)$$

Define the DC voltage conversion ratio k as $k = \frac{nV_2}{V_1}$. Initially suppose input voltage V_1 is greater than output V_2 , $0 < k \leq 1$. For reverse power conversion, $\frac{1}{k}$ can be applied to substitute k . Leakage inductance current neglecting L_m at t_0 instant is:

$$i_L(t_0) = -\frac{V_1(2kD_0 + 1 - k)}{4f_s L_s} \quad (3.5)$$

Substitute L_s with L_{12} donates the current passing though L_{12} for π -shaped equivalent circuit. Current waveforms of both L_{13} and L_{23} are triangle waves. Assume power is transmitted from primary to secondary side with $D_0 \in (0,1)$, resultant current (3.6) consists of i_{L12} and i_{L1} should be negative. For SPS modulation, D_0 is the only control variable of power transfer. Present D_0 with the function of k , a and M with $M \in (1, \infty)$.

$$i_R(t_0) = -\frac{V_1(2kD_0 + 1 - k)}{4f_s L_{12}} - \frac{V_1}{4f_s L_{13}} < 0 \quad (3.6)$$

$$D_0 > \frac{1}{2} - \frac{1}{2k} - \frac{1}{2kaM} \quad (3.7)$$

Repeat the same procedure whereas resultant current at t_1 should be positive.

$$i_R(t_1) = \frac{V_1(k - 1 + 2D_0)}{4f_s L_{12}} + \frac{kV_1}{4f_s L_{23}} > 0 \quad (3.8)$$

$$D_0 > \frac{1}{2} - \frac{k}{2} - \frac{k}{2M} \quad (3.9)$$

Substitute D_0 with $-D_0$ provides the ZVS restriction when power is transferred reversely. Overall ZVS requirement of the non-ideal SPS modulation with L_m involved is determined as:

$$\frac{1}{2} - \frac{k}{2} - \frac{k}{2M} < |D_0| < 1, \text{ when } 0 < k < \frac{M}{M+1} \quad (3.10)$$

$$0 < |D_0| < 1, \text{ when } \frac{M}{M+1} < k < 1$$

For ideal SPS modulation, the ZVS restriction is:

$$\frac{1}{2} - \frac{k}{2} < |D_0| < 1 \quad (3.11)$$

Comparison of the ZVS restrictions between the ideal (3.10) and non-ideal (3.11) SPS modulation strategies shows that, involving the magnetizing inductor in the converter could expand the range of the ZVS. As the equivalent branches of L_m in primary and secondary side modify the resultant current at switching instant by injecting inductive current. Smaller ratio M would provide wider range of eligible D_0 and contribute to the ZVS realization.

3.2.2 An advanced EPS modulation and its ZVS condition for DAB converter considering the magnetizing inductance

For EPS modulation there are two possible waveforms when π -shaped model is applied, distinguished with the relationship between primary inner phase shift $D_{IN,1}$ and D_o as shown in Fig. 3.2.5 [99, 100].

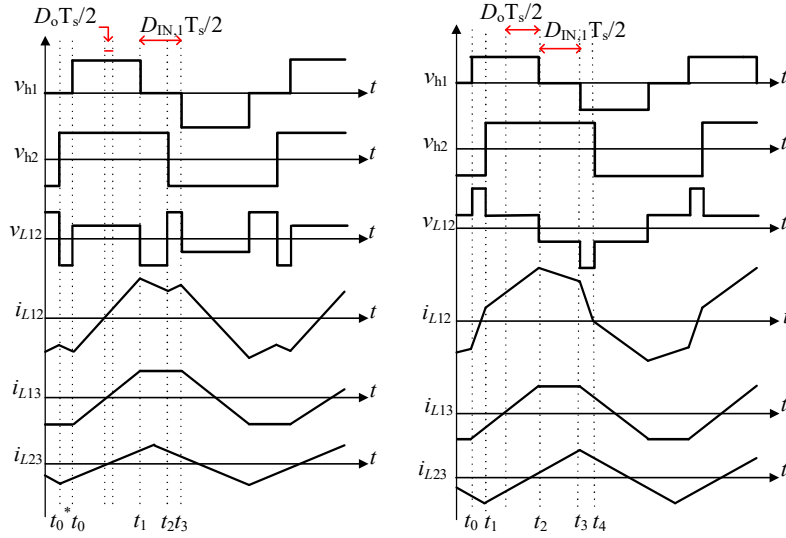


Fig. 3.2.5 (a) Waveforms of EPS modulated DAB when $0 < D_o \leq \frac{D_{IN,1}}{2}$ considering L_m (b) Waveforms of EPS modulated DAB when $\frac{D_{IN,1}}{2} < D_o \leq 1$ considering L_m , where different t refers to rising and falling edges of primary and secondary H-bridges

Assume power is transmitted from primary to secondary node, $D_o \in (0,1)$. If $D_o \leq \frac{D_{IN,1}}{2}$, voltage rising edge of secondary bridge will lead primary as shown in Fig. 3.2.5(a). Current of L_{12} and L_{13} at instant t_0 is:

$$i_{L12}(t_0) = \frac{V_1}{4f_s L_{12}} (2kD_o - kD_{IN,1} + D_{IN,1} + k - 1) \quad (3.12)$$

When $D_{IN,1}$ is applied, current of i_{L13} becomes a trapezoidal wave. While current of i_{L23} is still a triangle wave. Use D_o to control the transferred power while $D_{IN,1}$ is adjusted to meet the ZVS requirement. For ideal EPS modulation, ZVS requirement is:

$$1 - k < D_{IN,1} < 1 - \frac{2k}{1 - k} D_o \quad (3.13)$$

If considering the existence of L_m , ZVS condition is then (3.14).

$$1 - k - \frac{k}{M} < D_{IN,1} < 1 - \frac{2k}{1 - k + \frac{1}{aM}} D_o \quad (3.14)$$

When $\frac{D_{IN,1}}{2} < D_o \leq 1$, ZVS condition for ideal and non-ideal L_m is:

$$D_1 < 1 - \frac{2k(1 - D_o)}{1 + k} \quad (3.15)$$

$$D_1 < 1 - \frac{2k(1 - D_o)}{1 + k + \frac{1}{aM}}, D_o > \frac{1}{2} - \frac{k}{2} - \frac{k}{2M} \quad (3.16)$$

Based on the results from (3.15)-(3.16). Establish the Cartesian coordinate system with D_o and $D_{IN,1}$ as reference frames, area satisfying ZVS is shaded in Fig. 3.2.6(a), (b). Crossing points on the $D_{IN,1} = 2D_o$: $A = \left(\frac{1-k}{2}, 1-k\right)$, $B = \left(\frac{1-k}{2} - \frac{k}{2M}, 1-k - \frac{k}{M}\right)$ and $C = \left(\frac{1}{2} - \frac{Mk}{2+2aM}, 1 - \frac{Mk}{1+aM}\right)$.

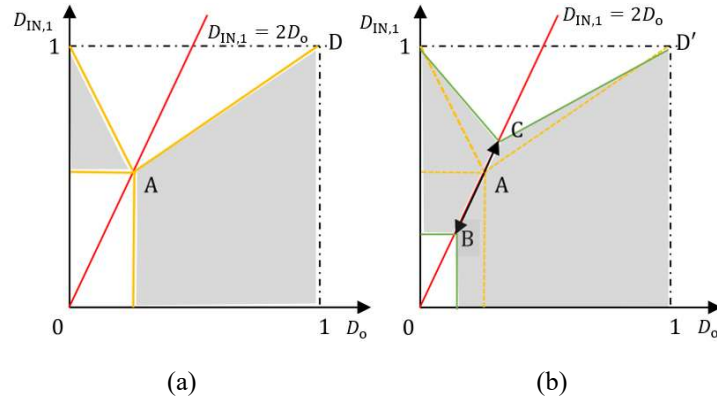


Fig. 3.2.6 (a) ZVS area of EPS modulation with L_m neglected (b) ZVS area considering L_m

Comparing two maps, existence of L_m has expanded the range of $D_{IN,1}$ and D_o available for ZVS. Smaller M results in the position of the point B and C drifting away from A, providing extended soft switching freedoms. Maximum average power transfer occurs at $D_o = \pm 0.5$, $D_o \in [0, 0.5]$ can cover all the power transfer possibilities in forward direction. Based on the ZVS maps, an advanced extended phase shift (AEPS) modulation method (3.17) is proposed to improve the ZVS condition, voltage utilization and reduce the current stress.

$$\left\{ \begin{array}{l} D_o \in [0,0.5] \\ D_{IN,1} = 0 \text{ when } \frac{M}{M+1} \leq k < 1 \\ D_{IN,1} = 1 - k - \frac{k}{M} \text{ when } 0 < k < \frac{M}{M+1} \\ D_{IN,2} = 0 \end{array} \right. \quad (3.17)$$

This coupling characteristic is sketched as a horizontal line passing through the point B. For EPS modulation neglecting the existence of L_m , a likewise modified extended phase shift (MEPS) modulation ($D_{IN,1} = 1 - k$) in (3.18) is analyzed as comparisons [13]. Plot these two EPS modulation methods in ZVS map as Fig. 3.2.7 (a), (b).

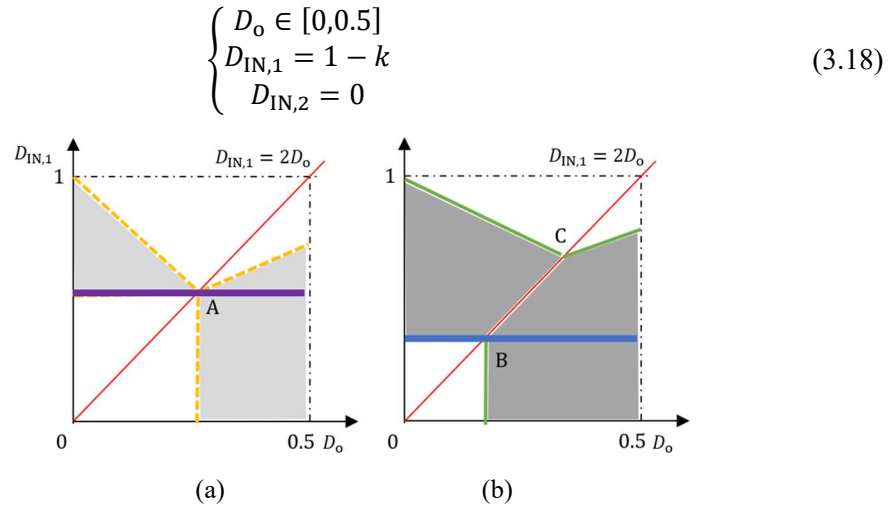


Fig. 3.2.7 (a) MEPS modulation (b) AEPS modulation

Express the average power equation of EPS modulation according to GPS modulation [85] with L_s replaced by L_{12} to include the existence of L_m . For MEPS with $D_{IN,1} = 1 - k$, power characteristic is:

$$P = \left\{ \begin{array}{l} \frac{nV_1V_2}{2f_s \frac{(aM+M+1)}{aM} L_{s1}} kD_o \text{ when } 0 \leq D_o \leq \frac{1}{2} - \frac{k}{2} \\ \frac{nV_1V_2}{2f_s \frac{(aM+M+1)}{aM} L_{s1}} \left[D_o(1-D_o) - \frac{(1-k)^2}{4} \right] \text{ when } \frac{1}{2} - \frac{k}{2} < D_o < \frac{1}{2} \end{array} \right. \quad (3.19)$$

For AEPS modulation, power characteristic is divided into two branches: If $1 - k - \frac{k}{M} < 0$, $D_{IN,1}$ equals to zero, modulation operates as SPS modulation. If $0 < 1 - k - \frac{k}{M} < 1$, coupling curve is positioned in positive axis. Power characteristic is:

$$P = \begin{cases} \frac{nV_1V_2}{2f_s \frac{(aM+M+1)}{aM} L_{s1}} \left(k + \frac{k}{M}\right) D_o & \text{when } 0 \leq D_o \leq \frac{1}{2} - \frac{k}{2} - \frac{k}{2M} \\ \frac{nV_1V_2}{2f_s \frac{(aM+M+1)}{aM} L_{s1}} \left[D_o(1 - D_o) - \frac{\left(1 - k - \frac{k}{M}\right)^2}{4} \right] & \text{when } \frac{1}{2} - \frac{k}{2} - \frac{k}{2M} < D_o < \frac{1}{2} \end{cases} \quad (3.20)$$

Plot the power versus D_o curve of two modulation methods with $k = 0.55$, $M = 5, 20$ and 100 , respectively. With the existence of L_m considered, proposed AEPS method demands reduced $D_{IN,1}$ to achieve ZVS under the same power transfer requirement. As both modulation methods have 100% secondary side voltage utilization, reduced $D_{IN,1}$ in AEPS modulation provides improved system voltage utilization.

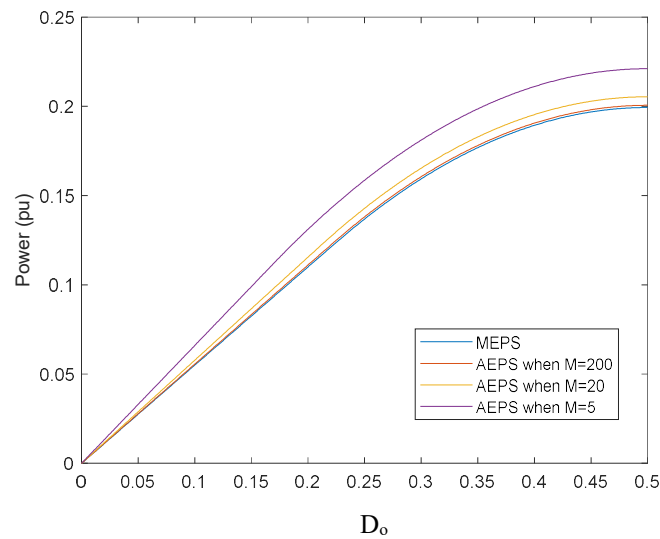


Fig. 3.2.8 Power characteristics of AEPS and MEPS modulation strategy

Fig. 3.2.8, when ratio M is small, AEPS would provide more accuracy in power transfer capability estimation. Besides, reduction in D_o and $D_{IN,1}$ could reduce the current stress, reducing the burden of the system operation.

3.3 A modulation related parameter dependency evaluation based on the non-ideal effects involved in MAB power characteristics

Besides the magnetizing inductance of the HF transformer, there are several other non-ideal effects that can have impact on the power characteristics of the modulation strategy, dead-time effect and hysteresis phenomenon, for example. These parameters are commonly ignored in theoretical power modeling of the DC-DC converter under ideal conditions. With the development of SiC and GaN power devices, operation frequency of the DAB or MAB application becoming higher and higher [116]. Disregard of these non-ideal effect will be reflected on the accuracy of the control and quality of power transfer in high switching frequency operated DAB and MAB converter systems, or even worse reducing the reliability of the converter systems. Besides the ignored non-ideal effect, measurement error of the components also affects the accuracy of power characteristic modelling in different aspects. This chapter presents a comprehensive analysis of parameter dependency including several typical non-ideal effects and convention measurement error that can have impact on the power modelling characteristic of the previous introduced modulation strategies.

3.3.1 Analysis of the dead-time effect

Dead time causing the voltage polarity reversal and phase drift phenomena of the IBDC is concerned in [186] and [187]. Ref [188] developed a power flow model over a short time scale that incorporates additional parameters, including the power semiconductor voltage loss and dead time for the first time. Since switching frequency of the DAB and MAB configured application is much higher compared to the time model was proposed, the dead-time effect of active bridge converter becomes an apparent issue.

A. Traditional power transfer model with dead-time effect neglected

Fig. 3.3.1 shows the traditional principle waveforms of the voltage, current and the switching actions of the four switches in a DAB converter when dead time effect is ignored under SPS modulation, where S1–S4 and Q1–Q4 are square-wave gate signals with 50% duty ratio, v_{h1} and v_{h2} are the equivalent AC output voltages of full-bridges H1 and H2, respectively, and i_L is the current of inductor L . Similarly with the analysis in the previous chapter, the average transmission power can be derived as the:

$$P = \frac{nV_1V_2D_0(1-D_0)}{2f_sL_s} \text{ where } D_0 \in [0,1].$$

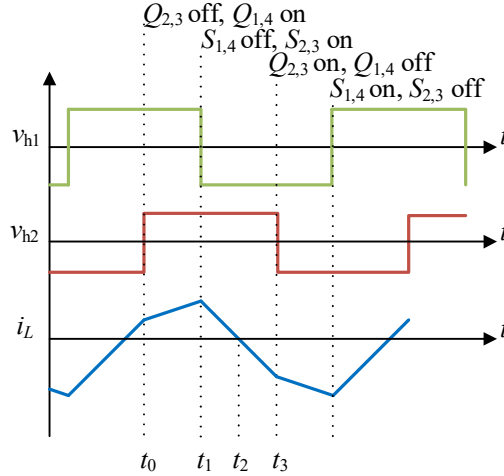


Fig. 3.3.1 Generic voltage waveforms of the SPS modulated DAB converter and its switchers

The traditional power characteristic in modulation strategies commonly recognizes the gate-drivers as ideal components, where switching actions is executed instantaneously. Both time and energy loss of the conductions during the on and off switching are ignored. With this assumption, the zero and maximum points of the transmission power occurred at $D_0 = 0$ and $D_0 = 0.5$, respectively, the transmission power increases with the increasement of D_0 when $D_0 \in [0,0.5]$, and the relation curve is symmetric around the median axis $D_0 = 0.5$. These conclusions are the general agreements, when idealization of the components is valid for the DAB applications with low switching frequencies. Or the operation region of the phase shift is D_0 is not small and the resolution of the controllable transferred power is not required to be high-precise. Compared to switching period and the phase shifted time, the time of the switching can be neglected at these circumstances.

B. Non-ideal operations when dead-time effect is considered

In practice, the dead time must be set in the hardware components to prevent the two switches in the same leg of the H-bridge shorting each other directly. For high switching frequency or the small valued D_0 operations, dead time will cause the change of the switching characterization. The most common of these is voltage polarity reversal which usually occurred at the zero-crossing instants of current. Due to the existence of the dead time, current might flows through D1 and D4 instead of flowing through the switches S2 and S3, as shown in Fig. 3.3.2, there is a voltage polarity reversal phenomenon in the primary side of the transformer.

This reversal can increase the backflow power, further affect the accuracy of the power characteristics, current stress, and efficiency, etc.

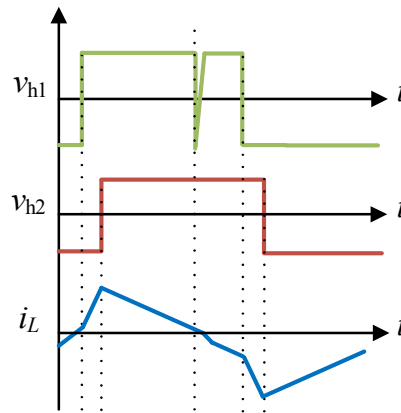


Fig. 3.3.2 Voltage polarity reversal phenomenon during the dead-time

Besides the voltage polarity reversal, phase drift is also a non-ideal phenomenon that has high occurrence rate. This phenomenon refers to the non-ideal change of slope in phase shift power characteristics. Under previous mentioned ideal conditions, this curve starts at $P = 0$ when $D_o = 0$. However, this curve is only valid for $D_o \gg T_D$, where T_D is the dead-time. When T_D is close to D_o , at beginning stage where D_o is not significant, instead of starting from $P = 0$, the minimum transferred power actually starts from the phase shift delay caused by the dead-time. Keep increasing D_o , later stage of this curve will return to the ideal situation, between these two stages, a rapid change of the slope can be observed, as sketched in Fig. 3.3.3.

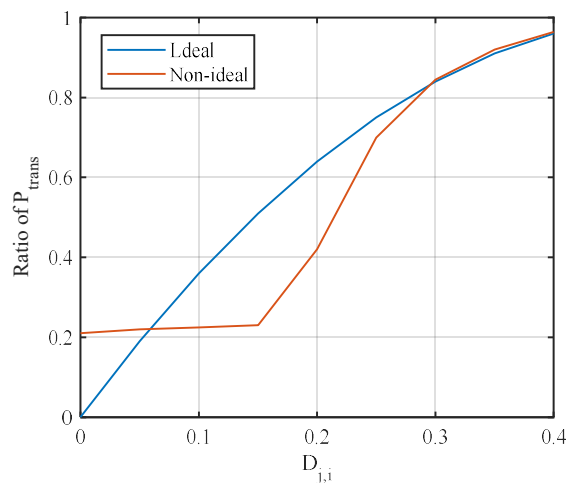


Fig. 3.3.3 Ideal (blue) and non-ideal (orange) dead-time considered curve of the transferred power with D_o

Both voltage polarity reversal and phase drift are recognized as the practical operation phenomena caused by the dead-time. They can be referred to the switching characterization and transmission power characterization, respectively. Appearance of these phenomena will definitely affect the average power transferred in one period.

According to [117], power characteristic of the SPS modulation considering dead-time can be divided into three states based on the voltage relationship of two H-bridges for DAB converter: boost state ($V_1 < V_2$), buck state ($V_1 > V_2$), and $V_1 = V_2$. The power characteristics under these three conditions can be concluded as the TABLE 3.1 below based on the relationship between D_o and m , where $k = \frac{V_1}{V_2}$, and m refers to the equivalent duty ratio of dead time in a half switching period.

TABLE 3.1

POWER CHARACTERISTIC OF DAB CONVERTER WITH DEAD-TIME CONSIDERED

Voltage state	Dead-time condition	Transferred power
Boost mode ($V_1 < V_2$)	$\frac{k(2m-1)+2m+1}{2} \leq D_o \leq 1$	$\frac{V_1^2}{2fL} \frac{4D_o(1-D_o)}{k}$
	$\frac{k(2m-1)+1}{2} \leq D_o$ < $\frac{k(2m-1)+2m+1}{2}$	$\frac{V_1^2}{2fL} \frac{4D_o(1-D_o) + [(2m-1)^2k^2 - (2m-2D_o+1)]}{k}$
	$m \leq D_o < \frac{k(2m-1)+1}{2}$	$\frac{V_1^2}{2fL} \frac{4D_o(1-D_o) + 4m(2D_o-m-1)}{k}$
	$\frac{2m-1+k}{2k} \leq D_o < m$	$\frac{V_1^2}{2fL} \frac{4D_o(1-D_o) + 4m(m-2D_o-1)}{k}$
	$\frac{2m-1+k}{k+1} \leq D_o < \frac{2m-1+k}{2k}$	$\frac{V_1^2}{2fL} \left[\frac{4D_o(1-D_o) + 4m(m-2D_o-1)}{k} + \frac{4(m-D_o)(2kD_o-1m-k+1)}{k(k-1)} \right]$
	$0 \leq D_o < \frac{2m-1+k}{k+1}$	$\frac{V_1^2}{2fL} \frac{4(1-m)^2(k-1)}{k(k+1)}$
Buck mode ($V_1 > V_2$)	$\begin{cases} \frac{k(2m-1)+2m+1}{2} \leq D_o \leq 1, m \geq \frac{k-1}{2k} \\ \frac{k-1}{2k} \leq D_o \leq 1, m < \frac{k-1}{2k} \end{cases}$	$\frac{V_1^2}{2fL} \frac{4D_o(1-D_o)}{k}$
	$m \leq D_o < \frac{k(2m-1)+2m+1}{2}$ and $m \geq \frac{k-1}{2k}$	$\frac{V_1^2}{2fL} \left[\frac{4D_o(1-D_o)}{k} + \frac{4(1-D_o)[k(1-2m)+2D_o-2m-1]}{k(k+1)} \right]$
	$\frac{(k-1)(1-m)}{k+1} \leq D_o < m$ and $m \geq \frac{k-1}{2k}$	$\frac{V_1^2}{2fL} \left[\frac{4(1-m)^2(k-1)}{k(k+1)} \right]$
	$0 \leq D_o < \frac{(k-1)(1-m)}{k+1}$ and $m \geq \frac{k-1}{2k}$	$\frac{V_1^2}{2fL} \left[\frac{4(1-m)^2(k-1)}{k(k+1)} \right]$
	$\frac{k(1-2m)-1}{2k} \leq D_o < \frac{k-1}{2k}$ and $m < \frac{k-1}{2k}$	$\frac{V_1^2}{2fL} \left[\frac{4(1-m)^2(k-1)}{k(k+1)} \right]$
	$0 \leq D_o < \frac{k(1-2m)-1}{2k}$ and $m < \frac{k-1}{2k}$	$\frac{V_1^2}{2fL} \frac{4(D_o+m)(1-D_o-m)}{k}$
Match mode ($V_1 = V_2$)	$2m \leq D_o \leq 1$	$\frac{V_1^2}{2fL} 4D_o(1-D_o)$
	$m \leq D_o < 2m$	$\frac{V_1^2}{2fL} 8(1-D_o)(D_o-m)$
	$0 \leq D_o < m$	0

3.3.2 Saturation of the HF transformer

Conventionally, theoretical calculation of the transformer parameters is based on the initial permeability of the magnetic core. With the high power density design purpose, the operating

current flowing through the transformer winding could be high. This high-power excitation can affect the magnetic flux density directly or indirectly through the temperature changes. According to the research [189], the interaction among magnetically nonlinear behavior of the core combined with unbalanced parameters of the circuits with the two transformer's secondary coils can cause core saturation even when elements connected to coils are passive elements. When core is saturated, the voltage induced in the windings will no longer match the wave-shape as the voltage powering the primary coil. The actual inductance could be much smaller than the labeled value initially input in the power characteristics of modulation or control.

For a normal operated transformer, the slope of current waveform should approximately maintain the same as the waveforms recorded from transformer node of a DAB converter shown in Fig. 3.3.4 (b). If a rapid change of the current waveform is observed at the edge instant of the voltage waveforms Fig. 3.3.4 (a). Transformer can be regarded as saturated. If the distortion of the current waveform is more severe, average power transferred should be reconsidered. To accurately estimate the average power, power characteristics for the saturated condition need to be prepared in advance, so that modulation can be switched to saturated mode if happened.

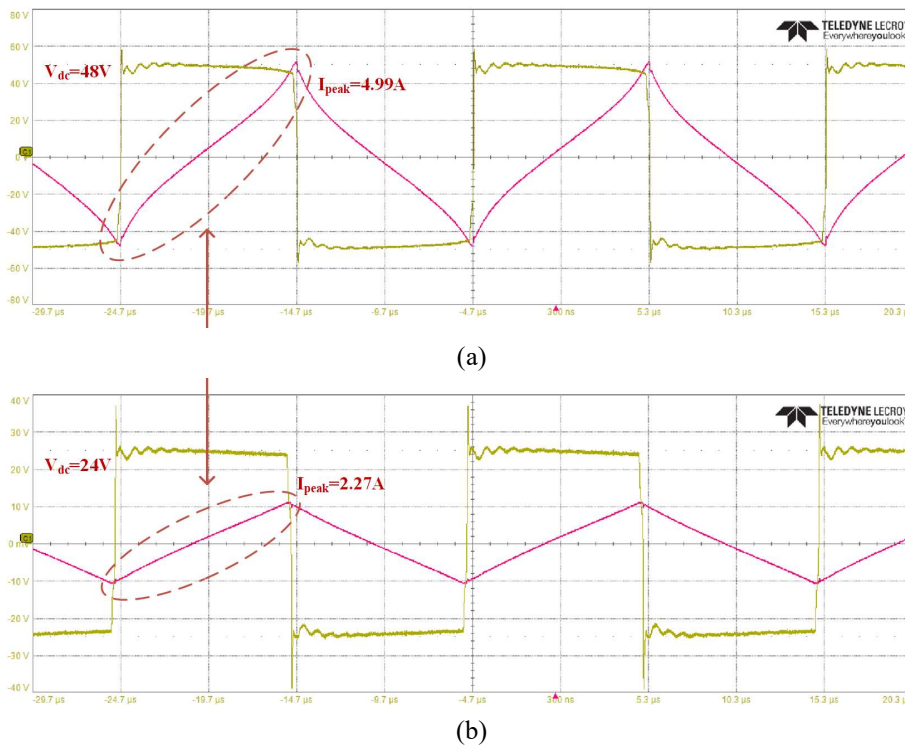


Fig. 3.3.4 Voltage and current waveforms at the transformer node of a DAB converter, (a) when transformer is saturated. (b) when transformer is operating normally.

However, saturation of the core may lead to a sudden temperature rise, whereas temperatures could be another element that affect the modelling of power transfer. Moreover, continuous operation under saturation can threaten the accuracy of control and safety of the overall system. Hence, instead of evaluating the power characteristics under saturation, analysis the cause of core saturation and avoid saturation would be a better option. In practical operation, saturation of the core can be avoided by limiting the power control variable D_o . Detailed analysis of core saturation condition and phase shift limitation is provided in Chapter 5.

3.3.3 Dependency evaluation for the common parameters involved in modulation power characteristics

Since the fundamental construction of modulation strategy is strongly correlated with the framework of power characteristic regardless of the modulation type, variation discussion of the DAB and MAB circuit component parameters which are involved in the power transfer is necessary. Besides the dead-time, these parameters also include: switching frequency, leakage inductances (for the integrated transformer), turn ratio, and terminal voltage. Some of these parameters can be selected with more considerations to improve the accuracy of the power transfer characteristics. Others may need typical measurement strategies to reduce the error as small as possible. Reducing the error between practical operating value and values used in power modeling for these two parameters can greatly improve the accuracy of modulation, since $\frac{nV_1V_2}{fL_s}$ is a common coefficient for all the modulations.

1) *Turn ratio, terminal voltage and leakage inductance*: These parameters are port related. For MAB converters, voltage control may lead to the port DC voltage floating within a certain range rather than fixing at an exact and stable value. Variation or deviation in voltage measurement can lead to the inaccuracy in model establishment, which refers to the error between the value of nV_1V_2 in modulation and in practical operation. Two possible solutions can be utilized to figure this issue, they can be selected according to the requirement of the application. The first solution is the generalized solution, that is using the practical MT with unity turn ratio and adjust the n in power characteristic according to the mapping of voltage. This solution is

suitable for the MAB converter application with variable output voltage requirement. However, operating voltage rating between ports can not be significant, otherwise error between n in modulation and practical operation may lead to the instability or miscalculation of control variables. The drawback of applying this solution is ripple of the output voltage would be increased. If the output voltage ripple is required to be as small as possible and voltage is fixed to a specified value during all the operations, turn ratios of the multiport PET should be designed based on the voltage and power probability distribution map in accordance with the input voltage properties and output requirement to achieve the best performance. The accuracy of the decoupling control highly correlated with the leakage inductance for each virtual DAB branch involved in the MAB converter when integrated HFMT is utilized to replace the MT and series inductors. From the reluctance model of the multiport PET, the theoretical self and mutual-inductances can be calculated as the steps mentioned in [157], where the self-inductance $L_{i,i}$ is defined as the inductance within the same coil and mutual-inductance $L_{i,j} (i \neq j)$ is defined as the inductance across two different loops. Then, by determining the inductive coupling coefficient, the T-model based magnetizing and leakage inductance in the transformer can be declared and redistributed to the sub-branch DAB circuits. Error between power modelling of modulation and practical parameter value is mainly caused by the inaccurate measurement. Hence, precision of the PET inductance measurement must be assessed to promise the accuracy of the power modelling. Despite of measuring the inductance from open and short circuit test by the LCR meter, square wave test with its voltage and frequency close to the operation condition should also be used to measure the leakage inductance of the transformer. Other measurement strategies including, sine current tests, LC resonant circuit test, series & anti-series connection tests could be used to get the self and mutual inductance parameters.

2) *Switching frequency*: Variation of the switching frequency not only affects the power transfer characteristic directly, but also has an impact on the permeability of the transformer and other magnetic components. Consequently, to ensure the continuously operation of the converter system with insignificant steady-state variation, the switching frequency of a specified application or an operation mode is better fixed.

3.4 Simulation and experimental validation

Establish the switching model in PLECS to compare the voltage and current performance of two modulation methods MEPS and AEPS. The specifications of the DAB converter used in the validation is listed in the TABLE 3.2. First verify the impact of magnetizing inductance on power transfer for SPS modulation. Fig. 3.4.1 shows the result of average power transferred when $M = 5, 20$ and 100 .

TABLE 3.2

SPECIFICATIONS OF THE DAB CONVERTER

Specifications	Symbol	Value
Input DC voltage	V_1	650 V
Output DC voltage	V_2	455 V
Transformer turn ratio	n	1:1
Primary bridge leakage inductance	L_{s1}	100 μ H
Secondary bridge leakage inductance	L_{s2}	80 μ H
MOSFET-on resistance	$R_{mos,on}$	80 m Ω
Diode-on resistance	$R_{D_{on}}$	40 m Ω
Switching frequency	f_s	50 kHz
Dead time	T_d	0.1 μ s

Reduction of M could bring more significant error in power estimation and modulate algorithm reversely. Thus, considering L_m in HF DAB is proved to be necessary.

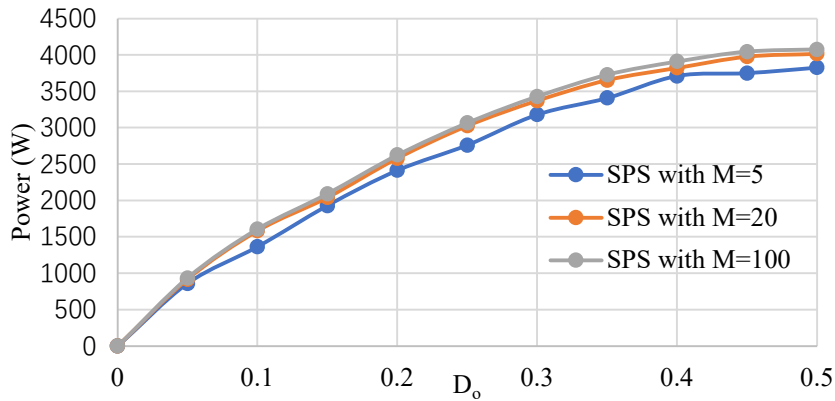


Fig. 3.4.1 Power transferred under SPS modulation with $M = 5, 20$ and 100

Extension of ZVS range could be verified by observing instantaneous voltage and current at switching instants. For ideal SPS modulation, theoretical ZVS boundary is $D_o = 0.15$ when $M = 5$. With the assistant of L_m , range is expanded and for $D_o = 0.1$, ZVS is realized, as validated in the Fig. 3.4.2.

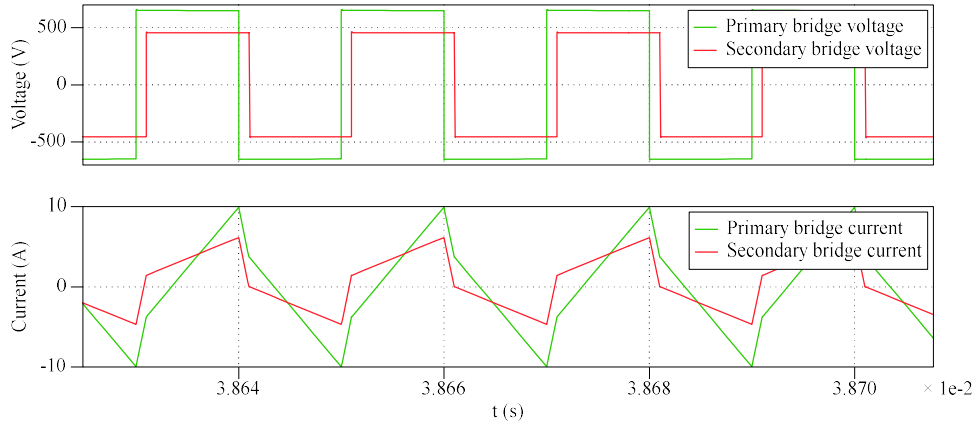


Fig. 3.4.2 Voltage and current of primary and secondary bridge for SPS modulation with L_m considered ($D_o = 0.1$)

Fig. 3.4.3 shows the power verses D_o for AEPS and MEPS modulation strategy, which is confirmed with the theoretical result in Fig. 3.2.8, the maximum deviation observed from the figure is close to 25%.

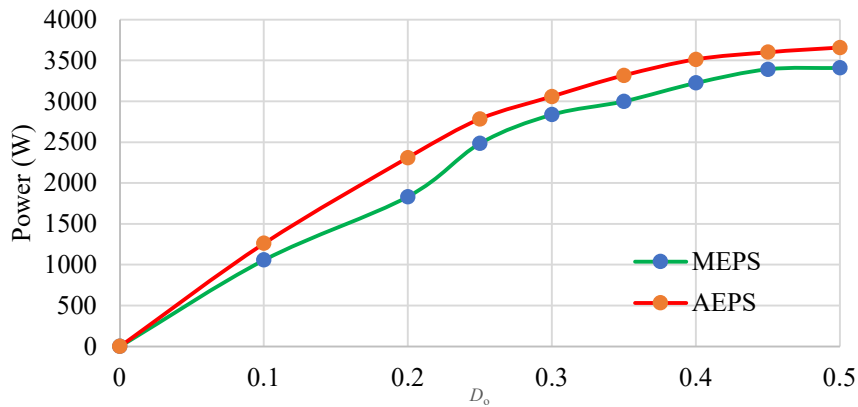


Fig. 3.4.3 Power of two advanced EPS modulation methods with $M=5$

Examine the ZVS capability for AEPS modulation. Boundary of soft switching for MEPS modulation is $D_o = 0.15$ when $M = 5$. While AEPS could extend this limitation down to $D_o = 0.08$ as shown in Fig. 3.4.4. Results proves that using the proposed modulation can expand the range of ZVS by 20%. Power conditions from two branches are examined available for soft switching in Fig. 3.4.5.

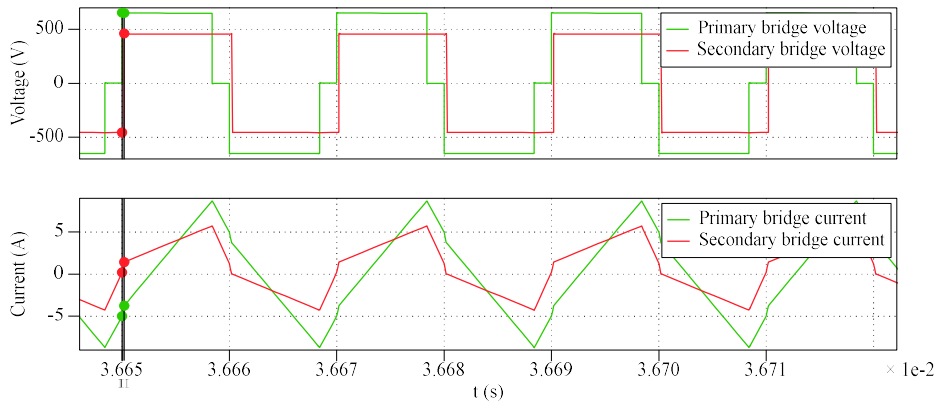
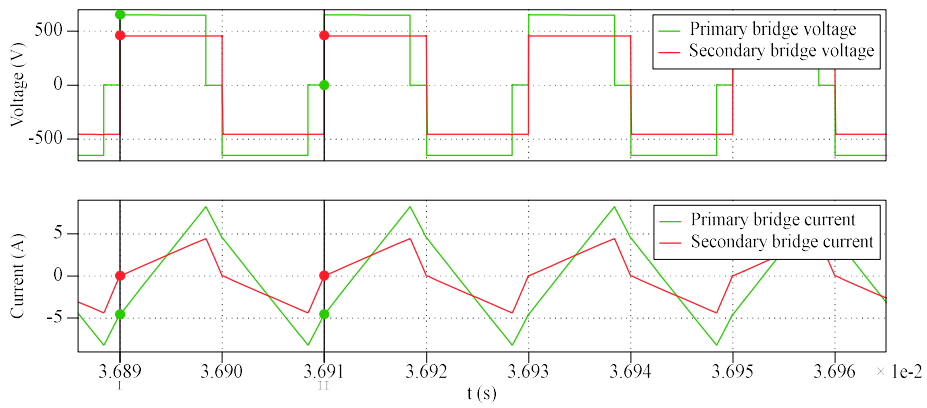
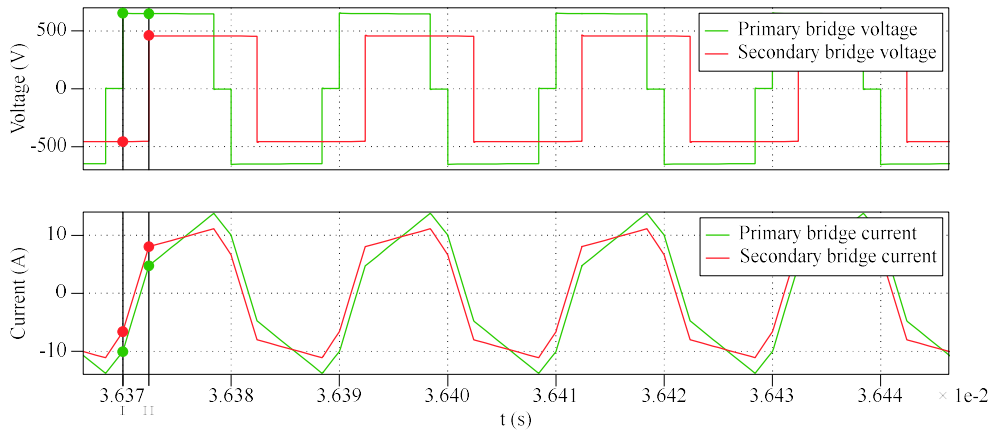


Fig. 3.4.4 Voltage and current of primary and secondary bridge ($D_o = 0.1$)



(a)



(b)

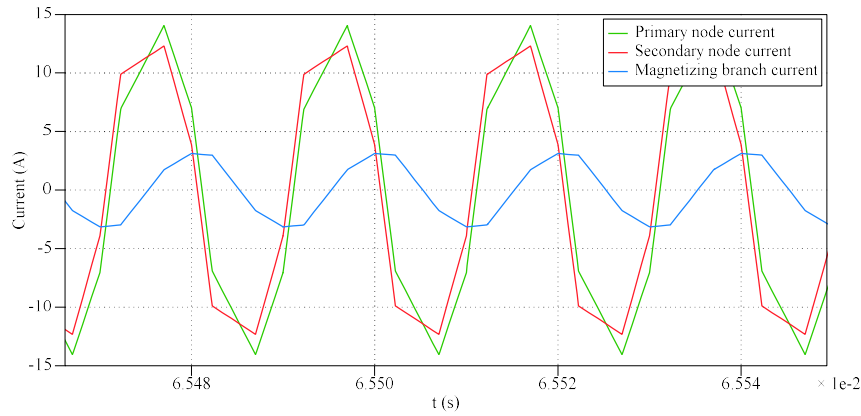
Fig. 3.4.5 (a) Voltage and Current waveform (1000W) (b) Voltage and Current waveform (3200W)

TABLE 3.3

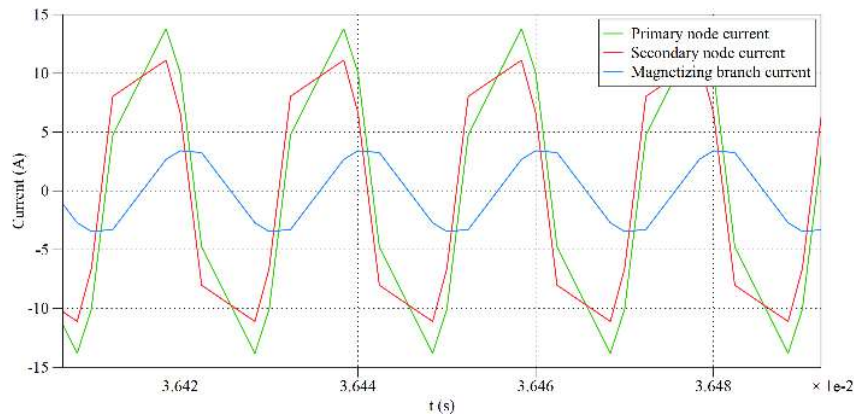
INNER AND OUTER PHASE SHIFT OF TWO MODULATIONS

MEPS modulation				AEPS modulation			
$P = 1000W$		$P = 3200W$		$P = 1000W$		$P = 3200W$	
D_o	$D_{IN,1}$	D_o	$D_{IN,1}$	D_o	$D_{IN,1}$	D_o	$D_{IN,1}$
0.0947	0.3	0.376	0.3	0.079	0.16	0.32	0.16

Determine the corresponding D_o and $D_{IN,1}$ for two modulation methods. As the $D_{IN,1}$ in TABLE 3.3 is the lowest boundary satisfying ZVS requirement, reduced $D_{IN,1}$ in proposed modified modulation proves an extended control freedom available for soft switching. In addition, when $1 - k - \frac{k}{M} < 0$, AEPS is under SPS mode with $D_{IN,1}$ fixed to zero, whose D_o is less than MEPS modulation. Hence, for the entire power transfer range, AEPS modulation demands smaller $D_{IN,1}$. Promising a preferable voltage utilization.



(a)



(b)

Fig. 3.4.6 (a) Current waveforms of MEPS (3200W) (b) Current waveforms of AEPS (3200W)

TABLE 3.4

PEAK AND RMS CURRENT OF TWO MODULATIONS AT 3200W TRANSFERRED POWER

	EPS modulation	Modified modulation
Peak to peak current (A)	$I_{Ls1} = 28.09, I_{Ls2} = 24.6, I_{Lm} = 6.26$	$I_{Ls1} = 27.72, I_{Ls2} = 22.34, I_{Lm} = 6.86$
RMS current (A)	$I_{Ls1} = 9.60, I_{Ls2} = 9.26, I_{Lm} = 2.24$	$I_{Ls1} = 9.26, I_{Ls2} = 8.58, I_{Lm} = 2.45$

With the reduction of outer and inner phase shift, AEPS modulation could provide reduced current stress. According to Fig. 3.4.6(a), (b) and TABLE 3.4, when power transferred is 3200W, peak to peak current of MEPS modulation in both primary and secondary leakage inductor is greater than the ones in AEPS modulation. Decrement of D_o in AEPS modulation assists the reduction of current stress, improves the converter efficiency by reducing the switching loss and electromagnetic interference. Reduction of RMS current in primary and secondary bridge cut the copper loss in the transformer winding. However, as the current in the magnetizing branch is raised, iron loss will be increased.

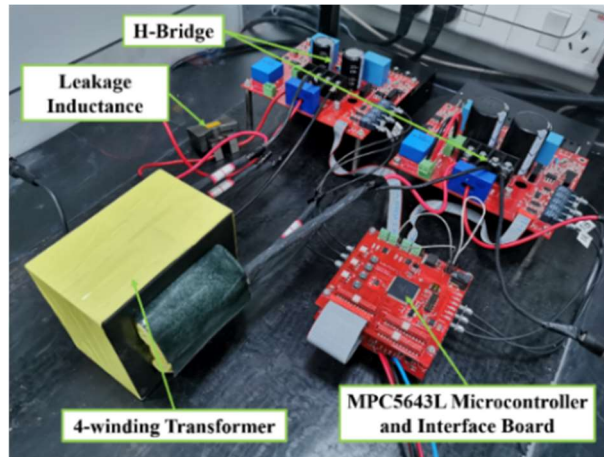


Fig. 3.4.7 Practical DAB plant with HF (50kHz) transformer

A practical DAB plant with 50 kHz, 1:1 turn ratio transformer has been built for further verification. Precise values of inductances in the plant at rated frequency is measured through the open circuit and short circuit test, which is shown in TABLE 3.5.

TABLE 3.5
MEASURED INDUCTANCES IN DAB PLANT

Leakage inductance (H)	Magnetizing inductance (H)	Ratio M
$L_{s1} = 5.78 \mu\text{H}, L_{s2} = 6.67 \mu\text{H}$	$L_m = 2500 \mu\text{H}$	416.7

With negligible value of leakage inductance, inductors could be connected in series with transformer to adjust the ratio M for further experimental investigations.

3.5 Summary of this chapter

From power characteristics of the SPS and EPS modulation, considering the existence of magnetizing inductance in DAB power characteristic contributes to the steady-state performance of voltage control. Magnetizing inductance could extend the soft switching range by injecting inductive current at switching moments. This extension is inversely proportional to the ratio between magnetizing and leakage inductance. From PLECS simulation results, it is verified that for system considering magnetizing inductance, proposed AEPS modulation could provide reduced current stress and better voltage utilization. Designing transformer with reasonable magnetizing inductance to leakage inductance ratio is a potential hardware solution for optimizing the performance of DAB converters.

Once the framework of the modulation is settled, it is of vital importance to promise the accuracy of the parameters involved in the power characterizes of the modulations. Some parameters are commonly ignored in ideal power transfer modelling, but they will have impact on the power characteristic under certain circumstances. When the converter is operating under high frequency, dead-time can affect the power transfer characteristic. Detailed characteristic is listed in TABLE 3.1 based on three voltage states. And when the transformer is operating under high current excitation, saturation of the core can lead to the distortion of the power characteristics. Under this condition, quality of the power transfer is could reach an unacceptably low level. In addition, saturation of the core can lead to the rapid rise in core temperature, which brings security risks to the entire system. Hence, instead of investigating the power characteristics of saturation condition, this phenomenon is better avoided. Limiting

the power control variable, which is outer phase shift, can effectively avoid the saturation of the core, the detailed calculation is introduced in Chapter 5.

4. Modular modulation based decoupling control strategies and its dynamic performance optimization

4.1 Chapter overview

Applying the MAB configurations in the electrified transportation applications has become a popular trend in the recent years. Fig. 4.1.1 shows a TAB converter utilized in the traction unit of the MEA. Through the multiport transformer, tractions motors can be driven simultaneously with asymmetrical load requirements.

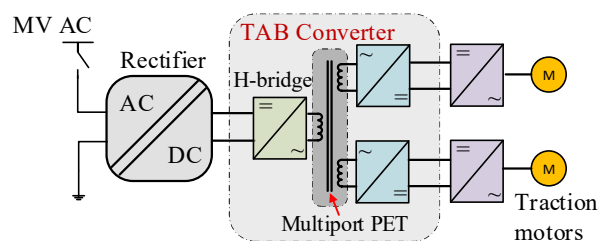


Fig. 4.1.1 Propulsion systems with TAB topology for MEAs

Besides MEA, MAB converters are also used in the multiport EV chargers to improve the charging efficiency and flexibility. As MAB based fast-charging EV chargers can satisfy the different charging voltage of EVs varied from 200 V to 800 V with acceptable ripples. Topology of this charger can be sketched as Fig. 4.1.2.

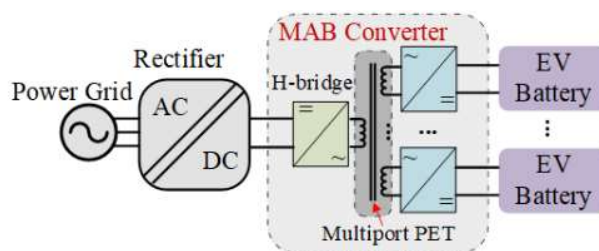


Fig. 4.1.2 Topology of MAB converter working as a multiport PET for EV charging.

Under varied voltage conditions, modulations of MAB converter require not only the quality of power transfer, but also the efficiency of transfer, that is disposing all the possible previous output and convert them into control variables. In addition, in decoupling-controlled MAB converter, SPS modulation is not suitable for ZVS realization. If inner phase shifts are involved, modulation will always be TPS-like, which demands consideration of all the inner and outer

phase shifts combinations. This modulation needs to balance the accuracy of control and practical efficient realization. It is well-known that the mainstream modulation strategies applied in the DAB and MAB converters are established according to some simplifications based on ideal conditions. Complicated modulations effects do provide more accurate control variables; however, control system may not be able to accomplish such huge number of calculations within short control period. Hence, a proper solution is designing decoupling control system supported by a modulation strategy that can included SPS and inner phase shift involved modulations, and allowing switch of these included fundamental modulations to meet different operating requirement while keeping high level of efficiency. With all these requirements achieved, GPS modulation becomes the new framework of the control system design. In this control-related chapters, two novel control strategies aiming to improve the dynamic performance and system flexibility are proposed for the MAB converters. Transferred power is represented in partial derivatives of average current based on the GPS modulation due to the iterative decoupling is constructed on the partial derivation calculations, which has demonstrated in detail in the modular modulation control chapter.

In the first part of this chapter, a power decoupling based configurable control (PDC-MPC) strategy inspired by the MPC is developed for the TAB converter. The proposed control strategy can achieve good transition performance and high control flexibility with good precision enabling conformity to variable DC voltage regulations. The operating principle of the PDC-MPC is divided into two phases: prediction of the DC current through a binary search and decoupling of the desired power of each isolated virtual branch to its phase shift angles under the SPS modulation strategy. Steady-state and dynamic performances of the proposed PDC-MPC for TAB converters were analyzed using modified cost function and predictive models.

In the second part, a modular modulation decoupling algorithm combined with a current decoupling control strategy to realize the voltage controls is proposed. This control strategy composes of the DC reference current generators and the current to phase shifts decoupling algorithm. GPS modulation was utilized in the decoupling algorithm to quantitatively characterize the relationship between the phase shift and the port average current, aiming at

achieving the ‘modular’ switching of the fundamental modulations. The complexity and accuracy of the proposed online offline Newton decoupling (O²ND) algorithm have been evaluated and compared with Newton decoupling (ND) algorithm and simplified Newton decoupling (SND) algorithm.

Effectiveness of both control strategies are verified through a comparative assessment by means of simulation and experimental results

4.2 Generalized phase shift modulation based decoupling control with model predictive control strategy for dynamic performance enhancement

The remainder of this chapter is organized as follows. In Chapter 4.2.1, the topology of the TAB and SPS modulation is demonstrated using an initial voltage prediction function. Chapter 4.2.2 introduces the approach of searching for the optimal current using a binary search algorithm and the logic of power decoupling based on Newton’s method. The modified voltage prediction function with a double-step prediction horizon is proposed and enhanced with an updated cost function. Experimental and simulation results are presented in Chapter 4.4.1 to validate the merits of the proposed control strategy.

4.2.1 A general introduction of applying Newton iteration with MPC control in MAB converter

In MIMO systems like MAB converter, linear control range restrictions and oscillation characteristics due to unquantified coupling relationships of PI-based voltage controllers limit steady-state control precision and dynamic performance. Hence, nonlinear control method is developed to solve this issue.

MPC is a nonlinear control method that has been recently implemented in power systems and power electronic converter controls [121-123]. This method has the benefits of fast dynamics, easy inclusion of nonlinearities, simple digital implementation, and can satisfy a set of constraints simultaneously. The control actions of MPC are obtained through online processing of an optimization problem with a predesigned cost function over a finite prediction horizon within each time step. Multistep prediction horizons are commonly implemented in

converters with simple topologies operated at low switching frequencies, whereas single-step horizon allows more flexibility [124, 125].

There are a few publications focusing on controlling DAB converters using MPC, some of which have focused on combining MPC with advanced modulation strategies [126, 127], whereas others have focused on practical implementations in DC microgrid [128-130]. Quantified modeling and control methodologies of specific MIMO converters have also been investigated, such as TAB and QAB converters. [131] proposed a modeling technique utilizing decoupling matrix-based PI for TAB converter to improve the dynamics. Ref [132] realized the TAB voltage balancing with reduced control variables through hardware modification, a generalized input impedance model of MAB converter investigated with the validation of TAB and QAB [133].

However, few studies discussed enhance the dynamics of MIMO systems through MPC with modular modulation method. MPC strategies used in the voltage control of DAB reported above can be classified into three variable prediction mode as introduced in Chapter 2.

Linearized fixed-step prediction methodologies of a and b have been validated to be effective in DAB applications through many researchers. However, for MIMO system under high switching frequency, linearized searching mode is not efficient enough and faces the dangerous of overrun. Whereas the proposed MPC based on the binary search is, faster in dynamic and less comprehensive than the adaptive step MPC whose step requires another control loop.

SPS modulation can satisfy the majority of DAB applications owing to its simplicity. However, when DC voltage ratio deviates from unity, the SPS-modulated DAB may have a high circulating current or power flow back, and lose its ZVS ability [94]. Considering the different applications and voltage ranges with multiple output ports, the voltage gain between two arbitrary ports may diverge from unity further. However, multiple control variables in the power transfer control of multiple ports are difficult to be modeled quantitatively without a modulation indicated power-decoupling. From this perspective, a control strategy with modular control and power decoupling was proposed to elevate the adaptability of MAB systems.

The decoupling of the desired power of each port analyses MIMO systems as multiple isolated virtual DAB branches, which reduces the burden of replacing modulation methods, whereas MPC provides good dynamic performance in searching of the desired power. The proposed PDC-MPC strategy has several advantages:

1. Fast transition: Advanced binary search and Newton's iteration method can be implemented in the proposed control strategy to accelerate data processing and control, thereby providing a better dynamic response.
2. Configurable control and modulation: The optimum future state variable is located through a binary search based on a prediction model and cost functions. With a specified reference average DC current, the power-decoupling unit can calculate the phase shifts of each isolated virtual branch using Newton's method based on the modulation strategy applied to the system [85]. In the proposed control strategy, MPC voltage controller controls the MAB as several isolated sub-DAB branches, whereas the modulation characteristics the power to phase shift relationship. Modulation based decoupling could be recognized as an open-loop module, which is completely independent from voltage control algorithm. Reference current searching algorithms in MPC can be substituted with different system demands, while switching the modulation method is easy to realize in power decoupling.
3. Extension in range of control and control precision during dynamics: With a quantified prediction model and consideration of its nonlinear voltage characteristics, the proposed PDC-MPC can extend the range of control while providing accurate control with elimination of steady-state voltage ripples and less oscillation in transition under asymmetrical load distributions.

4.2.2 A novel MPC based power decoupling control strategy for TAB converter

In this chapter, topology of the controlled plant, and the MPC voltage controller aimed to identify the optimum reference DC currents through binary search is firstly demonstrated. Then, a decoupling strategy was investigated by analyzing the relationship between the power and

phase shifts of each isolated virtual branch. The power decoupling equations under different phase shift specifications were characterized in one coordinate system, as shown in Fig. 4.2.4.

. A control diagram of the proposed strategy combines the MPC voltage controller and power decoupling is shown in Fig. 4.2.5. To eliminate the steady-state error and improve the overall performance, the initial MPC strategy was enhanced by a double-step prediction model with the current compensation term, new current searching logic, and modified cost function.

The topology of a TAB converter with one input port (Port 1) and two output ports (Ports 2 and 3) connected to two resistive loads is presented in Fig. 4.2.1. The H-bridges driven by PWM signals at each side of the HF transformer generate quasi-square voltages v_1 , v_2 , and v_3 . Power is instantly stored and released by the leakage inductance L_{s1} , L_{s2} , and L_{s3} , producing transforming AC currents i_{ac1} , i_{ac2} , and i_{ac3} and port DC current I_{dc1} , I_{dc2} , and I_{dc3} . The average power transferred between two ports for SPS modulation is the same as previous chapters: $P = \frac{nV_1V_2D_{j,i}(1-D_{j,i})}{2f_sL_s}$.

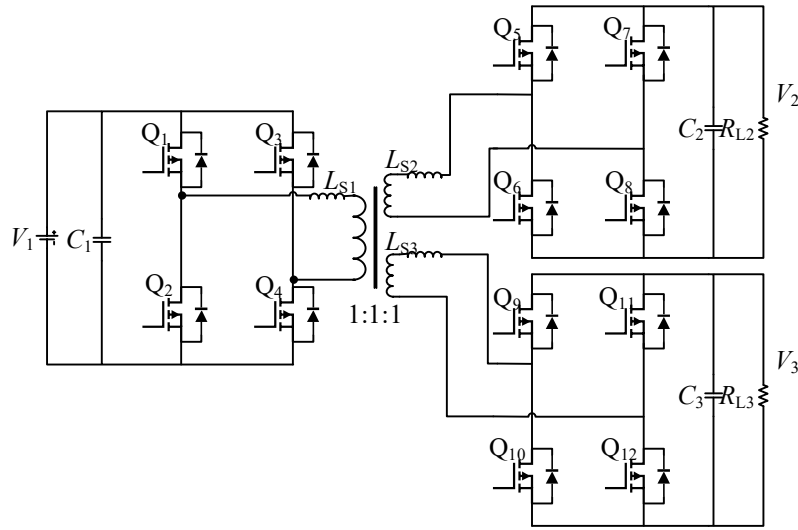


Fig. 4.2.1 A general topology of TAB converter with one input port and two output ports with pure resistive loads

where $D_{j,i} \in [-0.5, 0.5]$. L_s is the resulting leakage inductance. In an MAB converter with N ports, the desired power at one specified port is related to the outer phase shifts of all virtual branches containing this port, as power can be transferred bidirectionally and arbitrarily

between any pair of ports. Resulting in $\frac{n(n-1)}{2}$ degrees of freedoms of outer phase shift under SPS modulation if utilize Port 1 as the reference with $D_1 = 0$.

For the SPS modulated TAB converter with reference Port 1: $D_1 = 0$, there are three control variables: D_{21} , D_{31} and D_{32} , where $D_{32} = D_3 - D_2$, $D_{21} = D_2$, $D_{31} = D_3$. The control objective was to regulate and maintain the output voltage of each output port at the reference constant. The port current dynamic equation can be deduced from the load and capacitor current, where f_c is the control frequency, and T_c is the control period.

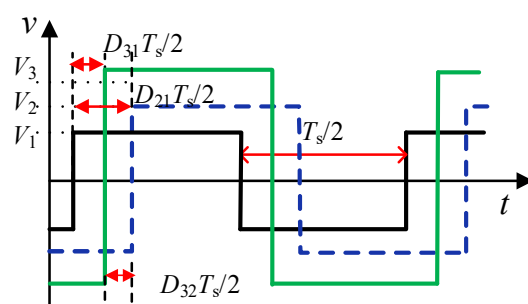


Fig. 4.2.2 Generic voltage waveforms of the SPS modulated TAB converter

$$I_j = I_{C,j} + I_{L,j} = C_j \frac{d\langle V_j \rangle_{T_c}}{dT_c} + \langle I_{load} \rangle_{T_s} \quad (4.1)$$

$$I_j = I_{C,j} + I_{L,j} = C_j f_c (V_j[k+1] - V_j[k]) + I_{L,j}[k] \quad (4.2)$$

It is assumed that load current would not fluctuate drastically within one switching period.

$$I_{L,j}[k] = I_{L,j}[k+1] \quad (4.3)$$

As a single-step prediction model, f_c is the same as f_s . The voltage prediction function between voltage is current is given by (4.4).

$$V_j[k+1] = \frac{I_j[k+1] + \left(C_j f_s - \frac{1}{R_j}\right) V_j[k]}{C_j f_s} \quad (4.4)$$

A. Preliminary Current Searching Algorithm and its Cost Function

A binary search is an algorithm that iteratively searches for an element within a sorted array by dividing the search interval by half [190, 191]. Utilize binary search strategy to search and optimize the optimum predicted average DC current $I_j[k + 1]$ in (4.4). The discretized output voltage prediction function with single-step horizon is given by Eq (4.5). A binary search iteratively selects the best candidate from a pair of predicted current values based on a cost function to narrow the range of search. Square of the cost function determines whether the search for the current should be continued. Flow chart of the binary search for the optimum predicted current is illustrated in Fig. 4.2.3.

The search begins with the presupposed upper and lower boundary; this boundary gradually converges and finalizes with an optimal average port DC current. Considering that power can be transferred bidirectionally, the lower boundary is set symmetrical with the upper boundary. Use x_1 and x_2 to represent the initial upper and lower boundaries, where $x_2 = -x_1$ ($x_1 > 0, x_2 > 0$).

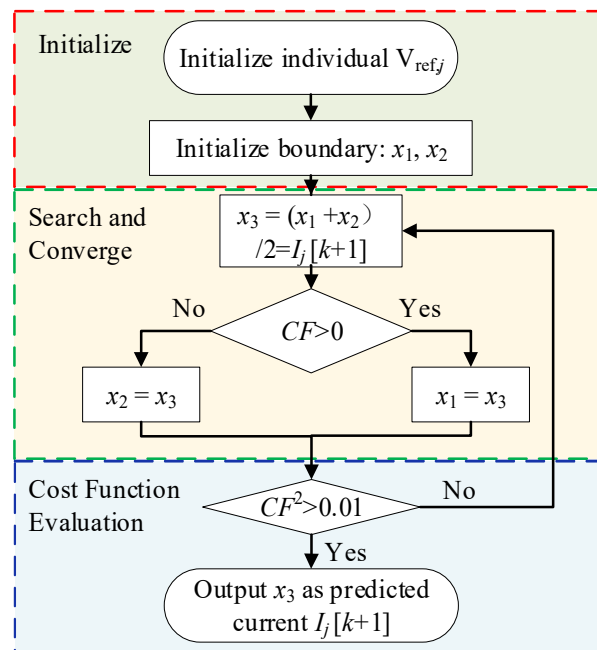


Fig. 4.2.3 Flowchart of the initialized reference current search of MPC

The predicted DC current x_3 in binary search based MPC is:

$$I_j[k + 1] = x_3 = \frac{x_1 + x_2}{2} \quad (4.5)$$

As $V_j[k + 1]$ monotonically increases with an increase in x_3 , the convergence direction of the binary search can be distinguished from the relationship between converge cost function CF and refence voltage.

$$CF = \frac{x_3 + \left(C_j f_s - \frac{1}{R_j}\right) V_j[k]}{C_j f_s} - V_{\text{ref}} \quad (4.6)$$

In MPC control strategies, square and absolute formula-forms are widely used in the cost function construction. Square of the cost function assesses whether current can be outputted as the reference current repeatedly. Comparing to the absolute formula, CF^2 provides more aggressive convergence when error is significant and flat convergence when error when error is insignificant, which achieves an effectiveness between control accuracy and control complexity. Initially define the maximum receivable error is as 0.01, as 1% percentage error is enough to achieve the accurate control of dynamic and steady-state performance. If the result of the cost function is greater than this error, the searching continues.

$$CF^2 = (V_{\text{ref},j} - V_j[k + 1])^2 \quad (4.7)$$

The preliminary cost function was established to describe the error between the predicted and reference voltages. This function is the initial one which validates and modifies the current searching module.

B. Power Decoupling Strategy for TAB Converters

The control system is divided into two phases. In the first phase, a binary search generates the optimal predicted DC currents, which is introduced in the previous chapter. These currents are than received and processed by power decoupling module, which can be recognized as an open loop algorithm, to obtain the phase shifts. Decoupling module is established on two principles:

1. The output voltage at each port relates to its capacitor current and the DC current at the receiving end of H-bridge, where DC current refers to the power injected or emitted, which is a variable controlled by the phase shifts of all the virtual branches. Hence, an optimum current always exists for a specified reference voltage.
2. The output voltage at one port monotonically increases with the increase in its transformer-side current, which could be observed from (4.4). This means the local optimum solutions from power decoupling are exactly the global optimum

Unlike the single-phase correspondence in current searching stage, the analysis of MAB with n ports as several isolation units [85], is based on the $n - 1$ ($D_1 = 0$ is fixed) dimensional nonlinear power equation:

$$\begin{cases} P_2 = f_2(D_2, \dots, D_N) = \sum_{i=1, i \neq 2}^n P_{2,i}(D_2 - D_i) \\ \dots \\ P_n = f_n(D_2, \dots, D_N) = \sum_{i=1, i \neq n}^n P_{n,i}(D_n - D_i) \end{cases} \quad (4.8)$$

For the TAB, the average power injected or supplied by Ports 2 and 3 can be represented with the port average DC current.

$$\begin{cases} P_2 \propto I_{2,j} = f_1(D_2, D_3) \\ P_3 \propto I_{3,j} = f_2(D_2, D_3) \end{cases} \quad (4.9)$$

Substituting (4.9) with the power characteristic of the SPS modulation, a general expression for the average DC current of Port 2 i_2 and Port 3 i_3 can be represented as (4.10).

$$\begin{cases} P_2(D_2, D_3) = \pm \frac{|D_2| |1 - |D_2|| V_1}{2f_s L_{12}} \pm \frac{||D_2| - |D_3|| |1 - ||D_2| - |D_3||| V_3}{2f_s L_{23}} \\ P_3(D_2, D_3) = \pm \frac{|D_3| |1 - |D_3|| V_1}{2f_s L_{13}} \pm \frac{||D_3| - |D_2|| |1 - ||D_3| - |D_2||| V_2}{2f_s L_{23}} \end{cases} \quad (4.10)$$

where $D_2 \in [-0.5, 0.5]$, $D_3 \in [-0.5, 0.5]$ and $|D_2 - D_3| < 0.5$. Absolute values in the decoupling equations change with the relationship deviation between phase shift D_2 and

D_3 . The condition $D_2 > D_3 > 0$ is used as an example for demonstration, where function (4.10) can be rewritten as (4.11).

$$\begin{cases} f_1(D_2, D_3) = \frac{D_2(1 - D_2)V_1}{2f_s L_{12}} + \frac{(D_2 - D_3)[1 - (D_2 - D_3)]V_3}{2f_s L_{23}} \\ f_2(D_2, D_3) = \frac{D_3(1 - D_3)V_1}{2f_s L_{13}} - \frac{(D_2 - D_3)[1 - (D_2 - D_3)]V_2}{2f_s L_{23}} \end{cases} \quad (4.11)$$

Convergence validation for this method has been demonstrated in the literature review part.

The Jacobi matrix of the function is as follows:

$$\mathbf{F}'(D_{out}) = \begin{bmatrix} \frac{\partial f_1}{\partial D_2} & \frac{\partial f_1}{\partial D_3} \\ \frac{\partial f_2}{\partial D_2} & \frac{\partial f_2}{\partial D_3} \end{bmatrix} \quad (4.12)$$

$$D_{j,i}^{k+1} = D_{j,i}^k - \mathbf{J}^{-1} \mathbf{F}(D_{j,i}^k) \quad (4.13)$$

Newton's iteration method requires calculation of the partial derivative for every step. Solving the inverse Jacobi matrix might utilize considerable computational resources under a high switching frequency, if a specific accuracy is set as the target. Hence, fixed-step iteration is better for realization. Based on a simulation result, after six iterations, the decoupled results of D_2 and D_3 reached the desired precision [192].

Constructing a three-dimensional coordinate system and defining D_2 , D_3 and average DC current (I_2/I_3) as coordinate arises. In each quadrant of D_2 - D_3 plane, the power-decoupling function varies with $|D_2| > |D_3|$ or $|D_2| < |D_3|$, resulting in eight forms of the decoupling equations. The current decoupling map can be generated by assembling all current conditions in the constructed coordinate system. Define voltage/inductance coefficients as follows to simplify the power calculation:

$$A = \frac{V_1}{2f_s L_{12}}, B = \frac{V_1}{2f_s L_{13}}, C = \frac{V_3}{2f_s L_{23}}, D = \frac{V_2}{2f_s L_{23}} \quad (4.14)$$

Set coefficient A as a unity base value. If B , C , and D are equal to A , then the curve is fully symmetrical. Fig. 4.2.4 shows the characteristics between I_{dc} and phase shifts with the reference voltage: $V_1 = V_2 = \frac{1}{2}V_3$. The labeled points indicate that both DC current curves are centrally symmetrical, in addition, curve I_{dc2} is centrally-symmetrical with I_{dc3} ; change of the voltage and leakage inductances between ports could stretch or compress the shape of the curve.

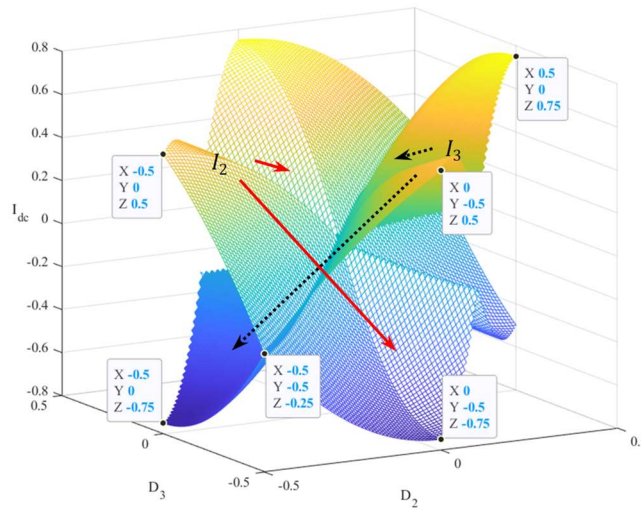


Fig. 4.2.4 Relationship of current decoupling when $A = B = C = \frac{1}{2}D$

C. Operating Principle of Proposed Control Strategy

The control diagram of the proposed PDC-MPC algorithm is shown in Fig. 4.2.5.

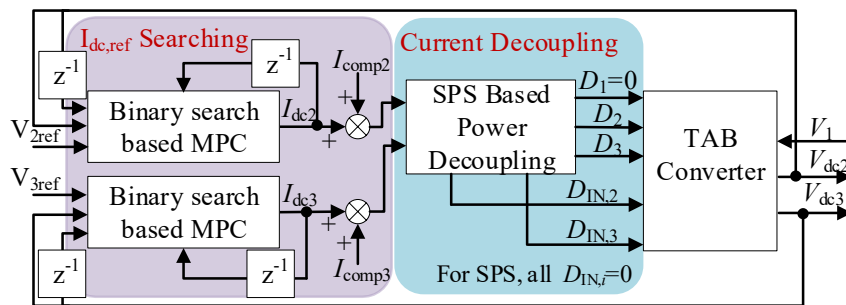


Fig. 4.2.5 Control diagram of proposed MPC

A prediction model of the TAB converter was established to characterize the output voltage in future states. Based on the prediction model and cost function in the voltage controller, MPC searches for and revises the optimal average DC current at each output port. With these currents,

Newton's method is then implemented to process the power decoupling according to the SPS modulation, finally PWM signals with the obtained phase shifts are sent to the corresponded H-bridges respectively to realize the voltage control. In the proposed control strategy, SPS based power decoupling is an open loop algorithm in which modulation strategy only characterize the relationship between transferred power and phase shift ratios, SPS modulation can be replaced by EPS or TPS with low computational burden, whereas binary search can be substituted by gradient descent, lagrange multiplication, or other search algorithms [193]. Compared the research works utilizing linear searching approaches in MPC, a binary search based MPC is more efficient in terms of time and complexity as it does not need to scan each element in the range.

D. Double-step Prediction Model and its Cost Function with Enhanced Current Searching

The initialized MPC control strategy has some severe drawbacks in terms of stability and steady-state performance, these phenomena will be later accessed by simulation and experimental validation. A larger voltage ripple and a steady state error appeared in both ports, as shown in TABLE 4.4. In addition, the system is sensitive to the perturbations. With a single-step search, the predicted current values of several subsequent control period cycles slide within a wide range, which increased the steady-state voltage ripple. During perturbations, this sliding caused the value of the predicted current to exceed the limitation.

Hence, a secondary-step search was performed to enhance the accuracy of the optimum current search based on a modified prediction model. Furthermore, the cost function was modified by introducing new elements to improve the steady state performance and promote system robustness.

The initial voltage prediction function was modified to (4.15) with a double-step prediction horizon. Thus, f_c became $\frac{1}{2f_s}$.

$$V_j[k+2] = \frac{I_j[k+2] - I_{load,j}[k]}{C_j f_c} + V_{load}[k+1] \quad (4.15)$$

With the previous assumption of load current and substituting $V_j[k + 1]$ expression (4.4) into (4.15), the prediction function was reorganized as (4.16):

$$V_j[k + 2] = \frac{I_j[k + 2] + I_j[k + 1] - 2I_{load,j}[k]}{C_j f_c} + V_{load}[k] \quad (4.16)$$

A boost-convergence term describing the output voltage deviation between predicted voltage and measure voltage was added to the cost function. With this deviation considered in the cost function, voltage ripple at steady state will keep decreasing during control process. The new cost function in (4.17) includes two elements.

$$\begin{cases} CF = \alpha G_1 + \beta G_2 \\ G_1 = (V_{refj} - V_j[k + 2])^2 \\ G_2 = (V_j[k + 2] - V_j[k])^2 \end{cases} \quad (4.17)$$

Term G_1 is responsible for the regulation of the output voltage, whereas term G_2 controls the voltage deviation reduction. When the output voltage V_j approaches to the referenced voltage V_{refj} , the value of element G_1 becomes insignificant compared with the voltage step-changing element G_2 . As the term βG_2 is always greater than zero, the decreasing magnitude of αG_1 might not be able to compensate for the value of βG_2 , leading to a steady-state error.

To eliminate the steady-state error, the current compensation term I_{comp} was added into the prediction function. I_{comp} is defined as the difference between the observed DC current at transformer node $I_{refj}[k - 1]$ and the predicted DC current from the last binary search iteration $I_j[k - 1]$.

$$I_{comp}[k] = I_{refj}[k - 1] - I_j[k - 1] \quad (4.18)$$

$$I_{refj}[k - 1] = C_j f_s (V_j[k] - V_j[k - 1]) + I_{load,j}[k - 1] \quad (4.19)$$

Hence, the new voltage prediction function with current compensation term is as follows:

$$V_j[k + 2] = \frac{\left(1 - \frac{1}{R_j C_j f_c}\right) I_j[k + 1] + I_j[k + 2] + 2I_{comp}[k] - \left(2 - \frac{1}{C_j f_c}\right) I_{load,j}[k]}{C_j f_c} + V_{load}[k] \quad (4.20)$$

As the prediction horizon of the voltage was extended to two control steps, the algorithm for optimum current search was also modified to a double-step search to comply with the new cost function and prediction model. A secondary step predicted current with $x_a = \frac{x_1+x_3}{2}$ and $x_b = \frac{x_2+x_3}{2}$ was substituted into the prediction function as $I_j[k+2]$ to compare the results of the cost functions. The one that with smaller result between x_a and x_b indicates the convergence direction for the next search.

In the modified binary search algorithm, the iteration was repeated nine times within each control period, as nine iterations could narrow the range of searching to $\frac{1}{512}$ of its initial values. Boundary of searching is initialized as twice of the rated DC port current to promise enough range of searching while saving number of iterations; the error is limited within 1%, which is based on the same reason as introduced before.

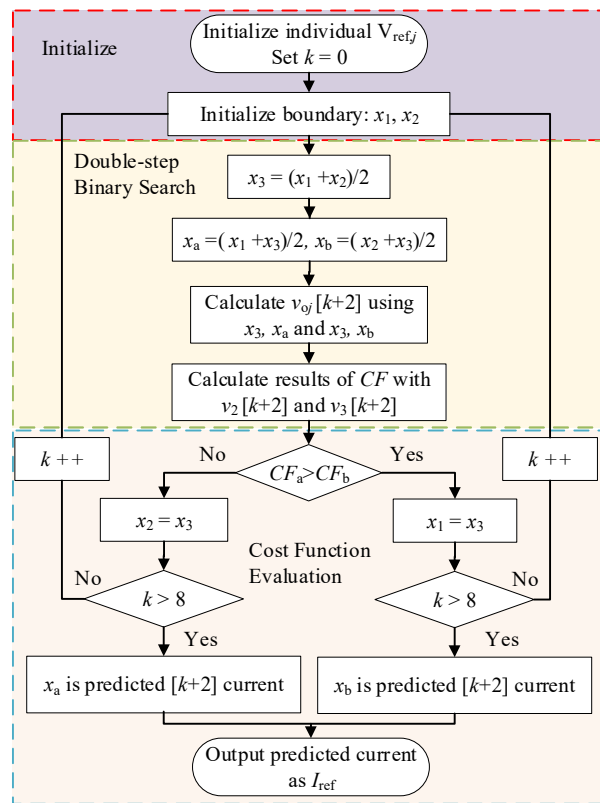


Fig. 4.2.6 Flow chart of the enhanced binary search for current prediction

An optimized control system was established with coefficients $\alpha = 1$ and $\beta = 2$ respectively. $\alpha \neq 1$ might lead to the scale-up or scale-down of the output voltage, whereas β is adjusted based on the steady-state ripple performance.

4.3 A modular modulation algorithm based decoupling control of Multiple Active Bridge converter for power transfer efficiency and flexibility improvements

4.3.1 Multiple Active Bridge Based Multiport EV Charger

This chapter proposes an accurate O^2ND algorithm with reduced control complexity. Following that, a modular modulation decoupling control strategy equipped with O^2ND is developed to realize the voltage control for MAB converters. The concept of ‘modular’ refers to the flexible inserting and switching of phase shift modulations. Besides, a DC current reference generator is developed to generate the reference current cooperating with the proposed modular modulation decoupling control system, as shown in Fig. 4.3.1.

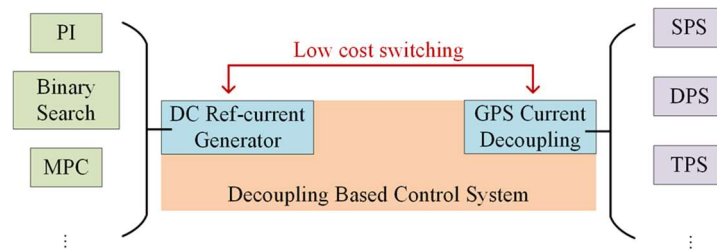


Fig. 4.3.1 The definition of the ‘modular’ in the proposed decoupling control strategy.

The proposed decoupling control methodology can realize accurate voltage control with good steady state and dynamic performance for the multiport EV chargers. This methodology separates the DC reference current generation and the current decoupling into two independent procedures. GPS modulation is introduced to indicate the power characteristics in the current decoupling algorithms, enabling the system to satisfy different constraints, such as soft switching.

In this part of Chapter 4, the GPS based current partial derivative table is first presented. Two iterative current decoupling algorithms are introduced with the coordination of this table. The O^2ND algorithm is then proposed with a trade-off comparison. A case study of controlling a

QAB converter by the proposed decoupling control strategy with a PI current reference generator and SSPS modulation is demonstrated, where the O²ND algorithm was applied in the current decoupling module.

4.3.2 An online offline Newton decoupling (O²ND) algorithm for current decoupling

Block diagram of the proposed O²ND control system is shown in Fig. 4.3.2, in which control processes are divided into three phases. First, inner phase shifts are calculated according to the indication of the modulation strategies by the ‘constraints satisfier’ module. Then, reference DC currents for each port are generated from the declared reference output voltages by the ‘DC current reference generator’ module. In this chapter of the research, the PI voltage controller is utilized in the later QAB case study. This PI can be replaced by nonlinear controllers depending on the application or operation requirements. Finally, these reference currents are delivered to the ‘current decoupling’ module, where optimization algorithm is responsible for the iterative calculation of the control variables. The final optimum outer phase shifts combined with the previously calculated inner phase shifts are sent to the gate-drive circuits of the MAB plant.

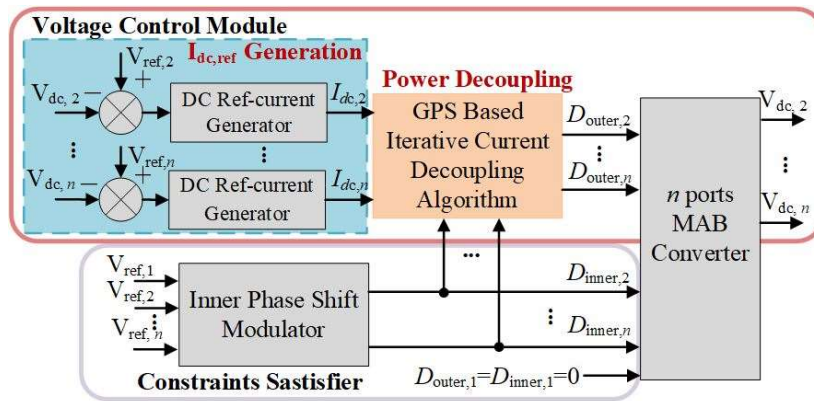


Fig. 4.3.2 Block diagram of the proposed current decoupling control.

In this chapter, two iterative current decoupling algorithms: ND and SND are demonstrated in the first place. O²ND method is then proposed with a quantitative computational burden comparison. To guarantee the effectiveness and accuracy of the optimization algorithms based current decoupling, there are two prerequisites, which can be examined by mathematical models:

1. Convergence of the iterative DC current to phase shifts calculations.
2. For each group of average DC currents in the controllable range, there exists only one set of optimal solution. In other words, local optimization should be global optimization.

The Newton based methods always require a set of specified initial points to begin the iteration. In this chapter, all the three algorithms use the same initial conditions: $D_{j,i} = 0$, as shown in Fig. 4.3.3 The universal starting condition can simplify the realization of the decoupling control and provide the observable performance comparisons between the algorithms. This universal iteration is named as the ‘zeroth iteration’, which is more approximate to a preparation step.

A. Decoupling of the current with ND algorithms

For a n ports MAB converter system, power received by one individual port P_i can be regarded as the superposition of the $(n - 1)$ virtual DAB branches as shown in previously Chapter 4.2.2. Since transferred power is presented in current form, deduction of the current from Jacobi matrix J requires the generalized form of current partial derivatives under all modular modulation power characteristics, which updates the TABLE 2.1 into the partial derivatives form as TABLE 4.1.

TABLE 4.1

GENERALIZED PARTIAL DERIVATES OF AVERAGE CURRENT IN DAB BRANCH WITH GPS MODULATION

(Note: if $|D_{j,i}| > \frac{1}{2}$, use $1 - |D_{j,i}|$ instead, but the derivative analysis should be opposed)

Zone	Conditions of Phase shifting	Partial derivatives $\frac{\partial i_{j,i}}{\partial D_i}$ (Base current: $\frac{V_{dc,j}}{4f_{sw}L_{j,i}}$)	Partial derivatives $\frac{\partial i_{j,i}}{\partial D_j}$ (Base current: $\frac{V_{dc,i}}{4f_{sw}L_{j,i}}$)
A	$D_{IN,j} \geq D_{IN,i}$ and $ D_{j,i} < \frac{1}{2}(D_{IN,j} - D_{IN,i})$	$2(1 - D_{IN,j})$	$-2(1 - D_{IN,j})$
B	$D_{IN,j} < D_{IN,i}$ and $ D_{j,i} < \frac{1}{2}(D_{IN,i} - D_{IN,j})$	$2(1 - D_{IN,i})$	$-2(1 - D_{IN,i})$
C	$\frac{1}{2} D_{IN,j} - D_{IN,i} \leq D_{j,i} < \min\left[\frac{1}{2}(D_{IN,j} + D_{IN,i}), 1 - \frac{1}{2}(D_{IN,j} + D_{IN,i})\right]$	$(2 - D_{IN,j} - D_{IN,i}) - 2 D_{j,i} $	$-(2 - D_{IN,j} - D_{IN,i}) + 2 D_{j,i} $
D	$D_{IN,j} + D_{IN,i} \leq 1$ and $ D_{j,i} \geq \frac{1}{2}(D_{IN,j} + D_{IN,i})$	$2 - 4 D_{j,i} $	$-2 + 4 D_{j,i} $

This table provides quantified indications for the power transfer relationship and further supports the ‘modular’ modulation decoupling control. By referring to the literature review, the

definition of the matrix norm and the positive semi-definite (PSD) property of the convex function, convergence of the matrix is guaranteed [194].

$$\begin{bmatrix} D_2^{k+1} \\ \vdots \\ D_n^{k+1} \end{bmatrix} = \begin{bmatrix} D_2^k \\ \vdots \\ D_n^k \end{bmatrix} - \begin{bmatrix} \frac{\partial I_2}{\partial D_2^k} & \cdots & \frac{\partial I_2}{\partial D_n^k} \\ \vdots & \ddots & \vdots \\ \frac{\partial I_n}{\partial D_2^k} & \cdots & \frac{\partial I_n}{\partial D_n^k} \end{bmatrix}^{-1} \begin{bmatrix} I_2(D^k) - I_{2,\text{ref}} \\ \vdots \\ I_n(D^k) - I_{n,\text{ref}} \end{bmatrix} \quad (4.21)$$

With the outer phase shift results D^k obtained from the former iteration, DC average currents are updated to D^{k+1} matrix according to (4.21). By repeating the decoupling iteration (4.21), combined with the TABLE 4.1 in each iteration, ND updates J and J^{-1} in each iteration. The flow charts of these processes are demonstrated in Fig. 4.3.3, where a is the number of iterations. Optimization of the Jacobi and current matrix is continuously repeated within one control period from the 1st to the a^{th} iteration. This calculation brings considerable computational burden to the MCU. If the computation overflows the switching period, decoupling module will not be able to execute the assignments, leading to the system failure and threaten the steady state performance.

B. Decoupling of the current with SND algorithms

To release the stress of the real-time computing, a simplified Newton's method is proposed [85]. Instead of updating partial derivative 'online' within each iteration, this algorithm uses the initial partial derivative solutions calculated from the zeroth iteration. Define an iteration without update of the partial derivative matrix as the 'offline' calculation. For all the following iterations of the SND, offline matrix $[\mathbf{F}'(\mathbf{D}^0)]^{-1}$ substitutes the online matrix $[\mathbf{F}'(\mathbf{D}^k)]^{-1}$ without update, as shown in Fig. 4.3.3, where b represents the total number of iterations. Update function of the SND is represented as (4.22), where partial derivatives of average current always located in the Zone A or B of the TABLE 4.1 when all D^0 begins with zero (reasons are explained in later section).

$$D^{k+1} = D^k - [\mathbf{F}'(\mathbf{D}^0)]^{-1} F(D^k) \quad (4.22)$$

Since the matrix J and J^{-1} are not updated after the zeroth iteration, SND has less online calculation in each iteration. The highlighted part in Fig. 4.3.3 also shows this property. However, the total number of iterations must be increased to ensure the proper accuracy. In addition, operation logic of SND makes it correlated strongly with the initial J matrix, leading to its convergence speed sensitive to the variation of the port parameters.

C. Proposed online offline iteration algorithm with Matlab-based accuracy and complexity evaluation

Use the QAB converter as an example for demonstration and algorithms comparison. DC current of the output ports can be represented by the sum of six virtual DC currents: $I_{1,2}$, $I_{1,3}$, $I_{1,4}$, $I_{3,2}$, $I_{4,2}$, $I_{4,3}$ in (4.23).

$$\begin{cases} I_{ac,2} = I_{1,2} + I_{3,2} + I_{4,2} \\ I_{ac,3} = I_{1,3} - I_{3,2} + I_{4,3} \\ I_{ac,4} = I_{1,4} - I_{4,2} - I_{4,3} \end{cases} \quad (4.23)$$

Define the step error as: $\left| \frac{D^{k+1} - D^k}{D^k} \right|$, repeat the iterative calculation for D_n^k until reaching 1% step error. Under the 50k Hz switching frequency, ratio of the hardware switching delay is no longer negligible and 1% step error can enhance the system precision and compensate the error brought by the inaccurate port inductance measurement. In the theoretical evaluation stage, 1% step error is an achievable target which requires reasonable number of iterations. In the practical systems, value of step error should be selected with the consideration of the MCU processing capability.

Normalize the Port 1 voltage as the base voltage. For the QAB converter with equally distributed port inductances, set the reference voltage as: $V_{2ref} = 1.2$ pu, $V_{3ref} = 1.4$ pu, $V_{4ref} = 1.6$ pu, respectively. D_n^k updated by the ND and SND after each iteration has been recorded in Fig. 4.3.3. SND requires six iterations to reach the anticipated requirement whereas ND only needs four. Increasing the Port 4 reference voltage to $V_{4ref} = 2$ pu, simplified method requires another additional iteration whereas ND maintains the same performance according to Fig. 4.3.4. Without the update of partial derivative matrix, convergence of the SND highly

depends on the initial derivative matrix $[F'(D^0)]^{-1}$. Through the results collection from different data sets, it is observed that the peak convergence rate always occurs at the first iteration, then gradually reduces when the updated results approach the accurate solutions.

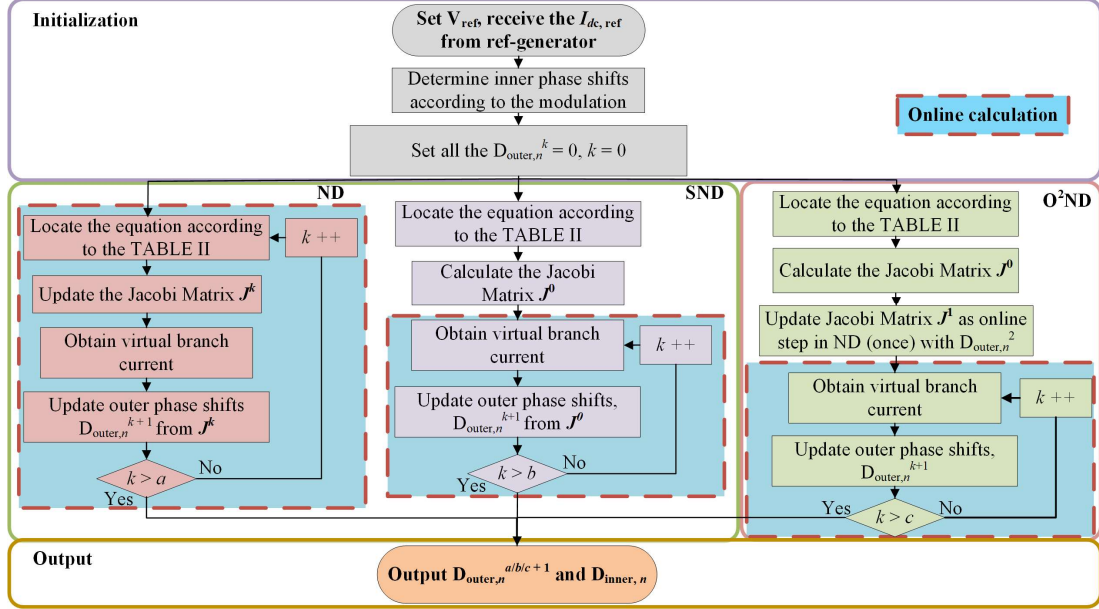


Fig. 4.3.3 Operation logic of three iterative current decoupling algorithms: ND (left), SND (middle), O²ND (right).

Hence, a two-step O²ND algorithm benefits from the advantages of ND and SND is proposed to reduce the control complexity while retaining the accuracy. This algorithm performs the first iteration with the online updates of the J matrix, and in all the following iterations, control variables are calculated ‘offline’ with the derivatives obtained from the first iteration. Update function of the proposed method can be represented as:

$$D^1 = D^0 - [F'(D^0)]^{-1}F(D^0) \quad (4.24)$$

$$D^{k+1} = D^k - [F'(D^1)]^{-1}F(D^k) \text{ when } k \geq 1$$

where $F'(D^1)$ is updated ‘online’ from the zeroth iteration. The online calculation is significantly reduced from $b - 1$ to 1 compared to the ND. Block diagram of the proposed algorithm is shown in the Fig. 4.3.3, where c is the total number of iterations. Plot the D_n^k of the O²ND with the same specifications in the previous content, performance improvement brought by the first online iteration are evident. O²ND algorithm requires five iterations to reach

the 1%-error precision under both conditions. Comparing to SND, it is more robust to the variations of the port reference voltage.

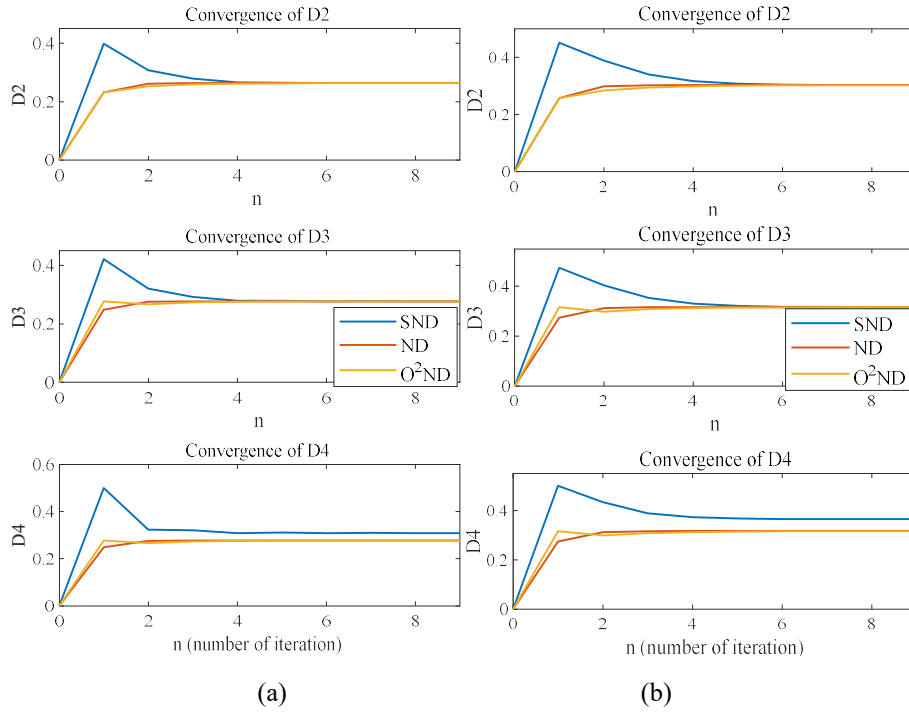


Fig. 4.3.4 Outer phase shift ratios after each iteration of three iterative current decoupling algorithms, where $D_1 = 0$, D_2 , D_3 , and D_4 are outer phase shifts: $D_{2,1}$, $D_{3,1}$, and $D_{4,1}$. (a) Under the initial reference voltage. (b) Under $V_{4ref} = 2$ pu condition.

To quantitatively compare the computational burden of the generalized n ports MAB topology in each control period, total numbers of additions and multiplications required for three algorithms are counted. Online update of the reverse Jacobi matrix J^{-1} calculation in ND and O^2ND is accomplished by the Gauss-Jordan method. Numbers of operands are counted under the most sophisticated partial derivative conditions. TABLE 4.2 shows the numbers of addition and multiplication operands of three decoupling algorithms with a times iteration. The total iteration numbers for ND, SND and O^2ND are set as 4, 5, and 10, respectively, to guarantee the 1% step error. From the observation of Fig. 4.3.5, when port number n is below 5, O^2ND has less control complexity. Whereas when port number is beyond 3, ND always has the highest complexity.

TABLE 4.2

COMPUTATIONAL BURDEN OF THREE DECOUPLING ALGORITHMS FOR N PORTS MAB CONVERTER
WITH A -TIMES ITERATIONS

	SND	ND	O ² ND
Online Addition	$N^2 - 2N + 1$	$N^3 + 8.5N^2 - 24.5N + 15$	$N^2 - 2N + 1$
Online Multiplication	$N^2 + 2N - 1$	$N^3 + 11.5N^2 - 24.5N + 14$	$N^2 + 2N - 1$
Total addition	$N^3 + (5 + a)N^2 + (2a - 19)N + (11 - a)$	$(a - 1)N^3 + (8.5a - 8.5)N^2 + (25.5 - 24.5a)N + (15a - 16)$	$2N^3 + (11.5 + a)N^2 - (35.5 + 2a)N + (22 + a)$
Total multiplication	$N^3 + (12 + a)N^2 + (2a - 28)N + (17 - a)$	$(a - 1)N^3 + (11.5a - 8.5)N^2 + (19.5 - 24.5a)N + (14a - 12)$	$2N^3 + (21.5 + a)N^2 + (2a - 60.5)N + (33 - a)$

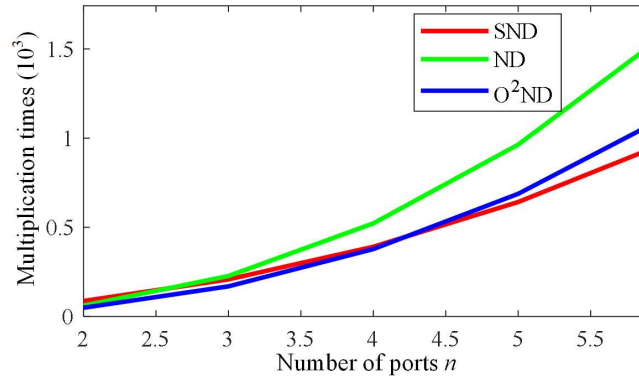


Fig. 4.3.5 Control complexity (measured by multiplications) with the increase of number of ports N for three current decoupling algorithms.

Besides the number of the ports, port parameters also affect the control complexity of the three algorithms at different level. These port parameters are contained in the power transfer characteristics under all the fundamental modulation strategies. Variation of these parameters affects the iterative algorithms in the form of the common coefficients: $turn\ ratio * \frac{V_{dc,j\ or\ i}}{4f_s L_{j,i}}$, which is multiplied by the partial derivative components in the matrix. These coefficients can be calculated in prior and saved as constants. They will not be updated during the iterations, which means the processes of the control law can maintain the same. The online calculation in each iteration for these three methods listed in the TABLE 4.2 will not be disturbed as well. However, variations of the coefficients do affect the speed of convergence. The variations of

other port parameters are similar to the port reference voltages. For SND, significant variations in port parameters require more total iterations, resulting in higher control complexity, whereas ND and the proposed O²ND are more robust to the variation of the port parameters.

4.3.3 Case study of the ‘Modular’ modulation with the O²ND current decoupling algorithm

To test the variable modulation adaption property, a case study utilizing the proposed ‘modular’ modulation decoupling control is demonstrated in this chapter. The proposed O²ND algorithm is utilized in the current decoupling module, while the PI reference current generator and SSPS modulation is inserted to achieve the soft switching.

A. Realizing soft switching with configurable modulations

Soft switching in the active bridge can be classified into two types as CB-ZVS and EB-ZVS according to their ZVS considerations [117] [183] as introduced in the previous chapter. In this research, soft switching refers to the ZVS-on of the CB ZVS with the consideration of the dead time effect. This constraint can be satisfied by SSPS modulation. Its inner phase shifts are calculated according to (4.25) to ensure that the current at the switching on moment is exactly zero. In this modulation, inner phase shifts are calculated in prior before the process of the current decoupling, and their value are fixed in the following iterations.

$$D_{\text{inner},n} = 1 - \frac{V_{\text{dc},1}}{V_{\text{ref},n}} \quad (4.25)$$

B. Control of the MAB converter with the proposed decoupling control strategy

Under the SSPS modulation, inner phase shift ratios are primary obtained through (4.25). All the three control freedoms are involved in the virtual branch. Reference DC currents are provided by the PI controller based on the transfer function (4.27). This transfer function is derived from the load current characteristic (4.26), where the load side equivalent circuit is sketched as Fig. 4.3.6.

$$I_n(s) = \frac{V_{dc,n}(s)}{\frac{1}{sC}} + \frac{V_{dc,n}(s)}{R_{load,n}} \quad (4.26)$$

$$G(s) = \frac{V_{dc,n}(s)}{I_n(s)} = \frac{1}{C_n s + \frac{1}{R_{load,n}}} \quad (4.27)$$

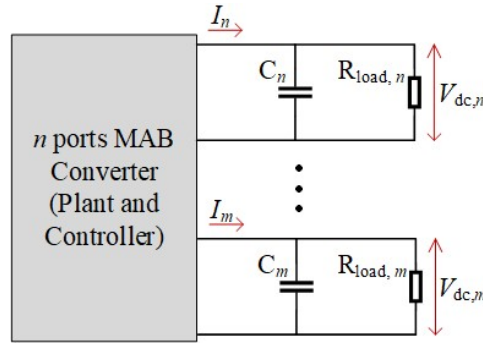


Fig. 4.3.6 The load side equivalent circuit of the MAB converter.

Parameters of the PI controller is initially calculated according to the damping coefficient. $k_p = 0.707$ is then slightly scaled up for better dynamic response. $n - 1$ PI current generator is required for the optimum DC current reference generation. The control scheme of the PI current generator is sketched in Fig. 4.3.7, where the current decoupling module is the same one as introduced in Fig. 4.3.2. Low pass filters are connected in serial to reduce the interference of HF harmonics.

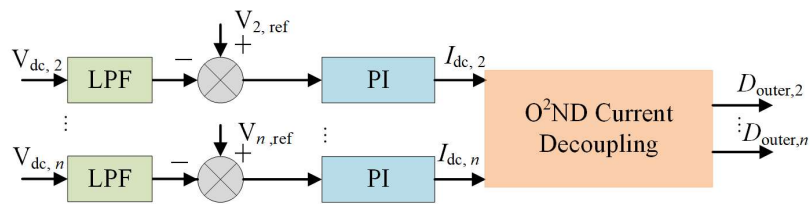


Fig. 4.3.7 Control diagram of the proposed modular decoupling control with PI controller used as the current reference generator.

4.4 Simulation and experimental validation

4.4.1 Experimental validation for the PDC-MPC

A. PI controller with power decoupling module

The TAB converter circuit was built in PLECS with specifications listed in TABLE 4.3. The soft switching is not taken into consideration as the setup is not optimally designed for ZVS evaluation but focuses on power management with MPC and decoupling. Soft switching modulation strategies for MAB could be applied into the decoupling module for ZVS realization.

To validate the effectiveness of the decoupling module, a PI controller without decoupling was established based on the small-angle approximation whose maximum controllable range of the phase shift is limited by the linearized interval. According to the approximation, when phase shift angle α is small, $\sin(\alpha) \cong \alpha$, whereas $D_{j,i}(1 - D_{j,i})$ can be approximated as $\sin\left(\frac{\pi}{4}D_{j,i}\right)$, which provides a simplified linearized power equation that holds only within typical range.

$$P_{j,i} = \frac{nV_1V_2\frac{\pi}{4}D_{j,i}}{2f_sL_s} \quad (4.28)$$

TABLE 4.3

CIRCUIT PARAMETERS AND SPECIFICATIONS OF TAB CONVERTER IN PLECS SIMULATION

Symbol	Definition	Value
V_1	Input voltage of port 1	25 V
V_2	Reference output voltage of port 2	40 V
V_3	Reference output voltage of port 3	45 V
$n_1:n_2:n_3$	Transformer turn ratio	1:1:1
L_{s1}	Port 1 leakage inductance	20 μ H
L_{s2}	Port 2 leakage inductance	20 μ H
L_{s3}	Port 3 leakage inductance	20 μ H
R_{L2}	Port 2 load resistance (50% load)	250 Ω
R_{L3}	Port 3 load resistance (50% load)	250 Ω
C_2	Port 2 DC link capacitor	300 μ F
C_3	Port 3 DC link capacitor	300 μ F
f_s	Switching frequency	20 kHz

With the quantified power characteristic, TAB converter controlled by PI with decoupling can be divided into two isolated DAB branches. Where PI parameters could be obtained individually according to the transfer function describing the gain between the output voltage and port average DC current. As the decoupling module was introduced, critical damping coefficient is utilized to provide more violent oscillations for dynamic response consideration: $k_p = 0.19$ and $k_i = 8.1$. For the PI controller without decoupling, parameters can be calculated by dividing the previous calculated parameters with the current to phase shift factor. The parameters of the PI without decoupling were: $k'_p = 0.03$, and $k'_i = 0.27$ where k'_p is scaled for faster dynamic.

B. Simulation results

Compared to the original PI controller, the PI controller with decoupling had better dynamic performance. Fig. 4.4.1 shows the voltage waveform under a step change at Port 2; at the instant of 0.8 s, the reference voltage at Port 3 was increased to 50 V from 45 V. The PI with decoupling was faster in transition and smaller in the overshoot. In the subsequent evaluations, the object of comparison was replaced with PI with a decoupling system. All the PI controllers in the subsequent chapters refer to the PI controller with power decoupling.

Fig. 4.4.2 shows the comparison of the output voltage waveforms of the TAB converter system using the PI controller and initialized MPC strategy. For the transition performance in the initial stage, the settling time of the PI controlled system was 0.4 s, whereas MPC only required 0.03 s to reach the steady state. This result verifies fast transition in the MPC. However, the initialed MPC exhibited a more significant steady-state voltage ripple. In addition, steady-state DC offsets were observed in MPC; the offset was 0.05 V and 0.2 V for Port 2 and 3 respectively.

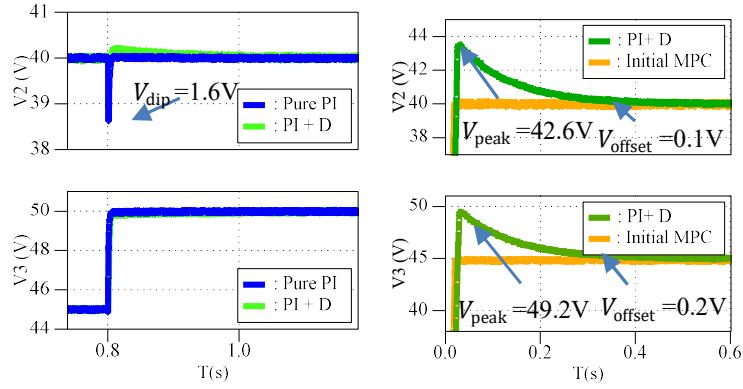


Fig. 4.4.1 Simulation waveform: Step change of referenced voltage from 45V to 50V at port 3 with PI controller and PI with power decoupling

Fig. 4.4.2 Simulation waveform: Output voltage of port 2 and port 3 at initiating stage under PI with decoupling and preliminary MPC

Fig. 4.4.3 shows the output voltage waveforms using the finalized PDC-MPC control strategy. The transition of initialing was faster than that for the PI with decoupling and MPC with the initial logic according to the TABLE 4.4. The steady-state ripple was reduced from 0.3 to 0.25 V. The current compensation term in the prediction function was effective in eliminating steady-state errors.

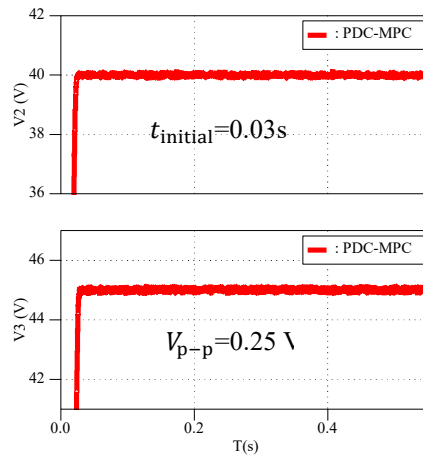


Fig. 4.4.3 Simulation waveform: Voltage waveform of port 2 and port 3 with finalized PDC-MPC

Based on the results presented in TABLE 4.4, it can be concluded that βG_2 reduced the steady-state ripple. A larger value of β could introduce higher attenuation to the sampling noise and oscillating phenomena. In addition, the transition may be slowed by a larger steady-state error. In the proposed control strategy, the dynamic response speed can be adjusted by modifying the control frequency. However, a higher control frequency utilizes considerable

MCU computational resources. Computational burden of the MPC with decoupling has been obtained in experimental validation.

The dynamic performance of the PDC-MPC was first examined with step changes in loads and reference voltage. Standardized port load conditions as full-load equals 475Ω , 50% load equals 250Ω and no load equals to 25Ω . Fig. 4.4.4 shows the voltage waveform under a step change in load of Port 3. When the load reduced from 50% to 25% at 0.8 s, a larger current was required to maintain a constant voltage. For the PI controller, a rapid change led to a phase shift that moved beyond the maximum limitation of the linearized range. The proposed PDC-MPC equipped with the prediction model and on-line load conditions extended the range of control and, provided accurate control variables within less time.

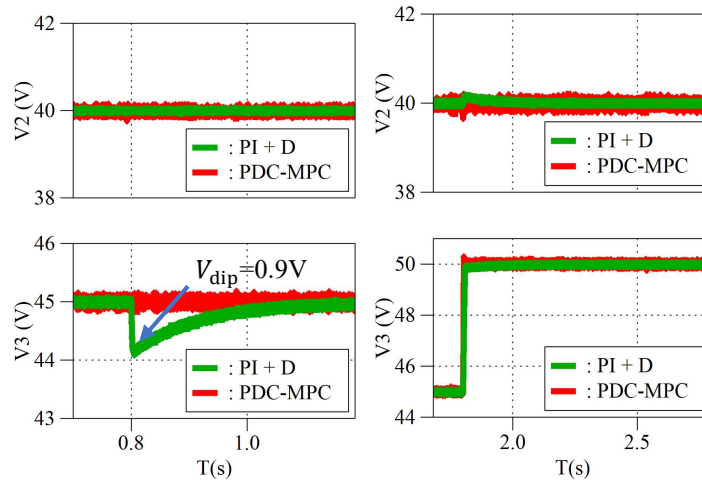


Fig. 4.4.4 Simulation waveform: Step change of load (50% to 25% at port 3) for PI controller and PDM-MPC

Fig. 4.4.5 Simulation waveform: Step change of referenced voltage at port 3 for PI controller and PDM-MPC

Fig. 4.4.5 shows the voltage waveform under a step change in the reference voltage at Port 3. Where PI coefficients are selected according to the simulation performances. At the instant of 1.8s, the reference voltage at Port 2 was changed to 50 V. Similar to the variation in load dynamics, MPC only required several control periods to update the target and to restablishe. The PI controller reacted slowly at the beginning after the variation appears, as the execution of control is based on the integration of the previous-state error but reacts significantly in the later

transition stage with significant overshoot. Resulting in a slower transition and limits the processing voltage dip or overshoot.

TABLE 4.4
COMPARISON BETWEEN THREE CONTROL STRATEGIES

	PI with Decoupling	Initial MPC	PDC-MPC
Initiation	0.4 s	0.03 s	0.04 s
Steady state ripple (p-p)	0.14 V	0.3 V	0.25 V
Steady state error	None	0.1 V & 0.2 V	None
Load change (50%-25%)	0.5 s	Unstable	0.16 s
Load change (50%-100%)	0.45 s	0.01s	0.01 s

A quantitative comparison of the three control strategies introduced in the previous chapters is presented in TABLE 4.4, verifies the proposed PDC-MPC had enhanced dynamic performance.

C. *Experimental validations*

The performance of the proposed methodology was verified through experiments. An RT Box was used as the digital control unit. Voltage sensors were connected to the RT Box through an analogue interface board. The PWM signals generated were emitted to drive the switching devices CMF20120D inside the H-bridges through a digital interface board. The plant used in the experiment was initially designed as a QAB converter consisting of four pairs of H-bridges and a multi-winding HF transformer. In this experiment, Port 4 was an open-circuit at the transformer node to allow the plant perform as a TAB converter. Port 1 was connected to a constant DC supply, and resistive loads were connected to Ports 2 and 3.

The parameters of the components used in the experiment and their specifications are listed in TABLE 4.5. As the leakage inductance in the multi-winding transformer was negligible, the inductors were connected to the transformer in series.

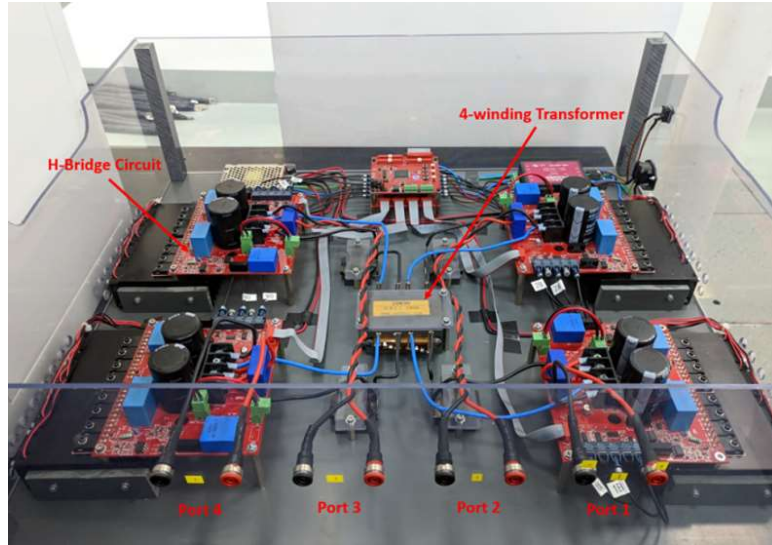


Fig. 4.4.6 TAB converter plant used in the experimental verification

TABLE 4.5

CIRCUIT PARAMETERS AND SPECIFICATIONS OF THE TAB CONVERTER IN EXPERIMENT

Symbol	Definition	Value
V_1	Input voltage of port 1	25 V
V_2	Reference voltage for port 2	40 V
V_3	Reference voltage for port 3	45 V
$n_1:n_2:n_3$	Transformer turn ratio	1:1:1
L_{s1}	Port 1 inductance	20 μ H
L_{s2}	Port 2 inductance	20 μ H
L_{s3}	Port 3 inductance	20 μ H
R_{L2}	Port 2 load resistance (initial)	250 Ω
R_{L3}	Port 3 load resistance (initial)	250 Ω
C_2	Port 2 DC link capacitor	330 μ F
C_3	Port 3 DC link capacitor	330 μ F
f_s	Switching frequency	20 kHz
f_c	Control frequency	10 kHz

a) *Control Complexity*: As a criterion of the control complexity, the execution time is directly measured by the RT Box Interface in the Fig. 4.4.7. It includes the time of the code implementation from receiving the DC current to output phase shifts generation of three control methodologies. PI voltage controller is rather easy in realization, whereas comparing with PI plus decoupling, 36% increasement in average execution time brings significant improvement in dynamic performance shown in the later results.

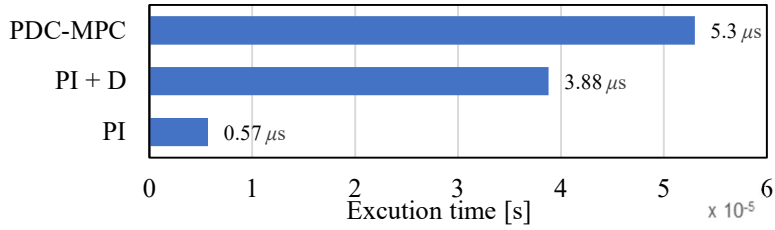


Fig. 4.4.7 Execution time of three control methodologies

b) *Cost function evaluation:* The relationship between the voltage deviation factor β and steady-state ripple was examined and sketched in Fig. 4.4.8. The existence of a voltage deviation term in the cost function reduces the steady-state voltage ripple. A significant value for β results in a system that is sensitive to small perturbations. This result proves the previous evaluation. Based on the figure, β was modified to 8, while α was maintained to be 1.

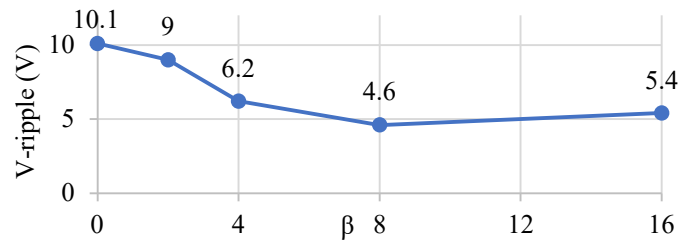


Fig. 4.4.8 Evaluation of deviation coefficient β and steady state voltage ripple

c) *Decoupling module examination:* Effectiveness of the decoupling module is examined by an open loop reference step change test, where reference currents were provided to the decoupling module as constants. To avoid the disturbance in DC current brought by the output voltage variations, constant resistance loads are replaced by the constant voltage loads. Constant voltage loads provided low voltage variations in capacitors; load current can be recorded as the port current.

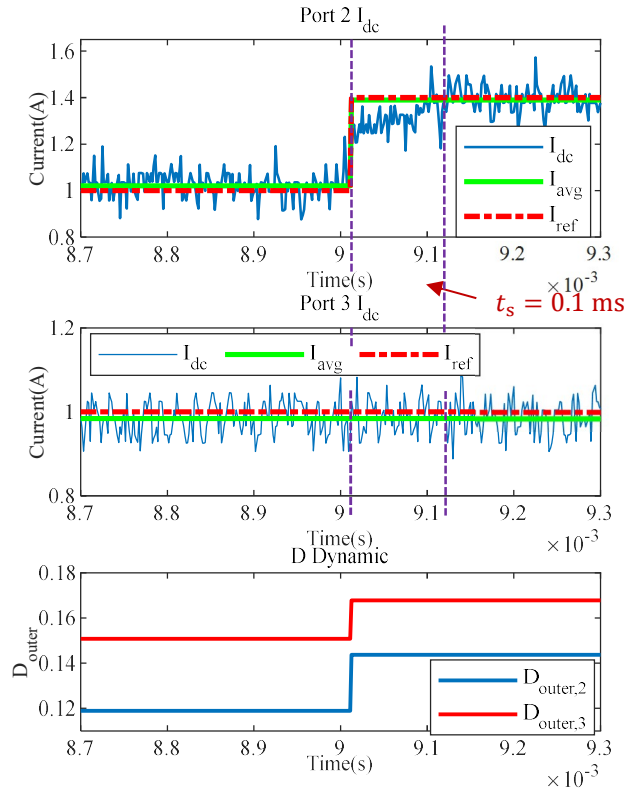


Fig. 4.4.9 Open-loop examination with average port DC reference current variation

Reference average current is initially set as: $I_{dcref,2} = I_{dcref,3} = 1\text{ A}$. $I_{dcref,2}$ was then increased to 1.4 A . As shown in the Fig. 4.4.9, D_2 and D_3 have been modified instantly after the reference variation, which can be observed from the DC current: $I_{dc,2}$ has responded to the dynamic within 0.1 ms whereas DC current of $I_{dc,3}$ remained as previous. Dynamic of the $I_{dc,avg}$ is corresponded with the reference variation.

d) Steady-state and dynamic performance: The steady-state voltage ripple of the proposed PDC-MPC could be maintained at a relatively low level close to that of the PI controller. Voltage and current at transformer side were shown in Fig. 4.4.10. For the dynamic performance, the initializing stage shown in Fig. 4.4.11 (a), the PI controlled system required 0.25 s to stabilise at the referenced voltage from zero whereas the MPC achieved a steady state within 0.01 s . The dynamic performance of the PDC-MPC and PI controller under step changes in loads at both Ports 2 and 3 is shown in Fig. 4.4.11(b), whereas Fig. 4.4.11(c) shows the waveform of the reference voltage variation at Port 3. The dynamics of the PDC-MPC was faster and its control was more accurate. Overshoots were difficult to eliminate in the PI-controlled system when step changes appeared. For the PDC-MPC, the prediction model

handled the variation within several control periods, whereas the control variables were updated in every cycle. The quantitative results presented in TABLE 4.6 also indicate the dynamic response capability of the PDC-MPC. Under all dynamic conditions, the transition period of the proposed PDC-MPC was at least five times faster than that of the PI with decoupling. However, ripple and overshoot were maintained at a low level.

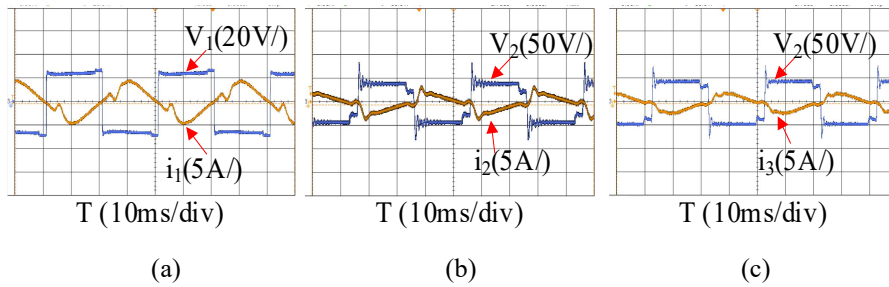


Fig. 4.4.10 Waveforms of AC voltage and AC current at each port (a) Port 1, (b) Port 2, (c) Port 3

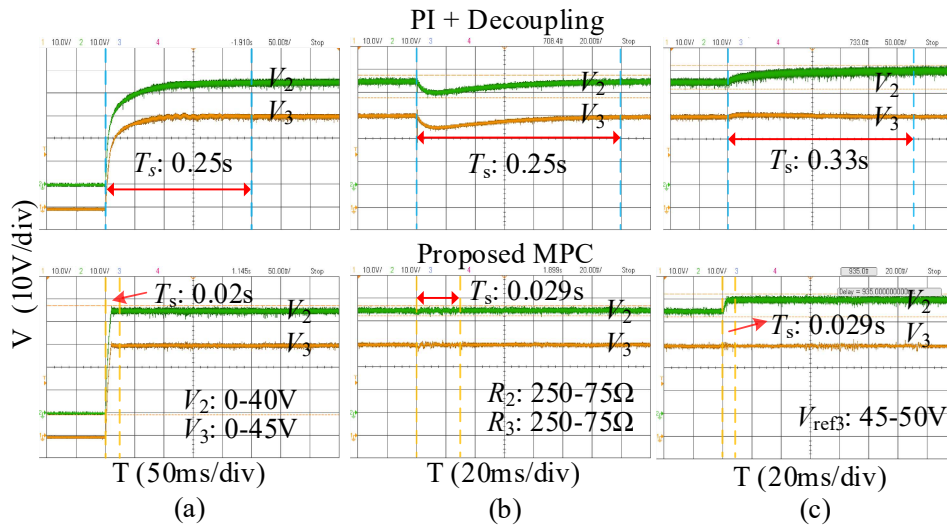


Fig. 4.4.11 Transition waveform comparison between PI + Decoupling and proposed MPC (a) Initiating stage, (b) Step change of loads, (c) step change of V_{ref}

TABLE 4.6

COMPARISON BETWEEN TWO CONTROL STRATEGIES

Measurement	PI with Decoupling	PDC-MPC
Initiation	0.25s	0.02s
Steady state ripple (p-p)	4.4V	4.6V
Load change (250Ω-75Ω)	0.14s	0.028s
Voltage step (45V-50V)	0.33s	0.029s

With a configurable search algorithm and low modulation method replacement burden, the proposed control strategy is equipped with high control flexibility. Compared to PI controllers,

the proposed strategy required only one-fifth and one-tenth of the transition period when step variations in load resistances and reference voltage appeared respectively. Good steady-state precision and control accuracy were achieved. The results of the simulations and experiments validated the performance of the proposed control strategy.

4.4.2 Experimental validation for the O²ND algorithm

In this chapter, the feasibility, and the improvement of the proposed O²ND algorithm are validated. Its control complexity has been compared to ND and SND by recording the execution time. The decoupling control strategy utilizing the proposed O²ND algorithm, inserted with the PI current reference generator and SPS/SSPS modulation (represented as ‘PI+D’ in the later contents) was evaluated in terms of the steady state behaviors and the dynamic responses. Its system performance is compared with the traditional pure SPS modulated PI control. The PLECS simulation and hardware experimental results are recorded for this verification. The controlled plant is a QAB converter with the specifications listed in the TABLE 4.8, where the control frequency refers to the frequency of updating the control variables.

TABLE 4.7

PARAMETERS OF THE QAB CONVERTER IN SIMULATION AND EXPERIMENT

Symbol	Definition	Value
V_1	Input voltage of Port 1	50 V
V_2	Initial reference voltage of Port 2	54 V
V_3	Initial reference voltage of Port 3	56 V
V_4	Initial reference voltage of Port 4	58 V
$n_1:n_2:n_3:n_4$	Transformer turn ratio	1:1:1:1
$L_{sx} (x = 1, \dots, 4)$	Port 1 to 4 series inductances	20 μ H
$R_{L,j} (j = 2,3,4)$	Output port load resistance	45-250 Ω
$C_j (j = 1, \dots, 4)$	DC link capacitor	340 μ F
f_s	Switching frequency	50 kHz
f_c	Control frequency	20 kHz

A. Simulation Results of the O²ND current Decoupling Control

The QAB converter has been built based on the control systems sketched in Fig. 4.3.7 with PLECS. With the current decoupling module, QAB converter is controlled as multiple isolated

DAB sub-branches, parameters of the PI current generator can be calculated from DAB voltage to current transfer function. For the PI without decoupling, parameters were calculated by dividing the normalized current factor in TABLE 2.4. Parameters of PI with and without decoupling algorithms are: $k_p = 0.07$, $k_i = 7.11$, and $k'_p = 0.042$, $k'_i = 0.167$, respectively.

a) *Steady state behaviour*: TABLE 4.8 shows the maximum steady state voltage ripple under the PI control and the proposed decoupling control using three iterative current decoupling algorithms. The total iteration numbers of the SND, ND and O²ND are 10, 4, and 5 as labeled in the brackets of the TABLE 4.8. These numbers are obtained with a 5% step error under the maximum port voltage variation condition, which is: 1.2pu, 1.5pu and 2pu for Port 2, 3, and 4 respectively. Referring to the TABLE 4.2, the total multiplication numbers within one control period are 391, 522, and 378 for the SND, ND and O²ND, respectively. Theoretically, the execution time of the proposed O²ND is 97% of SND and 72% of ND in percentage. This result proves the reduction of the computation burden brought by the proposed O²ND algorithm, as it achieves the similar steady state performance with less calculations.

TABLE 4.8

STEADY STATE VOLTAGE RIPPLE OF THREE ITERATIVE ALGORITHM APPLIED CONTROL STRATEGIES AND PURE PI CONTROL

	ND (4)	SND (10)	O ² ND (5)	PI
V _{dc2} ripple	0.041 V	0.022 V	0.025 V	0.03 V
V _{dc3} ripple	0.042 V	0.021 V	0.026 V	0.03 V
V _{dc4} ripple	0.045 V	0.023 V	0.028 V	0.03 V

b) *Dynamic Performance*: Enhancement in the dynamic performance of introducing the O²ND current decoupling algorithm was examined by applying the step change in reference voltage and loads. For the reference voltage step change with the asymmetrical loads condition 1: $R_{L2} = 250 \Omega$, $R_{L3} = 100 \Omega$, and $R_{L4} = 45 \Omega$, overall transition period of the O²ND current decoupling control is 0.22 s whereas PI requires 0.42 s according to Fig. 4.4.12(a). For the loads condition 2: $R_{L2} = R_{L3} = R_{L4} = 250 \Omega$, load step change was performed by reducing R_{L4} from 250 Ω to 100 Ω .

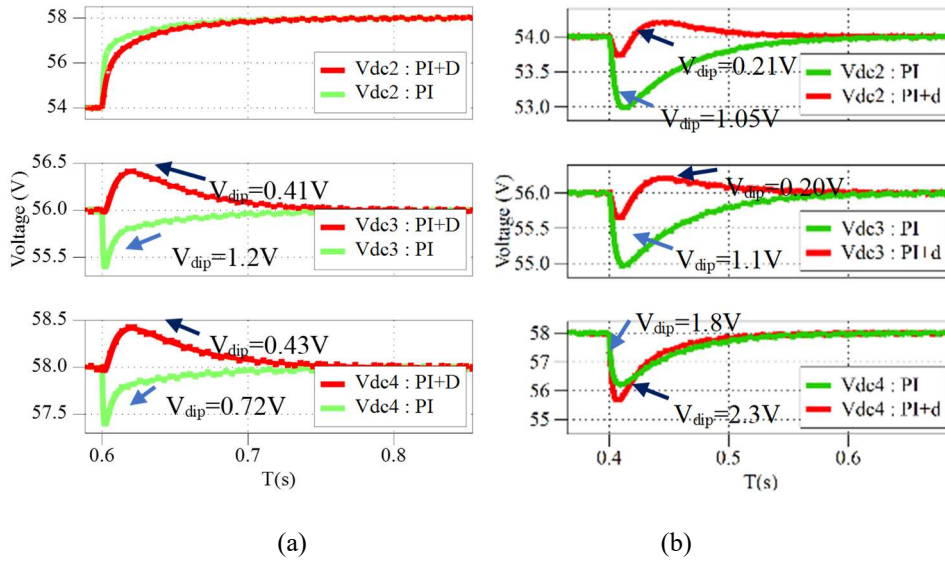


Fig. 4.4.12 Port voltage waveforms of the QAB converter with two control method under different step changes. (a) Step change of V_{ref2} from 54 V to 58 V with the loads condition 1. (b) Step change of R_{L4} from 250 Ω to 100 Ω with the loads Condition 2.

Fig. 4.4.12(b) shows PI controlled system costs 0.34s to restabilize while the decoupling control system takes 0.2 s. Under both conditions, dynamic response of the decoupling control is faster. A drawback of the decoupling control is observed at the Port 4 during the load step change, as its voltage dip is more significant compared to the pure PI controlled system. As large step change may lead to entire loop recalculation of iterations, voltage dip may appear during transient. Although dip may exist, time of the transient will still be shorter than PI controller.

c) Configurable modulation for ZVS: With the configurable modulation switching, ZVS can be achieved. AC voltage and current waveforms of the O²ND current decoupling controlled QAB converter inserted with the SPS and SSPS modulation are shown in Fig. 4.4.13(a) and (b). ZVS is realized in all four ports under the SSPS modulation, for the SPS one, Port 1 operates under the hard switching.

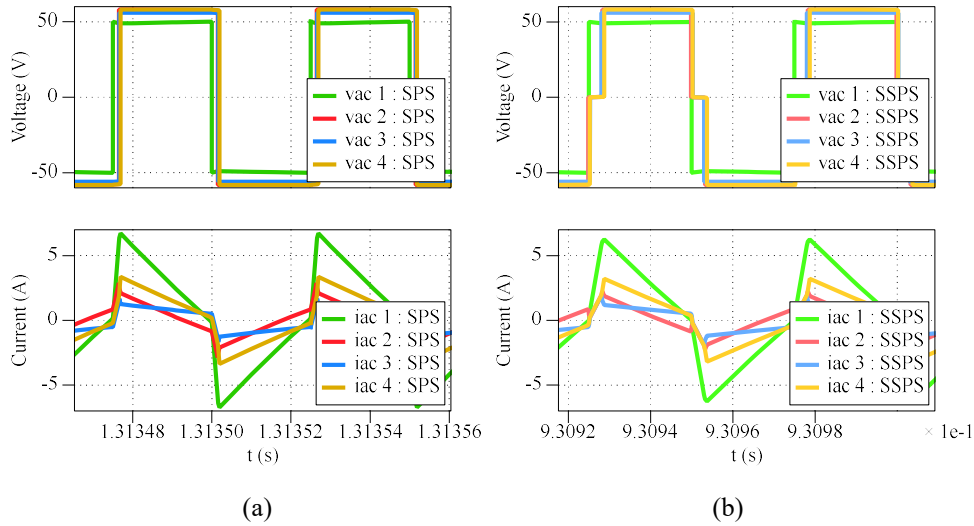


Fig. 4.4.13 Waveforms of AC voltage and AC current in each port with different modulation strategies under loads condition 1. (a) SPS modulation. (b) SSPS modulation.

B. Experimental Verification of the O^2ND current decoupling control

Merits of the proposed O^2ND current decoupling control are validated by the experimental results. The QAB converter used in the experiment consists of four H-bridges connected through a HF quadruple-phase PET shown in Fig. 4.4.6. Port 1 is connected to a constant DC supply whereas the resistive loads are connected to Port 2, 3, and 4. A PLECS RT Box was used as the digital control unit. Voltage sensors were connected to the RT Box through an analogue interface board. The generated PWM signals were emitted to CMF20120D inside the H-bridges to drive the switching devices through a digital interface board. Parameters in this experiment are the same as those in the TABLE 4.5.

a) Control Complexity: As a criterion of the control complexity, the execution time of the SND, ND and O^2ND decoupling algorithm in the QAB converter decoupling control system is directly measured by the RT Box Interface monitor. This execution time refers to the open loop operating time of the current decoupling counted from receiving the reference DC current to exporting the final phase shift variables highlighted in Fig. 4.3.3.

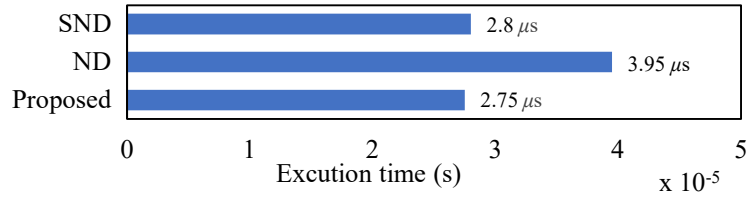


Fig. 4.4.14 Execution time of three decoupling algorithms.

The result in Fig. 4.4.14 shows the proposed O^2ND requires the smallest execution time, which is 98% of the SND and 69.6% of the ND, therefore verifies the theoretical evaluation in Fig. 4.3.5.

b) *Effectiveness of the O^2ND Decoupling Algorithm:* Open-loop test with step change in reference DC currents is performed to verify the effectiveness of the proposed O^2ND decoupling algorithm. The reference currents are directly provided to the decoupling module. To avoid the current disturbance caused by the load voltage increase, the resistive load has been replaced by the constant voltage load. Operating topology of this test is shown in Fig. 4.4.15.

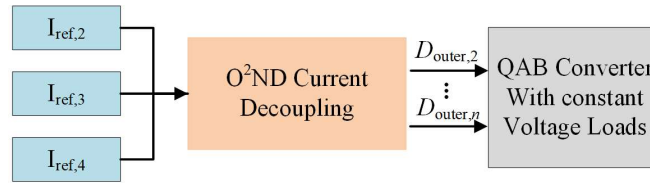


Fig. 4.4.15 The open loop validation of the O^2ND current decoupling algorithm.

Constant voltage loads resulted in low voltage variations in the DC-link capacitors. Hence, load current can be recognized as the port DC current. Initially, $I_{dcref,2} = I_{dcref,3} = I_{dcref,4} = 1$ A, then $I_{dcref,2}$ was increased to 1.4 A. As the current waveform shown in Fig. 4.4.16, $D_{outer,2}$ have been modified instantly to adapt to the change of the reference current. $I_{dc,2}$ has responded to the dynamic within 50 μ s whereas DC current of the Port 3 and 4 maintained the same.

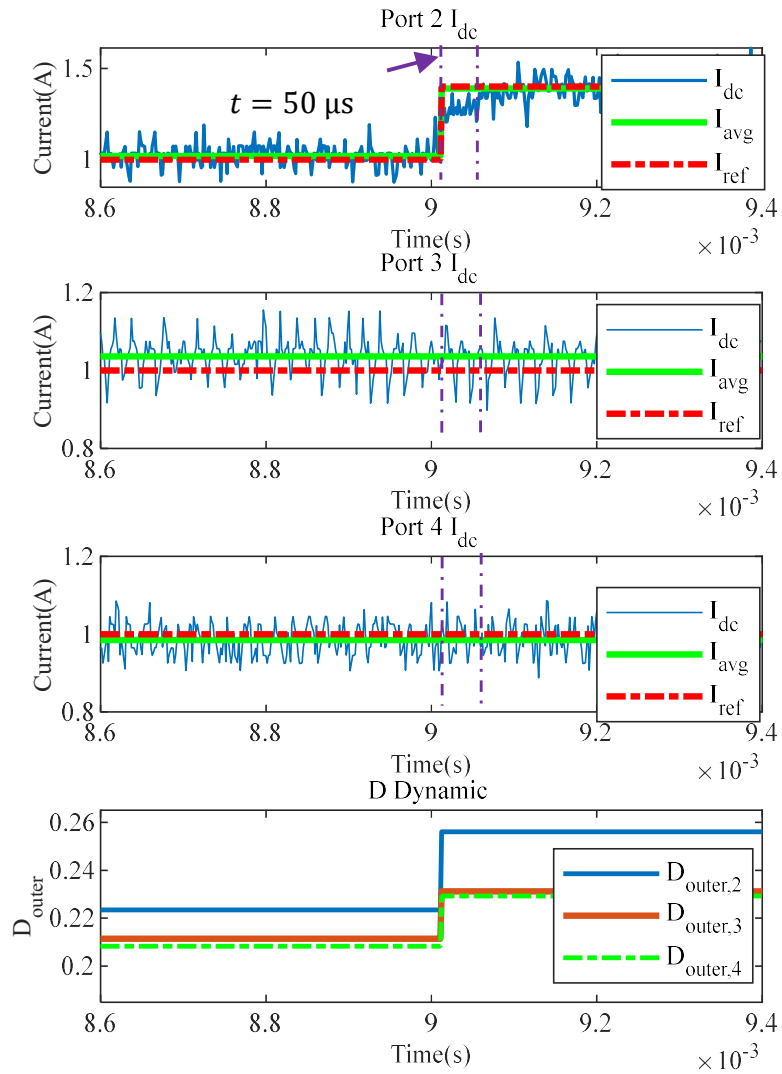


Fig. 4.4.16 Open-loop test with step change in reference DC current.

c) *Steady State Behavior:* With the O^2ND algorithm, voltage ripple at steady state has been reduced. For Port 2, 3, and 4 under the asymmetrical loads condition 1, the O^2ND decoupling control has the maximum steady state voltage ripple of 4.6 V, whereas for PI this value is 8 V, as shown in Fig. 4.4.17.

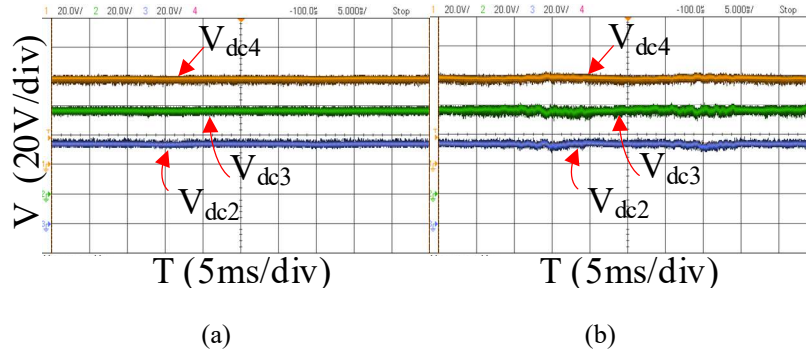


Fig. 4.4.17 Experimental results of the output port voltages in the QAB converter with SSPS modulation under loads condition 1. (a) O²ND decoupling control. (b) PI control.

d) Dynamic Performance: Dynamic performance enhancement and extension in the available control range brought by the decoupling module have been validated. Voltage waveforms under a step change in Port 2 reference voltage from 54 V to 58 V with the loads condition 1 are shown in Fig. 4.4.18(a) and Fig. 4.4.18 (b). The O²ND decoupling controlled system achieved the steady state with the new reference voltages within a short period, whereas PI controlled system lost control. With the implementation of the inner phase shift, the overshoot appeared in the PI controlled system lead its generated control variables exceeded the boundary of the linearized control range. Thus, PI controller can no longer maintain the power transfer control. The load step changes have been performed for further validations. Reduce the load R_2 from 250 Ω to 40 Ω at the steady state under loads condition 2 (all 250 Ω). As show in Fig. 4.4.18 (c) and Fig. 4.4.18 (d), proposed methodology requires less transition period to restabilize, voltage dip during the step is also less significant.

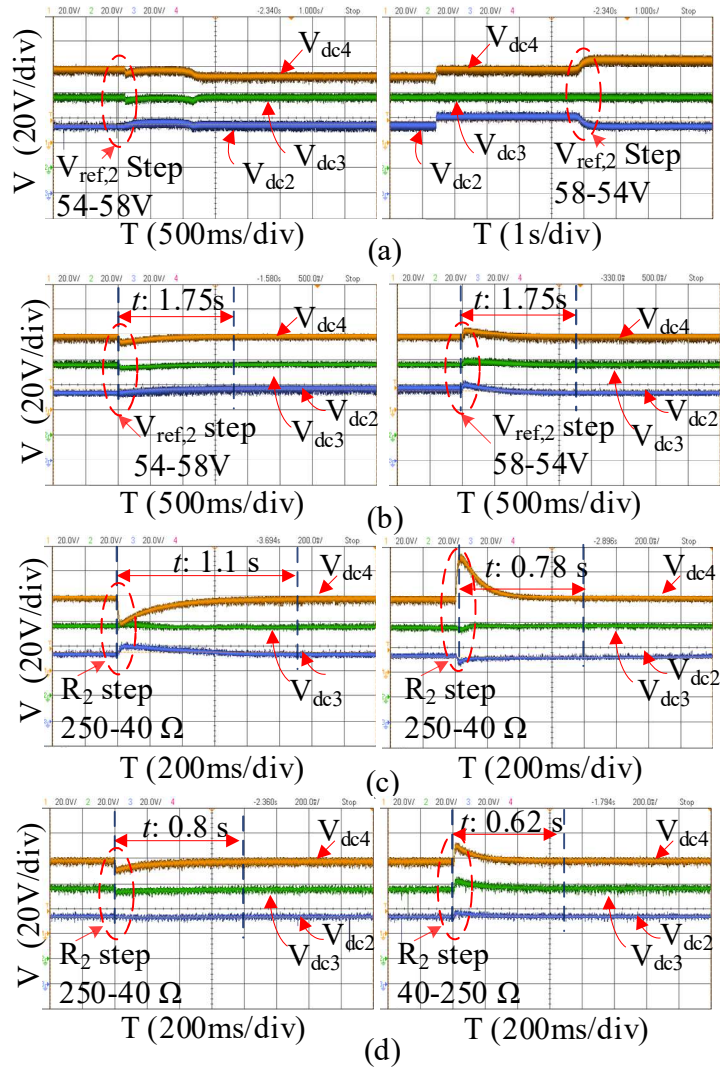


Fig. 4.4.18 Experimental results of the output voltages in the QAB converter with SSPS modulation under two control strategies. (a) PI control with step change in V_{ref2} under loads condition 1. (b) O^2ND current decoupling control with step change in V_{ref2} under loads condition 1. (c) PI control with load step in R_{L2} under loads condition 2. (d) O^2ND current decoupling control with load step in R_{L2} under loads condition 2.

e) 'Modular' modulation to achieve ZVS: As shown in Fig. 4.4.20, the instantaneous currents measured at the port series inductors are in opposite direction with the port voltages at the voltage rising edges, and the currents are positive when the top switches are turned off, for all the four ports. Fig. 4.4.19 shows the AC voltage and current waveforms of two upper switches in the port 2 H-bridge. Waveforms shows that $Q_{2,3}$ is switched off before the voltage rising edge, while the current flowing through is below zero. The same phenomenon can be observed at the resultant voltage falling edge. Overlapped part of two switches validates the effectiveness

of the inner phase shift modulation. Hence, if the port AC current (current flowing through the series inductor) is in the reverse direction of the resultant voltage at the rising/falling instants, ZVS is considered to be achieved.

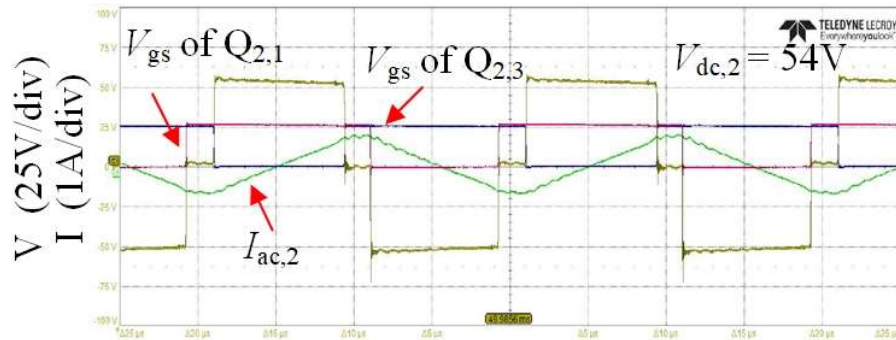


Fig. 4.4.19 The waveforms of resultant AC current and voltage of two upper switches in Port 2.

The circled switching actions in Fig. 4.4.20 prove the MOSFET are discharged when conducted, which means ZVS has been achieved in all the ports under the SSPS modulation. These results verify the effectiveness of the modular modulation ability of the proposed algorithm and decoupling control strategy. Soft switching modulation reduced the inner phase shifts, which improved the converter efficiency by reducing the switching losses. However, currents in the magnetizing branch raised, leading to certain iron loss increasement in the PET.

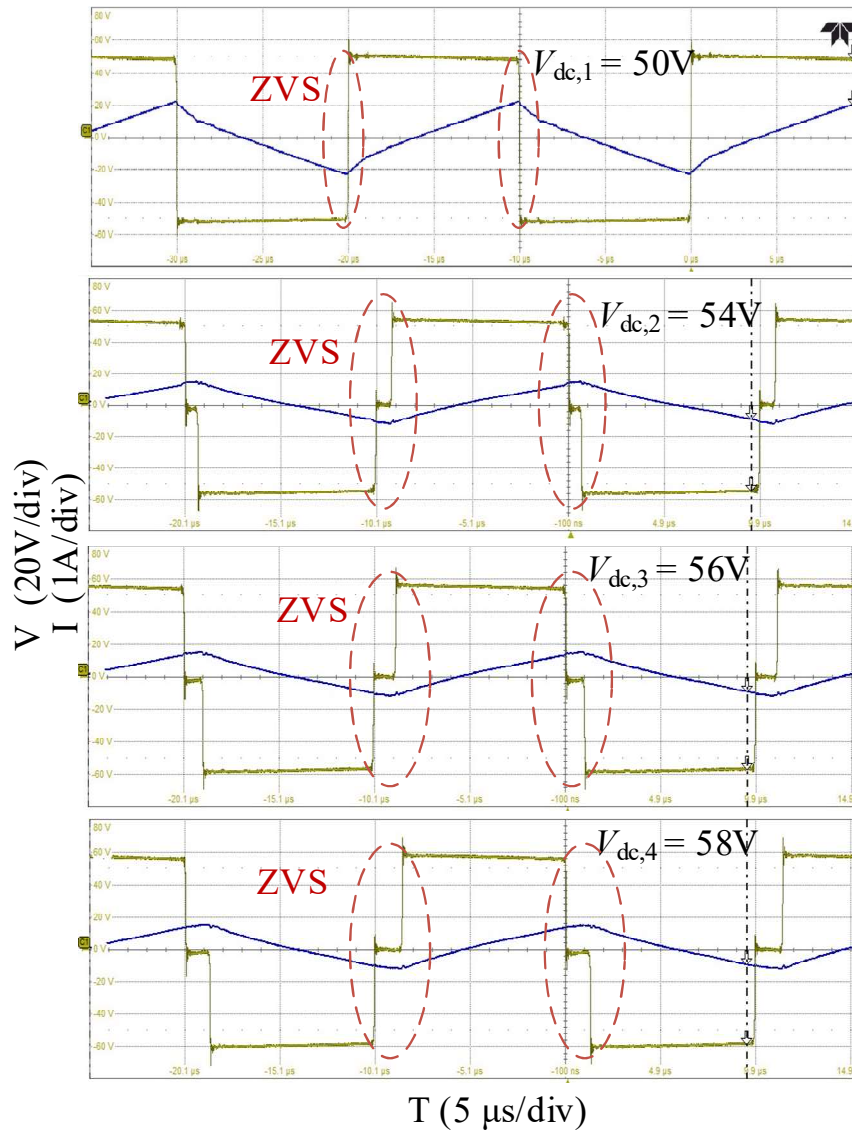


Fig. 4.4.20 Waveforms of the AC voltage and AC current in each port under SSPS modulation to achieve the soft switching.

4.5 Summary of this chapter

The study of PDC-MPC developed and validated a power-decoupling-based configurable MPC strategy to enhance the dynamic performance for the TAB converter. A binary search algorithm was applied in the MPC module to search for the optimum average DC current for the specified ports within several switching periods according to the desired voltage. Its power-decoupling module decouples the desired power of each isolated virtual branch to the phase shift angles. With a configurable search algorithm and low modulation method replacement burden, the proposed control strategy is equipped with high control flexibility. Compared to PI

controllers, the proposed strategy required only one-fifth and one-tenth of the transition period when step variations in load resistances and reference voltage appeared, respectively. Good steady-state precision and control accuracy were achieved. The results of the simulations and experiments validated the performance of the proposed control strategy.

In research of O²ND part, the development and validation of an iterative current decoupling algorithm combined with a modular modulation decoupling control system have been presented. The proposed O²ND algorithm balanced the control accuracy and complexity. The proposed control has high level of flexibility, of which both modulation strategies and DC reference current generator are switchable according to the operation and application requirement. This control methodology is suitable for controlling n -port MAB converters utilized in multiport EV chargers. In the case study part, the proposed O²ND algorithm is adhibited in the current decoupling module of control, PI controller was applied as the reference current generator whereas SPS and SSPS modulation has been inserted, respectively, for performance verifications. According to the QAB converter experimental results, the execution time of O²ND is 98% of SND and 69.6% of ND under a similar steady state ripple. For the traditional PI control, dynamic and steady-state voltage control performance is unsatisfactory when outer phase shift is beyond 0.2 under the unbalanced loads conditions. With the indication of power to phase shift characteristic in O²ND, the range of the accurate control has been expanded to twice that of the PI. A 20% transient time reduction was observed from the load step change test under symmetrical load condition, demonstrating the improvement of the dynamic performance. With the 'modular' property, soft switching and other features can be achieved conveniently.

5. Design of multi-winding integrated HF transformers with accurate and controllable leakage inductances

5.1 Chapter overview

Since the modulation and control strategies proposed in the previous chapters can realize the accurate control for practical MAB converter under varied voltage with flexibility to suit the integrated transformer, the next step of the research is designing this integrated transformer. The aim of decreasing volume consumption and promoting power density leads to the planar core and winding configurations selected for this integrated transformer. Magnetic integration has been focused on integrating the series inductors and a HFT into a single magnetic component by increasing the leakage inductance of the HFT. This brings a critical issue to the core design for the integrated transformer, whether structural modification is required for the selected core at the transformer design stage to achieve the aimed leakage inductance. Since equivalent series inductance in power characteristic is replaced by leakage inductance, accurate leakage inductance estimation strategy is also required.

This chapter firstly proposed a reluctance-based leakage inductance evaluation strategy for the accurate estimation with air-path leakage considered. As the common calculations of the winding-arrangement-dominated leakage inductance commonly ignores the air-path leakage fluxes. Based on the estimation of the threshold leakage inductance, an optimized magnetic integration procedure for planar transformer has been developed, which can help judge whether core modification is required and then provide winding arrangement coordination. 3D finite element analysis (FEA) simulation and prototype experiments were conducted to validate the theoretical analyses.

To implement integrated transformer in the generalized N -port MAB converters, a novel RSSC HFMT with split windings is developed in the second part of this chapter. The proposed HFMT can adjust the leakage inductances within a wide range by the magnetic integration control parameters, which includes lengths of extension legs, side and central pillars, horizontal air gaps, turns of windings and winding distribution ratio. Port consistency is promised by the

insertion of vertical flux barriers. Based on the magnetic circuit analysis, accuracy of leakage inductance estimation can be guaranteed. A cross-shape-core HFMT is designed for a QAB to validate the effectiveness of the proposed RSSC HFMT as a case study. 3D finite element analysis simulation and prototype experiments were conducted to validate the theoretical analyses.

5.2 Magnetic Integration for a DAB Converter Planar Transformer with Accurate Leakage Inductances Estimation

Effort should be paid to realize the controllable magnetic integration requirements besides satisfying the fundamental electrical power specifications for DAB converters. A precise theoretical leakage inductance estimation strategy needs to be developed combined with instructions of magnetic integration help selecting the winding and the core setups that can realize the aimed values of the leakage inductance.

However, in many research papers, the estimation of leakage inductances relays on empirical formulas. In addition, most reluctance or energy-based estimation methods in published literatures only calculates the leakage flux in the core or windings with the air-path leakage flux ignored, and none provided an accurate achievable range of the magnetic integration from minimum to maximum with its corresponding winding arrangement for core-structure-unchanged planar transformers. Novelty of this chapter is concluded as follows to figure these issues:

- a) Providing an accurate reluctance analysis and flux-distribution-based leakage inductance evaluation strategy for planar transformers. This strategy calculates both the coil based self-mutual inductances and self, mutual-leakage inductances with high accuracy with air-path leakage flux considered. Which helps maintaining the control and modulation accuracy when magnetic integration is applied to a DAB converter.
- b) Optimizing the transformer magnetic integration process. By obtaining the boundary leakage inductance through the proposed evaluation strategy, whether core structure needs to

be modified to satisfy the required inductance values can be judged at integrated transformer design stage.

c) Based on the processed magnetic integration procedure, a planar transformer with an improved practical winding arrangement is manufactured as a case study.

5.2.1 Definition of the equivalent leakage, magnetizing inductance with an optimized magnetic integration procedure for two-port integrated planar transformers

The leakage inductance in a transformer is conventionally considered as the inductive component that results from the imperfect magnetic linking of one winding to another. In integrated DAB converters, the leakage inductance is also required to store the transferred power between two bridges temporarily replacing responsibility of the series inductors [195]. Technically, this leakage inductance refers to the primary and secondary port-equivalent leakage inductance deduced from the T-shape transformer equivalent circuit [67]. In which, $L_{p,eq}$ and $L_{s,eq}$ is the primary and secondary port-equivalent leakage inductance, respectively. And $L_{m,eq}$ is the equivalent magnetizing inductance. All the leakage inductances in this research all refer to $L_{p,eq}$ and $L_{s,eq}$.

From the perspective of the coil electric-circuit model, the inductance in the transformer can be represented by the coil-based matrix: $\begin{bmatrix} L_{11} & L_{12} \\ L_{21} & L_{22} \end{bmatrix}$; where L_{11} and L_{22} is the self inductance of the primary and secondary coil, L_{12} and L_{21} is the mutual inductance between two coils, respectively. The leakage and magnetizing inductance can be transformed from the equivalent primary self reluctance \mathcal{R}_{p-eq} , secondary self reluctance \mathcal{R}_{s-eq} and mutual reluctance \mathcal{R}_{m-eq} as: $L_{11} = \frac{N_p^2}{\mathcal{R}_{p-eq}} + \frac{N_p^2}{\mathcal{R}_{m-eq}}$, $L_{12} = \frac{N_p N_s}{\mathcal{R}_{m-eq}} = L_{21}$, and $L_{22} = \frac{N_s^2}{\mathcal{R}_{s-eq}} + \frac{N_s^2}{\mathcal{R}_{m-eq}}$.

In this research, the flux linking different windings is divided into two types: core (magnetizing) flux and the leakage flux.

Core (magnetizing) flux: ϕ_c refers to the flux going through the desired main magnetic path inside the core and linking all the windings. The magnetic path of the main flux is entirely enclosed by the core, mean path length can be calculated according to the core structure geometry.

Leakage flux: ϕ_s refers to the flux not entirely going through the main magnetic path and linking one (itself) or multiple windings. These flux paths can be further distinguished as the self-leakage flux paths and mutual-leakage flux paths, respectively. For the two-port transformer in DAB converters, the self and mutual-leakage inductance can also be presented by a matrix $\mathbf{L}_{ST} = \begin{bmatrix} L_{s11} & L_{s12} \\ L_{s21} & L_{s22} \end{bmatrix}$, where L_{s11} and L_{s22} refer to the self-leakage inductances and $L_{s12}=L_{s21}$ is the mutual-leakage inductance [196]. Values of these components in \mathbf{L}_{ST} can be calculated from their reluctance. Based on the flux passing through these reluctance, equivalent magnetic circuit can be proposed and established. From a further step of matrix transformation, the equivalent inductance can be calculated.

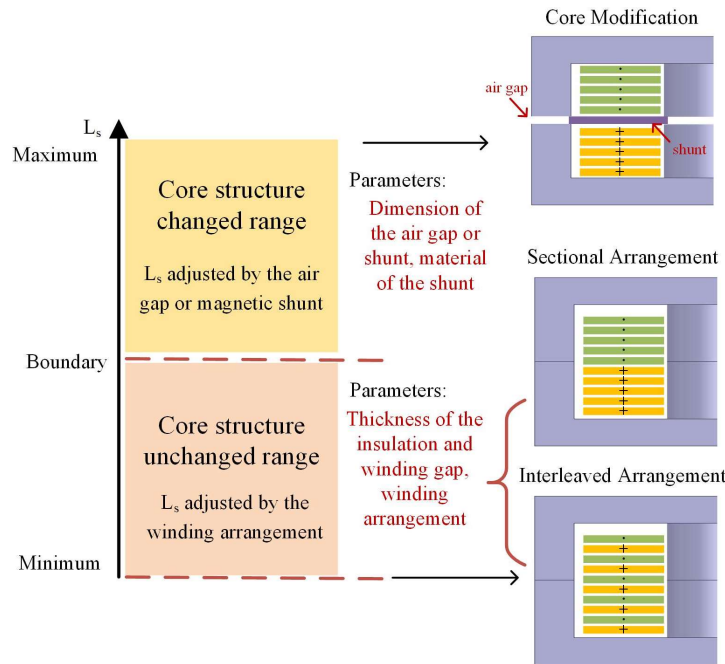


Fig. 5.2.1 The leakage inductance distribution map of controllable magnetic integration with their realization scenarios and adjusting parameters.

The range of the achievable L_s is classified into two regions as shown in Fig. 5.2.1, the minimum to the maximum of core-structure-unchanged stage, and the maximum of core-

structure-unchanged stage to the maximum of the air gap (or shunt) inserted stage. In core-structure-unchanged stage, magnetic integration is realized by adjusting the winding structure, connection, and arrangement. In core-structure-changed stage, integration is realized by adjusting the dimension of the air gap or shunt and the material of the shunt. When air gap or shunt is inserted, the leakage flux in the windings and air can be neglected. Boundary could be several times of the minimum and maximum can be tens of the minimum. Due to the reliability, power density and manufacturing difficulty considering, the boundary-maximum part is not discussed in detail in this chapter.

An optimized process of planar transformer magnetic integration with is proposed and sketched in Fig. 5.2.2. Similar to the design process of a traditional transformer, the first step and second step is the selection of the core according to the power and voltage specifications and calculate the turn of the windings. Then, based on the estimation of the maximum achievable leakage inductance for the selected core, whether core structure modification is demanded can be judged. Here an accurate leakage estimation strategy is necessary. After that, core and winding scenario can be selected in accordance with the boundary and estimation. FEA simulations will be used to check validate the previous results. And finally, core and windings can be manufactured and wounded.

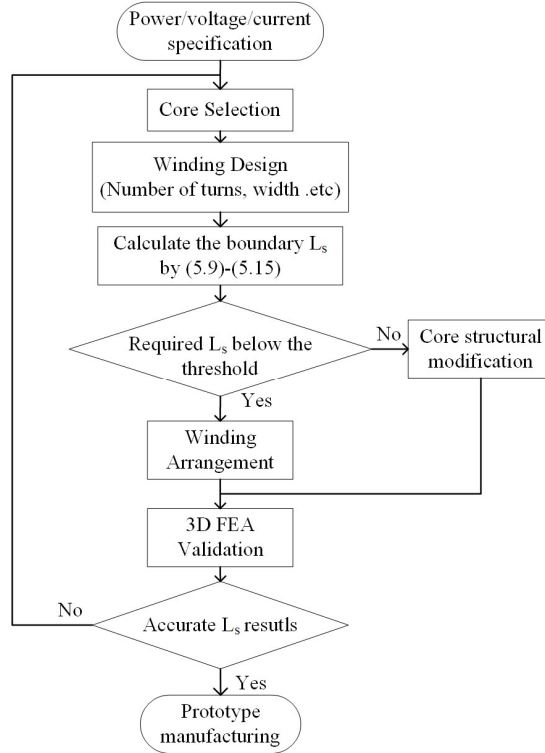


Fig. 5.2.2 The transformer magnetic integration procedures with the proposed reluctance-based evaluation strategy providing the threshold leakage inductance.

The minimum achievable L_s realized by the interleaved winding scenarios has been discussed by other researchers [161, 197]. Hence, magnetic integration process of a planar transformer with the boundary L_s is demonstrated as a case study with the proposed reluctance-based leakage inductance evaluation strategy implemented.

5.2.2 Core and winding design of the integrated two-port planar transformer

Electrical operating specification of this case study is: $P_t = 4 \text{ kW}$, $f = 50 \text{ kHz}$, $J_{\max} = 180 \frac{\text{A}}{\text{cm}^2}$, $V_{\text{dc}} = 48 \text{ V}$ and turn ratio is 1:1.

A. Core Selection

The main purpose of the core is to create a well-defined, predictable magnetic path for the flux. Core is selected based on its power handling capability, which is related to its area product variable A_p :

$$A_p = \frac{P_t \times 10^4}{K_f K_u B_m J f} = A_e \times A_w \text{ cm}^4 \quad (5.1)$$

where P_t is the rated transferred power, K_f is the waveform coefficient, for the DAB converter transferring the square waves, $K_f = 4.0$. K_u is the window coefficient, B_m is the maximum magnetic intensity in the core, J is current density and f is operating frequency according to [153]. A_p value can also be calculated from the core geometry, where A_w is the window area and A_e is the cross-sectional area. From a general estimation of the window coefficient equals to 0.6, the required A_p value is calculated as: 3.50 cm^4 . The core: ER51/38.1/25-JNP96 core with TDK_PC95 material can satisfy the demands. Reason of selecting PC95 is, it is a wide-temperature low-power consumption Mn-Zn ferrite material gathering all the benefits of PC45, 46 and 47, including low cost, simple manufacturing, excellent oxidation resistance, large residual magnetization, etc. Whereas ER shape is a common planar core shape with the advantage of high power density as its round-shape central leg and window structure can contain wider windings. The maximum magnetic intensity of the core is 0.53T. The A_e and A_w of this core is 3.18 cm^2 and 1.85 cm^2 , respectively, providing the geometrical A_p value as 5.88 cm^2 . The core geometry is sketched in Fig. 5.2.3 with its physical dimensions listed in TABLE 5.1.

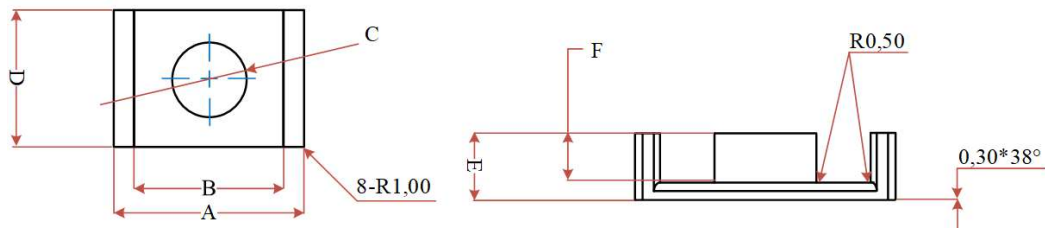


Fig. 5.2.3 The geometry of the ER51/38.1/25-JNP96 core.

TABLE 5.1

GEOMETRY PARAMETERS OF THE CORE

A(mm)	B(mm)	C(mm)	D(mm)	E(mm)	F(mm)
51.0	41.8	20.0	38.1	12.5	8.5

B. Turns of the planar winding

Winding design starts with the number of turns calculation:

$$N_p = \frac{V_{in} \times 10^4}{K_f B_{max} f A_e} = 1.44 \rightarrow 2 \quad (5.2)$$

Hence, turns of the primary and secondary winding is $N_p = N_s = 2$. Different from the wound winding, the winding in the planar transformer is in planar form. Width and depth of the printed circuit follows (5.3).

$$A = \left(\frac{I}{k \times T_{rise}^b} \right)^{\frac{1}{c}}, W = \frac{A}{t \times 1.378} \quad (5.3)$$

where A and W is the cross-section area and the width of the winding. Coefficient $k = 0.048$, $b = 0.44$ and $c = 0.725$ for the outer windings according to the IEEE IPC-2221. I is the current flowing through the winding and T_{rise} is the temperature rise. Set the T_{rise} as 35°C with the normal operating room temperature to be 25°C . The width for each turn of the surface planar winding is 8mm whereas the thickness is 3mm.

Due to the high rated operating frequency, single layer of winding with 3mm thickness can lead to severe skin effect, causing the additional temperature rise and reduction of the power transfer efficiency, as shown in (5.4).

$$depth = \sqrt{\frac{\rho}{\pi f \mu_0 \mu_r}} \quad (5.4)$$

where ρ is the resistivity, f is the frequency, μ_0 and μ_r is the permeability of the air and the relative permeability of the material. 0.5 mm conductors are paralleled in six to replace the 3 mm single conductor.

5.2.3 Accurate estimation of the equivalent magnetizing and leakage inductance

Theoretical estimations of the equivalent magnetizing inductance, the equivalent leakage inductance based on the energy and the proposed reluctance modeling strategy is demonstrated in this chapter.

A. Theoretical calculation of the magnetizing inductance

The magnetizing inductance can be calculated from (5.5) by part.

$$\mathcal{R} = \frac{l}{\mu_0 \mu_r A} \quad (5.5)$$

where l is the mean magnetic path length (MPL) and A is the cross-sectional area. Both primary and secondary windings of this planar transformer are wound on the central leg. Compared to the primary and secondary windings separately wound on two side legs, the central wound arrangement distributes have more balanced leakage flux distribution. Cross-sectional area of the central leg is usually much larger than the side leg for the planar magnetic core, central wound structure provides smaller overall reluctance compared to the side-wound structure, leading to greater leakage inductance and a reduced magnetizing inductance. This property can help achieve the accurate maximized-magnetic integration aim. The mean MPL of the core/magnetizing and the equivalent magnetic circuit is sketched as Fig. 5.2.4 and Fig. 5.2.5, respectively.

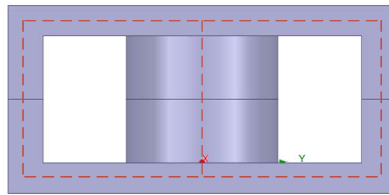


Fig. 5.2.4 Mean magnetic path in the magnetic core.

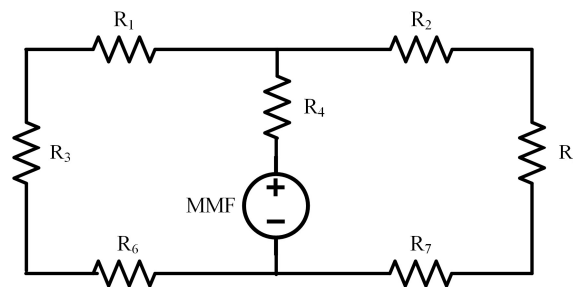


Fig. 5.2.5 The equivalent magnetic circuit of the core.

According to Fig. 5.2.3 and TABLE 5.1, calculate the reluctance by part: $\mathcal{R}_1 = \mathcal{R}_2 = \mathcal{R}_6 = \mathcal{R}_7 = 36709.56/\text{H}$, $\mathcal{R}_3 = \mathcal{R}_5 = 28894.67/\text{H}$, $\mathcal{R}_4 = 16119.28/\text{H}$. Recognize the equivalent magnetizing reluctance as the core reluctance, $\mathcal{R}_c = \mathcal{R}_4 + (\mathcal{R}_1 + \mathcal{R}_3 + \mathcal{R}_6) || (\mathcal{R}_2 + \mathcal{R}_5 + \mathcal{R}_7) = 67283.43/\text{H}$, and L_m can be calculated by (5.6): $L_m = 59.45 \mu\text{H}$.

$$L_m = \frac{N_p N_s}{\mathcal{R}_c} \quad (5.6)$$

B. Energy based leakage inductance evaluation

The 2-turn planar conductors with 0.5mm single-layer thickness planar winding are paralleled in six. The primary winding is placed at the lower position with the total thickness of b mm and secondary winding at the upper position with thickness of d mm, thickness of the gap between primary and secondary winding is c mm. Vertically, assume the magnetic field outside the coil is short-circuited by the core, and the magnetic pressure drop in the core is zero. Hence, the sectionalized winding structure with vertical MMF distribution is sketched in Fig. 5.2.6.

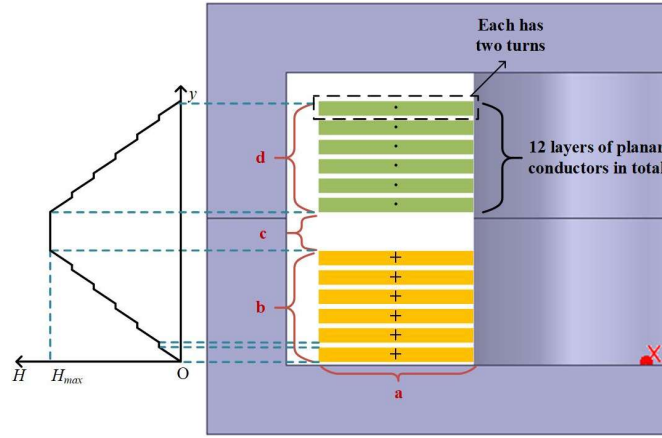


Fig. 5.2.6 The vertical MMF distribution for a planar transformer.

Define the thickness of the individual insulation layer between the winding layer as h_i , and thickness of the individual conductor layer as h_w . The relation between the magnetic field intensity H_z and the vertical geometric position $z \in (0, b)$ is represented as (5.7) where n refers to the n^{th} layer of the winding [159].

$$H(z) = \begin{cases} (n-1)\frac{I_p}{a} + [z - (n-1)(h_w + h_i)]I_p & \text{when } (n-1)(h_w + h_i) < z \leq (n-1)h_i + nh_w \\ n\frac{I_p}{a} & \text{when } (n-1)h_i + nh_w < z \leq n(h_i + h_w) \end{cases} \quad (5.7)$$

From the observation of the MMF distribution map and its equation, within the width range of the primary winding, the magnetic field intensity increases linearly with position z and reaches the maximum when $z = b$. Within the range of $(n-1)h_i + nh_w < z \leq n(h_i + h_w)$

and $b < z < b + c$, there is no current and the strength of the magnetic field maintains constant. When $z \in (b + c, b + c + d)$, where the magnetic loop encircles the secondary winding with the inverse current flow direction, the magnetic intensity starts to reduce.

The magnetic energy stored in the primary winding E_p can be represented by (5.4) to (5.6) according to Ref. [159]. With this energy, the equivalent leakage inductance can be calculated by (5.8) as: $L_{p-eq} = L_{s-eq} = 0.037 \mu\text{H}$ when $h_i = 0.2 \text{ mm}$ and $c = 0.4 \text{ mm}$, where l_w is the width of the core.

$$L_{p-eq} = \frac{1}{3} \mu_0 l_w [2h_w N_p^3 + h_i (2N_p^3 - 3N_p^2 + N_p)] \quad (5.8)$$

Note that, the L_{p-eq} calculated using this strategy is the equivalent leakage inductance referred to the definitions in previous chapters. This evaluation only considered the energy stored in the windings. Since the air has the same permeability as the copper, part of the energy is stored in the air of the window. The air-path leakage flux caused by the imperfect magnetic linking between two coils has been ignored. Estimated leakage inductance from this strategy will therefore be smaller than the actual value.

C. The proposed reluctance-based leakage inductance evaluation with air leakage flux considered

The above demonstrated energy strategy has been widely used by many researchers to evaluate or design a transformer [168-170]. Besides the energy evaluation, the equivalent leakage inductance can be calculated from the reluctance-based evaluation [171]. All these works only evaluate the leakage flux in the windings or core since the leakage flux in the air is distributed neither uniformly nor symmetrically, and the mean path length of the air leakage path hard to be quantified. Therefore, the representative length path estimation and its equivalent magnetic circuit transformation method are introduced and developed.

According to the core geometry, the MMF source is considered locating at the center of the central leg. The equivalent reluctances including the core reluctance, self-leakage reluctance, and mutual-leakage reluctance, can be recognized as connected in series or parallel with this

source. The magnetic path of the self-leakage reluctance for the primary winding consists of the path inside the core and the path in the air. The shortest possible path length encloses the coil starts from center of the central leg and passing through the outer-most edge of the primary coil. The longest path starts from the center line and passing through the inner surface of the side leg, both paths are sketched in Fig. 5.2.7.

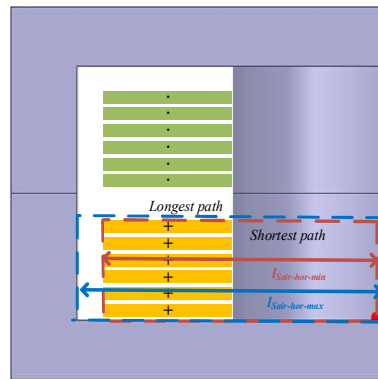


Fig. 5.2.7 The shortest and the longest (enclose the entire coil) magnetic path of the self-leakage flux.

The core-part self-leakage reluctance can be calculated identical to the core reluctance. Whereas for the air-path self-leakage reluctance, the vertical and horizontal part needs to be calculated individually. In sectionalized winding arrangement, the path length of the vertical part equals to the height of coils, which is b . Its equivalent cross-sectional area is a ring whose width measures from surface of the central leg to the outer vertical face of the coil as shown in Fig. 5.2.8(a). For the horizontal part, the path length can be calculated using the average value: $\frac{1}{2}(l_{\text{Sair-hor-mi}} + l_{\text{Sair-hor-max}})$. Its equivalent cross-sectional area equals to the side area of the cylindrical. Radius of the bottom circle can be measured from the central line to the outer surface of the winding. While the height is still calculated from the average value. Since the vertical distribution of primary coil and secondary coil is symmetrical, this height equals to half the height of the window H_{window} . The horizontal cross-sectional area is shown in Fig. 5.2.8 (b).

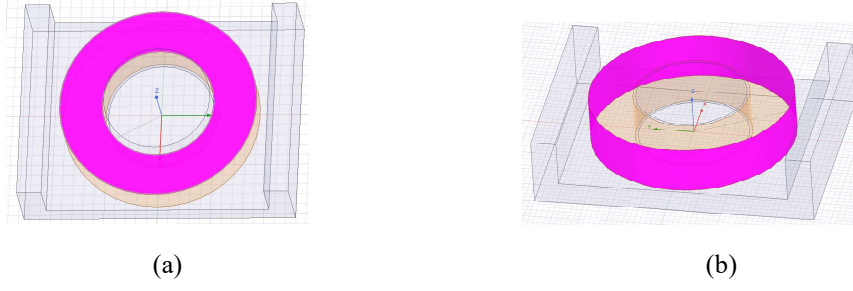


Fig. 5.2.8 The equivalent cross-sectional area. (a) The vertical air-path self-leakage reluctance, (b) The horizontal air-path self-leakage reluctance.

As the magnetic paths in the air are not distributed uniformly, a self length-representative coefficient k_s has been multiplied to the path length for the air-path reluctance calculations. Value of $k_s \in (0,1)$ because the positions closer to cores have higher magnetic lines distribution-density. In addition, many leakage flux lines did not enclose the outer edge of the conductor when entering the core. The vertical and horizontal representative self-leakage air path length is calculated as (5.9) with $k_s = 0.95$. This coefficient can be further improved according to the 3D-FEA simulation results.

$$l_{\text{Sair-hor-rep}} = k_s \times \frac{1}{2} (l_{\text{Sair-hor-min}} + l_{\text{Sair-hor-max}}) \quad (5.9)$$

$$l_{\text{Sair-ver-rep}} = k_s \times b$$

The representative path length in horizontal and vertical is: $l_{\text{Sair-hor-rep}} = 9.215 \text{ mm}$ and $l_{\text{Sair-ver-rep}} = 8.075 \text{ mm}$. Calculate their reluctance by part: $\mathcal{R}_{\text{Score-central}} = 6294.19 / \text{H}$, $\mathcal{R}_{\text{Score-bottom}} = 29272.7 / \text{H}$, $\mathcal{R}_{\text{Sair-ver-rep}} = 8.145 \times 10^6 / \text{H}$, and $\mathcal{R}_{\text{Sair-hor-rep}} = 7.42 \times 10^6 / \text{H}$. The total self-leakage reluctance can be calculated as (5.10): $\mathcal{R}_{\text{self}} = 15.6 \times 10^6 / \text{H}$. Whereas the self-leakage inductance L_{s11} in L_{st} can be calculated as (5.11): $L_{s11} = 0.256 \mu\text{H}$. The air-path leakage reluctance contributed more than 90% of the resultant self-leakage reluctance. In conventional transformer design processes, leakage inductances are supposed to be as small as possible, hence the air-path leakage can be neglected. However, in the integrated transformer, air-path leakage should be estimated accurately to quantify the power transfer capability.

$$\mathcal{R}_{\text{self}} = \mathcal{R}_{\text{Score-central}} + \mathcal{R}_{\text{Score-bottom}} + \mathcal{R}_{\text{Sair-hor-rep}} + \mathcal{R}_{\text{Sair-ver-rep}} \quad (5.10)$$

$$L_{s11} = \frac{N_p^2}{\mathcal{R}_{\text{self}}} \quad (5.11)$$

The previous shortest path refers to the shortest length that encloses the entire coil, substitute the vertical length of the shortest path by the single layer thickness, and the cross-sectional area by the average ring provides highly approachable results, but the complexity of the calculation will be increased significantly. Similarly, sketching the shortest and the longest path of the mutual leakage flux path in (5.11). The shortest path in the air starts from uppermost surface of the primary winding and passes through the lowermost surface of the secondary winding. The longest path starts from the uppermost surface of the secondary winding and passes through the lowermost surface of the primary winding.

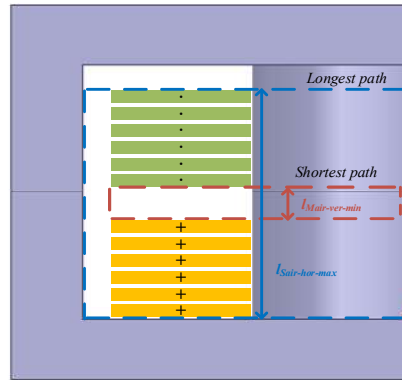


Fig. 5.2.9 The shortest and the longest magnetic path of the mutual-leakage flux.

The representative length of the mutual leakage path, however, should not be calculated from the average of values. As the route of the longest mutual-leakage flux path is close to the surface of the core, flux will prefer to take the path with lower reluctivity. Leading to the magnetic flux density along the longest path much lower than the one along the shortest path. This theory can be validated by the flux line distribution map in the later chapter. Hence, length of the shortest path is more representative. Define the representative path length of the air-part mutual-leakage flux as the shortest path $l_{\text{Mair-ver-min}}$ multiplied by a mutual representative coefficient k_m . Since the mean path of the mutual leakage inductance path will be greater than the minimum

value, k_m will be greater than 1, this theory can be validated by the flux line simulation as well. The horizontal and vertical air-part path lengths are calculated as (5.12).

$$l_{\text{Mair-hor-rep}} = k_m \times 2 \times l_{\text{Mair-hor-min}} \quad (5.12)$$

$$l_{\text{Mair-ver-rep}} = k_m \times c$$

When $k_m = 1.2$, $l_{\text{Mair-hor-re}} = 20.4 \text{ mm}$, $l_{\text{Mair-ver-rep}} = 0.48 \text{ mm}$. Calculate reluctance by part: $\mathcal{R}_{\text{Mcore-central}} = \frac{307.04}{\text{H}}$, $\mathcal{R}_{\text{Mair-ver-rep}} = 0.502 \times \frac{10^6}{\text{H}}$, $\mathcal{R}_{\text{Mair-hor-rep}} = 16.43 \times \frac{10^6}{\text{H}}$. The mutual-leakage reluctance and inductance, $\mathcal{R}_{\text{mutual}}$ and L_{s12} in L_{st} can then be calculated as (13)-(14): $\mathcal{R}_{\text{mutual}} = 16.93 \times \frac{10^6}{\text{H}}$ and $L_{s12} = 0.236 \text{ } \mu\text{H}$.

$$\mathcal{R}_{\text{mutual}} = \mathcal{R}_{\text{Mcore-central}} + \mathcal{R}_{\text{Mair-hor-rep}} + \mathcal{R}_{\text{Mair-ver-rep}} \quad (5.13)$$

$$L_{s12} = \frac{N_p N_s}{\mathcal{R}_{\text{mutual}}} \quad (5.14)$$

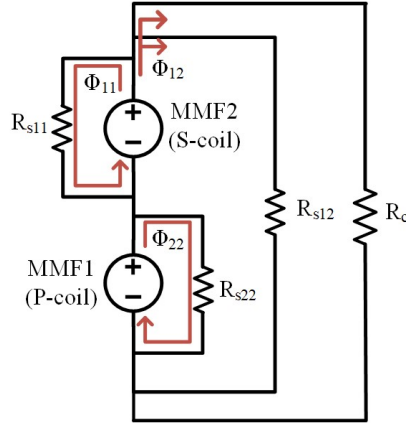


Fig. 5.2.10 Equivalent magnetic circuit of the transformer.

The self and mutual-leakage inductance should be transformed to the port-equivalent leakage inductance. This step is coordinated by the equivalent magnetic circuit sketched in Fig. 5.2.10. According to the coil-based inductance matrix, the flux ϕ_{12} linking the primary and secondary coil, is recognized as the mutual flux, no matter the flux is entirely in the core or partially in the air. The mutual reluctance is then: $\mathcal{R}_{\text{mutual}} || \mathcal{R}_c = 67017.1 / \text{H}$, $L_{\text{mutual}} = 59.69 \text{ } \mu\text{H}$. Define

the flux linking only primary and secondary coil as the ϕ_{11} and ϕ_{22} , respectively. The coupling coefficient M can be calculated by (5.14) as 0.99786.

$$M = \frac{\phi_{12}}{\phi_{11} + \phi_{12}} = \frac{\frac{MMF_1 + MMF_2}{\mathcal{R}_{\text{mutual}} \parallel \mathcal{R}_c}}{\frac{MMF_1}{\mathcal{R}_{\text{self}}} + \frac{MMF_1 + MMF_2}{\mathcal{R}_{\text{mutual}} \parallel \mathcal{R}_c}} \quad (5.15)$$

With the coefficient M , model in Fig. 5.2.10 can be transformed to T-shape model, whereas the equivalent leakage inductance in the primary side can be deduced: $L_{p\text{-eq}} = \frac{L_{m\text{-eq}}}{M} (1 - M) = 0.128 \mu\text{H}$. The final result of this strategy is almost 4 times larger than the energy based evaluation. Which is brought by the consideration of the mutual-leakage and energy distributed in the air. It is proved that, when the leakage flux is not significant, the flux leaked in the air can not be ignored as these leakage is the dominant element of the resultant reluctance.

The evaluation shows that, for the two-port planar transformer, the port-equivalent leakage inductance is more relevant to the air-part vertical representative path length of the self-leakage reluctance when the core structure is not modified. This result can hence provide the winding arrangement scenarios instructions for the magnetic integration processes. For the sectionalized winding arrangement, reducing the single-layer thickness of the insulation and increasing the gap between two coils can lead to the reduced self-leakage reluctance and increased mutual-leakage inductance. Providing a reduced coupling coefficient. The boundary leakage inductance can then be achieved by this winding scenario. To validate this conclusion, reduce the insulation thickness to 0.05 mm and increase the gap thickness to 3.9 mm. The new and the previous arrangement are represented in Fig.5.2.11(a) and (b).



Fig.5.2.11 Two winding arrangements for the validation of the proposed, (a) Insulation thickness $h_i = 0.05$ mm, thickness of the gap between two coils is $h_g = 3.9$ mm. (b) Insulation thickness $h_i = 0.2$ mm, thickness of the gap between two coils is $h_g = 0.4$ mm.

Repeat the steps of (5.9) to (5.15) with the same representative coefficients. The coupling coefficient and the leakage inductance are: $M' = 0.99705$ and $L'_{p-eq} = 0.176 \mu\text{H}$. Also calculate the inductances using the previous mentioned energy evaluation, the results are listed in TABLE 5.2.

The proposed strategy can be validated in the minimum leakage inductance arrangement as well. For the interleaved winding arrangement, air-part vertical representative path length of the self-leakage reluctance is the thickness of the single-layer winding, which is relatively fixed. Increasing the insulation thickness provides larger mutual-leakage reluctance and larger coupling coefficient. This trend results consistent with the empirical winding arrangement aimed to minimize the leakage loss. The estimations and the conclusions are validated by the FEA simulation in the next chapter.

TABLE 5.2
THEORETICAL RESULTS FOR TWO STRUCTURES WITH DIFFERENT STRATEGIES

	Energy evaluation	Proposed strategy
Insulation=0.2 mm Gap=0.4 mm	0.037 μH	0.128 μH
Insulation=0.05 mm Gap=3.9 mm	0.030 μH	0.176 μH

5.3 A Radially symmetrical star-shape core multi-winding transformer with controllable magnetic integration for N -port MAB converters

For the MT core scenarios that rely on sharing the same flux path by all the windings to maintain the port consistency, air gaps need to be inserted into the core structure, or magnetic shunts need to be inserted between the windings if large leakage inductances are required to achieve the magnetic integration [157, 159, 172]. However, once shunt and air gaps are applied, consistency between the ports becomes hard to promise. In addition, leakage estimation of these MT scenario is a tough work.

To remove the conflict between port consistency and magnetic integration, a novel RSSC structure with split winding HFMT is developed for the generalized N -port MAB converter. Different from the conventional MT configuration, the proposed HFMT scenario divides each port-winding into two parts: major windings wound on the central pillar and minor part on the side pillar. Only central pillar flux path is shared by all the coils, while the side pillar loop provides a leakage flux path with long path length to achieve the integration required large leakage inductances. The value of the leakage inductance can be controlled by adjusting the integration control parameters, achieving the controllable integration. Beside these integration control parameters, vertical air gaps are inserted in the central pillar as the flux barrier to balance the flux and guarantee the port consistency. Detailed novelty of this chapter is listed below.

- a) Proposed a RSSC structure to achieve magnetic integration for the generalized MAB converters. With the novel core structure design, the total magnetizing inductance path length of an integrated N -port HFMT will be shorter than a separated MT. Integrated scenario can thus providing higher system power density than a separate MT with series inductors scenario.
- b) Deduction of the leakage inductance shows its value is highly related to the turns of side pillar winding and the side-pillar-loop reluctance. Hence, proposed scenario utilizes the length of the extension legs, thickness of the horizontal air gap on the central and side pillars, winding distribution ratio and turns of winding to adjust the leakage inductances within a wide range. These parameters provide fully controllability for the leakage

inductances. Leakage flux of one port can even be controlled individually by adjusting the corresponding side pillar parameters if necessary. These parameters can provide more flexibility for the transformer and the MAB converter than all the existed MT solutions.

- c) Port consistency, which refers to the consistency of equivalent port leakage inductance, is guaranteed by inserting the vertical air gaps at the central pillar. Once flux paths are balanced by these flux barriers, accuracy of the self, mutual, magnetizing and leakage inductance are also improved. Errors between calculation results and the finished values can be minimized.
- d) A four-port cross-shaped HFMT is designed for a QAB converter, as a case study to demonstrate its controllable magnetic integration capability. Compared to other MT cores, this core also reduced the complexity of design and is good in manufacturability. As the core can be manufactured by part and assembled instead of integrated metal printing. This scenario is more suitable for the large power applications when the size of the core will be significant, and the price of printing could be expensive.

5.3.1 Integration theory for the N-port RSSC HFMT

Configuration of the proposed RSSC consists of a central pillar and N side pillars (limbs), where N always equals to the port number of the MAB converter. These side pillars are evenly distributed around the central pillar with angle between two adjacent pillars equals to $(\frac{360}{N})^\circ$, and they are physically connected to the central pillar through the extension legs. Cross-sectional area of one side pillar equals to $\frac{1}{N}$ of the central in most cases.

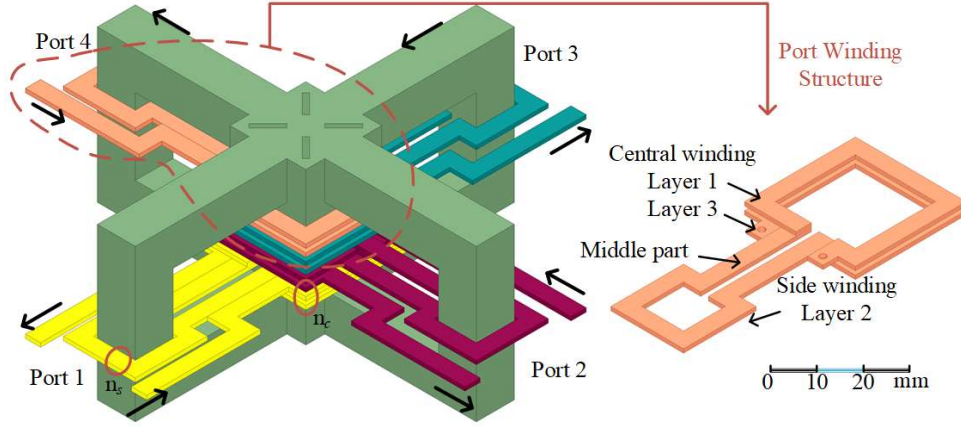


Fig.5.3.1 3D overall and port winding configuration of a four-port example from the proposed RSSC HFMT

For each port winding, the majority turns are located on the central pillar with its number of turns defined as n_c , while the rest turns n_s are wound on the side pillar. A four-port configuration of the proposed HFMT is shown in Fig.5.3.1. Horizontal air gap is inserted in the central pillar to adjust the magnetizing inductance, and four vertical air gaps are inserted in the central pillar to balance the flux, whose detailed theory is introduced in later chapters. Once port is consistent, accurate inductance estimation can be realized.

A. Magnetic circuit analysis and inductance definition

Self and mutual inductance of an N -port HFMT can be represented by a $N \times N$

$$\text{matrix: } \mathbf{L}_{\text{self-mutual}} = \begin{bmatrix} L_{1,1} & L_{1,2} & \cdots & L_{1,j} \\ L_{2,1} & L_{2,2} & \cdots & L_{2,j} \\ \vdots & \vdots & \ddots & \vdots \\ L_{i,1} & L_{i,2} & \cdots & L_{i,i} \end{bmatrix}. \text{ With unity turn ratios and port consistency, all}$$

the self inductance $L_{i,i}$ of this HFMT are with identical values, and the same for all the mutual inductance $L_{i,j}$ ($i \neq j$), where $i, j \in \{1, \dots, N\}$. Theoretical values of the elements in the matrix can be calculated by the flux linkages as: $L = \frac{n\Phi}{I} = \frac{n \text{MMF}}{I \mathcal{R}}$. Whereas n is the turns of winding and reluctances can be obtained from the physical structure of the core. Due to the split of the windings, equivalent magnetic circuit of the transformer consists of $2N$ MMF sources, can be sketched as Fig.5.3.2. In which, \mathcal{R}_s refers to the resultant reluctances of one side loop, which contains two extension legs and one side pillar, while \mathcal{R}_c refers to the resultant reluctances of the central pillar.

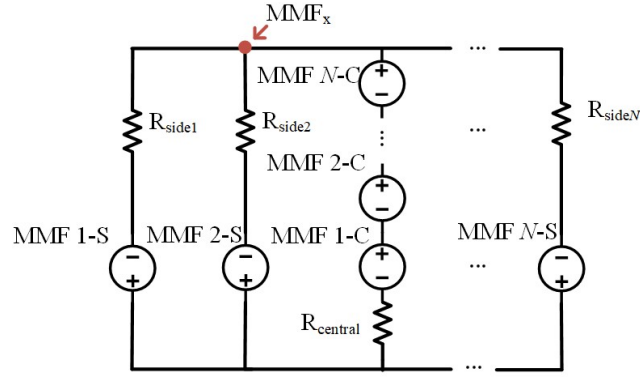


Fig.5.3.2 Equivalent magnetic circuit of the proposed RSSC HFMT

To calculate self-mutual inductances, all the current excitations are removed except Winding 1: MMF_1 , flux passing through the central pillar equals to the sum of the flux passing through all the side pillars. Use Kirchoff's Law to calculate the equivalent MMF at the parallel node highlighted with red in Fig.5.3.2 and define the inductances.

$$\frac{MMF_x}{\frac{1}{N} \mathcal{R}_s} + \frac{MMF_x + MMF_{1s}}{\mathcal{R}_s} = \frac{MMF_{1c} - MMF_x}{\mathcal{R}_c} \quad (5.16)$$

$$MMF_x = \frac{\mathcal{R}_s MMF_{1c} - \mathcal{R}_c MMF_{1s}}{N\mathcal{R}_c + \mathcal{R}_s}$$

Self inductance: The current I_1 causing the magnetic flux linkage passing through whole Winding 1, which includes the Central Coil 1 and Side Coil 1; that is also linking it, is defined as the self inductance L_{self} :

$$L_{1,1} = \frac{\frac{n_c(MMF_{1c} - MMF_x)}{\mathcal{R}_c} + \frac{n_s(MMF_x + MMF_{1s})}{\mathcal{R}_s}}{I_1} \quad (5.17)$$

Mutual inductance: The current I_1 causing the magnetic flux linkage passing through Winding 2, which includes the Central Coil 2 and Side Coil 2, is defined as the mutual inductance L_{mutual} :

$$L_{12} = \frac{\frac{n_c(MMF_{2c} - MMF_x)}{\mathcal{R}_c} + \frac{n_s MMF_x}{\mathcal{R}_s}}{I_2} \quad (5.18)$$

Leakage and magnetizing inductances: Since leakage flux inside the core and air gaps are significant comparing to the ones in the window-air and windings, mutual inductance can be approximated as the magnetizing inductance, whereas leakage inductance L_s can be obtained by $L_s = L_{\text{self}} - L_{\text{mutual}}$. Represent (5.17) and (5.18) by (5.16), self, mutual or magnetizing and leakage inductances is calculated in (5.19) and (5.20).

$$\begin{cases} L_{\text{self}} = \frac{\mathcal{R}_c(N-1)n_s^2 + \mathcal{R}_s(Nn_c^2 + 2n_cn_s + n_s^2)}{\mathcal{R}_s(n\mathcal{R}_c + \mathcal{R}_s)} \\ L_{\text{mutual}} = \frac{-n_s^2\mathcal{R}_c + \mathcal{R}_s(2n_cn_s + Nn_c^2)}{\mathcal{R}_s(N\mathcal{R}_c + \mathcal{R}_s)} \end{cases} \quad (5.19)$$

$$L_s = \frac{n_s^2}{\mathcal{R}_s} \quad (5.20)$$

According to (5.20), the leakage inductance is highly depending on the side loop reluctance \mathcal{R}_s and has no relationship with the number of total ports N . Length of the extension leg, winding distribution ratio and turns, side pillar horizontal air gap, these parameters with the ability of changing the \mathcal{R}_s and n_s would be the major leakage inductance control parameters.

A. Flux density saturation evaluation

Since the proposed HFMT is operating in a MAB converter system under phase shift control, relationship between phase shift and transferred power is represented as (5.21) when the most fundamental phase shift control strategy: single phase shift (SPS) modulation is applied.

$$P_{\text{SPS}} = \frac{aV_iV_jD_{o,i,j}(1 - D_{o,i,j})}{2fL} \quad (5.21)$$

where a is the turn ratio of the transformer, for a port-consistent HFMT, $a = 1$. V_i and V_j is the input and output voltage, respectively, $D_{o,i,j}$ is the outer phase shift between input and output ports, f is switching frequency, L is the inductance of the series connected inductor. For the integrated HFMT, L should be substituted by leakage inductance.

With winding located on the side pillars, the operation may lead to the saturation of one individual side-pillar when large output voltage or phase shift occurred at this port. Hence, flux

density of the side pillar should be evaluated to prevent this saturation. For conventional two-port transformer, flux density can be calculated according to the turns of winding as (5.22).

$$B_{\max} = \frac{V_{\text{dc}}}{n_p K_f f A_e} \quad (5.22)$$

where V_{dc} is the output voltage, K_f is the waveform coefficient, for the MAB converter, input and output voltage are square waves, $K_f = 4$. n_p is the turns of the primary winding, and A_e is the cross-sectional area. When applied to HFMT, $n_p A_e$ is replaced by $(n_c A_c + n_s A_s)$, where A_c and A_s is the cross-sectional area of central and side pillar, respectively. Since summation of the side pillars cross sectional areas equal to central cross-sectional area: $n A_s = A_e$, (5.22) can be rewritten as (5.23). $B_{\max,c}$ refers to the maximum flux density of the central pillar during operation, and this flux density is not related to the phase shift.

$$B_{\max,c} = \frac{N V_{\text{dc}}}{K_f A_c f (N n_c + n_s)} \quad (5.23)$$

Similarly, represent the maximum flux density of side pillar in (5.24), this density is affected by the phase shift.

$$B_{\max,s} = \frac{V_{\text{dc}}}{K_f A_s f} \left[\frac{1 - \frac{(N-1)D_{o,i,j}}{2}}{(N n_c + n_s)} + \frac{2(N-1)D_{o,i,j}}{N n_s} \right] \quad (5.24)$$

From (5.23) and (5.24), it is obvious that when phase shift is 0, $B_{\max,c} = B_{\max,s}$. If power is transferred between the ports ($D_{o,i,j} \neq 0$), $B_{\max,s}$ will always greater than $B_{\max,c}$. Hence, $B_{\max,s}$ should be restricted below saturation flux density B_{sat} to prevent the core from saturation by limiting the maximum phase shift during the operation of the MAB converter. Eqn (5.24) shows $B_{\max,s}$ is independent with A_s , n_s , n_c and have no concern with the air gap or the extension leg. This feature provides the indication of the design procedures, A_s and A_c can be selected in prior to satisfy the B_{sat} restriction, whereas the subsequent leakage control through adjusting dimension of the air gaps or extension legs will not change the $B_{\max,s}$ condition.

Empirically, traditional magnetic core with central-side split structure, cross-sectional area of the central pillar is equal to the sum of the side ones to balance the flux entering and exiting the central pillar. Nevertheless, for this RSSC, this equality may not strictly adhere to. Since saturation of the side pillar will come easier than the central, A_s can be expanded slightly beyond $\frac{1}{N}$ to provide more tolerance of the saturation. By adjusting these parameters, leakage inductance of the proposed HFMT can be controlled flexibility without changing the cross-sectional area of the core calculated from AP method.

B. Volume reluctance of the proposed integrated HFMT

Volume of integrated core can be generally calculated as:

$$Vol_{core} \approx A_c l_c + N A_s l_s \quad (5.25)$$

where l_c and l_s is the mean path length of the central pillar and side loop, respectively. To handle the same power, separate structure requires an MT and N individual series inductors. Inductance of each series inductor $L_{series} = L_s$ and magnetizing inductance of the separate MT, $L_{MT} = L_m$. Suppose turns of winding for the series inductor $n_{series} = n_s$, to achieve the same reluctance, mean path length L_{series} and cross-section area A_{series} should satisfy $\frac{l_{series}}{A_{series}} = \frac{l_s}{A_s}$. Therefore, total volume of N series inductors can be represented as:

$$Vol_L \approx N \frac{l_s}{A_s} A_{series}^2 \quad (5.26)$$

To achieve at least the same flux density saturation restriction as the integrated HFMT, the minimum possible A_{series} should be A_s . As a result, the minimum overall volume of N separate series inductors are equal to the sum of the side-pillar volume of integrated HFMT: $N A_s l_s$. While for the separate MT, mean path length l_{MT} will always be greater than l_c if cross-sectional area of MT $A_{MT} = A_c$, since the L_m of the integrated HFMT shared part of the flux path with the L_s . For these reasons, the proposed HFMT can achieve higher power density compared to the separate structures.

5.3.2 A four-port case study of the proposed HFMT scenario applied in a QAB converter

A. Core configuration of the proposed HFMT

When the proposed integrated HFMT is applied in a QAB converter, the cross-shape core can be regarded as two pair of EE-shape planar cores orthogonally conjugated at a common central pillar. Geometry of the core is sketched as Fig.5.3.3(a) in 3D view, Fig.5.3.3 (b) in 2D view. Whereas geometry parameters are listed in the TABLE 5.3.

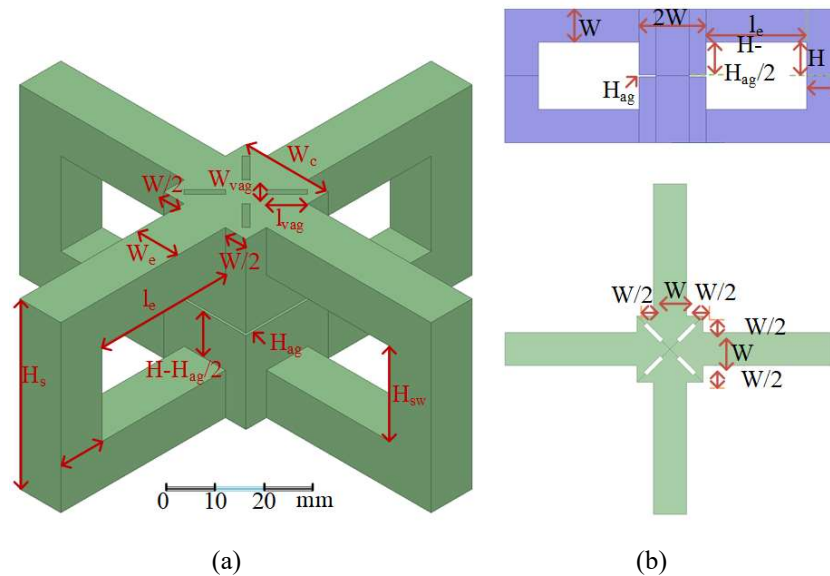


Fig.5.3.3 3D and 2D view of the four-port cross-shape core. (a). 3D configuration of the core. (b). 2D front, side views, and top view of the core.

TABLE 5.3

GEOMETRY PARAMETERS AND SPECIFICATIONS OF THE CROSS-SHAPE CORE

Symbol and value	Definition
$W_s = W$	Width of the side pillar square
$H_s = 2(H + W)$	Height of the side pillar
$H_{sw} = 2H$	Height of the side pillar window
$l_e = l_e$	Length of the extension leg
$W_e = W$	Width of the extension leg square
$W_c = 2W$	Width of the central pillar square
$H_{ag} = H_{ag}$	Thickness of the central pillar air gap
$H_{ag,s} = H_{ag,s}$	Thickness of the side pillar air gap
$W_{vag} = W_{vag}$	Width of each vertical flux barrier
$l_{vag} = l_{vag}$	Length of each vertical flux barrier

The cross-shape core has one central pillar and four side pillars connected by eight extension legs. Cross-sectional shape of the central and side pillars are squares to uniform the winding on it. Cross-sectional shape of the extension leg is the same as the side pillar to homogenize the flux density distribution along the side loop flux path. Using the parameters in TABLE 5.3 to represent the side loop reluctance \mathcal{R}_s and central pillar reluctance \mathcal{R}_c .

$$\mathcal{R}_s = \frac{2H + W}{W^2 \mu_0 \mu_r} + 2 \left(\frac{l_e + \frac{W}{2}}{W^2 \mu_0 \mu_r} + \frac{W}{2W^2 \mu_0 \mu_r} \right) \quad (5.27)$$

$$\mathcal{R}_c = \frac{H_{ag}}{(2W)^2 \mu_0} + \frac{2H - H_{ag} + W}{(2W)^2 \mu_0 \mu_r} \quad (5.28)$$

where μ_0 and μ_r is the permeability of air and core material, respectively.

B. Winding configuration of the proposed HFMT

The four-port transformer has four port windings, each winding has n_c turns of central coil placed on the central pillar, and n_s turns on the side pillar. Ratio between the turns of winding on central and side pillar is defined as the distribution ratio: $S = \frac{n_c}{n_s}$, $S \in [1, +\infty]$. Central and side coils are connected in series through an additional middle part. A winding arrangement example of $n_s = 1$ and $n_c = 2$ is sketched in Fig.5.3.1. Configuration of the winding can be variable according to the length of the extension leg. If l_e is narrower than twice of the winding width, central coils could be connected to the side ones directly without middle part. Since the winding configuration in the proposed HFMT can be regarded as the planar windings, its length and thickness can be calculated by the external printed planar winding equations (5.29).

$$A = \left(\frac{I}{k \times T_{rise}^b} \right)^{\frac{1}{c}}, W = \frac{A}{t \times 1.378} \quad (5.29)$$

where $k = 0.024$, $b = 0.44$, and $c = 0.725$ are constants resulting from curve fitting to the IPC-2221 curves.

C. Air gap configuration of the proposed HFMT

According to the core geometry in Fig.5.3.3, four vertical flux barriers and one horizontal air gap are inserted in the central pillar. These barriers have rectangle cross-shape are distributed evenly on two diagonal lines of the central square, thoroughly running through the central pillar.

The function of these barriers is to rectify the mean path length of the flux lines linking two adjacent side pillars. Protruding corners of the central pillar provide shortcuts for the flux lines. With these shortcuts, the average flux path length for a pair of adjacent pillars will be shorter than the length of one opposite pair. Instead of passing the central point or vertices of the central square, flux lines can go diagonally through the vertical plane as shown in the Fig.5.3.4(a). This phenomenon can lead to the unbalance between reluctances $\mathcal{R}_{i,j(i \neq j)}$, and further resulting in the inconsistency of the mutual inductances $L_{i,j(i \neq j)}$ and leakage inductance L_S .

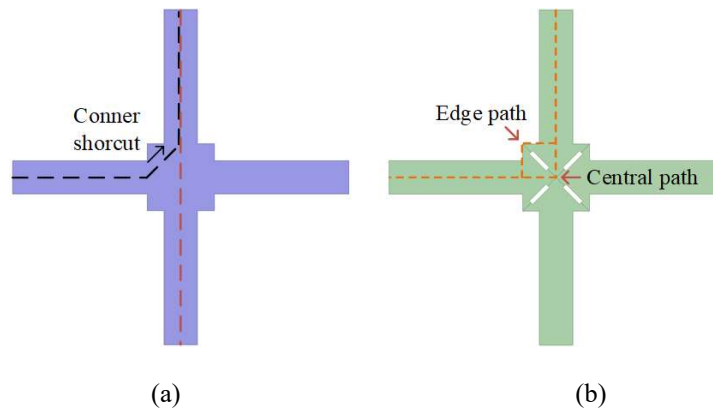


Fig.5.3.4 Mean flux paths, (a). without flux barriers between two adjacent pillars (black) and opposite pillars (red). (b) with flux barriers between two adjacent pillars (orange).

Once flux barriers are inserted in the central pillar, flux lines previously taking shortcuts are forced diverting to the central-point route or the outer edge route as shown in the Fig.5.3.4(b). Theoretically, these flux barriers should start from the central point and extended to the edges of the square to force as many unbalanced routes diverting to edge or central paths as possible. For the practical core assembling consideration, length of these gaps is restricted to increase the physical linking strength of the core structure. Effectiveness of the barriers are validated by the flux line simulations in the later chapters.

Different from the barriers, horizontal gaps in central pillar are inserted to adjust the reluctance of the main flux path. Through this adjustment, magnetizing inductance, ratio of the flux entering the main flux path and leakage flux path are also affected, thus slightly influence the leakage inductance. According to (5.20), horizontal air gaps in the side pillar is a leakage inductance control parameter. However, inserting air gaps in side pillars brings an aggressive reduction of the leakage inductance, which is analyzed in the 2D simulation. In QAB case study, side air gaps are not applied.

D. Comparison for the proposed HFMT and other MT scenarios

Since the proposed core configuration is developed from the EE-shaped planar core configuration, its benefit is inherited from the planar core when compared to the conventional shell-typed MT. These benefits include: high power density, high efficiency, good heat condition and parameter stability that promises the accuracy of the designed leakage inductance. As the aim of the magnetic integration is to achieve higher overall system power density, shell-typed core is rather large in volume and heavy due to its round wounded winding configuration. In on-board applications, this configuration is replaced by the planar core transformer.

In this research, there several reasons of the proposed scenario are compared to a separate EE-shaped-core MT scenario but not an integrated EE-based MT version with all the windings placed in the central pillar. First, integrated EE MT configuration can not achieve large leakage inductance shunt are not inserted in the structure. Since in this scenario, all the flux path inside the core forms the magnetic inductance paths, whereas leakage paths only exist in the air. If wide air gaps are inserted in the main flux path, leakage inductance dose increase, however, efficiency will decrease immediately. Second, integrated EE scenario can not achieve controllable magnetic integration. Once shunts are inserted between windings, adjusting the leakage inductance will be significantly complicated. As shunt-controlled leakage inductance is coupled with the port consistency and magnetizing inductance, achieving the aimed leakage inductance requires multiple iterative design cycle to maintain the aimed magnetizing inductance and rebalance the port consistency. Quantified volume and operating comparison between EE separate scenario and proposed HFMT are provided in the next two chapters.

In MAB converter, the majority fault condition refers to the short circuit due to the overcurrent. This short circuit mainly appeared at the port windings and the connection points of MT. Probability of this failure depends on the insulation between adjacent coils and welded joints. For the short circuit fault, reduced number of components and physical coupling between components in integrated scenario can promote the reliability of the converter system. As the reliability of the individual component has remained the same. With low probability, open circuit fault could also happen at the nodes of MT. For this fault, there is no reliability difference between integrated and separate scenario. Hence, the overall reliability of the system is regarded as improved comparing to the nonintegrated scenario.

5.3.3 Impact of the magnetic integration control parameters and generalized design procedures for the proposed RSSC HFMT

Magnetic integration control parameters contain core-geometry related parameters: length of the extension legs, thickness of horizontal air gap in central and side pillars, and winding related parameters: winding distribution ratio, and turns of windings. Whereas flux barrier is regarded as a flux balancing component. To straightforwardly show the relationship between parameters and inductances, initial parameters aimed to satisfy a set of specific electrical specifications listed in the TABLE 5.4 is applied to the case study core.

TABLE 5.4
ELECTRICAL SPECIFICATIONS OF THE FOUR-PORT CROSS-SHAPE HFMT

Symbol	Definition	Value
P_t	Rated transferred power	10 kW
V_{in}	Rated input voltage	100 V
J_{max}	Maximum current density	180 A/cm ²
$n_1:n_2:n_3:n_4$	Transformer turn ratio	1:1:1:1
K_u	Assumed filling factor	0.2
f	Rated operating frequency	50 kHz

All the other parameters are regarded as initial values when demonstrating the control capability of one specific magnetic integration control parameter. Initial dimension of the core is calculated by the AP method in (5.1) [153].

The core material is selected to be TDK_PC95, that is commonly used in the HF transformer designed to satisfy high power density. The turn ratio is set as 1:1:1:1 for the port-consistency consideration. Final geometry parameters of this case study example are shown in the TABLE 5.5.

TABLE 5.5
INITIAL GEOMETRY PARAMETERS OF THE CORE

W	H	H_{ag}	l_e	A_e	A_w
10 mm	10 mm	0.5 mm	30 mm	4 cm ²	6 cm ²

Calculate the total windings required for one port winding according to Faraday's Law. Since in this transformer, turns of windings are distributed on both side and central pillar, which has different cross-sectional area, the turns calculation has been modified from (5.30) to (5.31). And the results of (5.31) is $4N_c + N_s \approx 9.43$.

$$n_p = \frac{V_{dc}}{K_f B_{max} f A_e} \quad (5.30)$$

$$V_{dc} = K_f B_{max} f n_c A_c + K_f B_{max} f n_s A_s \quad (5.31)$$

Initially, three turns of winding are positioned on the central pillar $n_c = 3$ as the first, third and fourth turns of winding, and one $n_s = 1$ is positioned on the side pillar as the second turn. Although $n_c = 2$, $n_s = 2$ and $n_c = 1$, $n_s = 6$, winding distribution also satisfies the winding calculations, the low winding coupling coefficient makes these two scenarios ineffective in practical transformer use.

According to the discussions in Chapter II 5.3.2, volume of the inductors in EE-separate scenario equals to the overall volume of the side pillars in HFMT scenarios, which is 40 cm³. Whereas for the EE-shaped MT, A_c' and A_w' are the same as RSSC HFMT to handle the required power, A_s' is half of A_c' , and horizontal pillar has the same cross-sectional area as A_s' . Final geometry parameters of this case study example are shown in the TABLE 5.6, whereas the 3D configuration is shown in Fig. 5.3.5.

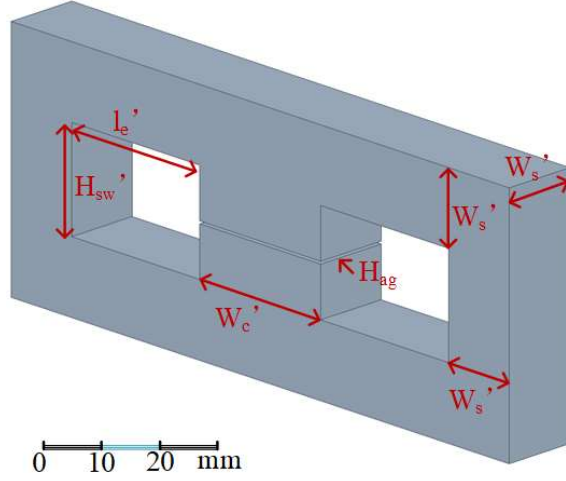


Fig. 5.3.5 3D core configuration of the EE separate scenario

TABLE 5.6

CORE GEOMETRY PARAMETERS OF THE SEPARATE EE CORE

W_s'	H_{sw}'	l_e'	W_c'	H_{ag}'
$10\sqrt{2}$ mm	20 mm	30 mm	$20\sqrt{2}$ mm	0.5 mm

The core volume of EE scenario is calculated as 52.97 cm^3 according to the model and configuration. Overall volume for the separate scenario is hence 92.97 cm^3 . For the proposed HFMT, this volume is 72 cm^3 , which provided 22.56% core reduction. With magnetic integration, wires are no longer required to connect the series inductors and MT, which provides additional reduction of space for the entire system. With the RSSC configuration, multiple windows can provide more space to distribute the windings.

Through the Steinmetz's equation, maximum core loss can be estimated under maximum flux density condition [198].

$$P_v = C_m f^X B^Y \quad (5.32)$$

where P_v is the time average power loss per unit volume (m^3), f is frequency, B is flux density, C_m , X and Y are named as Steinmetz coefficients that are material parameters generally found empirically from its B-H hysteresis curve. Maximum core loss for this cross-shaped core is 84.73 W . Copper loss for the windings when $n_c = 3$, $n_s = 1$ is 48.96 W . Hence,

the theoretical efficiency for the integrated scenario is $\eta_{int} = 98.66\%$. Do the same calculation for the EE MT scenario. With the same material, its core loss is 62.33 W and its copper loss is 27.85 W. Estimated efficiency for the separate scenario is 99.07%. Results show that the proposed scenario can maintain the efficiency at an acceptable level.

A. Length of the extension legs

Length of the extension legs l_e is proportional to the \mathcal{R}_s and is not related with \mathcal{R}_c . Fix all the other parameters and increases the l_e from 10 mm to 100 mm, nonlinear attenuation is observed for both self and mutual inductance. Relationship between self, magnetizing (mutual), leakage inductance, and extension length l_e is sketched in the Fig.5.3.6.

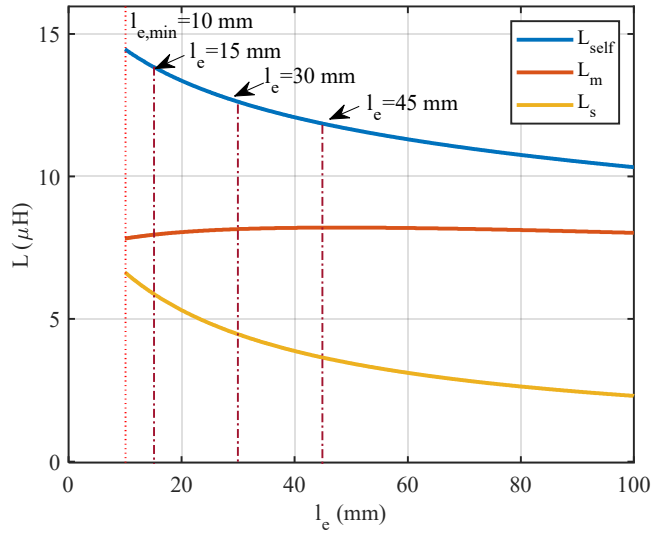


Fig.5.3.6 Relationship between extension leg length l_e and self, magnetizing(mutual), leakage inductances.

Longer l_e brings greater \mathcal{R}_s , comparing to the initial parameters, 50% increase of the l_e causes 18.6% reduction of L_s , whereas 50% decrease causes 31.8% augmentation of the L_s . This evidence proves l_e can be regarded as a major magnetic integration control parameter. However, extension length has an immediate impact on the overall volume of the HFMT. 50% change of the length will lead to a huge reduction of the power density. As a consequence, this parameter is better adjusting within small deviations from its initial value.

B. Distribution ratio and truns of windings

Capability of distribution ratio is firstly examined with n_s fixed as 1. Theoretically, both self and mutual inductance increases when S increased. It should be noticed, the value of $(4n_c + n_s)$ must satisfy the minimum restriction when increasing the ratio S , and both n_c , n_s should be positive integers. To show the S change with a wide range, assume $(4n_c + n_s) \approx 50$. Sketch the curves of inductances verse distribution ratio in Fig.5.3.7. The realizable winding distribution are labeled next to each S points.

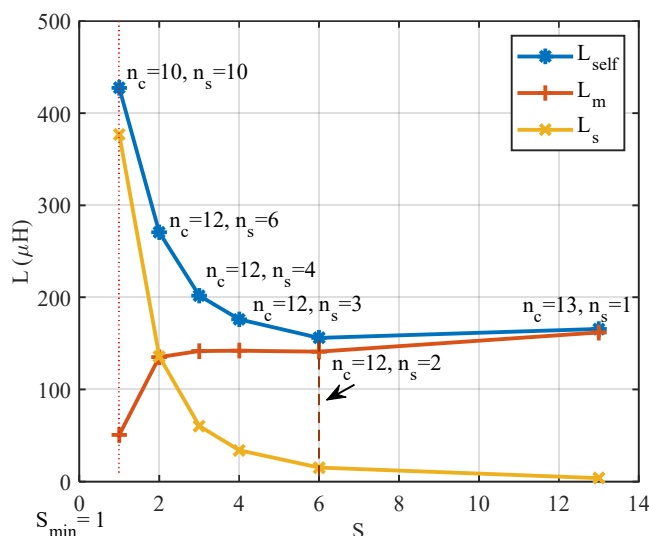


Fig.5.3.7 Distribution ratio verses self inductance, mutual inductance, and. leakage inductance

According to the curve, when the ratio equals to 1, leakage inductance is greater than the magnetizing and transformer cannot fulfill the fundamental electrical power transfer requirement. With the increasement of the winding ratio, L_{self} decreased and L_{mutual} increased, while S is inversely proportional to the L_s .

The winding scenario under $S = 2, 3, 4, 6$ also shows the impact of n_s on leakage inductance when n_c is fixed. L_s is linearly proportional to the square of n_s , which conform to (5.20). Percentage change of L_s for S and n_s is more significant comparing to the extension length. Both turns of the windings and distribution ratio are major magnetic integration control parameters. Adjusting S only changes the volume and weight of the overall HFMT slightly, which barely has no impact on the power density. Moreover, expense of increasing turns of winding is much lower than modifying the core. Hence, adjusting the

winding related parameters is considered as the most cost-effective magnetic integration control realization strategy. If significant leakage inductance is required, S and n_s should be increased simultaneously. In practical transformer construction, n_c and n_s must also consider the vertical space of the core.

C. Thickness of the horizontal air gap in central pillar

The horizontal air gap is inserted in the middle of the central pillar to modify the flux entering the main flux paths. Thickness of this air gap H_{ag} dominates the \mathcal{R}_c , and is not associated with \mathcal{R}_s . Similar to l_e , increasing \mathcal{R}_c cause nonlinear attenuation of both self and mutual inductance.

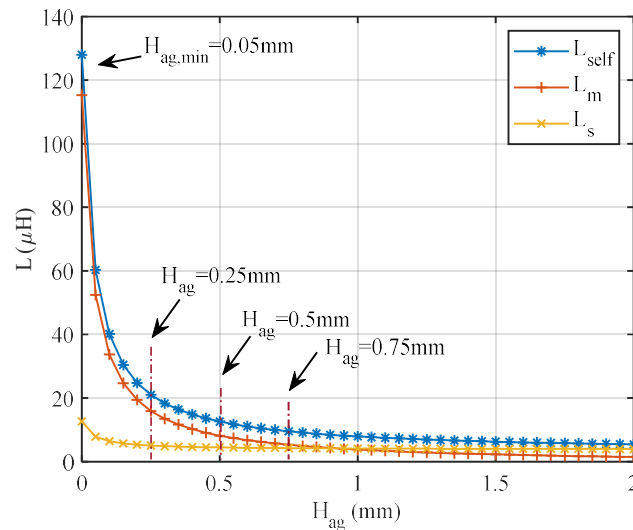


Fig.5.3.8 Thickness of central horizontal air gap verses self inductance, mutual inductance, and leakage inductance.

Relationship between self, mutual inductance, and H_{ag} ranged from 0.05 mm to 5 mm is sketched in the Fig.5.3.8. Results show that, 50% reduction of the H_{ag} led to 13.2% of leakage inductance decrement, while 50% increase brings 4.9% of augmentation, which conforms to the expectation. Keep expanding this air gap, leakage inductance will exceed the magnetizing inductance at $H_{ag} = 0.85 \text{ mm}$. Although in (5.20) L_s shows no relationship with \mathcal{R}_c , modifying the ratio of the flux entering the central pillar still brings tiny growth of the leakage inductance. H_{ag} is regarded as a minor magnetic integration control parameter and its main function is modifying L_m .

D. Thickness of the horizontal air gap in side pillar

Like the central pillar, horizontal air gap can be inserted in the middle of the side pillars. Thickness of this air gap $H_{ag,s}$ dominates \mathcal{R}_s , which is inversely proportional to the leakage inductance L_s . Relationship between self, mutual inductance, and horizontal air gap thickness $H_{ag,s}$ ranged from 0.05 mm to 1 mm is sketched in the Fig.5.3.9.

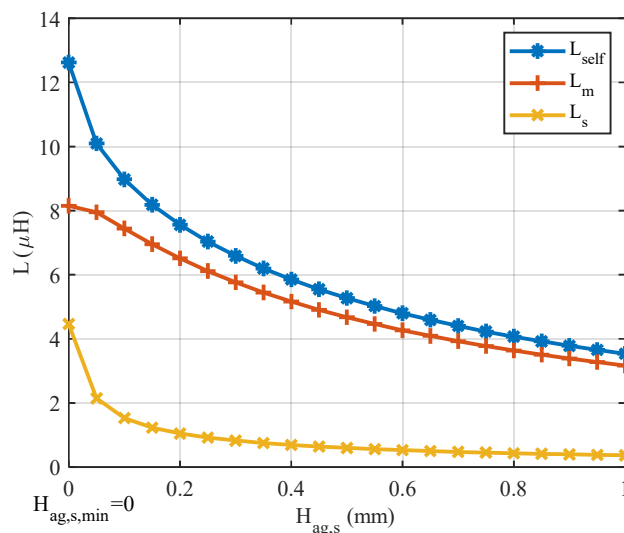


Fig.5.3.9 Thickness of side horizontal air gap verses, a). Self inductance, b). mutual inductance, c). Leakage inductance.

Results shows insertion of the $H_{ag,s}$ significantly reduces the leakage inductance. 0.05 mm $H_{ag,s}$ reduces the L_s to less than half, and 0.15 mm decreases the L_s to about a quarter. Considering the case study is aimed for magnetic integration which requires a significant leakage inductance, $H_{ag,s}$ is better eliminated. Besides, $H_{ag,s} = 0$ also provide benefits in practical core assembling, core structure can be physically connected through the side pillars and bobbins are not demanded.

E. Generalized integrated HFMT design procedures

Based on the previous analyzation of magnetic circuit and magnetic integration parameters, conclude the general procedures for designing a proposed HFMT operating in an N -port MAB in Fig.5.3.10.

Once the aimed L_s is confirmed according to the electrical specifications, A_s and A_s are firstly designed. n_s is then selected stem from these two parameters. Obtain the \mathcal{R}_s , and adjust

the integration control parameter until L_s is close to the target, then core dimension can be determined. If the core can satisfy the B_{sat} restriction, the rest parameters can be selected according to the L_m . After validated by 3D FEA simulation, an integrated HFMT is successfully designed.

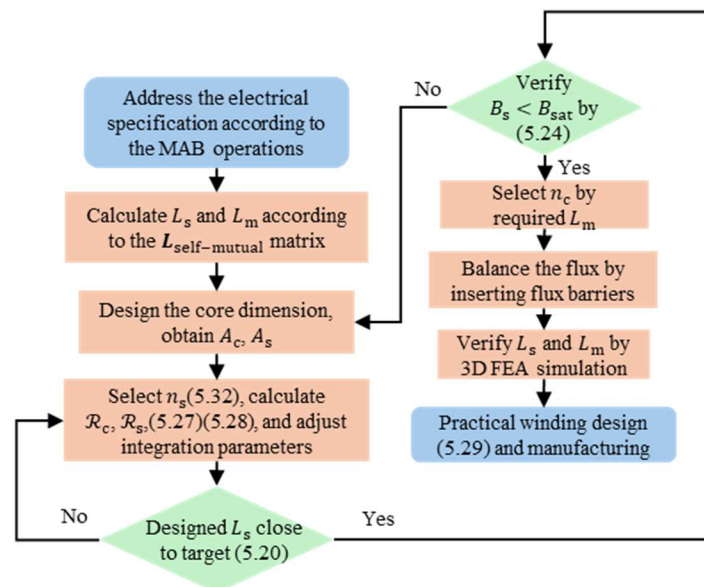


Fig.5.3.10 The generalized design procedure of applying the proposed integrated HFMT in a N -port MAB converter.

5.4 Saturation evaluation for the practical multiport HF transformers

A. Saturation of the two-port HF transformer

As mentioned in the previous chapter, saturation of the transformer can lead to the distortion of the waveform, reduce the quality of power transfer, and threaten the safety of the system. To avoid the core saturation during the operation, core design should consider the saturation restriction under maximum power transfer. And the maximum power transfer specification can also provide the limitation for the outer phase shift D_o if D_o is related to the saturation.

Evaluation of the saturation conditions start with the common two-port E-shape-core planar transformer. For whom, central-side split core structure is the most distinctive feature, e.g, ER and EQ core. In most designs, winding configuration of this core shaped transformer is placing all the coils on the central leg and construct the same magnetic path for two windings.

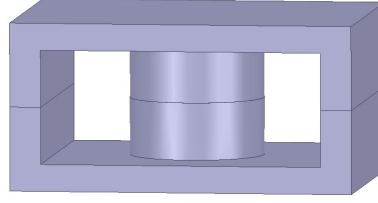


Fig.5.4.1 ER-shaped core structure

Empirically, traditional magnetic core with central-side distributed structure, cross-sectional area of the central pillar is equal to the sum of the side ones. This consideration is based on balancing the flux entering and exiting the central pillar. The maximum flux density B_{\max} should be restricted below the saturation flux density B_{sat} according to the turns of winding as (5.33).

$$B_{\max} = \frac{V_{\text{dc}}}{n_{\text{p}} K_{\text{f}} f A_{\text{e}}} \leq B_{\text{sat}} \quad (5.33)$$

where V_{dc} is the output voltage, K_{f} is the waveform coefficient, for both DAB and MAB converter, $K_{\text{f}} = 4$. n_{p} is the turns of the primary winding, and A_{e} is the cross-sectional area of the core. For a two-port port-consistent HFT with unity turn ratio and central-wound configuration, flux density is equal along the central and side pillar. Since two MMF sources are connected in series and reluctance of the parallel branch is equal. Hence, for these types of two-port core, saturation will not appear individually in one side pillar. Both side and central pillar has the same saturation restriction, and this restriction is not related to the power-control phase shift D_{o} .

B. Saturation of the RSSC HFMT

However, when it comes to the proposed RSSC HFMT, situation becomes different. MAB configured applications may require system port working under varied voltage conditions. This variation in coil excitation combined with the split winding distribution can lead to the maximum operating flux density in side pillar greater than the central and achieving the saturation in prior.

The saturation restriction for central pillar can be deduced from (5.33), since winding in the proposed HFMT is in split configuration, $n_p A_e$ is substituted by $(n_c A_c + n_s A_s)$, where A_c and A_s is the cross-sectional area of central pillar and side pillar, respectively. Since summation of the side pillars cross sectional areas equal to central cross-sectional area: $n A_s = A_c$, (5.33) can be rewritten as (5.34). $B_{\max,c}$ refers to the maximum flux density of the central pillar during operation, and this flux density is not related to the phase shift.

$$B_{\max,c} = \frac{NV_{dc}}{K_f A_c f (Nn_c + n_s)} = \frac{V_{dc}}{K_f A_s f (Nn_c + n_s)} \quad (5.34)$$

For integrated transformer applied in a generalized MAB converter with N ports, overall maximum operating flux density should consider the flux density directly from the side-pillar coil (5.35) and the equivalent flux density from the central-pillar coil (5.36), Suppose all the outer phase shifts are identical $D_{o,ij} = D_{out}$. Overall saturation restriction for one individual side pillar can be represented by (5.37), this density is affected by the phase shift.

$$B_{s\text{-itsel,max}} = \frac{V_{dc}}{4A_s f_{sw}} \frac{2(N-1)D_{out}}{Nn_s} \quad (5.35)$$

$$B_{c\text{-eq,max}} = \frac{V_{dc}}{4A_s f_{sw}} \frac{1 - \frac{(N-1)D_{out}}{2}}{(Nn_c + n_s)} \quad (5.36)$$

$$B_{\max,s} = \frac{V_{dc}}{K_f A_s f} \left[\frac{1 - \frac{(N-1)D_{out}}{2}}{(Nn_c + n_s)} + \frac{2(N-1)D_{out}}{Nn_s} \right] \quad (5.37)$$

From the (5.34) and (5.37) it is obvious, $B_{\max,s}$ depends on the value of n_c , n_s and D_{out} , and when phase shift is 0, $B_{\max,c} = B_{\max,s}$. If power is transferred between the ports, that is $D_{out} \neq 0$, $B_{\max,s}$ will always be greater than $B_{\max,c}$. Maximum operation flux density of side pillar $B_{\max,s}$ should be clamped at a lower value to prevent the side pillar saturated in prior.

The first solution is reducing $B_{\max,c}$ and $B_{\max,s}$ simultaneously to prevent saturation, which refers to increasing the common parameter A_s . The benefit of this solution is, leakage inductance is only related to the air gap in the side and central pillar, adjusting the cross-section

area will not affect the leakage inductance. Which means, prevention of saturation will not disturb the design of leakage inductance. However, expand the A_s without changing A_c might lead to the unbalance in flux since the relationship $A_c = NA_s$ no longer exists. In addition, A_s is directly in relation to the volume of the transformer. If increasement of A_s can not be compensated by greater maximum D_{out} , power density of the transformer is reduced. Hence, this solution leads to a more complicated trade-off between optimization of power density and saturation. In this trade off, ratio between $(N - 1)D_{out}$ and $(Nn_c + n_s)$ needs to be investigated, since $\frac{2(N-1)D_{out}}{Nn_s}$ will always be a positive element. Reduction of D_{out} and increasement of $(Nn_c + n_s)$, A_s should be performed simultaneously. Non-integrated MT with separate inductors should be considered as the minimum reference power density standard of this adjustment.

As discussed in the previous chapter, if in separate MT and series inductor scenario, turns of the series inductor equals turns of side coil in RSSC HFMT, which is $n_{s-L} = n_s$, to achieve the same equivalent leakage inductance, $\mathcal{R}_{sL} = \mathcal{R}_s$ needs to be promised. If the cross-sectional area of inductor is the same as the side-pillar in RSSC, the overall volume of the series inductors will equal to the summation volume of side pillars, whereas volume of the central pillar will always be smaller than the volume of a separate MT. Hence, proper adjustment for RSSC increase the volume of the side pillar appropriately, reducing the $B_{m,S,max}$ while promising the power density is beyond the separate scenario. Comparison of these two scenarios is listed in the TABLE 5.7 below.

TABLE 5.7

COMPARISON BETWEEN SEPARATE HFMT AND INTEGRATED HFMT SCENARIO

Element	Integrated HFMT	Separate HFMT
L_m	$\frac{nN_C N_C R_S \pm 2N_C N_S R_S - R_C N_S N_S}{R_S(nR_C + R_S)}$	$\frac{N_C' N_C'}{R_C'}$
L_S	$\frac{N_S N_S}{R_S}$	$\frac{N_S N_S}{R_S}$
$B_{m,C,max}$	$\frac{nV_{dc}}{4A_C f_{sw}(nN_C \pm N_S)}$	$\frac{V_{dc}}{4A_C' f_{sw}(N_C')}$
$B_{m,S,max}$	$\frac{V_{dc}}{4A_S f_{sw}} \left[\frac{1 - \frac{(n-1)D_{out}}{2}}{(nN_C \pm N_S)} + \frac{2(n-1)D_{out}}{nN_S} \right]$	$\frac{V_{dc} D_{out}}{2A_S' f_{sw} N_S'}$
Vol	$Vol_{core} = A_C l_C + nA_S l_S$	$Vol_{core} = A_C' l_C' + nA_S' l_S'$

The reason leading to the saturation or the non-ideal B-field changes contains frequency variation, current excitation variation, temperature change.

5.5 Simulation and experimental validation

5.5.1 Simulation and experimental validation for the two-port integrated planar transformer designed by the reluctance-based strategy

The 3D model of the magnetic core with winding arrangements Fig.5.2.11(a) and (b) were built in the ANSYS Maxwell. The 2D longitudinal cross-sectional map was firstly simulated for the observation of the magnetic flux line. Distribution of the flux map is recorded to validate correctness of the representative air-part flux path length. Then, 3D-FEA simulation is performed to verify the accuracy of the theoretical calculation.

A. Optimization of the practical winding arrangement for the two-port integrated planar transformer

The ordinary practical realization method for the 6-layer-parallel width-fixed winding is utilizing the spiraling winding structure shown in Fig.5.5.1(a). This structure has two significant drawbacks:

- a) As the topmost and the bottommost layer of the spiraling winding only have half turn of the winding, this structure requires greater overall winding thickness.
- b) The insulation between each layer of the winding is conventionally realized by the flat insulating film or tape. Among which insulating film usually has higher insulation temperature. For spiral winding, flat film insulation will be unfulfillable, and the tape is hard to be wrapped uniformly on the conductor.

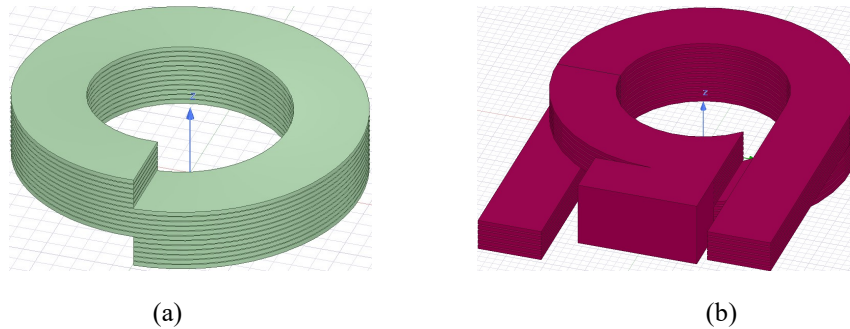


Fig.5.5.1 Two practical winding arrangements. (a). The traditional parallel spiraling winding structure. (b). The proposed middle connected parallel winding structure.

Hence, a middle connected parallel strategy is proposed to solve this issue in practical, with the winding structure shown in Fig.5.5.1(b). Besides the in and out terminals, the middle point of each single layers is also connected by cutting a hole in the parallel connecting position of each turn of winding and linking them with an inserted cylindrical copper rod. Benefits of this proposed structure include smaller vertical height requirements of the core window, lower cost and easier practical building. The disadvantage is difference between parallel part of the windings should be limited, otherwise unbalances might occur between primary and secondary coil.

B. FEMM simulation results

2D plot of flux lines under rated operating current excitations with the same current direction in primary and secondary coils are shown in Fig.5.5.2.

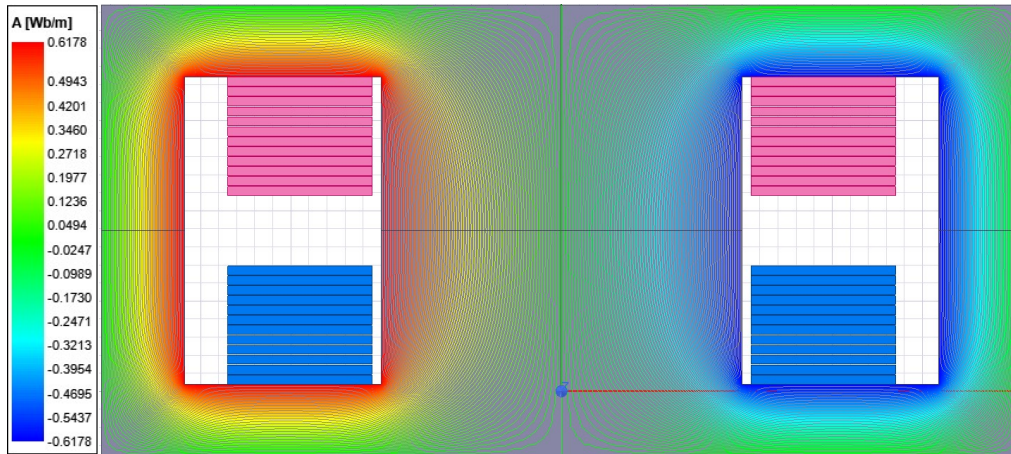


Fig.5.5.2 Flux lines plot with rated operating current direction.

According to the plot, the flux density-fields in the coils and air are too small to be observed comparing to the main flux in the core. Which makes the leakage flux lines invisible. Hence, rated current excitation with the opposite direction applied to the primary and secondary coils, so that the flux lines created by the primary and secondary coils can be neutralized in the core to sketch the flux lines with lower density.

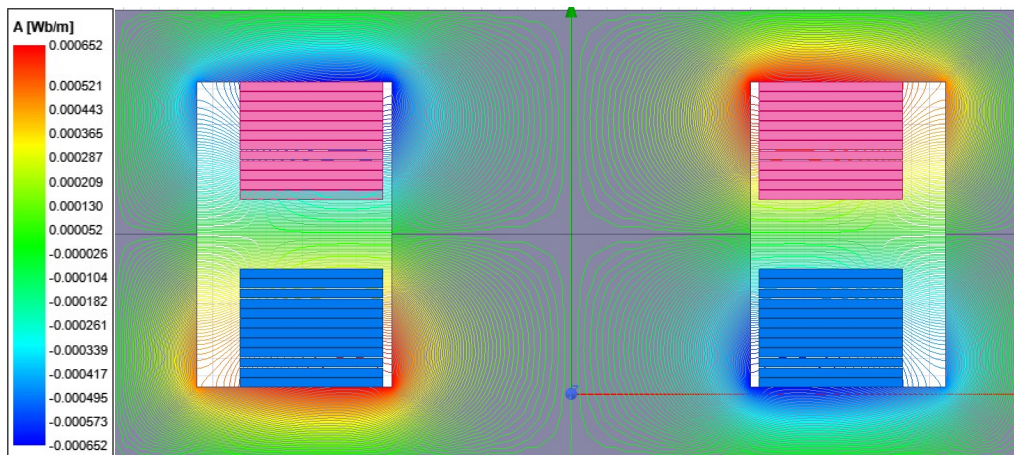


Fig.5.5.3 Flux lines plot with current excitation direction in the secondary coil reversed.

The flux lines of the self-leakage flux can be observed in Fig.5.5.3. Compared to the main flux, its magnitude is only 1% of the main flux. Distribution of the self-leakage flux lines validates the evaluation in the previous discussion. The coefficient is necessary as density of the flux lines are higher at the positions closer to the edges of the window.

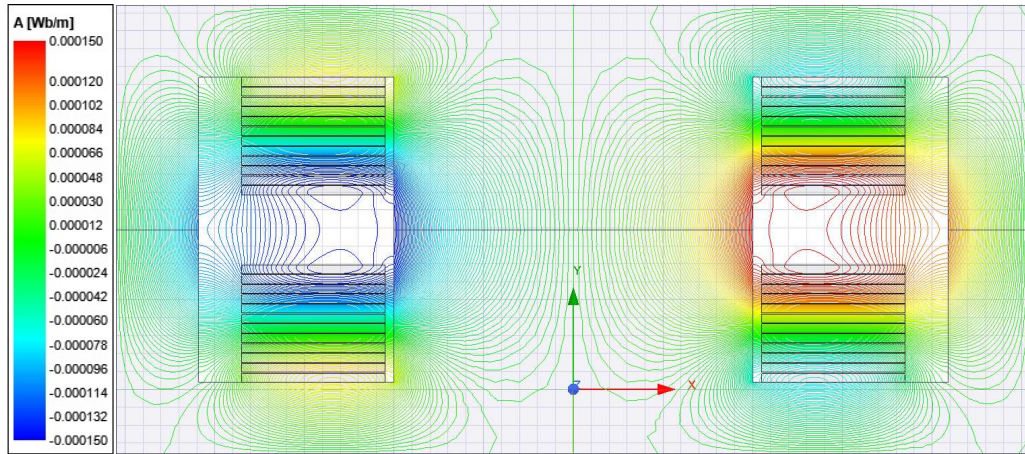


Fig.5.5.4 Flux lines plot the current excitation direction in half of the primary and secondary coils reversed (use the reversion to neutralize the main flux generated by primary winding and secondary windings).

Since the mutual leakage-flux is even smaller, reverse the excitation directions for half of the current source in primary and secondary coils, the flux lines are observed in Fig.5.5.4, with its magnitude equals to one-fifth of the self-leakage flux. This double reverse is to further neutralize the self-leakage flux on the basis of neutralizing the main flux, otherwise mutual leakage flux can not be observed due to its extremely small order of magnitude. The flux lines of the mutual leakage flux highly concentrated in the gap areas, which validates the correctness of the proposed mutual-leakage evaluation processes. It can also be observed that many leakage flux lines terminals did not enclose the outer edge of the conductor when entering the core. All the three maps prove that representative coefficient is necessary in the equivalent reluctance evaluation.

C. 3D-FEA simulation results

The 3D FEA simulation is used for the validation since 2D simulation can not involve the fringing effect. Rated current excitation is applied to the primary side, whereas the secondary side is open circuit. Models of two arrangements have been built with the middle connected parallel winding structure. Their sectional views are shown in Fig. 5.5.5.

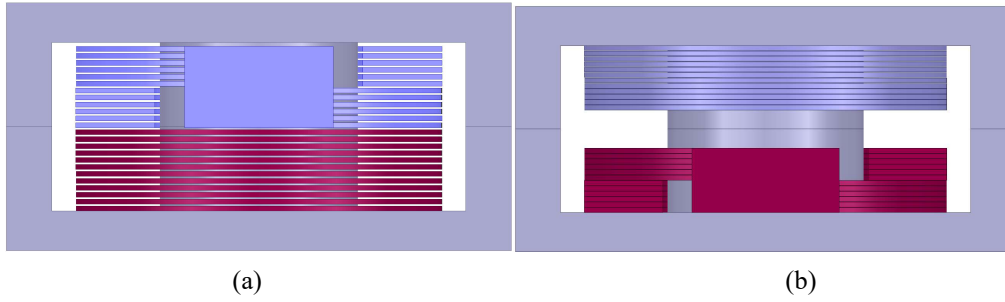


Fig. 5.5.5 Models of two winding arrangements in FEA simulation (a) Insulation thickness $h_i = 0.2$ mm, thickness of the gap between two coils is $h_g = 0.4$ mm, (b) The proposed arrangement with $h_i = 0.05$ mm, $h_g = 6.95$ mm.

1). *Effectiveness and accuracy validation of the proposed strategy*: Record the simulation results of the self-mutual inductance in matrix form for the winding scenario in Fig. 5.5.5(a): $\begin{bmatrix} L_{11} & L_{12} \\ L_{21} & L_{22} \end{bmatrix} = \begin{bmatrix} 62.116\mu\text{H} & 61.987\mu\text{H} \\ 61.987\mu\text{H} & 62.116\mu\text{H} \end{bmatrix}$. Because of the unity turn ratio, the mutual inductance is the equivalent magnetizing inductance: $L_{m\text{-eq}} = 61.987 \mu\text{H}$, whereas the equivalent leakage inductance can be calculated as $L_{11} - L_{12}$ or $L_{21} - L_{22}$: $L_{s\text{-eq}} = 0.129 \mu\text{H}$. This result only has 0.78% deviation to the theoretical calculation in Chapter 5.2.

2). *Correctness validation of the boundary magnetic integration*: Record the simulation results for the scenario in Fig. 5.5.5(b): $\begin{bmatrix} L_{11} & L_{12} \\ L_{21} & L_{22} \end{bmatrix} = \begin{bmatrix} 62.046\mu\text{H} & 61.879\mu\text{H} \\ 61.879\mu\text{H} & 62.046\mu\text{H} \end{bmatrix}$. $L_{m\text{-eq}} = 61.879 \mu\text{H}$ and $L_{s\text{-eq}} = 0.167 \mu\text{H}$. Simulation results of both arrangements are listed in the TABLE 5.8.

TABLE 5.8

3D FEA SIMULATION RESULTS FOR TWO WINDING ARRANGEMENTS

	Insulation=0.2 mm Gap=0.4 mm	Insulation=0.05 mm Gap=3.9 mm
Leakage inductance	0.129 μH	0.167 μH

The estimated L_m is 59.45 μH , which has 3.95% error in percentage. There are several reasons causing this error. Firstly, the magnetizing inductance result from the simulation is effectively the mutual inductance calculated from the mutual reluctance, this reluctance is the equivalent to the parallel of core reluctance and mutual-leakage reluctance. The equivalent parallel reluctance is smaller than the core reluctance, leading to the larger magnetizing

inductance. Since the mutual-leakage reluctance is much larger than the core reluctance, this part of the error can be neglected. Secondly, the initial permeability is used for the magnetizing inductance estimation, whereas the permeability is smaller than its initial value under the rated current excitation condition due to the dynamic of the B-H curve. The error between the estimation and simulation is within the acceptable range. The comparison between these two sets of the results validates the idea in the previous chapter: reducing the insulation and increasing the gap between coils can provide greater port leakage inductance is verified. Winding arrangement scenario aimed to achieving the boundary leakage inductance should minimize the representative path length of the self-leakage reluctance and maximize the representative path length of the mutual-leakage reluctance.

D. Experimental validation results

A prototype of the integrated planar transformer shown in Fig.5.5.6 is manufactured for the final validation. The winding arrangement of this prototype is 0.5 mm-thickness conductor paralleled as the middle-connected structure referred to Fig.5.2.11(b). Thickness of insulation h_1 is 0.075mm, which is 150% of the model in the previous simulation. LCR meter and H-bridge square wave generator have been used to perform the open and short-circuit test.

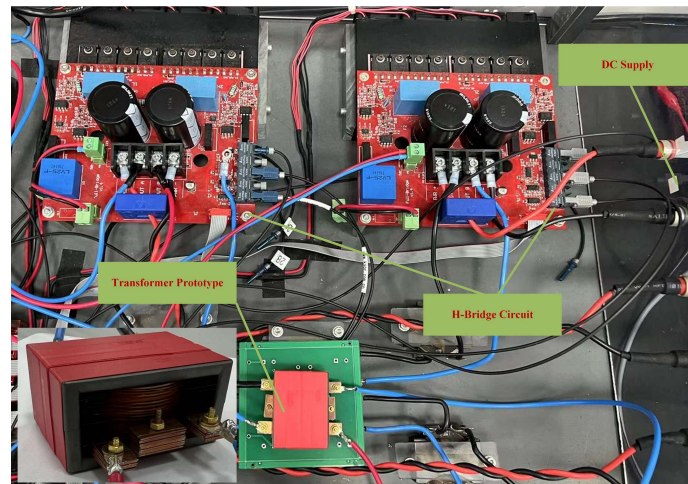


Fig.5.5.6 The transformer prototype and DAB converter.

a) *Magnetizing inductance measurement:* First measures the magnetizing inductance. The H-bridge provides a square wave voltage excitation to the primary side of the transformer with secondary side open circuited. Record the voltage and current waveforms at the primary side

under rated and half of the rated voltage in Fig.5.5.7. It is observed that due to the small leakage inductance, the operating condition in Fig.5.5.7(b) is close to saturation.

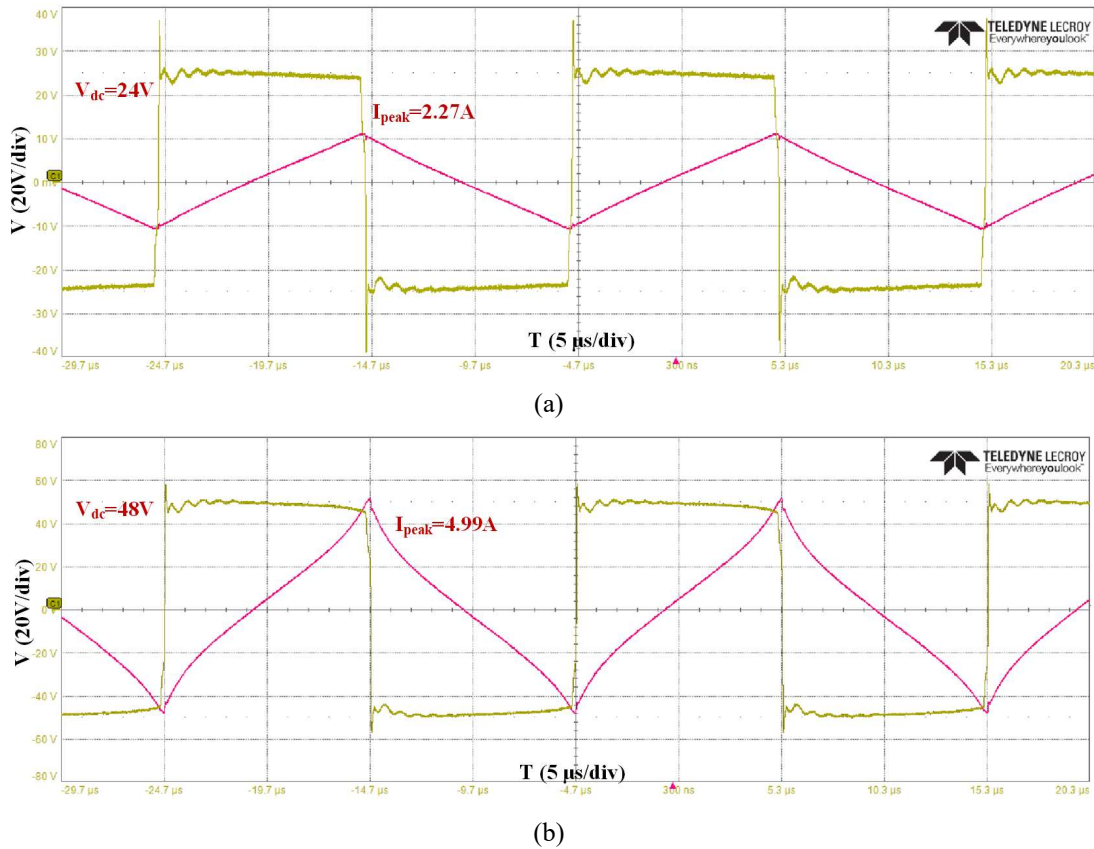


Fig.5.5.7 Voltage and current waveform of the open-circuit test. (a) half rated voltage: $V_{dc} = 24 V$, (b) rated voltage: $V_{dc} = 48 V$.

The equivalent magnetizing inductance can be calculated by the equation $L = \frac{V}{\frac{di}{dt}}$: $L_{half-rated} = 55.10 \mu H$ and $L_{rated} = 48.02 \mu H$. The measured inductance can be regarded as the equivalent magnetizing inductance, reduction of the measure results from half-rated to rated voltage is because of the decrease of the permeability. The measured value is close to the calculations and simulation results. Waveform measurement is only used to test the magnetizing inductance. Since leakage inductance of this transformer is too small, measured inductance is the resultant inductance of leakage inductance and probe series inductance. Hence, an LCR meter is used to measure the leakage inductance.

b) Leakage inductance measurement: The leakage inductance is measured by the GW instek LCR-821 meter with the short-circuit test. Settings of LCR meters is 50k Hz and 1.25 V voltage excitation, the measured results are shown in L-R form. Magnitude of voltage excitation is

restricted to 1.25 V due to it is the maximum voltage output of the LCR meter. The measured results are recorded as in TABLE 5.9.

TABLE 5.9

OPEN AND SHORT CIRCUIT LCR MEASUREMENT RESULTS

Type of Test	Specifications	Value
Open-circuit	Half-rated V	55.10 μ H
Test	Rated V	48.02 μ H
Short-circuit	Primary short circuit	0.35 μ H
Test	Secondary short circuit	0.34 μ H

Calculate the equivalent inductance from the table: $L_{s-eq} = 0.17\mu\text{H}$. Which is close to the simulation result of $0.167\mu\text{H}$.

c) *DAB converter performance*: The designed transformer has been connected in a DAB converter circuit without series inductors to perform as an integrated high frequency transformer (HFT). Set $V_{dc1} = 48\text{ V}$ and connect the secondary to a resistive load. Record the AC and DC waveforms as shown in the Fig.5.5.8. The operation waveforms shows that this designed transformer can be used as an integrated transformer in a DAB converter circuit. Since the leakage inductance is not large enough, gradient of the current at switching moment might be significant. This may lead to high temperature rise in the core and restrict the maximum power transfer capability.

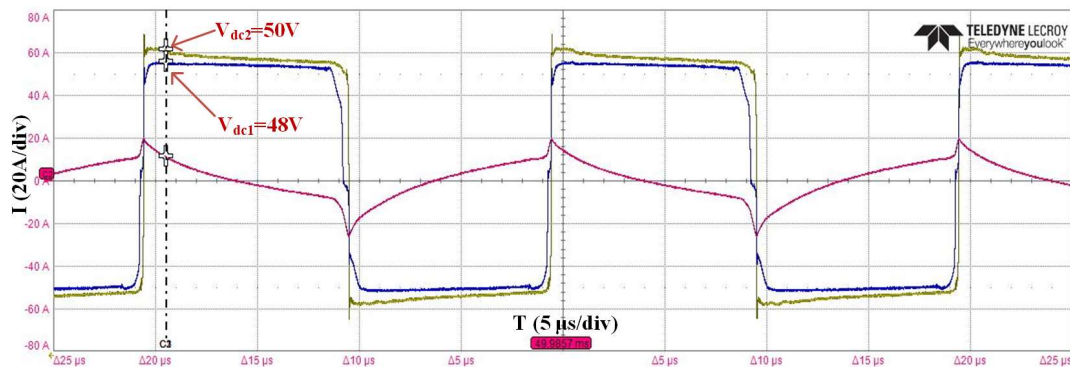


Fig.5.5.8 Voltage and current waveform of the transformer prototype operated in a DAB converter as an integrated HFT.

5.5.2 Simulation and experimental validation for the four-port case study of the proposed RSSC HFMT

The 2D and 3D model were built in the ANSYS Maxwell for simulation validation. The 2D simulation is to validate the flux line rectification provided by the flux barriers. Then, 3D FEA simulation is performed to verify the accuracy of the theoretical calculation. Effectiveness and accuracy of the magnetic integration control parameters is also examined by a set of 3D models. Finally, an initial parameter based prototype is manufactured, tested by LCR meter and operated in a QAB converter system.

A. 2D flux line distribution

2D plot of flux lines under current excitations in four port-coils are shown in Fig.5.5.9. Since cross-sectional plane of the windings and the overlooking flux line distribution is not on a common plane, excitation sources plane has been moved to the cross-sectional plane of the extension leg.

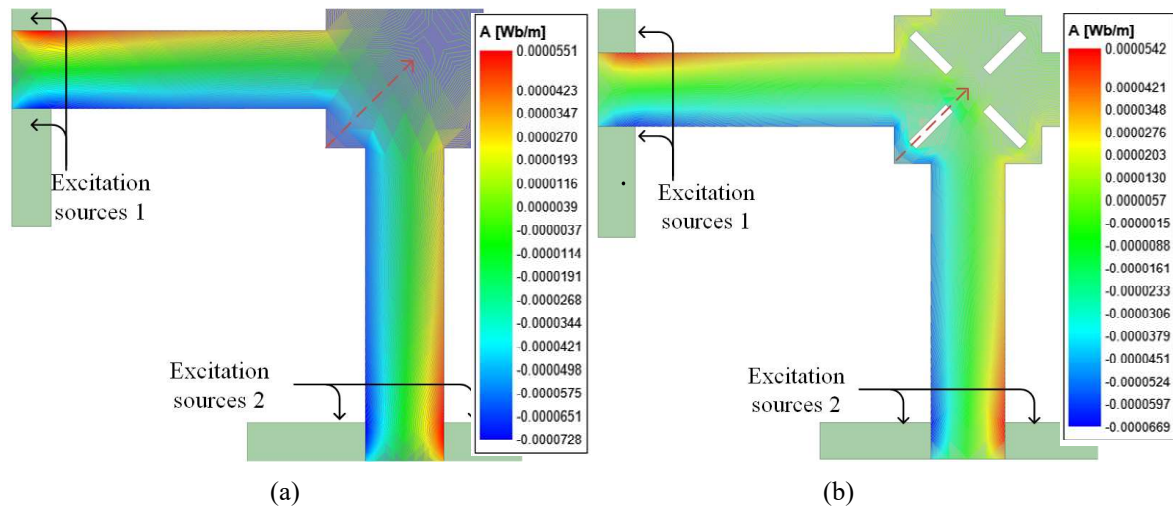


Fig.5.5.9 Flux line distribution in overlooking plane, a). Without flux barriers. (b) With flux barriers.

Along the red arrow shown in the Fig.5.5.9(a), density of flux line distribution, which can be observed by the colour of the map, is not uniformed. Density of distribution is firstly low, increased along the arrow and then decreased to a rather low level, this unbalance is in consistent with the expectation.

Fig.5.5.9(b) shows the flux line distribution after rectified by the flux barriers. Except the corner of the central pillar, flux lines are evenly distrusted along the arrow. This also validates

the hypothesis that the best flux barrier structure is extend the gap to the edge of the central square.

B. 3D FEA simulation for magnetic integration control parameters validation

Simplified 3D FEA model is constructed according to Fig.5.3.1, where all the windings are represented in regular cuboids. Comparison of the theoretical calculations and simulation results are listed in TABLE 5.10 to TABLE 5.12 for core related magnetic control parameters and TABLE 5.13 for winding related parameters.

a) *Initial parameters*: Simulation result of the self-mutual inductance matrix is :

$$\begin{bmatrix} 11.18 & 6.63 & 6.51 & 6.47 \\ 6.63 & 10.75 & 6.43 & 6.51 \\ 6.51 & 6.43 & 10.76 & 6.63 \\ 6.47 & 6.51 & 6.63 & 11.21 \end{bmatrix} \mu\text{H}. \text{ The average magnetizing inductance of simulation is:}$$

$L_m = 6.51 \mu\text{H}$, and leakage inductance: $L_s = 4.47 \mu\text{H}$. The self-mutual inductance matrix shows that, mutual inductance $L_{i,j}$ between the port windings are not identically equal even if vertical air gaps have been inserted. However, the maximum variation between mutual is limited within $0.2 \mu\text{H}$, which is below 5% of the average. This inconsistency can be further optimized by applying the interleaved winding structure. The theoretical calculated initial parameters group $L_{m,cal} = 8.15 \mu\text{H}$, which is 25.2% larger than the simulations. Besides this initial parameter set, all the other calculated L_m are greater than the simulation results. The major reason is during the calculations, central pillar is regarded as a solid pillar, whereas in simulation model, insertion of the air gaps increased the reluctance of the central pillar, leading to decrement of the L_{self} and L_{mutual} .

b) *Extension leg length l_e* : Prolong the length of extension leg to 45 mm. Result of the inductances are listed in TABLE 5.10, where L_s is 18.8%. Then shorten the length of extension leg to 15 mm, L_s is increased by 35.3%, This change is almost the same comparing to the calculations. Besides, results validate the mutual & magnetizing inductance is insignificant when the extension length increased, whereas the leakage inductance has decreased. This trend is in line with the expectation.

TABLE 5.10

SIMULATION AND CALCULATION COMPARISON FOR LENGTH OF EXTENSION LEG l_e WITH $n_c = 3$ AND $n_s = 1$

Parameter setting	Calculation results (μH)			Simulation results (μH)		
	L_{self}	L_m	L_s	L_{self}	L_m	L_s
$l_e = 15 \text{ mm}$	14.10	8.21	5.89	12.18	6.13	6.05
Initial parameters	12.62	8.15	4.47	10.98	6.51	4.47
$l_e = 45 \text{ mm}$	11.85	8.20	3.64	10.19	6.56	3.63

c) *Thickness of the central horizontal air gap*: Extend the thickness of central horizontal air gap to 0.75 mm, and then reduce it to 0.25 mm. The variation of the new leakage inductance is within 1% of the initial according to the results in TABLE 5.11. This trend confirms with the deduced theory that central horizontal air gap only has tiny impact on the L_s . Unlike the L_s , adjusting the H_{ag} can greatly change the magnetizing inductance. Hence, the main purpose of adjusting the H_{ag} is modifying the \mathcal{R}_s , and the ratio of $\frac{L_m}{L_s}$.

TABLE 5.11

SIMULATION AND CALCULATION COMPARISON FOR CENTRAL AIR GAP H_{ag} WITH $n_c = 3$ AND $n_s = 1$

Parameter setting	Calculation results (μH)			Simulation results (μH)		
	L_{self}	L_m	L_s	L_{self}	L_m	L_s
$H_{\text{ag}} = 0.25 \text{ mm}$	20.99	15.93	5.06	17.08	12.66	4.42
Initial parameters	12.62	8.15	4.47	10.98	6.51	4.47
$H_{\text{ag}} = 0.75 \text{ mm}$	9.53	5.28	4.25	8.57	4.11	4.46

d) *Thickness of the side horizontal air gap $H_{\text{ag},s}$* : In contrast with the central air gap, modifying the side horizontal air gap $H_{\text{ag},s}$ can greatly change the leakage inductance as shown in TABLE 5.12. Extend $H_{\text{ag},s}$ from zero to 0.05mm and 0.15mm, the leakage inductance has decreased by 58.4% and 77.2%, respectively. This trend verifies the correctness of the deduced equation of leakage inductance. Since L_s result of 0.05mm air gap is still too small to be accepted for a magnetic integrated MT, the side horizontal air gap is set to be zero.

TABLE 5.12

SIMULATION AND CALCULATION COMPARISON FOR SIDE AIR GAP $H_{ag,s}$ WITH $n_c = 3$ AND $n_s = 1$

Parameter setting	Calculation results (μH)			Simulation results (μH)		
	L_{self}	L_m	L_s	L_{self}	L_m	L_s
Initial parameters	12.62	8.15	4.47	10.98	6.51	4.47
$H_{ag,s} = 0.05$ mm	10.10	7.95	2.14	8.16	6.30	1.86
$H_{ag,s} = 0.15$ mm	8.18	6.95	1.23	6.77	5.75	1.02

e) *Distribution ratio and truns of windings*: Since the previously calculated total turn of winding is 3 and distribution ratio S is defined greater than zero, the only possible S selection is 2. To show the impact of the S , requirement of winding is changed to the same one as in the evaluation in Chapter 5.3. Result of the inductances with varied $S = 6, 3, 2$ are listed in TABLE 5.13.

TABLE 5.13

SIMULATION AND CALCULATION COMPARISON FOR WINDING PARAMETERS WITH INITIAL CORE STRUCTURAL PARAMETERS

Parameter setting	Calculation results (μH)			Simulation results (μH)		
	L_{self}	L_m	L_s	L_{self}	L_m	L_s
$\frac{n_c}{n_s} = 12:2$	156.15	141.06	15.08	153.18	130.94	22.24
$\frac{n_c}{n_s} = 12:4$	201.89	141.57	60.32	179.85	107.74	72.11
$\frac{n_c}{n_s} = 12:6$	270.72	135.00	135.72	229.37	77.36	152.01

Impact of S on leakage inductance validates the analysis in the previous chapter.

C. Four port RSSC HFMT Prototype experimental validation

To test the accuracy of the theoretical estimation and simulation results, a prototype HFMT is manufactured based on the initial parameters. The magnetic core is initially cut into 8 pieces and glued together. Configuration of the half core and assembled HFMT is shown in the Fig.5.5.10(a) and Fig.5.5.10(b). Once manufactured, this HFMT can still adjust its leakage inductance by modifying the horizontal airgap, turns of winding and ratio of winding distribution.

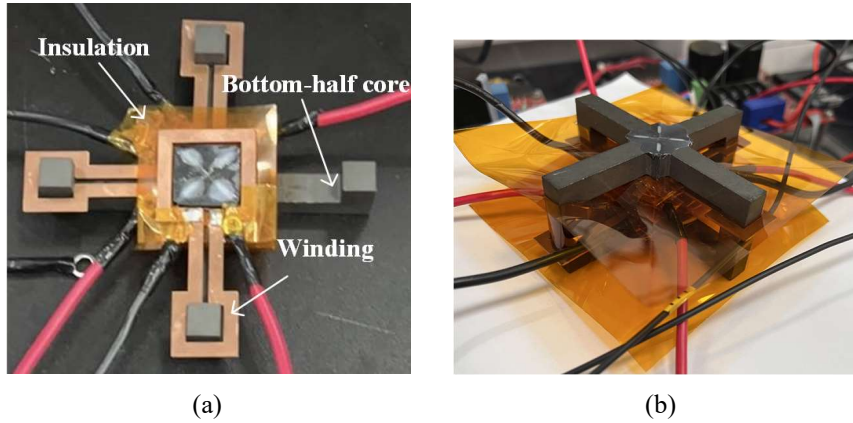


Fig.5.5.10 Configuration of the HFMT, (a) Bottom-half core before assembled. (b) The assembled HFMT

The leakage and magnetizing inductances with varied air gaps are measured by the LCR meter through short circuit and open circuit tests. The calculated results are shown in the TABLE 5.14.

TABLE 5.14

LCR METER EXPERIMENTAL RESULTS OF THE HFMT PROTOTYPE WITH VARIABLE AIR GAPS

LCR Test	Specifications	Value
L_m	Initial parameter	4.51 μH
L_s	Initial parameter	1.95 μH
L_m	$H_{ag} = 0.65 \text{ mm}$, $H_{ag} = 0.15 \text{ mm}$	2.62 μH
L_s	$H_{ag} = 0.65 \text{ mm}$, $H_{ag} = 0.15 \text{ mm}$	1.50 μH
L_m	$H_{ag} = 0.80 \text{ mm}$, $H_{ag} = 0.30 \text{ mm}$	1.97 μH
L_s	$H_{ag} = 0.80 \text{ mm}$, $H_{ag} = 0.30 \text{ mm}$	1.30 μH
L_m	$H_{ag} = 0.95 \text{ mm}$, $H_{ag} = 0.45 \text{ mm}$	1.96 μH
L_s	$H_{ag} = 0.95 \text{ mm}$, $H_{ag} = 0.45 \text{ mm}$	1.13 μH

The changing trend of inductance verses air gap conforms to the evaluations and simulation results. Since the prototype is assembled from parts, tiny gaps between connection surfaces of top-half and bottom-half core are impossible to be filled completely. The LCR measurement is close to the results of $H_{ag,s} = 0.05 \text{ mm}$, L_m is smaller than the simulation and L_s is slightly greater than the simulation, all these phenomena reflect this situation.

Calculate the results: $L_s = 1.95 \mu\text{H}$ and $L_m = 4.51 \mu\text{H}$. Since the prototype is assembled from parts, tiny gaps between connection surfaces of top-half and bottom-half core are impossible to be filled completely. The LCR measurement is close to the results of $H_{ag,s} =$

0.05 mm, L_m is smaller than the simulation and L_s is slightly greater than the simulation, all these phenomena reflect this situation. The only solution to solve this problem is utilize the one-step forming manufacturing technique.

Test the HFMT prototype in the QAB converter platform with one input port and three output ports connecting to the pure resistive loads. 50V input voltage is provided by a constant DC power supply. The topology of the testing plant is shown in the Fig.5.5.11, where the proposed HFMT is directly connected to the H-bridges without series inductors. SPS control is applied to the system and the phase shift $D_{o,1,2}$, $D_{o,1,3}$, $D_{o,1,4}$ is 0.02, 0.06 and 0.10 respectively.

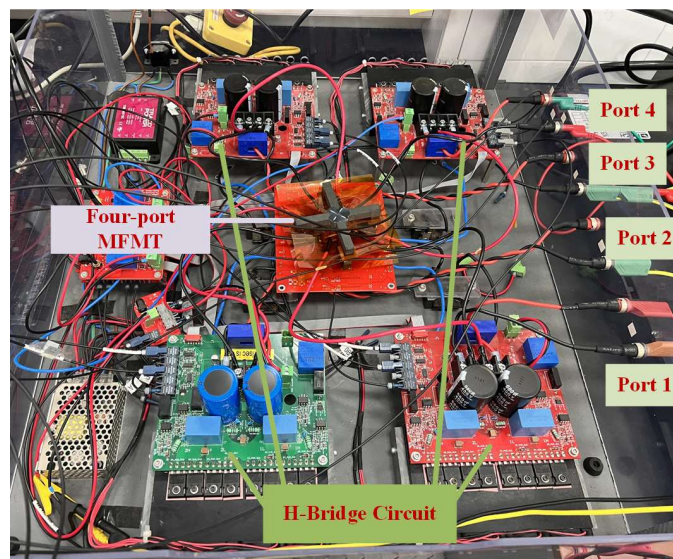
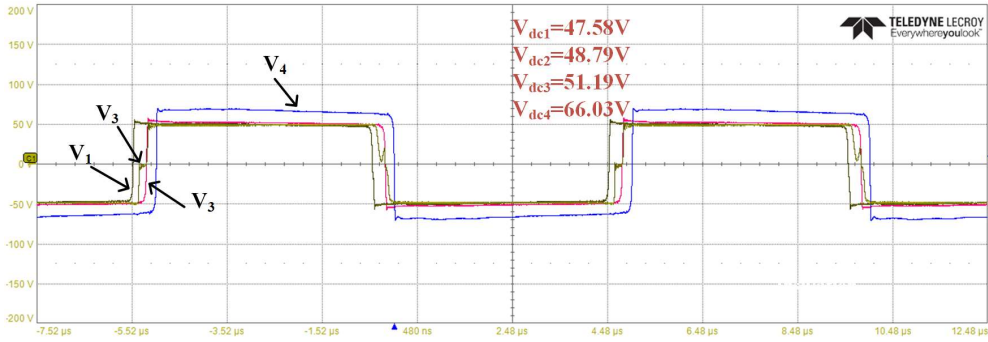
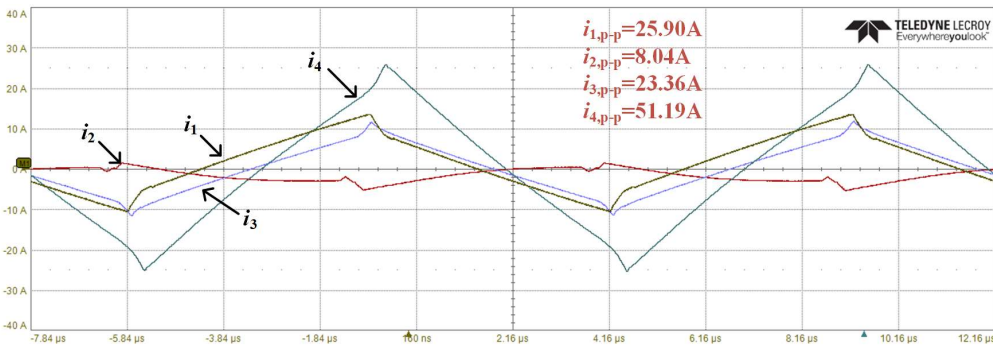


Fig.5.5.11 The proposed four-port HFMT operating in a QAB converter plant with one input port and three output ports connected to pure resistive loads

Fig.5.5.12(a) and Fig.5.5.12(b) exhibited the voltage and the corresponding current waveforms at transformer sides of four QAB ports. Waveforms prove the proposed HFMT can working normally in a QAB converter system without the involvement of series inductors. Current Port 2 is in reversed direction since it is emitting power.



(a)

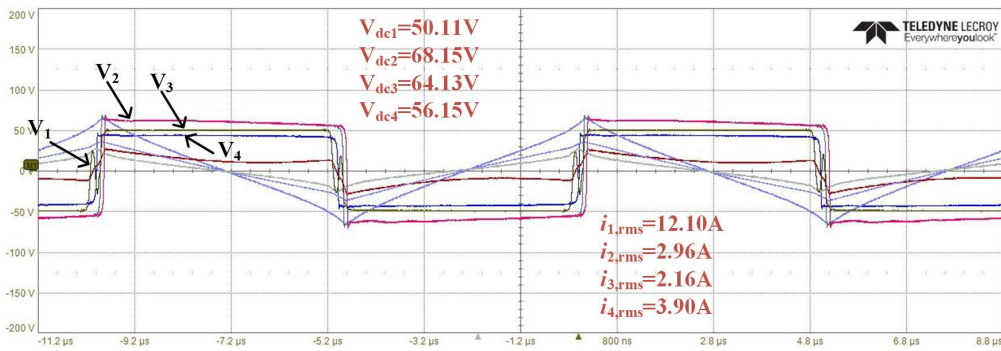


(b)

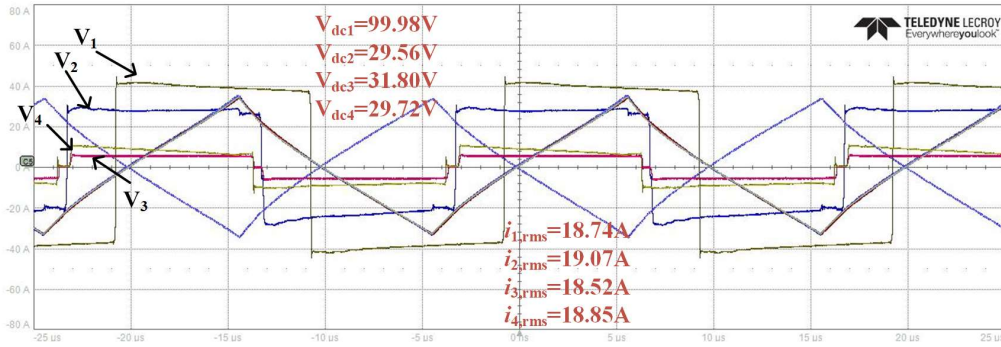
Fig.5.5.12 The port waveforms of the QAB converter, (a) Voltage waveforms, (b) Current waveforms.

$$i_j = \frac{|D_{o,1,j}| |1 - |D_{o,1,j}|| V_1}{2f2L_s} + \sum \pm \frac{||D_{o,1,j}| - |D_{o,1,i}|| |1 - |D_{o,1,j}| - |D_{o,1,i}|| V_i}{2f2L_s} \quad (5.38)$$

Calculate the leakage inductances with the phase shift settings and the actual transferred power by (5.38). The average leakage inductance derived from the waveform results is $\bar{L}_s = 1.75 \mu\text{H}$, which is 5.9% greater than the 0.05 mm simulation result. This value is close to the LCR measurement as well.



(a)

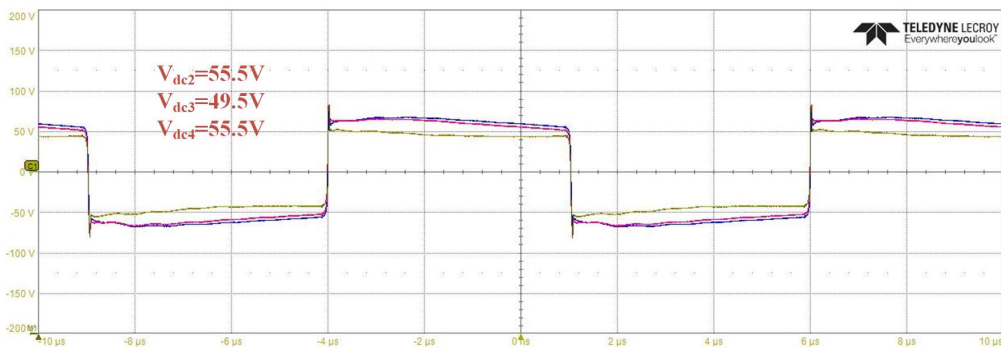


(b)

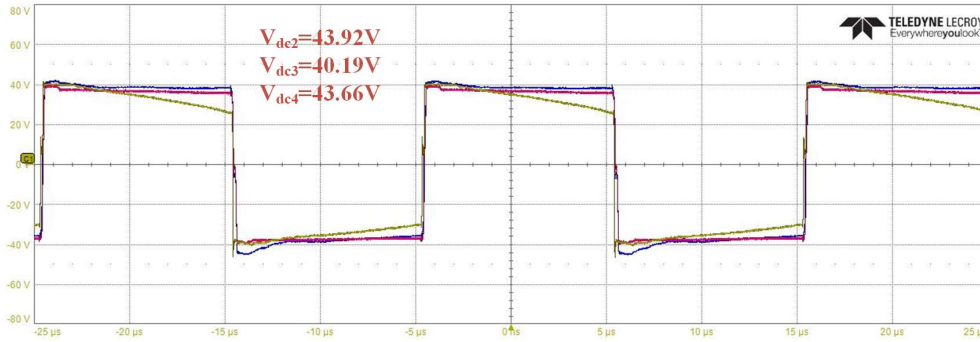
Fig. 5.3.11 Efficiency test with voltage and current waveform, (a) 50V input voltage boost mode, (b) 100V input buck mode

Efficiency under 50V-input boost mode and 100V-input buck mode operation condition can be calculated according to voltage and RMS current recorded in Fig. 5.3.11(a) and Fig. 5.3.11(b). The efficiency is 92.16% and 91.54%.

Due to the eddy current loss, hysteresis loss and thermal loss, the practical efficiency is lower than the theoretical calculation. However, as the efficiency of the integrated scenario has included the inductor and the printed H-bridge circuit will have relatively low losses, 6.5% and 7.12 % reduction of the efficiency can still maintain the system overall efficiency over 90%. Voltage regulation at 50V when 10Ω load is symmetrical connected to Port 2, 3, and 4 can be calculated by the recorded voltage waveform in Fig. 5.3.12(a) and Fig. 5.3.12(b), which is 20.86%, 21.30%, and 18.90%, respectively. The measured voltage results validate the effectiveness of the proposed RSSC integration scenario, with the integrated leakage inductance, voltage regulation is higher than conventional value in separate MT.



(a)



(b)

Fig. 5.3.12 Voltage regulation test at 50V input, (a) Port 2, Port 3, and Port 4 are open circuits, (b) Port 2, Port 3, and Port 4 are connected to 10Ω symmetrical loads

5.6 Summary of this chapter

First part of this chapter proposed and validated an equivalent reluctance- based leakage inductance evaluation strategy with the air-path leakage flux considered. Based on the estimation from this strategy, the boundary leakage for a selected core can be calculated with high accuracy. An optimized magnetic integration process which can help judging whether a selected core requires structural modification and provide further winding arrangement instructions, is then developed to achieve the transformer magnetic integration for DAB converter. The threshold leakage inductance can be realized by the sectionalized winding arrangement with the maximum layer gap and minimum coil gap. Compared to energy-based evaluation for two winding arrangements with error percentages of 71.32% and 82.04%, the proposed strategy provides both leakage inductance matrix and self-mutual inductance matrix with high accuracy. The estimation errors have been reduced to 0.78% and 3.95%, respectively. The results of the simulation and experiments validated the precision of the proposed strategy and the effectiveness of the process. The proposed strategy can be implemented to the multi-port integrated transformer design for multiport active bridge (MAB) applications with a suitable π -shape transformation.

Second part of this chapter proposed an oval RSSC structure with split winding HFMT for the generalized N-port MAB converters to improve the power density. The controllability of the parameters are theoretically analyzed and verified by the 3D FEA simulation. Insertion flux barriers guarantees the port consistency variation within 5%. Estimation of the leakage

inductance is verified by a cross-shape core HFMT for QAB converters. The four-port RSSC HFMT can operate normally in a QAB plant without series inductors and the measured results is approximately the same as theoretical and simulation results. Error between estimated simulation and experimental measurement is about 5% for both LCR and waveform validations. All these results validates the effectiveness of the proposed magnetic integrated RSSC HFMT.

6. Conclusions and future work

6.1 Conclusions

To enhance the power density DC-DC MIMO systems, MAB converter topology has been proposed to replace the multiple SISO converter array topology. Power characteristics of the MAB topology is nonlinear, the traditional PI controller with SPS modulation can not satisfy the MAB application. Moreover, power density of MAB converter can be further improved by applying the magnetic integration for the HFMT. Therefore, these has closely investigated the modulation strategies to promise the quality and efficiency of power transfer, and advanced control strategies to improve the dynamic performances while restricting the computational burden for the entire control. All the presented modulation and control methods have been validated in a QAB converter. After developing the modulation and control for the MAB plant, a generalized HFMT is designed with controllable and accurate leakage inductances. This design is validated by a case study of four-port HFMT prototype. Therefore, Chapter 2 reviewed the attempts to improve the fundamental modulations and modified modulations considering the non-ideal effects to improve the quality of power transfer. Nonlinear controls and decoupling control strategies for dynamic and steady-state performance enhancement, and MT design scenarios to improve the power density of the system. In Chapter 3, from power characteristics of the SPS and EPS modulation, an AEPS modulation considering the existence of magnetizing inductance in DAB power characteristic can positively contribute to the quality of power transfer is developed. From simulation and experimental results, it is verified that for system considering magnetizing inductance, proposed AEPS modulation could provide reduced current stress and better voltage utilization. Non-ideal effects and measurement error of the parameters involved in the power characteristics that are commonly ignored in ideal power transfer modelling have also been discussed. Chapter 4 aims to develop a modular modulation based decoupling control to improve the dynamic performance and flexibility of the control. Compared to PI controllers, he proposed PDC-MPC the proposed strategy required only one-fifth and one-tenth of the transition period when step variations in load resistances and reference voltage appeared, respectively. Good steady-state precision and control accuracy were achieved. The results of the simulations and

experiments validated the performance of the proposed control strategy. And in research of O^2ND part, the development and validation of an iterative current decoupling algorithm combined with a modular modulation decoupling control system have been presented. In the QAB converter experimental results, the execution time of O^2ND control methodology is 98% of SND and 69.6% of ND under a similar steady state ripple. For the traditional PI control, dynamic and steady-state voltage control performance is unsatisfactory when outer phase shift is beyond 0.2 under the unbalanced loads conditions. With the indication of power to phase shift characteristic in O^2ND , the range of the accurate control has been expanded to twice that of the PI. A 20% transient time reduction was observed from the load step change test under symmetrical load condition, demonstrating the improvement of the dynamic performance. With the ‘modular’ property, soft switching and other features can be achieved conveniently. In Chapter 5, an equivalent reluctance-based leakage inductance evaluation strategy with the air-path leakage flux considered is firstly proposed. According to the experimental validation, energy-based evaluation for two winding arrangements has the error percentages of 71.32% and 82.04%, while the proposed strategy reduced these errors to 0.78% and 3.95%, respectively. An optimized magnetic integration process which can help judging whether a selected core requires structural modification and provide further winding arrangement instructions is then developed. In second part of this chapter, an oval RSSC structure with split winding HFMT for the generalized N-port MAB converters is developed. Insertion of flux barriers of this design guarantees the port consistency variation within 5%. The four-port RSSC HFMT prototype can operate normally in a QAB plant without series inductors and the measured results is approximately the same as theoretical and simulation results. Error between estimated simulation and experimental measurement is about 5% for both LCR and waveform validations.

In sum, as has been verified by the simulation and experimental results, this thesis has fulfilled the objectives that have been stated in the introduction by providing overall improvement in the control, modulation and system power density for generalized MAB converter. Hence, the integrated MAB topology can be used in electrified transportation application to promote the overall power density, whereas the different voltage ratings and constraint like ZVS can be achieved by the advanced GPS modulations modular modulation decoupling controls.

6.2 Future work

The following research works are recommended as future extensions to the modulation, control and hardware improvement of integrated MAB converter presented in this thesis:

- a) The presented modulation considering non-ideal effects have not been involved in the power characteristics of GPS modulation in the MAB converter. A trade-off between computational burden increasement of involving these effects in power characteristics and power transfer quality promotion is necessary. And based on this evaluation, a modified GPS and be developed.
- b) The transformer inductance matrix transformation and reorganization to cooperate the decoupling control. If the integrated transformer has varied port leakage inductance, a transformation method needs to be developed when designing this transformer and relocating its leakage inductance when decoupling the MAB into virtual DAB sub-branches.
- c) The proposed modular modulation based decoupling control can suit other advanced nonlinear control strategies with better performances. These control methods can be further considered and tested in the practical operation.
- d) Magnetic integrated transformer can provide high power density, but due to its multi-winding distribution and core structure, temperature rise will be severe and lead to the saturation of the core. A thermal model of the integrated MT must be established with detailed thermomechanical analyzation.
- e) Further integration of the H-bridge circuit and winding of transformer can be developed to reduce the volume of the overall system.
- f) More investigations need to be conducted to extend the utilization of integrated MAB in the on-board electrified transportation applications.

References

1. Roy, S. and L. Umanand, *Integrated Magnetics-Based Multisource Quality AC Power Supply*. IEEE Transactions on Industrial Electronics, 2011. **58**(4): p. 1350-1358.
2. Jain, P.K., J.R. Espinoza, and J. Hua, *Performance of a single-stage UPS system for single-phase trapezoidal-shaped AC-voltage supplies*. IEEE Transactions on Power Electronics, 1998. **13**(5): p. 912-923.
3. Rodriguez, J., et al., *Multilevel Voltage-Source-Converter Topologies for Industrial Medium-Voltage Drives*. IEEE Transactions on Industrial Electronics, 2007. **54**(6): p. 2930-2945.
4. Buticchi, G., L. Costa, and M. Liserre, *Improving System Efficiency for the More Electric Aircraft: A Look at dc/dc Converters for the Avionic Onboard dc Microgrid*. IEEE Industrial Electronics Magazine, 2017. **11**(3): p. 26-36.
5. Hegazy, O., J.V. Mierlo, and P. Lataire, *Analysis, Modeling, and Implementation of a Multidevice Interleaved DC/DC Converter for Fuel Cell Hybrid Electric Vehicles*. IEEE Transactions on Power Electronics, 2012. **27**(11): p. 4445-4458.
6. Lee, Y., A. Khaligh, and A. Emadi, *Advanced Integrated Bidirectional AC/DC and DC/DC Converter for Plug-In Hybrid Electric Vehicles*. IEEE Transactions on Vehicular Technology, 2009. **58**(8): p. 3970-3980.
7. Murthy-Bellur, D. and M.K. Kazimierczuk, *Isolated Two-Transistor Zeta Converter With Reduced Transistor Voltage Stress*. IEEE Transactions on Circuits and Systems II: Express Briefs, 2011. **58**(1): p. 41-45.
8. Kashif, M. *Bidirectional flyback DC-DC converter for hybrid electric vehicle: Utility, working and PSPICE computer model*. in *2012 Asia Pacific Conference on Postgraduate Research in Microelectronics and Electronics*. 2012.
9. Chung, H.S.H., C. Wai-Leung, and K.S. Tang, *A ZCS bidirectional flyback DC/DC converter*. IEEE Transactions on Power Electronics, 2004. **19**(6): p. 1426-1434.
10. Zhang, F. and Y. Yan, *Novel Forward-Flyback Hybrid Bidirectional DC-DC Converter*. IEEE Transactions on Industrial Electronics, 2009. **56**(5): p. 1578-1584.
11. Lee, J.Y., Y.S. Jeong, and B.M. Han, *A Two-Stage Isolated/Bidirectional DC/DC Converter With Current Ripple Reduction Technique*. IEEE Transactions on Industrial Electronics, 2012. **59**(1): p. 644-646.
12. Zhang, Z., et al., *Analysis and Design of a Bidirectional Isolated DC-DC Converter for Fuel Cells and Supercapacitors Hybrid System*. IEEE Transactions on Power Electronics, 2012. **27**(2): p. 848-859.

13. Hui, L., P. Fang Zheng, and J.S. Lawler, *A natural ZVS medium-power bidirectional DC-DC converter with minimum number of devices*. IEEE Transactions on Industry Applications, 2003. **39**(2): p. 525-535.
14. Souza, E.V.d. and I. Barbi. *Bidirectional Current-Fed Flyback-Push-Pull DC-DC Converter*. in *XI Brazilian Power Electronics Conference*. 2011.
15. Zhang, Z., O.C. Thomsen, and M.A.E. Andersen, *Optimal Design of a Push-Pull-Forward Half-Bridge (PPFHB) Bidirectional DC-DC Converter With Variable Input Voltage*. IEEE Transactions on Industrial Electronics, 2012. **59**(7): p. 2761-2771.
16. Roggia, L., et al., *Integrated Full-Bridge-Forward DC-DC Converter for a Residential Microgrid Application*. IEEE Transactions on Power Electronics, 2013. **28**(4): p. 1728-1740.
17. Wang, K., et al. *Bi-directional DC to DC converters for fuel cell systems*. in *Power Electronics in Transportation (Cat. No.98TH8349)*. 1998.
18. Zhao, B., et al., *Overview of Dual-Active-Bridge Isolated Bidirectional DC-DC Converter for High-Frequency-Link Power-Conversion System*. IEEE Transactions on Power Electronics, 2014. **29**(8): p. 4091-4106.
19. Jiang, C. and H. Liu, *A Novel Interleaved Parallel Bidirectional Dual-Active-Bridge DC-DC Converter With Coupled Inductor for More-Electric Aircraft*. IEEE Transactions on Industrial Electronics, 2021. **68**(2): p. 1759-1768.
20. Chen, L., et al., *Phase-Shift Modulation for a Current-Fed Isolated DC-DC Converter in More Electric Aircrafts*. IEEE Transactions on Power Electronics, 2019. **34**(9): p. 8528-8543.
21. Mastromauro, R., et al., *A ground power unit based on paralleled interleaved inverters for a More-Electric-Aircraft*. 2014. 216-221.
22. Jiang, C. and H. Liu, *A Novel Interleaved Parallel Bidirectional Dual-Active-Bridge DC-DC Converter With Coupled Inductor for More-Electric Aircraft*. IEEE Transactions on Industrial Electronics, 2021. **68**(2): p. 1759-1768.
23. Provost, M.J., *The More Electric Aero-engine: a general overview from an engine manufacturer*. 2002. 246-251.
24. Mastromauro, R., et al., *SiC MOSFET Dual Active Bridge Converter for Harsh Environment Applications in a More-Electric-Aircraft*. Vol. 2015. 2015.
25. Rajashekara, K., *Power Electronics for More Electric Aircraft*, in *Power Electronics for Renewable Energy Systems, Transportation and Industrial Applications*. 2014. p. 365-386.
26. Wheeler, P. and S. Bozhko, *The More Electric Aircraft: Technology and challenges*. Electrification Magazine, IEEE, 2014. **2**: p. 6-12.

27. Wheeler, P., *Technology for the more and all electric aircraft of the future*. 2016. 1-5.
28. Areerak, K., et al., *Stability Study for a Hybrid AC-DC More-Electric Aircraft Power System*. IEEE Transactions on Aerospace and Electronic Systems - IEEE TRANS AEROSP ELECTRON SY, 2012. **48**: p. 329-347.
29. Christou, I., et al., *Choice of optimal voltage for more electric aircraft wiring systems*. Electrical Systems in Transportation, IET, 2011. **1**: p. 24-30.
30. Tariq, M., et al., *Aircraft Batteries: Current Trend towards More Electric Aircraft*. IET Electrical Systems in Transportation, 2016. **7**.
31. Hirst, M., et al., *Demonstrating the more electric engine: A step towards the power optimised aircraft*. Electric Power Applications, IET, 2011. **5**: p. 3-13.
32. Ganey, E., *Selecting the Best Electric Machines for Electrical Power-Generation Systems: High-performance solutions for aerospace More electric architectures*. Electrification Magazine, IEEE, 2014. **2**: p. 13-22.
33. Rohouma, W., et al., *A Four-Leg Matrix Converter Ground Power Unit With Repetitive Voltage Control*. Industrial Electronics, IEEE Transactions on, 2015. **62**: p. 2032-2040.
34. Trentin, A., et al., *Power flow analysis in electro-mechanical actuators for civil aircraft*. Electric Power Applications, IET, 2011. **5**: p. 48-58.
35. Villani, M., et al., *Electromechanical Actuator for Helicopter Rotor Damper Application*. Industry Applications, IEEE Transactions on, 2014. **50**: p. 1007-1014.
36. Friedrich, G., et al., *Integrated starter generator: Need of an optimal design and control approach. Application to a permanent magnet machine*. Vol. 43. 2005. 1529-1534.
37. Jie, C. and W. Anhua, *New VF-power system architecture and evaluation for future aircraft*. IEEE Transactions on Aerospace and Electronic Systems, 2006. **42**(2): p. 527-539.
38. Kisacikoglu, M.C., M. Kesler, and L.M. Tolbert, *Single-Phase On-Board Bidirectional PEV Charger for V2G Reactive Power Operation*. IEEE Transactions on Smart Grid, 2015. **6**(2): p. 767-775.
39. Wen, H., et al., *Fault Diagnosis and Tolerant Control of Dual-Active-Bridge Converter With Triple-Phase Shift Control for Bidirectional EV Charging Systems*. IEEE Transactions on Transportation Electrification, 2021. **7**(1): p. 287-303.
40. Assadi, S.A., et al., *Active Saturation Mitigation in High-Density Dual-Active-Bridge DC-DC Converter for On-Board EV Charger Applications*. IEEE Transactions on Power Electronics, 2020. **35**(4): p. 4376-4387.

41. Xue, L., et al., *Dual Active Bridge-Based Battery Charger for Plug-in Hybrid Electric Vehicle With Charging Current Containing Low Frequency Ripple*. IEEE Transactions on Power Electronics, 2015. **30**(12): p. 7299-7307.
42. Jiang, W. and B. Fahimi, *Multiport Power Electronic Interface—Concept, Modeling, and Design*. IEEE Transactions on Power Electronics, 2011. **26**(7): p. 1890-1900.
43. Solero, L., et al. *Performance of a 10 kW power electronic interface for combined wind/PV isolated generating systems*. in *PESC Record. 27th Annual IEEE Power Electronics Specialists Conference*. 1996.
44. Boora, A., et al., *Voltage-Sharing Converter to Supply Single-Phase Asymmetrical Four-Level Diode-Clamped Inverter With High Power Factor Loads*. Power Electronics, IEEE Transactions on, 2010. **25**: p. 2507-2520.
45. Ma, D., W.-H. Ki, and C.-y. Tsui, *A pseudo-CCM/DCM SIMO switching converter with freewheel switching*. Solid-State Circuits, IEEE Journal of, 2003. **38**: p. 1007-1014.
46. Nami, A., et al., *Multi-output DC-DC converters based on diode-clamped converters configuration: Topology and control strategy*. Power Electronics, IET, 2010. **3**: p. 197-208.
47. Boora, A., F. Zare, and A. Ghosh, *Multi-output buck-boost converter with enhanced dynamic response to load and input voltage changes*. IET Power Electronics, 2011. **4**.
48. Kim, S.K., et al., *Dynamic Modeling and Control of a Grid-Connected Hybrid Generation System With Versatile Power Transfer*. IEEE Transactions on Industrial Electronics, 2008. **55**(4): p. 1677-1688.
49. Chen, Y.M., et al., *Multi-Input Inverter for Grid-Connected Hybrid PV/Wind Power System*. IEEE Transactions on Power Electronics, 2007. **22**(3): p. 1070-1077.
50. Yang, P., et al., *Synthesis and Analysis of Double-Input Single-Output DC/DC Converters*. IEEE Transactions on Industrial Electronics, 2015. **62**(10): p. 6284-6295.
51. Yang, Z., et al. *Traction technology for Chinese railways*. in *The 2010 International Power Electronics Conference - ECCE ASIA -*. 2010.
52. Cao, J. and A. Emadi, *A New Battery/UltraCapacitor Hybrid Energy Storage System for Electric, Hybrid, and Plug-In Hybrid Electric Vehicles*. IEEE Transactions on Power Electronics, 2012. **27**(1): p. 122-132.
53. Tong, Y., et al. *A nonisolated multiple-input multiple-output DC-DC converter for DC distribution of future energy efficient homes*. in *IECON 2014 - 40th Annual Conference of the IEEE Industrial Electronics Society*. 2014.
54. Nahavandi, A., et al., *A nonisolated multiinput multioutput DC–DC boost converter for electric vehicle applications*. IEEE Transactions on Power Electronics, 2015. **30**(4): p. 1818-1835.

55. Zandi, M., et al., *Energy Management of a Fuel Cell/Supercapacitor/Battery Power Source for Electric Vehicular Applications*. IEEE Transactions on Vehicular Technology, 2011. **60**(2): p. 433-443.
56. Wang, L., E.G. Collins, and H. Li, *Optimal Design and Real-Time Control for Energy Management in Electric Vehicles*. IEEE Transactions on Vehicular Technology, 2011. **60**(4): p. 1419-1429.
57. Payman, A., et al., *An Adapted Control Strategy to Minimize DC-Bus Capacitors of a Parallel Fuel Cell/Ultracapacitor Hybrid System*. IEEE Transactions on Power Electronics, 2011. **26**(12): p. 3843-3852.
58. Thounthong, P., S. Pierfederici, and B. Davat, *Analysis of Differential Flatness-Based Control for a Fuel Cell Hybrid Power Source*. IEEE Transactions on Energy Conversion, 2010. **25**(3): p. 909-920.
59. Bharadwaj, S., K. Santha, and S. Arulmozhi. *Design And Analysis Of Integrated Dual-Input Dual-Output DC-DC Converter For Electric Vehicle And Drives Applications*. in *2023 9th International Conference on Electrical Energy Systems (ICEES)*. 2023.
60. Ferahtia, S., et al., *A hybrid power system based on fuel cell, photovoltaic source and supercapacitor*. SN Applied Sciences, 2020. **2**.
61. Taghizad-Tavana, K., et al., *A Comprehensive Review of Electric Vehicles in Energy Systems: Integration with Renewable Energy Sources, Charging Levels, Different Types, and Standards*. Energies, 2023. **16**: p. 630.
62. Bhatti, A., et al., *Electric vehicles charging using photovoltaic: Status and technological review*. Renewable and Sustainable Energy Reviews, 2015. **54C**: p. 34-47.
63. Nazih, Y., et al., *A Ring-Connected Dual Active Bridge Based DC-DC Multiport Converter for EV Fast-Charging Stations*. IEEE Access, 2022. **10**: p. 52052-52066.
64. Vasiladiotis, M. and A. Rufer, *A Modular Multiport Power Electronic Transformer With Integrated Split Battery Energy Storage for Versatile Ultrafast EV Charging Stations*. IEEE Transactions on Industrial Electronics, 2015. **62**(5): p. 3213-3222.
65. Qing, C., et al. *A new model for multiple-winding transformer*. in *Proceedings of 1994 Power Electronics Specialist Conference - PESC'94*. 1994.
66. Doncker, R.W.A.A.D., D.M. Divan, and M.H. Kheraluwala, *A three-phase soft-switched high-power-density DC/DC converter for high-power applications*. IEEE Transactions on Industry Applications, 1991. **27**(1): p. 63-73.
67. Kheraluwala, M.N., et al., *Performance characterization of a high-power dual active bridge DC-to-DC converter*. IEEE Transactions on Industry Applications, 1992. **28**(6): p. 1294-1301.

68. Kheraluwala, M.H. and R.W.D. Doncker. *Single phase unity power factor control for dual active bridge converter*. in *Conference Record of the 1993 IEEE Industry Applications Conference Twenty-Eighth IAS Annual Meeting*. 1993.
69. Biela, J., et al., *SiC versus Si—Evaluation of Potentials for Performance Improvement of Inverter and DC–DC Converter Systems by SiC Power Semiconductors*. IEEE Transactions on Industrial Electronics, 2011. **58**(7): p. 2872-2882.
70. Fan, H. and H. Li, *High-Frequency Transformer Isolated Bidirectional DC–DC Converter Modules With High Efficiency Over Wide Load Range for 20 kVA Solid-State Transformer*. IEEE Transactions on Power Electronics, 2011. **26**(12): p. 3599-3608.
71. Madhusoodhanan, S., et al., *Solid-State Transformer and MV Grid Tie Applications Enabled by 15 kV SiC IGBTs and 10 kV SiC MOSFETs Based Multilevel Converters*. IEEE Transactions on Industry Applications, 2015. **51**(4): p. 3343-3360.
72. Sabahi, M., et al., *Flexible Power Electronic Transformer*. IEEE Transactions on Power Electronics, 2010. **25**(8): p. 2159-2169.
73. Bhatnagar, M. and B.J. Baliga, *Comparison of 6H-SiC, 3C-SiC, and Si for power devices*. IEEE Transactions on Electron Devices, 1993. **40**(3): p. 645-655.
74. Inoue, S. and H. Akagi. *A bi-directional isolated DC/DC converter as a core circuit of the next-generation medium-voltage power conversion system*. in *2006 37th IEEE Power Electronics Specialists Conference*. 2006.
75. Krismer, F. and J.W. Kolar, *Closed Form Solution for Minimum Conduction Loss Modulation of DAB Converters*. IEEE Transactions on Power Electronics, 2012. **27**(1): p. 174-188.
76. Naayagi, R.T. and A.J. Forsyth. *Bidirectional DC-DC converter for aircraft electric energy storage systems*. in *5th IET International Conference on Power Electronics, Machines and Drives (PEMD 2010)*. 2010.
77. Shamshuddin, M.A., et al. *Solid State Transformers: Concepts, Classification, and Control*. Energies, 2020. **13**, DOI: 10.3390/en13092319.
78. Brooks, J.L., *Solid State Transformer Concept Development*. Port Hueneme, CA, USA: Naval Construction Battalion Center, Naval Mater Command,, 1980.
79. Gao, C., et al., *Generalized Model of n-Port Modular Multi-Active-Bridge Converter With Multiple-Phase-Shift Modulation*. IEEE Transactions on Transportation Electrification, 2024: p. 1-1.
80. Wang, H., et al., *High-Frequency-Link-Based Reactive-Power Optimal Control for Modular Multi Active Bridge Converter*. IEEE Journal of Emerging and Selected Topics in Industrial Electronics, 2023: p. 1-4.

81. Wang, H., et al. *Comparison and Improvement of ZVS Operation Under Different Modulation Strategies for Modular Multi Active Bridge Converters*. in *2023 IEEE Energy Conversion Congress and Exposition (ECCE)*. 2023.
82. Wang, H., et al., *ZVS Soft Switching Operation Region Analysis of Modular Multi Active Bridge Converter Under Single Phase Shift Control*. *IEEE Transactions on Industrial Electronics*, 2023. **70**(7): p. 6865-6875.
83. Zumel, P., et al. *Overall analysis of a modular multi active bridge converter*. in *2014 IEEE 15th Workshop on Control and Modeling for Power Electronics (COMPEL)*. 2014.
84. Costa, L.F., G. Buticchi, and M. Liserre, *Optimum Design of a Multiple-Active-Bridge DC–DC Converter for Smart Transformer*. *IEEE Transactions on Power Electronics*, 2018. **33**(12): p. 10112-10121.
85. Gu, C., et al., *Modeling and Control of a Multiport Power Electronic Transformer (PET) for Electric Traction Applications*. *IEEE Transactions on Power Electronics*, 2016. **31**(2): p. 915-927.
86. Xu, Q., et al., *Analysis and Comparison of Modular Railway Power Conditioner for High-Speed Railway Traction System*. *IEEE Transactions on Power Electronics*, 2017. **32**(8): p. 6031-6048.
87. Safayatullah, M., et al., *A Comprehensive Review of Power Converter Topologies and Control Methods for Electric Vehicle Fast Charging Applications*. *IEEE Access*, 2022. **10**: p. 40753-40793.
88. Hou, N. and Y.W. Li, *Overview and Comparison of Modulation and Control Strategies for a Nonresonant Single-Phase Dual-Active-Bridge DC–DC Converter*. *IEEE Transactions on Power Electronics*, 2020. **35**(3): p. 3148-3172.
89. Zhao, B., Q. Yu, and W. Sun, *Extended-Phase-Shift Control of Isolated Bidirectional DC–DC Converter for Power Distribution in Microgrid*. *IEEE Transactions on Power Electronics*, 2012. **27**(11): p. 4667-4680.
90. Krismer, F. and J.W. Kolar, *Accurate Power Loss Model Derivation of a High-Current Dual Active Bridge Converter for an Automotive Application*. *IEEE Transactions on Industrial Electronics*, 2010. **57**(3): p. 881-891.
91. Bai, H., C.C. Mi, and S. Gargies, *The Short-Time-Scale Transient Processes in High-Voltage and High-Power Isolated Bidirectional DC–DC Converters*. *IEEE Transactions on Power Electronics*, 2008. **23**(6): p. 2648-2656.
92. Kumar, A., A.H. Bhat, and P. Agarwal. *Comparative analysis of dual active bridge isolated DC to DC converter with single phase shift and extended phase shift control techniques*. in *2017 6th International Conference on Computer Applications In Electrical Engineering-Recent Advances (CERA)*. 2017.

93. Bai, H., Z. Nie, and C.C. Mi, *Experimental Comparison of Traditional Phase-Shift, Dual-Phase-Shift, and Model-Based Control of Isolated Bidirectional DC–DC Converters*. IEEE Transactions on Power Electronics, 2010. **25**(6): p. 1444-1449.
94. Shao, S., et al., *Circulating Current and ZVS-on of a Dual Active Bridge DC-DC Converter: A Review*. IEEE Access, 2019. **7**: p. 50561-50572.
95. Xu, G., et al., *Decoupled EPS Control Utilizing Magnetizing Current to Achieve Full Load Range ZVS for Dual Active Bridge Converters*. IEEE Transactions on Industrial Electronics, 2022. **69**(5): p. 4801-4813.
96. Oggier, G.G., et al. *Extending the ZVS operating range of dual active bridge high-power DC-DC converters*. in *2006 37th IEEE Power Electronics Specialists Conference*. 2006.
97. Oggier, G.G., G.O. García, and A.R. Oliva, *Switching Control Strategy to Minimize Dual Active Bridge Converter Losses*. IEEE Transactions on Power Electronics, 2009. **24**(7): p. 1826-1838.
98. Oggier, G., G.O. García, and A.R. Oliva, *Modulation strategy to operate the dual active bridge DC-DC converter under soft switching in the whole operating range*. IEEE Transactions on Power Electronics, 2011. **26**(4): p. 1228-1236.
99. Zhang, Z., et al. *An Improved DC Bias Elimination Strategy with Extended Phase Shift Control for Dual-Active-Bridge DC-DC*. in *2019 Chinese Automation Congress (CAC)*. 2019.
100. Qin, H. and J.W. Kimball, *Generalized Average Modeling of Dual Active Bridge DC–DC Converter*. IEEE Transactions on Power Electronics, 2012. **27**(4): p. 2078-2084.
101. Hirose, T. and H. Matsuo. *A consideration of bidirectional superposed dual active bridge dc-dc converter*. in *The 2nd International Symposium on Power Electronics for Distributed Generation Systems*. 2010.
102. Zhao, B., et al., *Current-Stress-Optimized Switching Strategy of Isolated Bidirectional DC–DC Converter With Dual-Phase-Shift Control*. IEEE Transactions on Industrial Electronics, 2013. **60**(10): p. 4458-4467.
103. Bai, H. and C. Mi, *Eliminate Reactive Power and Increase System Efficiency of Isolated Bidirectional Dual-Active-Bridge DC–DC Converters Using Novel Dual-Phase-Shift Control*. IEEE Transactions on Power Electronics, 2008. **23**(6): p. 2905-2914.
104. Zhao, B., Q. Song, and W. Liu, *Efficiency Characterization and Optimization of Isolated Bidirectional DC–DC Converter Based on Dual-Phase-Shift Control for DC Distribution Application*. IEEE Transactions on Power Electronics, 2013. **28**(4): p. 1711-1727.
105. L. Zhu, J.S.L., and F. C. Lee, *Start-up circuit and control for high power isolated DC/DC converters*. U.S. Patent, 2003.

106. Krismer, F. and J.W. Kolar. *Accurate small-signal model for an automotive bidirectional Dual Active Bridge converter*. in *2008 11th Workshop on Control and Modeling for Power Electronics*. 2008.
107. Guo, Z., M. Li, and X. Han, *Triple-Phase Shift Modulation Scheme of DAB Converter With LCL Resonant Tank*. *IEEE Transactions on Transportation Electrification*, 2022. **8**(2): p. 1734-1747.
108. Lin, F., et al., *Automatic Triple Phase-Shift Modulation for DAB Converter With Minimized Power Loss*. *IEEE Transactions on Industry Applications*, 2022. **58**(3): p. 3840-3851.
109. Capó-Llitas, M., et al., *Analytical and Normalized Equations to Implement the Optimized Triple Phase-Shift Modulation Strategy for DAB Converters*. *IEEE Journal of Emerging and Selected Topics in Power Electronics*, 2023. **11**(3): p. 3535-3546.
110. Li, X., et al., *Artificial-Intelligence-Based Triple Phase Shift Modulation for Dual Active Bridge Converter With Minimized Current Stress*. *IEEE Journal of Emerging and Selected Topics in Power Electronics*, 2023. **11**(4): p. 4430-4441.
111. Wu, K., C.W.d. Silva, and W.G. Dunford, *Stability Analysis of Isolated Bidirectional Dual Active Full-Bridge DC–DC Converter With Triple Phase-Shift Control*. *IEEE Transactions on Power Electronics*, 2012. **27**(4): p. 2007-2017.
112. Vardhan, H., M. Odavic, and K. Atallah. *Comprehensive analysis and design optimization of the Dual Active Bridge DC-DC converter with finite magnetizing inductance*. in *2023 IEEE Applied Power Electronics Conference and Exposition (APEC)*. 2023.
113. Yin, S., et al. *Impact of the Transformer Magnetizing Inductance on the Performance of the Dual-Active Bridge Converter*. in *2021 IEEE 22nd Workshop on Control and Modelling of Power Electronics (COMPEL)*. 2021.
114. Anwar, S. and D. Costinett. *Modeling Dual Active Bridge Converter Considering the Effect of Magnetizing Inductance for Electric Vehicle Application*. in *2018 IEEE Energy Conversion Congress and Exposition (ECCE)*. 2018.
115. Soleimanifard, M. and A.Y. Varjani. *Extended Phase Shift Control in Dual Active Bridge Converter Considering Magnetizing Inductance of Transformer*. in *2021 29th Iranian Conference on Electrical Engineering (ICEE)*. 2021.
116. Buffolo, M., et al., *Review and Outlook on GaN and SiC Power Devices: Industrial State-of-the-Art, Applications, and Perspectives*. *IEEE Transactions on Electron Devices*, 2024. **71**(3): p. 1344-1355.
117. Zhao, B., et al., *Dead-Time Effect of the High-Frequency Isolated Bidirectional Full-Bridge DC–DC Converter: Comprehensive Theoretical Analysis and Experimental Verification*. *IEEE Transactions on Power Electronics*, 2014. **29**(4): p. 1667-1680.

118. Gao, S., et al. *Analysis of DAB Dead-Time Effect Based on Extended-Phase-Shift Control*. in *IECON 2023- 49th Annual Conference of the IEEE Industrial Electronics Society*. 2023.
119. Jin, X., et al. *Improved Triple-phase-shift Control for DAB Converter to Minimize Current Stress with All-ZVS Operation Considering Dead-time Effect*. in *2021 IEEE 12th Energy Conversion Congress & Exposition - Asia (ECCE-Asia)*. 2021.
120. Song, C., et al. *Dead-time effect analysis of dual active bridge DC-DC converter with dual-phase-shift control*. in *2017 Chinese Automation Congress (CAC)*. 2017.
121. Kouros, S., et al., *Model Predictive Control—A Simple and Powerful Method to Control Power Converters*. *IEEE Transactions on Industrial Electronics*, 2009. **56**(6): p. 1826-1838.
122. Vazquez, S., et al., *Model Predictive Control: A Review of Its Applications in Power Electronics*. *IEEE Industrial Electronics Magazine*, 2014. **8**(1): p. 16-31.
123. Vazquez, S., et al., *Model Predictive Control for Power Converters and Drives: Advances and Trends*. *IEEE Transactions on Industrial Electronics*, 2017. **64**(2): p. 935-947.
124. Geyer, T. and D.E. Quevedo, *Multistep Finite Control Set Model Predictive Control for Power Electronics*. *IEEE Transactions on Power Electronics*, 2014. **29**(12): p. 6836-6846.
125. Cortes, P., et al. *Predictive control of a three-phase UPS inverter using two steps prediction horizon*. in *2010 IEEE International Conference on Industrial Technology*. 2010.
126. Chen, L., et al., *Moving Discretized Control Set Model-Predictive Control for Dual-Active Bridge With the Triple-Phase Shift*. *IEEE Transactions on Power Electronics*, 2020. **35**(8): p. 8624-8637.
127. Sun, J., et al., *Improved Model Predictive Control for Three-Phase Dual-Active-Bridge Converters With a Hybrid Modulation*. *IEEE Transactions on Power Electronics*, 2022. **37**(4): p. 4050-4064.
128. Chowdhury, S., et al., *Model Predictive Control for a Dual-Active Bridge Inverter With a Floating Bridge*. *IEEE Transactions on Industrial Electronics*, 2016. **63**(9): p. 5558-5568.
129. Xiao, Q., et al., *Model Predictive Control for Dual Active Bridge in Naval DC Microgrids Supplying Pulsed Power Loads Featuring Fast Transition and Online Transformer Current Minimization*. *IEEE Transactions on Industrial Electronics*, 2020. **67**(6): p. 5197-5203.
130. Chen, L., et al., *Model Predictive Control for Dual-Active-Bridge Converters Supplying Pulsed Power Loads in Naval DC Micro-Grids*. *IEEE Transactions on Power Electronics*, 2020. **35**(2): p. 1957-1966.
131. Biswas, I., D. Kastha, and P. Bajpai, *Small Signal Modeling and Decoupled Controller Design for a Triple Active Bridge Multiport DC-DC Converter*. *IEEE Transactions on Power Electronics*, 2021. **36**(2): p. 1856-1869.

132. Naseem, N. and H. Cha, *Triple-Active-Bridge Converter With Automatic Voltage Balancing for Bipolar DC Distribution*. IEEE Transactions on Power Electronics, 2022. **37**(7): p. 8640-8648.
133. Yang, J., et al., *A Generalized Input Impedance Model of Multiple Active Bridge Converter*. IEEE Transactions on Transportation Electrification, 2020. **6**(4): p. 1695-1706.
134. Tao, H., et al., *Transformer-Coupled Multiport ZVS Bidirectional DC–DC Converter With Wide Input Range*. IEEE Transactions on Power Electronics, 2008. **23**(2): p. 771-781.
135. Grabarek, M., M. Parchomiuk, and R. Strzelecki. *Conjugated control of triple active bridge converter with common HFT*. in *2017 11th IEEE International Conference on Compatibility, Power Electronics and Power Engineering (CPE-POWERENG)*. 2017.
136. Wang, L., Z. Wang, and H. Li, *Asymmetrical Duty Cycle Control and Decoupled Power Flow Design of a Three-port Bidirectional DC-DC Converter for Fuel Cell Vehicle Application*. IEEE Transactions on Power Electronics, 2012. **27**(2): p. 891-904.
137. Tran, Y.K., F.D. Freijedo, and D. Dujic, *Open-loop power sharing characteristic of a three-port resonant LLC converter*. CPSS Transactions on Power Electronics and Applications, 2019. **4**(2): p. 171-179.
138. Liao, M., et al., *Machine Learning Methods for Feedforward Power Flow Control of Multi-Active-Bridge Converters*. IEEE Transactions on Power Electronics, 2023. **38**(2): p. 1692-1707.
139. Cai, Y., et al., *Dynamic Performance Enhancement of a Triple Active Bridge with Power Decoupling-Based Configurable Model Predictive Control*. IEEE Transactions on Transportation Electrification, 2022: p. 1-1.
140. Akbar, S.M., et al., *Model Predictive Control With Triple Phase Shift Modulation for a Dual Active Bridge DC-DC Converter*. IEEE Access, 2021. **9**: p. 98603-98614.
141. Tahir, H.H. and A.A.A. Al-Rawi. *Variable Structure Control Design of Process Plant Based on Sliding Mode Approach*. in *2006 Chinese Control Conference*. 2006.
142. Iqbal, M., A.I. Bhatti, and Q. Khan. *Dynamic sliding modes control of uncertain nonlinear MIMO three tank system*. in *2009 IEEE 13th International Multitopic Conference*. 2009.
143. Lee, S., Y.C. Jeung, and D.C. Lee, *Voltage Balancing Control of IPOS Modular Dual Active Bridge DC/DC Converters Based on Hierarchical Sliding Mode Control*. IEEE Access, 2019. **7**: p. 9989-9997.
144. Bagheri, F., et al., *An Adaptive Sliding Mode Control for a Dual Active Bridge Converter With Extended Phase Shift Modulation*. IEEE Access, 2023. **11**: p. 91260-91274.
145. Tiwary, N., et al., *A Robust Voltage Control of DAB Converter With Super-Twisting Sliding Mode Approach*. IEEE Journal of Emerging and Selected Topics in Industrial Electronics, 2023. **4**(1): p. 288-298.

146. Jeung, Y.C. and D.C. Lee, *Voltage and Current Regulations of Bidirectional Isolated Dual-Active-Bridge DC–DC Converters Based on a Double-Integral Sliding Mode Control*. IEEE Transactions on Power Electronics, 2019. **34**(7): p. 6937-6946.
147. Agamy, M.S., et al., *A High Power Medium Voltage Resonant Dual Active Bridge for MVDC Ship Power Networks*. IEEE Journal of Emerging and Selected Topics in Power Electronics, 2017. **5**(1): p. 88-99.
148. Seidel, A. and B. Wicht, *Integrated Gate Drivers Based on High-Voltage Energy Storing for GaN Transistors*. IEEE Journal of Solid-State Circuits, 2018. **53**(12): p. 3446-3454.
149. Shin, H.J. and T.W. Kim, *Ultra-High-Image-Density, Large-Size Organic Light-Emitting Device Panels Based on Highly Reliable Gate Driver Circuits Integrated by Using InGaZnO Thin-Film Transistors*. IEEE Journal of the Electron Devices Society, 2019. **7**: p. 1109-1113.
150. Wang, J., et al., *In-Depth Design and Multiobjective Optimization of an Integrated Transformer for Five-Phase LLC Resonant Converters*. IEEE Transactions on Power Electronics, 2022. **37**(11): p. 13538-13553.
151. Wu, H., et al., *Integrated Transformers With Magnetic Thin Films*. IEEE Transactions on Magnetics, 2016. **52**(7): p. 1-4.
152. FRROXCUBE, *Design of Planar Power Transformer*.
153. McLyman, C.W.T., *Transformer and Inductor Design Handbook*. 4th Edition ed. 2017, Boca Raton: Marcel Dekker, Inc. 667.
154. Bo, Y., C. Rengang, and F.C. Lee. *Integrated magnetic for LLC resonant converter*. in *APEC. Seventeenth Annual IEEE Applied Power Electronics Conference and Exposition (Cat. No.02CH37335)*. 2002.
155. Wenduo, L. and J.D.v. Wyk. *Design of integrated LLCT module for LLC resonant converter*. in *Twentieth Annual IEEE Applied Power Electronics Conference and Exposition, 2005. APEC 2005*. 2005.
156. Ouyang, Z., O.C. Thomsen, and M.A.E. Andersen. *The analysis and comparison of leakage inductance in different winding arrangements for planar transformer*. in *2009 International Conference on Power Electronics and Drive Systems (PEDS)*. 2009.
157. D'Antonio, M., S. Chakraborty, and A. Khaligh, *Planar Transformer With Asymmetric Integrated Leakage Inductance Using Horizontal Air Gap*. IEEE Transactions on Power Electronics, 2021. **36**(12): p. 14014-14028.
158. Park, C.W. and S.K. Han. *Design of an integrated magnetics structure for LLC resonant converter*. in *IECON 2017 - 43rd Annual Conference of the IEEE Industrial Electronics Society*. 2017.

159. Zhang, J., et al., *Leakage Inductance Calculation for Planar Transformers With a Magnetic Shunt*. IEEE Transactions on Industry Applications, 2014. **50**(6): p. 4107-4112.
160. Meinhardt, M., et al. *New method for integration of resonant inductor and transformer-design, realisation, measurements*. in *APEC '99. Fourteenth Annual Applied Power Electronics Conference and Exposition. 1999 Conference Proceedings (Cat. No.99CH36285)*. 1999.
161. Li, B., Q. Li, and F.C. Lee, *High-Frequency PCB Winding Transformer With Integrated Inductors for a Bi-Directional Resonant Converter*. IEEE Transactions on Power Electronics, 2019. **34**(7): p. 6123-6135.
162. Li, M., Z. Ouyang, and M.A.E. Andersen, *High-Frequency LLC Resonant Converter With Magnetic Shunt Integrated Planar Transformer*. IEEE Transactions on Power Electronics, 2019. **34**(3): p. 2405-2415.
163. Pavlovsky, M., S.W.H.d. Haan, and J.A. Ferreira. *Partial Interleaving: A Method to Reduce High Frequency Losses and to Tune the Leakage Inductance in High Current, High Frequency Transformer Foil Windings*. in *2005 IEEE 36th Power Electronics Specialists Conference*. 2005.
164. Huang, J., et al. *An Integrated Three-phase Transformer for Partial Parallel Dual Active Bridge Converter*. in *2019 10th International Conference on Power Electronics and ECCE Asia (ICPE 2019 - ECCE Asia)*. 2019.
165. Li, B., Q. Li, and F.C. Lee. *A novel PCB winding transformer with controllable leakage integration for a 6.6kW 500kHz high efficiency high density bi-directional on-board charger*. in *2017 IEEE Applied Power Electronics Conference and Exposition (APEC)*. 2017.
166. Wan, Z., et al., *Optimization Design of High-Frequency Matrix Transformer for Solid-State Transformer*. IEEE Transactions on Power Electronics, 2024: p. 1-12.
167. Eslamian, M., M. Bigdeli, and A. Abu-Siada, *High frequency modeling of dry type detuned reactor for transient studies: Simulation and experimental analyses*. Electric Power Systems Research, 2024. **228**: p. 110102.
168. Hernandez, I., F.d. Leon, and P. Gomez, *Design Formulas for the Leakage Inductance of Toroidal Distribution Transformers*. IEEE Transactions on Power Delivery, 2011. **26**(4): p. 2197-2204.
169. Schlesinger, R. and J. Biela, *Improved Analytical Triple-2D Leakage Inductance Model of Cone Winding Matrix Transformers*. IEEE Open Journal of Power Electronics, 2023. **4**: p. 252-264.
170. Qiao, G., et al. *Precise Evaluation of Leakage Inductance of High-Frequency Transformer*. in *2020 7th International Forum on Electrical Engineering and Automation (IFEEA)*. 2020.
171. Chen, X., et al., *Magnetizing and Leakage Inductance Integration for Split Transformers With Standard UI Cores*. IEEE Transactions on Power Electronics, 2022. **37**(11): p. 12980-12985.

172. Ansari, S.A., J.N. Davidson, and M.P. Foster, *Fully-Integrated Planar Transformer With a Segmental Shunt for LLC Resonant Converters*. IEEE Transactions on Industrial Electronics, 2022. **69**(9): p. 9145-9154.
173. Li, M., et al. *Analysis and modeling of integrated magnetics for LLC resonant converters*. in *IECON 2017 - 43rd Annual Conference of the IEEE Industrial Electronics Society*. 2017.
174. Li, M., Z. Ouyang, and M.A.E. Andersen. *High frequency LLC resonant converter with magnetic shunt integrated planar transformer*. in *2018 IEEE Applied Power Electronics Conference and Exposition (APEC)*. 2018.
175. Zhang, J., et al. *Leakage inductance calculation for planar transformers with a magnetic shunt*. in *2013 IEEE Energy Conversion Congress and Exposition*. 2013.
176. Lee, E.S., et al., *High Efficiency Integrated Transformer Design in DAB Converters for Solid-State Transformers*. IEEE Transactions on Vehicular Technology, 2022. **71**(7): p. 7147-7160.
177. Park, Y., S. Chakraborty, and A. Khaligh, *DAB Converter for EV Onboard Chargers Using Bare-Die SiC MOSFETs and Leakage-Integrated Planar Transformer*. IEEE Transactions on Transportation Electrification, 2022. **8**(1): p. 209-224.
178. Rashidi, M., et al., *Design and Development of a High-Frequency Multiport Solid-State Transformer With Decoupled Control Scheme*. IEEE Transactions on Industry Applications, 2019. **55**(6): p. 7515-7526.
179. Shafei, A.E., et al. *A Complete Design of a High Frequency Medium Voltage Multi-Port Transformer*. in *2019 8th International Conference on Renewable Energy Research and Applications (ICRERA)*. 2019.
180. Kumar, B.M., et al. *Comparative study of dual active bridge isolated DC to DC converter with single phase shift and dual phase shift control techniques*. in *2017 Recent Developments in Control, Automation & Power Engineering (RDCAPE)*. 2017.
181. Lai, Y. and S. Chen. *New switching control technique to improve the efficiency under light load condition for LLC converter with large magnetizing inductance*. in *2015 IEEE International Telecommunications Energy Conference (INTELEC)*. 2015.
182. Wang, C., et al. *Efficiency improvement in adjustable deadtime of LLC resonant converters*. in *2014 International Conference on Intelligent Green Building and Smart Grid (IGBSG)*. 2014.
183. Everts, J., et al., *Optimal ZVS Modulation of Single-Phase Single-Stage Bidirectional DAB AC-DC Converters*. IEEE Transactions on Power Electronics, 2014. **29**(8): p. 3954-3970.
184. Xintao, G., et al. *A 10kW DC-DC system based on a bidirectional high-frequency isolated dual active bridge DC-DC topology*. in *2011 IEEE Power Engineering and Automation Conference*. 2011.

185. Zhang, J.M., et al. *A novel ZVS DC/DC converter for high power applications*. in *APEC. Seventeenth Annual IEEE Applied Power Electronics Conference and Exposition (Cat. No.02CH37335)*. 2002.
186. Everts, J., et al. *Charge-based ZVS soft switching analysis of a single-stage dual active bridge AC-DC converter*. in *2013 IEEE Energy Conversion Congress and Exposition*. 2013.
187. Spreen, J.H., *Electrical terminal representation of conductor loss in transformers*. IEEE Transactions on Power Electronics, 1990. **5**(4): p. 424-429.
188. L.Dowell, P., *Effects of eddy currents in transformer windings*. Proc. IEEE, Aug. 1966. **113**, no. **8**, pp. **1387–1394**.
189. Stumberger, G., et al., *Prevention of Iron Core Saturation in Multi-Winding Transformers for DC-DC Converters*. IEEE Transactions on Magnetics, 2010. **46**(2): p. 582-585.
190. Mauchly, J., *Theory and techniques for the design of electronic digital computers*. GW Patterson, ed, 1946. **1**: p. 9.7-9.8.
191. VARGA, R. and H. MA, *The art of computer programming. Vol. 3: sorting and searching*. 1973, Addison-Wesley Publishing Company Inc, Second edition. p. 422.
192. Gu, C., et al., *A Multiport Power Conversion System for the More Electric Aircraft*. IEEE Transactions on Transportation Electrification, 2020. **6**(4): p. 1707-1720.
193. Knuth, D.E., *The Art of Computer Programming/Sorting and Searching, Volumes 3*. 1973, Addison Wesley.
194. Dennis, J.E. and J.M. Jorge, *Quasi-Newton Methods, Motivation and Theory*. SIAM review, 1977. **19**(1): p. 46-89.
195. Biela, J. and J.W. Kolar. *Electromagnetic integration of high power resonant circuits comprising high leakage inductance transformers*. in *2004 IEEE 35th Annual Power Electronics Specialists Conference (IEEE Cat. No.04CH37551)*. 2004.
196. Gu, C., et al. *Lumped-Parameter Equivalent Circuit Models of a Multi-Winding Transformer for DAB and MAB Applications*. in *2022 IEEE Transportation Electrification Conference and Expo, Asia-Pacific (ITEC Asia-Pacific)*. 2022.
197. Barrios, E.L., et al., *High-Frequency Power Transformers With Foil Windings: Maximum Interleaving and Optimal Design*. IEEE Transactions on Power Electronics, 2015. **30**(10): p. 5712-5723.
198. Huber, J.E., et al., *Analysis and cell-level experimental verification of a 25 kW all-SiC isolated front end 6.6 kV/400 V AC-DC solid-state transformer*. CPSS Transactions on Power Electronics and Applications, 2017. **2**(2): p. 140-148.